University of Southampton

University of Southampton Research Repository

Copyright © and Moral Rights for this thesis and, where applicable, any accompanying data are retained by the author and/or other copyright owners. A copy can be downloaded for personal non-commercial research or study, without prior permission or charge. This thesis and the accompanying data cannot be reproduced or quoted extensively from without first obtaining permission in writing from the copyright holder/s. The content of the thesis and accompanying research data (where applicable) must not be changed in any way or sold commercially in any format or medium without the formal permission of the copyright holder/s.

When referring to this thesis and any accompanying data, full bibliographic details must be given, e.g.

Thesis: Author (Year of Submission) "Full thesis title", University of Southampton, name of the University Faculty or School or Department, PhD Thesis, pagination.

Data: Author (Year) Title. URI [dataset]

University of Southampton

Faculty of Engineering and Physical Sciences

School of Physics and Astronomy

Membrane Quantum Well Lasers and Tantalum Pentoxide Optical Waveguides

by

Stephen Constantine Richardson

ORCID ID 0009-0008-2346-0372

Thesis for the degree of Doctor of Philosophy

11 December 2025

University of Southampton

Abstract

Faculty of Engineering and Physical Sciences

School of Physics and Astronomy

Doctor of Philosophy

Membrane Quantum Well Lasers for Photonic Integrated Circuits

by

Stephen Constantine Richardson

This thesis investigates two different optical technologies, membrane quantum well lasers and tantalum pentoxide rib waveguides and resonators. The former technology is explored as a potential coherent light source and amplifier for photonic integrated circuits. The latter technology is studied with the aim of exploiting the material's high nonlinear properties to generate Kerr frequency combs for various applications such as optical telecommunications and remote sensing.

Membrane quantum well lasers are semiconductor edge emitting laser devices, where stimulated emission occurs in the quantum well regions and is enhanced due to the strong waveguiding effect. The laser is optically pumped while in contact with a silicon carbide or silicon dioxide on silicon wafer as part of the heatsinking system. Oxidised silicon is of great interest due to the fact that many wafers are silicon based. Here I demonstrate the device's lasing performance such us output power, spectral tunability, single and multiple laser cavity operation using imaging and pump beam shaping techniques. Phase locked laser arrays were particularly investigated with respect to their mutual phase relationship on a silicon dioxide substrate.

Models were developed to simulate waveguiding inside the membrane quantum well lasers and therefore, the display the guided transverse electric and magnetic modes to extract information such as effective and group refractive index and free spectral range between the laser's longitudinal modes. An attempt was also made to simulate laser arrays based on gain – guiding.

Tantalum pentoxide rib waveguides and micro – ring and racetrack resonators were fabricated inside a cleanroom via photolithography and electron beam lithography for comparison. Transmission spectra were acquired from the structures to calculate optical losses, quality factors, resonant probe wavelengths in the vicinity of $1.55\ \mu m$, linewidth full – width at half – maximum, free spectral ranges and resonator finesse. Despite quality factors being of the order of 10^5, no Kerr frequency combs were observed.

Models were developed to simulate waveguiding in tantalum pentoxide linear waveguides and resonators, from which effective refractive indices and effective areas were extracted after sweeping the probe wavelength. A numerical model was created and introduces the propagation mode parameters to generate Kerr frequency combs.

Table of Contents

List of Tables

List of Figures

List of Publications and Conference Presentations

[1] Jonathan R. C. Woods, Jon Gorecki, Jake Daykin, **Stephen Richardson**, Michael Jetter, Roman Bek, Emelia Branagan-Harris, Grace Hooper, James S. Wilkinson, Anne C. Tropper, and Vasilis Apostolopoulos "Semiconductor in-plane membrane quantum-well lasers", Proc. SPIE PC12021, Novel In-Plane Semiconductor Lasers XXI, PC1202105 (9 March 2022).

[2] Jonathan R. C. Woods, Jon Gorecki, Roman Bek, **Stephen C. Richardson**, Jake Daykin, Grace Hooper, Emelia Branagan-Harris, Anne C. Tropper, James S. Wilkinson, Michael Jetter, Peter Michler, and Vasilis Apostolopoulos. Coherent waveguide laser arrays in semiconductor quantum well membranes. Optics Express, 30(18):32174, Aug 2022.

[3] **Stephen C. Richardson**, Jonathan R. C. Woods, Jake Daykin, Jon Gorecki, Roman Bek, Nicholas T. Klokkou, James S. Wilkinson, Michael Jetter, and Vasileios Apostolopoulos. III-V compound semiconductor membrane quantum well waveguide lasers emitting at 1 μm. EPJ Web of Conferences, 266:01011, Oct 2022.

[4] Jake Daykin, Jonathan R. C. Woods, **Stephen C. Richardson**, Oliver J. Trojak, Jonathan M. Silver, Folly Eli Ayi-Yovo, Nicholas T Klokkou, Amy S. K. Tong, Patrick Gill, Alberto Politi, Peter Horak, James S. Wilkinson, and Vasilis Apostolopoulos "Tantalum pentoxide micro-resonators for Kerr micro-comb generation", Proc. SPIE PC12334, Emerging Applications in Silicon Photonics III, PC123340J (11 January 2023).

[5] **Stephen Richardson**, Jonathan Woods, Jake Daykin, Jon Gorecki, Roman Bek, Nicholas Klokkou, James Wilkinson, Michael Jetter, and Vasileios Apostolopoulos "III-V compound semiconductor membrane quantum well waveguide lasers emitting at 1 μm", Proc. SPIE PC12334, Emerging Applications in Silicon Photonics III, PC123340H (11 January 2023).

[6] Jake Daykin, Nicholas T. Klokkou, **Stephen C. Richardson**, Jonathan R. C. Woods, Roman Bek, Jon Gorecki, James S. Wilkinson, Michael Jetter, Peter Michler, and Vasilis Apostolopoulos "Semiconductor quantum well membranes for tunable coherent waveguide laser arrays", Proc. SPIE 12404, Vertical External Cavity Surface Emitting Lasers (VECSELs) XII, 1240404 (17 March 2023).

[7] Nicholas Klokkou, **Stephen C. Richardson**, Jake Daykin, J. R. C. Woods, J. Gorecki, Roman Bek, Michael Jetter, and Vasilis Apostolopoulos "Membrane quantum well waveguide lasers", Proc. SPIE PC12868, Vertical External Cavity Surface Emitting Lasers (VECSELs) XIII, PC128680E (13 March 2024).

[8] Vasilis Apostolopoulos, Nicholas Klokkou, **Stephen C. Richardson**, Michael Jetter, Roman Bek, Peter Michler, Jon Gorecki, Ananya Ghatak, and Konstantinos G Makris

"Membrane quantum well waveguide lasers", Proc. SPIE 13346, Vertical External Cavity Surface Emitting Lasers (VECSELs) XIV, 133460I (21 March 2025).

Research Thesis: Declaration of Authorship

Print name: Stephen Constantine Richardson

Title of thesis: Membrane Quantum Well Lasers and Tantalum Pentoxide Optical Waveguides

I declare that this thesis and the work presented in it are my own and has been generated by me as the result of my own original research.

I confirm that:

1. This work was done wholly or mainly while in candidature for a research degree at this University;
2. Where any part of this thesis has previously been submitted for a degree or any other qualification at this University or any other institution, this has been clearly stated;
3. Where I have consulted the published work of others, this is always clearly attributed;
4. Where I have quoted from the work of others, the source is always given. With the exception of such quotations, this thesis is entirely my own work;
5. I have acknowledged all main sources of help;
6. Where the thesis is based on work done by myself jointly with others, I have made clear exactly what was done by others and what I have contributed myself;
7. Parts of this work have been published as: please see List of Publications and Conference Presentations:

Signature: ..... Date:.....

Acknowledgements

This PhD project took place at the Quantum, Light and Matter Group, School of Physics and Astronomy, Faculty of Physical Sciences and Engineering, University of Southampton from September 2020 to September 2024, during which I encountered amazing new people, and learnt a lot about myself. I would like to show my appreciation towards everyone who was part of this journey.

I want to begin by thanking my supervisor, Professor Vasileios Apostolopoulos, for giving me the opportunity to work on this project, his guidance and support throughout the years, and for being a very understanding person especially when it came to mental health.

I would like to thank Dr Peter Horak for giving me the opportunity to meet up with him on numerous occasions and enlighten me with his knowledge of theoretical physics and simulations. I would, also, like to thank Neil Sessions for managing the cleanroom, training me, and dedicating time to discuss cleanroom processes. Without him, this PhD would not be possible. I also want to show my gratitude to Dr Jonathan Woods and Dr Jake Daykin from the University of Southampton for sharing their expertise on optics and lasers.

Dr Oliver Trojak from the University of Southampton and Dr Jonathan Silver from the National Physical Laboratories were instrumental in conducting some of the waveguide characterisation experiments to whom I am grateful for.

I would like to thank all new friends I met from the Quantum, Light and Matter Group as well as the Optoelectronics Research Centre. Besides talking about our PhDs and drinking, I value all the discussions we had and activities we did together. I got to learn about other nation's cultures and discover England.

I am grateful for the continuous support, patience and love I received from all my friends, relatives and my Seascout group from Greece, relatives from England, and friends from China. I will never forget all those video calls and social media messaging.

Also, I joined the Southampton Sailing Club. There I met and interacted with many wonderful people and shared stories during sailing and social activities. I became a committee member, acquired more sailing knowledge, built my confidence, and explored the south coast of England by sailing. I cherish all the memories and experiences I gained.

I am grateful for Dr Nicholas Klokkou's priceless insights, advice and guidance. I am glad I got to spend time with him and hoping for a friendship to flourish forever. In the Scouts we have a saying, *new friends are like silver but old are gold*. He instantly became gold.

Finally, I want to show my appreciation and love towards my parents, Chrysseis and Clive, and my siblings, Helen and Mark and their families for their endless support and love. Thank you for being there for me.

Definitions and Abbreviations

CCD ..... Charged – Coupled Device

CMOS ..... Complementary Metal – Oxide Semiconductor

CW ..... Continuous Wave

DBR ..... Distributed Bragg Reflector

DC ..... Direct Current

DI ..... Deionised (Water)

DMD ..... Digital Micromirror Device

DOF ..... Depth of focus

FSR ..... Free Spectral Range

FWHM ..... Full – Width at Half – Maximum

FWM ..... Four – Wave Mixing

GNLSE ..... Generalised Nonlinear Schrödinger Equation

GVD ..... Group – Velocity Dispersion

HF ..... Hydrofluoric Acid

IBS ..... Ion Beam Sputtering

IBM ..... Ion Beam Milling

ICP ..... Inductively Coupled Plasma

IPA ..... Isopropanol

IR ..... Infrared (Radiation)

LASER ..... Light Amplification by Stimulated Emission of Radiation

LF ..... Low Frequency

LIDAR ..... Light Detection and Ranging

LLE ..... Lugiato – Lefever Equation

LPF ..... Long Pass Filter

MECSEL ..... Membrane External – Cavity Surface – Emitting Laser

MIR ..... Mid Infrared (Radiation)

MQW ..... Multiple Quantum Well

MQWL..... Membrane Quantum Well Laser

ND ..... Neutral Density (Filter)

NLSE..... Nonlinear Schrödinger Equation

NPL..... National Physical Laboratory

OPSL ..... Optically Pumped Semiconductor Laser

OSA ..... Optical Spectrum Analyser

PECVD ..... Plasma – Enhanced Chemical Vapour Deposition

PIC ..... Photonic Integrated Circuit

PID ..... Proportional – Integral – Derivative (Servo)

PML ..... Perfectly Matched Layer

QW ..... Quantum Well

RF ..... Radio frequency

RIE..... Reactive Ion Etching

RPM..... Revolutions per Minute

SBC ..... Scattering Boundary Condition

SC ..... Supercontinuum

SDL..... Semiconductor Disk Laser

SEM ..... Scanning Electron Microscopy

SOI..... Silicon – On – Insulator

SPM ..... Self – Phase Modulation

SRS..... Stimulated Raman Scattering

TE ..... Transverse Electric (Mode)

TEC..... Thermoelectric Cooler

TEM ..... Transmission Electron Microscopy

TEOS..... Tetraethyl Orthosilicate

TM ..... Transverse Magnetic (Mode)

UV ..... Ultraviolet (Radiation)

VECSEL..... Vertical External – Cavity Surface – Emitting Laser

WDM ..... Wavelength – Division Multiplexing

WG ..... Waveguide

WGM ..... Whispering Gallery Mode

Chapter 1

Introduction and Theory

Optically pumped semiconductor lasers (OPSLs), also known as semiconductor disk lasers (SDLs) are semiconductor photonic devices consisting of quantum wells (QWs), where stimulated emission occurs. OPSL date back to the 1960s and remained a scientific curiosity until the mid - 1990s when its potential capabilities for high power and excellent beam quality were first fully demonstrated [1]. OPSLs applications vary as they emit from ultraviolet (UV) to mid infrared (MIR) radiation and successfully produce ultrafast pulses [1][2][3]. OPSLs are capable of edge emission, nominating them for potential interfacing with photonic integrated circuits (PICs) e.g., tantalum pentoxide (Ta_2O_5). Tantalum pentoxide or tantala is of great interest due to its high nonlinear properties, which are significant for spectral broadening effects. The focus of my PhD involves work done mainly on edge emitting OPSLs but also tantalum pentoxide micro resonator waveguides, aiming to couple the two devices. In this chapter I outline the physics governing surface and edge emitting quantum well lasers as well as tantalum pentoxide waveguides.

1.1 The Laser

Light Amplification by Stimulated Emission of Radiation (LASER or laser) is an optoelectronic device which emits visible or invisible light through an optical amplification process. As indicated by its name, stimulated emission is the driving atomic process behind the laser idea. Assuming two energy levels in a material known as gain medium or active material (Figure 1.1), an electron requires energy to jump from the lowest energy level (ground state) to the highest (excited state), a transition known as absorption. An electron in the higher energy level may transition radiatively to the lower energy level via two processes, spontaneous emission, or stimulated emission. Spontaneous emission is the process where the electron will spontaneously decay, releasing energy in the form of a photon. Stimulated emission is the process where an incident electromagnetic wave of specific frequency forces the electron in the excited state to drop in the ground state by releasing light in the same frequency and coherent to the incoming wave thus amplifying the light. The more electrons exist in the excited state relative to the ground state, which is known as population inversion, the higher the amplification or gain.

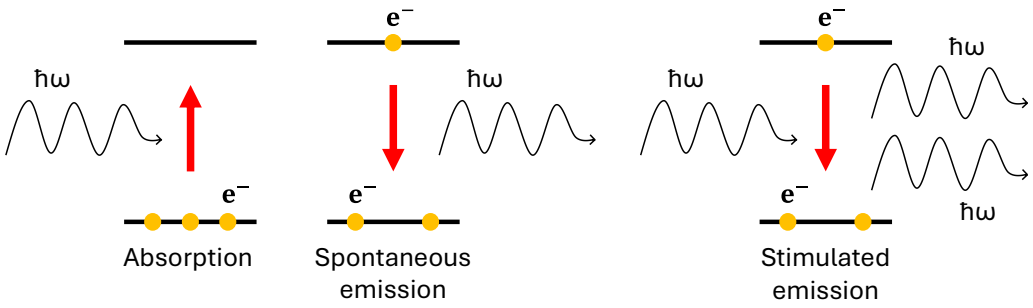

Figure 1.1 The three atomic processes describing a laser gain medium: absorption, spontaneous emission, and stimulated emission. Absorption occurs when electrons absorb energy sufficient to jump from the ground state to the excited state. Spontaneous emission is the radiative spontaneous decay of electrons from the excited state to the ground state. Stimulated emission is the forced radiative transition from the excited state to the ground state, where emitted photons are of the same frequency and are coherent to the incident wave thus amplifying the incoming light.

The scheme of a laser is key to support stimulated emission. A typical laser consists of two highly reflective mirrors, and the active material which is placed between the mirrors (Figure 1.2). These components compose the laser cavity or optical resonator in which standing electromagnetic waves form after light produced from the material bounces off the two mirrors. However, one of the two mirrors is partially reflective making it an output coupler to allow part of the light to exit the cavity. To initiate the process, the gain medium's electrons require to absorb energy sufficient to jump from the ground state to the higher energy levels. Depending on the laser design, this is achieved either by optical pumping i.e., irradiating the active material with light of higher frequency compared to the generated laser light, electrical pumping, or electrical discharge. Afterwards, some electrons radiatively spontaneously decay and the produced light, which corresponds to the energy difference between the two energy levels where population inversion occurs, is reflected by the cavity's mirrors. The reflected light propagates through the gain medium and induces stimulated emission thus generating and amplifying the laser light. The more passes light do inside the laser cavity, the more amplified the laser light is.

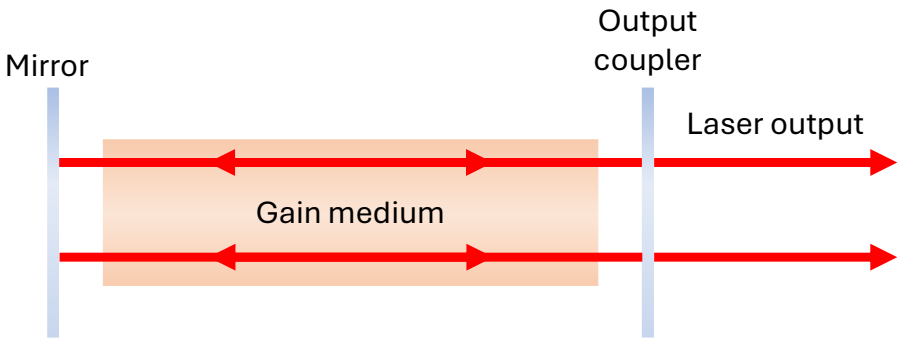

Figure 1.2 The laser cavity. The optical resonator consists of the gain medium and two highly reflective mirrors. Population inversion and stimulated emission occur in the active material, which is initiated by spontaneous emission and its light bouncing off the mirrors, which in turn is initiated by absorption by giving energy to the system either optically or electrically. One of the mirrors is the output coupler to allow laser light to exit the cavity.

Lasers are of great interest because their properties make them suitable for multiple applications. These properties include monochromaticity, coherence, directionality, and brightness. Two circumstances lead to monochromaticity. Only the electromagnetic wave with a frequency corresponding to the energy level difference where population inversion occurs is amplified. In addition, the laser cavity supports only resonant frequency wave oscillations. This gives rise to narrow laser linewidths compared to the broader spontaneous emission linewidths.

Coherence involves the phase relationship between the stimulated emission's photons and the incident photons enabling the atomic transition. The former deals with the phase relationship between electromagnetic waves at different locations in space at fixed times and the latter deals with the phase relationship at different times at a fixed positions in space.

Directionality is due to the optical resonator's reflective mirrors. Radiative transitions emit photons towards all directions; however, the laser cavity's reflective mirrors favour the ones along the cavity. Even so, the laser beam diverges due to diffraction by its nature and from optical elements such as the output coupler.

Finally, brightness is the laser's power emitted over a surface area and solid angle. Brightness and therefore optical power or light intensity is associated with optical amplification. The higher the population inversion in the gain medium the stronger stimulated emission is and hence gain increases. Consequently, light intensity rises exponentially, until gain saturates.

1.2 Quantum Well Lasers

Laser materials vary in their atomic and molecular properties, giving access to different light wavelengths ranging from infrared (IR) to X-Rays [4]. Some gain media include solid-state materials, dyes, and gases but also semiconductors [4]. Some semiconductor lasers are quantum well based.

Quantum wells are finite potential energy wells with discrete energy levels capable of confining charge carriers and whose width are $10\,nm$ wide or less [5]. QWs are formed by epitaxially growing semiconductor layers between confining semiconductor layers or barriers. The confined semiconductors have a low direct band gap energy, E_g, compared to the barriers.

The active region is the confined semiconductor layer. Population inversion occurs in the active region between the lower energy states of both conduction and valence band, $E_{c1} - E_{v1}$, as can be seen in Figure 1.3. The semiconductor layers are non – resonantly optically pumped with energy greater than the band gap energy of both confined and barrier layers. The electrons that acquire energy to move from the valence to the conduction band transition to the lower quantum state of the QW in the conduction band via multiphonon interactions. Electron – hole pairs are formed and recombine radiatively emitting light at a frequency corresponding to $E_{c1} - E_{v1}$. Fermi's Golden Rule allows transitions only between same quantum number energy states in an infinite QW, whereas in a finite QW, transitions can occur between different quantum numbers as well, however those transitions are less probable [6].

Multiple QWs (MQWs) are introduced because of their advantageous features such as electron overflow prevention in individual QWs [7], and optical gain and absorption increase. However, QW separation needs to be adequate to minimise the quantum tunnelling effect and avoid wave function overlap, otherwise electrons and holes will not be strongly confined in the QWs.

Whether it is a single QW or MQW laser device, the band gap energy and hence, emission wavelength may be affected by various reasons. The laser wavelength is predefined during the design and fabrication process by the QW thickness [8], [9], [10], semiconductor molar fraction [11], [12], strain due to lattice mismatch between semiconductor layers, spin – orbit coupling, Jahn – Teller distortion, and hydrostatic perturbation [13]. Laser wavelength tuning is achieved by varying the device's temperature [14], however, a more prominent tuning technique used in lasers, is the implementation of birefringent filters or tuners [15], [16], [17], [18].

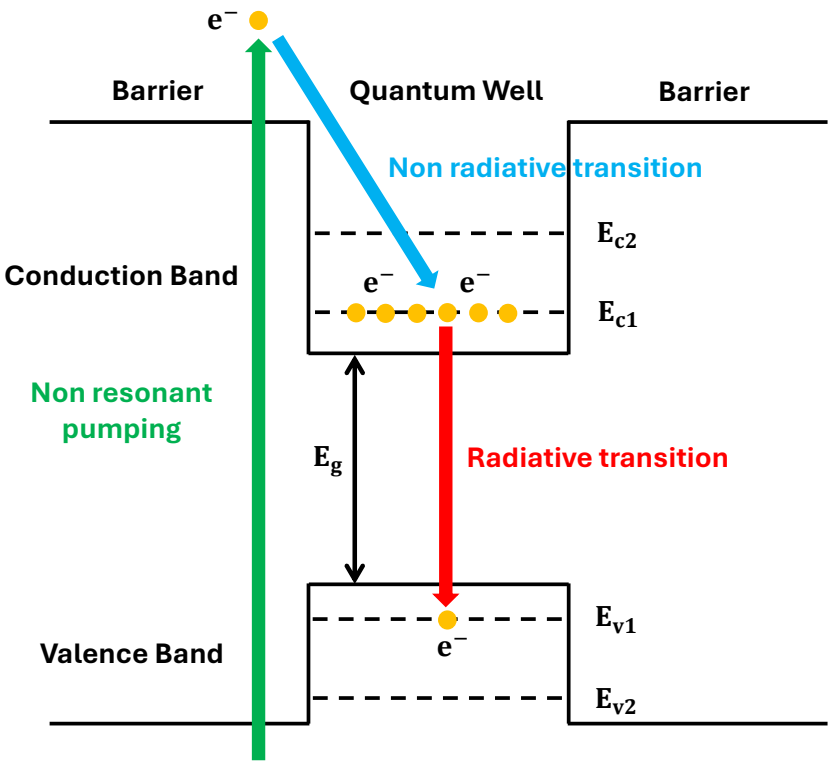

Figure 1.3 Optically pumped unstrained quantum well laser. Electrons jump to the conduction band via non resonant optical pumping and transition to the lower energy levels of the QW. Electrons recombine radiatively with the holes in the valence band emitting light at a frequency corresponding to $E_{c1} - E_{v1}$.

1.3 Vertical External – Cavity Surface – Emitting Lasers

Vertical external – cavity surface – emitting lasers (VECSELs) are semiconductor QW lasers, mainly consisting of III – V materials, which lase perpendicular to the device's surface or parallel to the layer growth direction. VECSELs continue to be extensively researched due to their properties and application range [19]. VECSELs emit from UV to IR wavelengths depending on the semiconductor materials used to create the QWs, offer relatively high slope efficiencies and excellent beam quality, which degrades at higher optical powers, and is suitable for picosecond to femtosecond pulse generation via mode – locking mechanism [3], [19].

VECSELs are implemented in various laser cavity configurations such as linear cavity, V – cavity, Z – cavity, and multiple gain cavity [19]. A typical linear VECSEL optical resonator [19] consists of a distributed Bragg reflector (DBR), where the gain chip is grown onto, and an output coupler mirror (Figure 1.4). The DBR acts as one of the reflective mirrors and is placed on a heat spreader substrate which in turn is in contact with a heatsink to dissipate excess heat accumulating in the gain chip, which allows for laser threshold reduction. The DBR with the output coupler provide the optical feedback inside the resonator.

In addition, a capping and window layer can be found grown on top of the gain region adding

to the optical thickness (Figure 1.5). The former layer prevents further etching during the fabrication process and oxidation, whereas the latter prevents charge carrier recombination on the surface. VECSELs are usually optically pumped with a laser source at a wavelength absorbed by interband transitions in the barriers. In the case of a linear cavity, incidence would be at an oblique angle (Figure 1.4).

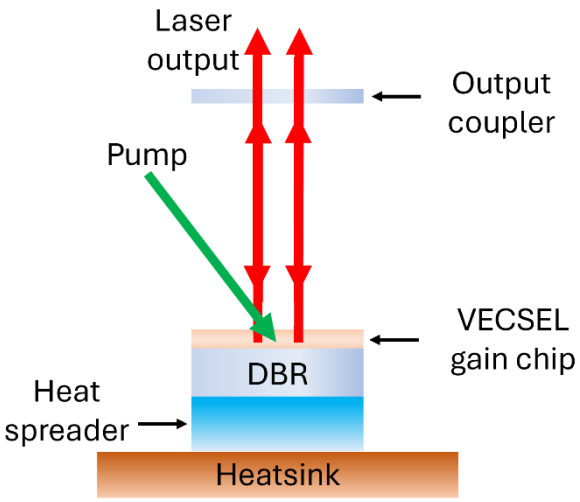

Figure 1.4 Linear VECSEL optical resonator. The laser cavity consists of the gain region, and two reflective mirrors with one being the output coupler and the other being a DBR. The VECSEL QW structure is grown onto the DBR which is in contact with a heat spreader substrate which in turn is situated on a heatsink to remove excess heat accumulating in the gain medium. Lasing is achieved by optically pumping the gain region from top to bottom at oblique angles of incidence.

The low single – pass gain is due to the short interaction between the laser mode and active region; however, the mirrors allow for multiple passes and, also, it is compensated by the existence of MQWs. These factors contribute to increase of optical gain [19]. In addition, because the gain region thickness is small, scattering and absorption losses may affect less the laser performance [4]. The VECSEL gain chip is designed in such a way that the standing electromagnetic wave peaks coincide with QW positions (Figure 1.5). This design allows for strong coupling between quantum – confined carriers and light and, therefore, increasing population inversion for stimulated emission in the active region, as the laser mode interacts more with QWs [2].

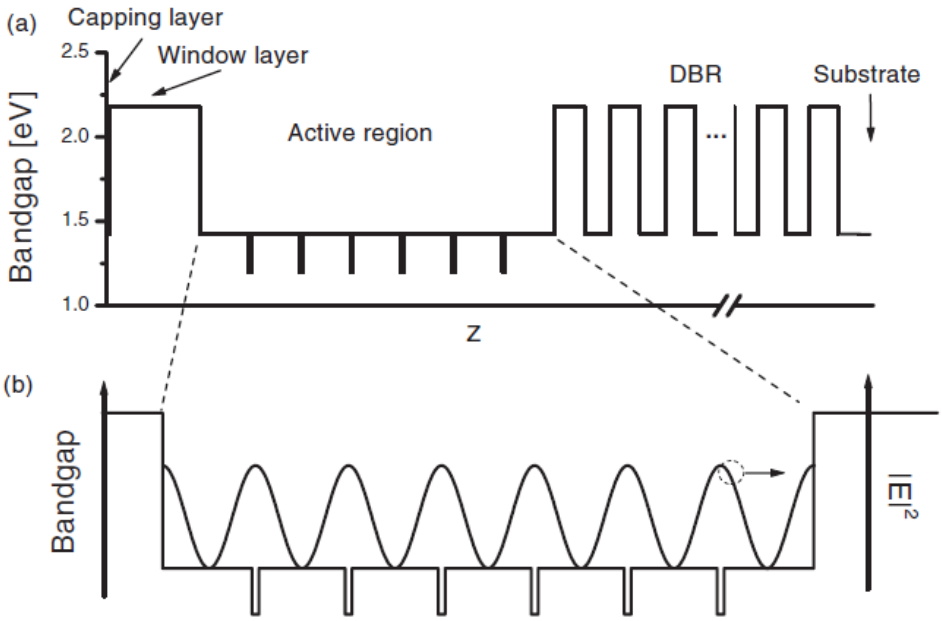

Figure 1.5 Resonant mode in VECSEL gain region [2]. (a) This scheme depicts the band gap energy distribution along the VECSEL structure thickness which contains six QWs spaced at half – wavelength intervals. (b) The standing electromagnetic wave's intensity variation is depicted with respect to the VECSEL's thickness, where the antinodes coincide with the QW positions.

1.4 Membrane External – Cavity Surface – Emitting Lasers

Membrane external – cavity surface – emitting lasers (MECSELs) are similar to VECSELs and were recently developed [15] to demonstrate lasing normal to the QW structure without the DBR. The DBR's absence offers many advantages [15]. Now the MECSEL structure consists of the gain region only making it faster to grow and cost effective. Furthermore, the MECSEL gain medium is not required to be lattice matched with a DBR, which reduces stresses, improves its crystallinity, and makes it have versatile wavelength designs. Finally, the MECSEL demonstrated an improved slope efficiency compared to a VECSEL as heat dependent intrinsic losses are reduced and could potentially operate at smaller pump thresholds should the quality of bonding with the heatsink suffice [15].

The MECSEL optical resonator includes the gain region, sandwiched by two heat spreaders, which are placed in a heatsink chamber to dissipate heat. In addition, two reflective mirrors with one being the output coupler provide the optical feedback inside the laser cavity (Figure 1.6). Population inversion is achieved via non resonant optical pumping at an oblique angle [15], or the incoming light can be parallel to the laser mode. The latter can be realised by replacing one laser mirror with an antireflection mirror, allowing the pump wavelength to enter the optical resonator but reflect the laser wavelength (Figure 1.6).

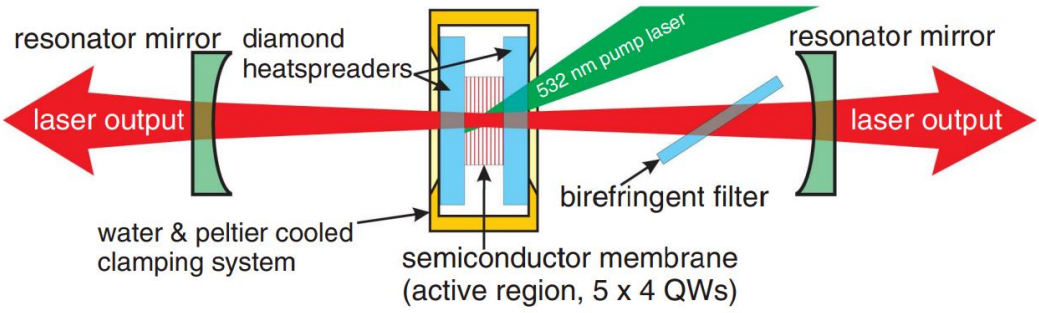

Figure 1.6 MECSEL optical resonator [15]. The gain region is sandwiched between two heat spreaders, which are contact bonded to a heatsink for heat extraction. Two resonator mirrors provide the optical feedback inside the laser cavity with one being the output coupler. Optical pumping is performed at an oblique angle or parallel to the optical axis of the linear cavity. The latter requires an antireflection mirror to transmit the pump wavelength and reflect the laser wavelength.

1.5 Membrane Quantum Well Lasers

VECSELs and MECSELs exhibit parasitic edge emitting or lateral lasing [20], [21], [22], which is perpendicular to the semiconductor layer growth direction. It is characterised as “parasitic” as it affects the laser’s performance by limiting the output optical power. Although parasitic, this MECSEL gain chip functionality may prove promising to utilise with PICs. The research work presented in this thesis focuses on edge emitting MECSELs and hereafter they will be referred to as Membrane Quantum Well Lasers (MQWLs) [22].

Early edge emitting semiconductor lasers include the homojunction laser and the double – heterostructure laser [4]. The homojunction laser exhibits lasing within a p – n junction once an appropriate bias voltage is applied or external optical power, where both p – type and n – type are of the same material. However, the active region’s great thickness increases laser threshold, unless operating at very low temperatures, and a portion of the laser beam is absorbed by the material [4]. The double – heterostructure laser consists of a bulk semiconductor active region sandwiched between a p – and n – type semiconductor layer of the same material (barriers), where charge carrier recombination occurs within the active region and optical feedback is provided by the cleaved end facet – air interface. Laser threshold is reduced compared to the homojunction laser as light confinement is improved due to high refractive index contrast between active region and the barrier regions resulting in waveguiding, the greater barrier band gap energy allowing for stronger confinement of charge carriers within the active region, and less laser beam is absorbed by the barriers as they have greater band gap energy [4]. As the semiconductor active region thickness decreases to create QWs, light and carrier confinement increases, which in turn reduces the laser threshold and temperature dependence of optical gain [4], [23].

Edge emission in MQWLs is realised by the gain region’s end facets – air interface, which

function as partial reflective laser mirrors resembling a plane – parallel optical resonator and along with the gain medium, form a new laser cavity in the system. The new laser cavity does not require additional laser mirrors to operate thus further simplifying the previous VECSEL and MECSEL configurations. Vertical lasing is not possible because there are no external laser mirrors to allow multiple passes through the small gain length meaning that the optical gain cannot overcome losses. Population inversion is similarly realised with optical pumping by delivering the pump light from top to bottom (Figure 1.7). The membrane gain region is sandwiched between heat spreaders but to reduce heat accumulation, the top heat spreader can be completely removed. The remaining structure is contact bonded to a heatsink.

Another ability demonstrated by the MQWL is light waveguiding. The gain medium is the waveguide's core, and its heat spreaders or air and bottom heat spreader are the top and bottom cladding, respectively. In order to attain waveguiding and hence total internal reflection in the core, the gain medium's group refractive index must be greater than that of the top and bottom cladding. The higher the refractive index contrast is between membrane gain medium and substrate, the stronger the overlap of the guided laser mode with the QWs is, increasing optical gain.

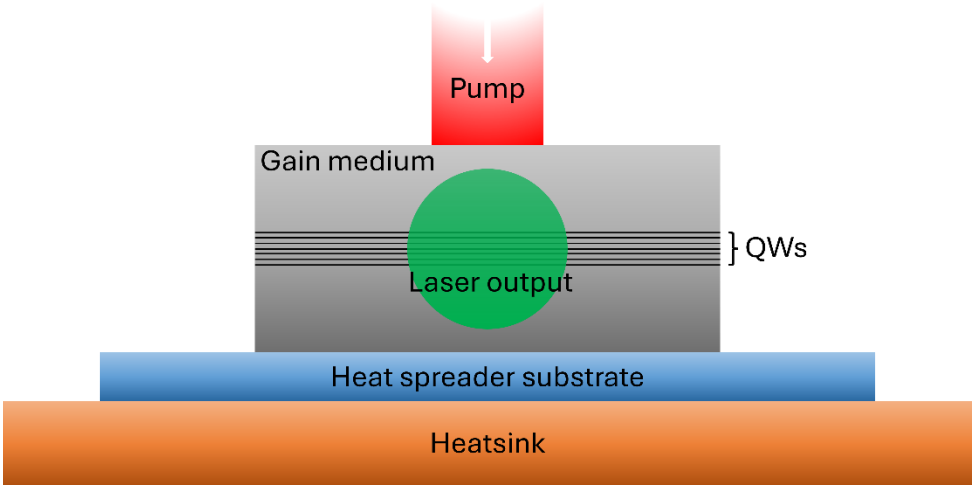

Figure 1.7 Membrane Quantum Well Laser side view. In this configuration, the membrane gain medium is sandwiched between air and a heat spreader substrate which in turn is contact bonded to a heatsink to remove heat from the device. The optical pump is delivered from top to bottom which initiates population inversion in the QWs, and optical feedback is provided by the structure's end facets – air interface creating an edge emitting semiconductor laser. Here, the laser mode is perpendicular to the page and green coloured.

1.6 Spectral Broadening in Optical Waveguides

MQWLs potentially are suitable to interface with PICs as a means to probe nonlinear material waveguides for spectral broadening processes, where the temporal and spectral features of light change due to the interplay between dispersive and nonlinear phenomena. In this work it is shown that the MQWLs can operate as a single cavity or laser arrays. In Figure 1.8 a co – packaging concept of butt – coupling without a lens with the MQWL being placed in an etched pit of the substrate wafer [24] is shown, demonstrating multiple laser cavity operation to probe a waveguide, a waveguide Y – junction and potentially other structures.

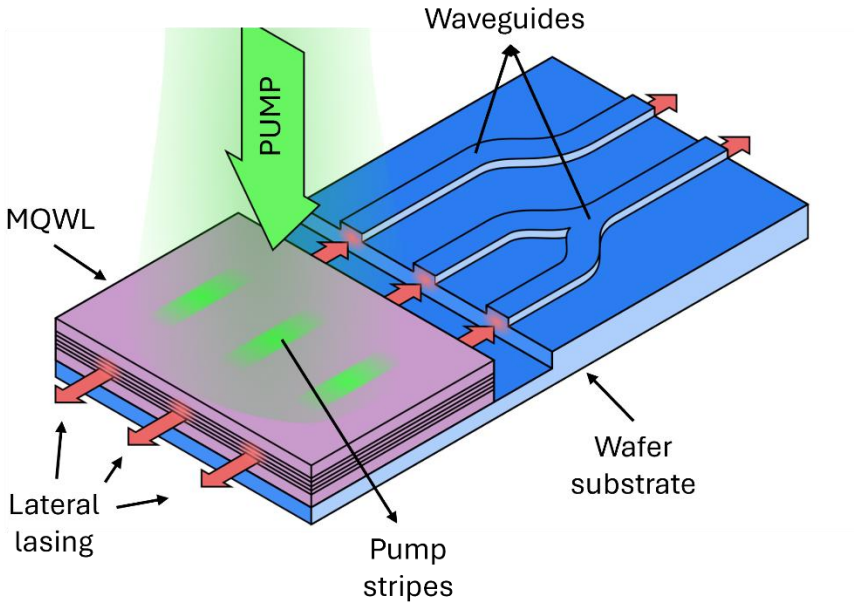

Figure 1.8 Co – packaging of optically pumped MQWL with optical waveguides. In this case, the MQWL is pumped by a customised pump beam profile consisting of stripes to create an array to simultaneously probe a waveguide and a Y – junction.

Dispersion mainly refers to chromatic dispersion which is the medium's bound electrons' linear response to different wavelengths. The response becomes nonlinear when the probe electromagnetic fields are intense, giving rise to nonlinear effects. The interplay between dispersion and nonlinearity creates wave packets known as optical solitons [25], [26]. The interplay mainly involves self - phase modulation (SPM) or Kerr effect, where the material's refractive index shifts due to high light intensity, and group - velocity dispersion (GVD), a form of chromatic dispersion, where the wave packet's group velocity depends on the wavelength, broadening or compressing the wave packet in the time domain.

If GVD is negative or positive, then it is characterised as anomalous or normal, respectively. Positive GVD makes shorter wavelengths move faster (up – chirp), whereas negative GVD enables longer wavelengths to move faster (down – chirp). A soliton is fundamental when dispersion and nonlinear effects balance out and is supported within the anomalous GVD regime. Higher order solitons are produced when the nonlinear effects have a greater impact to the incoming electromagnetic wave than dispersion, whose temporal and spectral features vary periodically. Higher order solitons break down to fundamental solitons (Figure 1.9a) as they are perturbed by nonlinear effects such as self - steepening, and intrapulse Raman scattering [26]. The solitons shift to longer wavelengths due to Raman Stokes scattering. In addition, higher order dispersion and waveguide losses lead to energy transfer from solitons to narrow band wave packets in the normal GVD regime giving rise to pulses that spread because of the medium's chromatic dispersion, which are known as dispersive waves (Figure 1.9b) [25], [26].

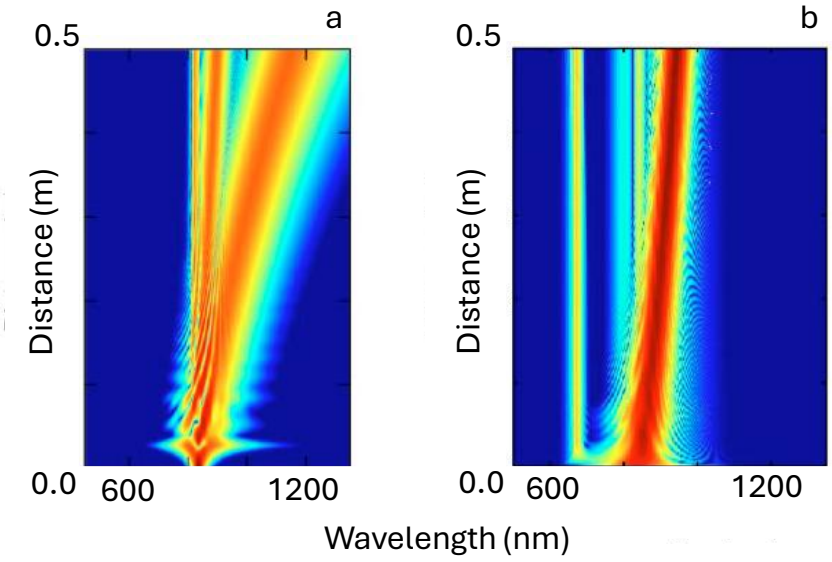

Figure 1.9 Numerical simulations of spectral broadening in optical waveguides (reproduced from [25]). The probe wavelength, $835\ nm$, is injected at the optical waveguide's end facet at $0.0\ m$ and as it propagates along the structure it is subjected to spectral broadening. (a) This figure demonstrates soliton fission. In this case, Raman scattering is introduced in the simulation and the soliton order is 3. The injected optical pulse undergoes spectral broadening and eventually it breaks in multiple pulses due to Raman scattering with each one becoming a fundamental soliton. The resulting fundamental solitons is equal to the soliton order. (b) This plot demonstrates dispersive wave generation with one fundamental soliton present. In this scenario, Raman scattering is introduced again as well as higher order dispersion. Raman scattering red shifts the fundamental soliton, however, higher order dispersion transfers energy from the soliton to a narrow band wave packet in the normal GVD, which is known as a dispersive wave (yellow pulse on the left from the fundamental soliton).

Spectral broadening is a product of higher order solitons in the anomalous GVD regime and includes supercontinuum (SC) or Kerr frequency comb generation. SC generation (Figure 1.9) is a spectral broadening process where short optical pulses or continuous waves (CWs) propagate through a nonlinear medium, producing a continuous broadened spectrum extending over $100\ THz$ [26]. Nonlinear mechanisms responsible for SC generation are SPM and stimulated Raman scattering (SRS) [26]. Kerr frequency combs, which are optical frequency combs, are generated after a CW couples into a micro resonator (Figure 1.10 and Figure 1.11), where its intensity builds up, and interacts nonlinearly via Kerr effect and four - wave mixing (FWM) [27], [28], [29].

A micro resonator, which has a ring or racetrack shape, is an optical waveguide loop in which only resonant wavelengths couple in from a linear waveguide known as the input and output bus waveguide. When the probe wavelength meets the resonance condition, [30] for micro – rings and [31] for racetracks, light coupled in the resonator constructively interferes with the input light creating an interferometer. That wavelength is characterised as resonant.

Light experiences point coupling in a ring configuration, whereas in the racetrack geometry a linear segment parallel to the bus waveguide, effectively forming a directional coupler. Light

coupling is expressed by the coupling coefficient, κ (Figure 1.10). The coupling coefficient takes values from 0 to 1. When $\kappa = 0$, then no light couples into the resonator from the bus waveguide, whereas when $\kappa = 1$, then all light couples into the resonator from the bus waveguide. The latter case is known as critical coupling, where all power couples into the resonator and the transmission coefficient in the bus waveguide, t, equals the resonator losses [32], [33], [34].

By comparing the two resonator types and assuming same wavelength propagation and gap between bus waveguide and resonator, the racetrack has a larger footprint and potentially experience greater losses, however, it is more flexible to adjust resonance and free spectral range (FSR), and therefore, finesse, because both radius, R, and linear segment, L, can be tailored (Figure 1.10). The micro – ring can only adjust its radius to change resonator conditions and properties with small radii possibly leading to greater bend losses [35]. Besides finesse, resonance is associated with the quality factor, i. e. how well the laser wavelength matches the resonator's natural frequency. The higher the quality factor, the longer light remains inside the resonator and builds up intensity for it to react nonlinearly with the medium's atoms.

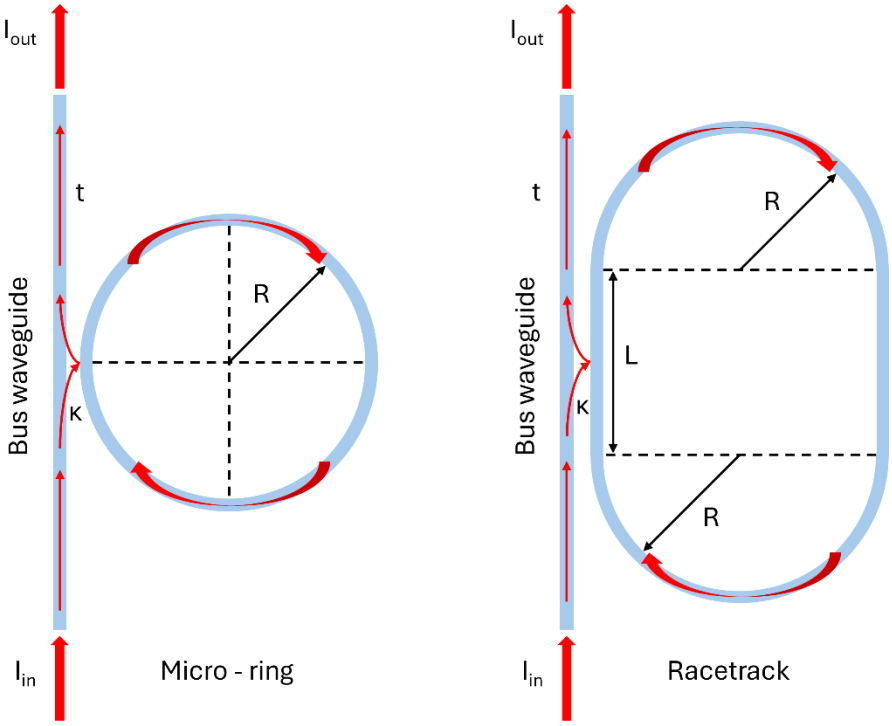

Figure 1.10 Micro – ring and racetrack resonators.

Critical coupling is an ideal case for Kerr comb generation as all light builds up and interacts nonlinearly with resonator's material. Kerr frequency combs and SC are of great interest due to their range of applications such as wavelength – division multiplexing (WDM) in

telecommunications and optical interconnects [36], [37], light detection and ranging (LiDAR) [38], [39], and spectroscopy [40], [41].

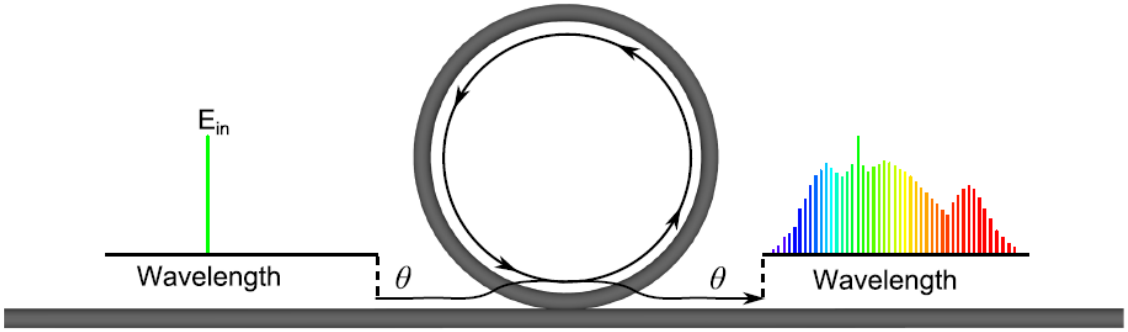

Figure 1.11 Kerr frequency comb generation in optical micro - ring waveguide resonator [42]. Continuous wave light propagates in the straight waveguide or bus waveguide and its resonant to – the – cavity wavelengths will couple to the micro – ring. Coupled light intensity builds up inside the resonator and interacts nonlinearly with the medium. Spectral broadening is generated inside the resonator and only resonant wavelengths couple to the bus waveguide giving rise to discrete and equally spaced frequencies.

Supercontinuum generation in optical waveguides is described by the nonlinear Schrödinger equation (NLSE) [26]:

$$D_z A_c(z,T) + j\frac{\beta_2}{2} D_{TT} A_c(z,T) + \frac{a_L}{2} A_c(z,T) = j\gamma |A_c(z,T)|^2 A_c(z,T) \quad (1.1)$$

where D is Euler's notation for derivatives, z is the waveguide's length, A_c is the complex envelope field's slowly varying amplitude, T is the retarded time, j is the complex number, β_2 is the second order term of the modal wave number's Taylor expansion, $\mathrm{a_L}$ is the linear absorption, and γ is the nonlinear parameter. The mathematical terms $D_z A_c(z,T)$, $(\beta_2/2) D_{TT} A_c(z,T)$, $(a_L/2) A_c(z,T)$, and $\gamma |A_c(z,T)|^2 A_c(z,T)$ respectively describe the envelope's evolution along the waveguide, dispersion, losses, and nonlinearities. The generalised version of equation 1.1, known as generalised NLSE or GNLSE, considers higher order dispersion and more nonlinear effects. Equation 1.1 mainly describes optical pulses propagating in a straight waveguide [26]; however, it readily applies for CW propagation [43].

To describe Kerr frequency combs in micro resonator waveguides, equation 1.1 is modified to derive the Lugiato – Lefever Equation (LLE) [42], [44]:

$$t_{RT} D_t A_c(t,T) = \left[-a - j\delta_0 + jL \sum_{k \geq 2} \left\{ \frac{\beta_k}{k!} (jD_T)^k \right\} + j\gamma L |A_c(t,T)|^2 \right] A_c(t,T) + \sqrt{\theta} A_{c,in} \quad (1.2)$$

where t_{RT} is the round trip time, t expresses the slowly varying time domain, L is the roundtrip length of the resonator, $a = (a_L + \theta)/2$ are the total cavity losses, θ is the power transmission coefficient, $\delta_0 = 2\pi l - \varphi_0$ is the detuning term, l is the order of the cavity's resonance closest to the driving field, and φ_0 is the linear phase accumulated by the intracavity field with respect to the pump field over one round trip. The term $\sqrt{\theta}A_{c,in}$ describes coupling from the bus waveguide to the resonator. The term $jL\sum_{k\geq 2}\left\{\frac{\beta_k}{k!}(jD_T)^k\right\}$ is the dispersion term and considers higher – order dispersion. The term $t_{RT}D_tA_c(t,T)$ describes the time evolution of the envelope field, where $t = mt_{RT}$ and m is the roundtrip index, allowing for the equation to run multiple times in a simulation, which resembles light propagating multiple times inside the micro resonator.

1.7 Tantalum Pentoxide Waveguides

Tantalum pentoxide (Ta_2O_5) or tantala, is a solid material initially used for making capacitors to store high electrical energy due to its high relative permittivity [45], which is 24 at room temperature [46]. Besides its electrical properties, tantalum pentoxide offers many significant optical properties making it a Complementary Metal – Oxide - Semiconductor (CMOS) compatible inorganic compound used for optical waveguide technologies [47], [48], [49], [50], [51].

To begin with, tantalum pentoxide has a broad transmission window, $0.3 - 12.0\ \mu m$ [52], [53], which includes the zero dispersion wavelength, $1.3\ \mu m$, and the low loss wavelength, $1.55\ \mu m$, in silicon dioxide single – mode optical fibres [54]. In addition to tantala's broad transmission window, wavelengths in the $0.3 - 2.0\ \mu m$ range are near absorption free [52], [53]. Annealed tantala has a $0.06\ \frac{dB}{cm}$ propagation loss at wavelength $1550nm$ [48], which is smaller than recent loss findings for silica-on-silicon waveguides, $0.73\ dB/cm$ [55]. Extremely low losses, $3\ dB/m$, at $1.55\ \mu m$ transmission wavelength were reported in [50] for a tantalum pentoxide core waveguide cladded by silicon dioxide. With respect to the losses at $1.55\ \mu m$, tantalum pentoxide has a high refractive index, 2 [50], [56], [57], compare to the refractive index of silica, 1.44 [58], at resulting in stronger light confinement within the waveguide's core. What is more, the refractive index of tantala responds less to temperature change due to a smaller thermo – optic coefficient than silicon – based glasses [59], [60], [61].

Tantalum pentoxide is a material whose nonlinear properties have been exploited to generate SC spectra [43] spectra and Kerr frequency combs [56]. Tantalum pentoxide's nonlinear index reportedly is three times greater than that of silicon nitride (Si_3N_4) [43], [62], [63], enhancing the nonlinear effects. Nonlinearities are enhanced by inducing second – order nonlinearities in tantalum pentoxide if it undergoes thermal poling [64]. Two – photon absorption losses could

occur in the medium, but this is not the case in this work. Tantalum pentoxide has a high band gap energy, $E_g = 3.8 - 4.5\ eV$ [43][53][65], corresponding to UV wavelengths. Two – photon absorption occurs only when the photon energy, E_γ, is $E_g/2 < E_\gamma < E_g$ [66], where $E_g/2$ lies in the visible range of the electromagnetic spectrum. The incident wavelengths used in this work are near infrared.

Finally, tantalum pentoxide waveguide structures have found themselves in various applications due to material's numerous properties. These waveguides have been shown to be suitable hosts for erbium (Er) [67], ytterbium (Yb) [68], [69], neodymium (Nd) [70] or thulium (Tm) ions [71] to generate lasers adding to the coherent light source pool for photonic integrated circuits. Other applications of tantalum pentoxide waveguide structures include evanescent field sensing [72], and metasurface optics [73].

1.8 Thesis Outline

This PhD project consists of two objectives and one final goal. The first aim involves research conducted on MQWLs and MQWL arrays, whereas the second one deals with Kerr frequency comb generation from tantalum pentoxide optical resonators. The final aim is to integrate both technologies and evaluate their performance.

Chapter 2 focuses on characterising the MQWL on silicon carbide and oxidised silicon substrates and evaluate their function as coherent light sources in photonic integrated circuits. Both experimental work and simulations are shown. Experiments include device characterisation with imaging techniques, allowing for the capture of real and reciprocal space images of the MQWL, creation of phase locked laser arrays and power scaling, and temperature spectral tuning. Simulations were created to reproduce laser arrays and explore their mutual phase relationship and model waveguide mode propagation within the waveguide MQWL.

Chapter 3 specifically explores MQWL laser arrays experimentally and with computer modelling. In this chapter, pump spot beam shaping techniques are implemented to pump the MQWL with different geometries and simultaneously create adjacent laser oscillators that couple into each other and explore their dynamics. Additional computer models were developed to simulate laser array coupling.

Chapter 4 is dedicated to Kerr frequency comb generation from tantalum pentoxide micro resonators. The chapter presents the linear waveguide and resonator fabrication process in the cleanroom facility, waveguide optical loss measurements, and resonator characterisation. The chapter also includes waveguide mode propagation simulations and numerical simulations of Kerr frequency comb generation based on the Lugiato – Lefever equation.

Chapter 5 summarises the conclusions from Chapters 2, 3 and 4, and showcases the future work. As time restrictions did not allow for the final aim of integration to be realised, an extensive discussion over MQWL co – packaging with tantalum pentoxide linear waveguides and resonators is presented.

Chapter 2

Membrane Quantum Well Lasers

Lasers have previously been used in a waveguide configuration [74], [75] whether the active region is solid – state [76], [77], gas and liquid [78], or semiconductor QW or quantum dot [23], [79], [80], [81]. In this project, membrane quantum well lasers are for potential uses as coherent light sources compatible with photonic integrated circuits. In the article, the research group presents experiments conducted on the membrane chips on both silicon carbide and oxidised silicon substrates. The paper explored aspects such as the evolution of threshold pump power with pump spot size, temperature spectral tuning, and the investigation of laser arrays and their phase relationship. These features were investigated by retrieving information from real and reciprocal space imaging techniques, and spectrum recording. Initial experimentation involved MQWLs on a SiC substrate. Research then expanded to MQWLs on oxidised silicon on silicon substrates to demonstrate operation with CMOS compatible materials, and, also, compare to results obtained from the SiC substrate case. Numerical simulations presented in this chapter were performed by Dr Jon Gorecki, whereas the membrane gain chip fabrication, laser array, power scaling and laser mode size experiments were conducted by Dr Jake Daykin and Dr Jonathan Woods.

2.1 Membrane Gain Medium

The MQWL gain structure used throughout this research is epitaxially grown and has previously been used in a MECSEL configuration [82]. In the structure's final form, it has an overall thickness of $1.5754\ \mu m$ with each semiconductor layer consisting of alternating crystalline III – V group materials including gallium indium phosphide ($Ga_{0.94}In_{0.06}P$), gallium arsenide (GaAs), indium gallium arsenide ($In_{0.13}Ga_{0.87}As$,) and gallium arsenide phosphide ($GaAs_{0.94}P_{0.06}$) with $64\ \%$ of the structure consisting of pure GaAs (Figure 2.1).

Population inversion occurs in the $10\ nm$ thick $In_{0.13}Ga_{0.87}As$, which in total are ten to increase optical gain and prevent electron overflowing. The $In_{0.13}Ga_{0.87}As$ layers are confined by $21\ nm$ thick $GaAs_{0.94}P_{0.06}$ to form QWs as the latter has a greater band gap energy [11]. The

phosphorus concentration reduces strain in QWs [82], [83] and gain structure curving, resulting in an effective bonding with the substrate heat spreader. The QWs in turn are situated between 90.6 nm thick GaAs layers, which reduce the probability of wave function overlap and hence quantum tunnelling between QWs. In a MECSEL setup, GaAs also adds to the structure's thickness so that the standing wave's antinodes coincide with the QW location [82]. The two outermost GaAs layers are $100\ nm$ thick. Finally, the semiconductor layers mentioned above are sandwiched between two $20\ nm$ thick $Ga_{0.94}In_{0.06}P$ capping layers, which prevent oxidation and provide a selective etch stop during post – processing [82].

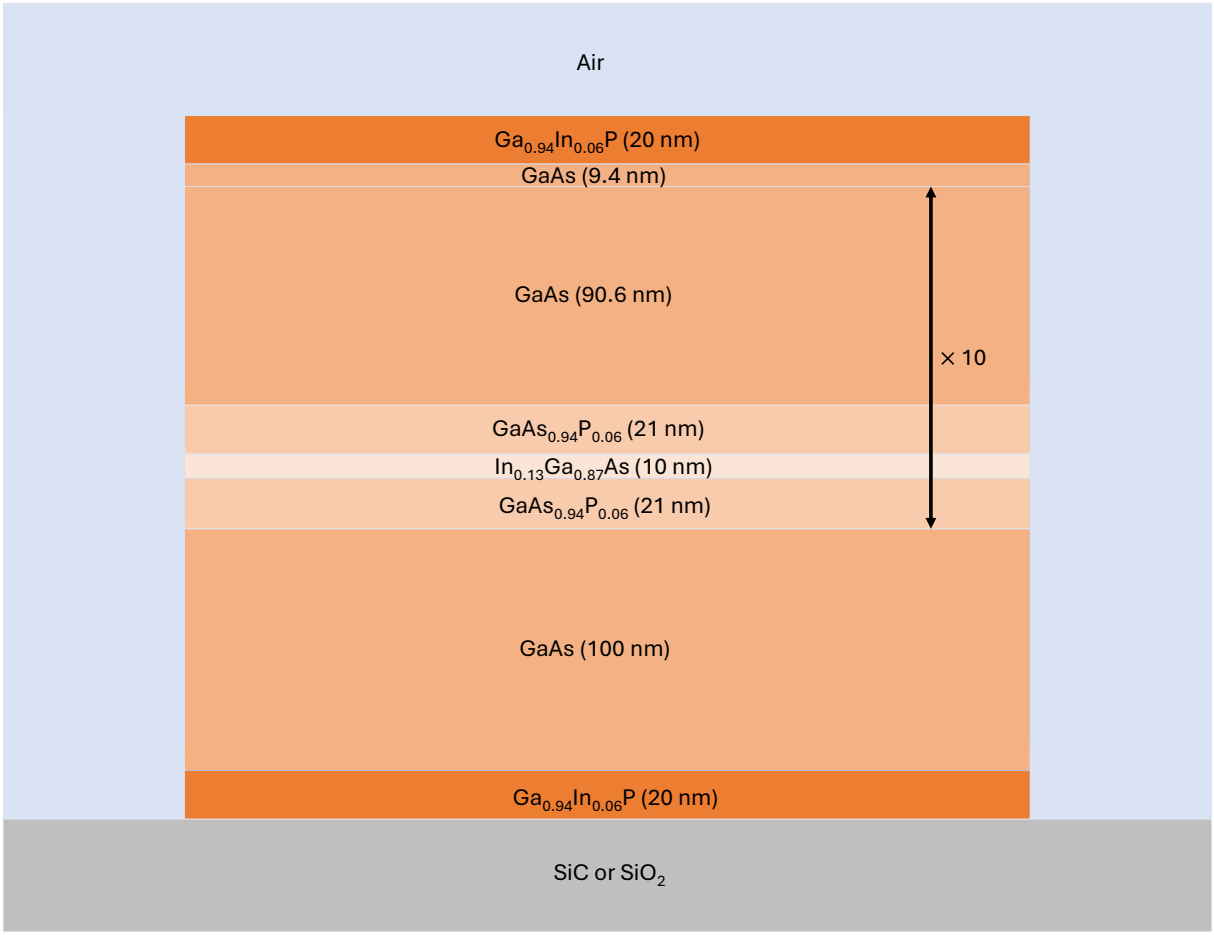

Figure 2.1 Cross – section of membrane quantum well laser gain medium in its final form. This $1.5754\ \mu m$ thick structure contains ten epitaxially grown InGaAs/GaAsP QWs to increase optical gain and reduce electron overflowing and is bonded to a SiC or SiO_2 heat spreader substrate.

Before post-processing, the membrane gain medium is grown on a $200\ nm$ thick aluminium arsenide (AlAs) sacrificial layer which in turn is grown on a GaAs substrate. In preparation of the final MQWL gain medium (Figure 2.2), the structure's side is adhered to a silicon wafer. This allows to remove the GaAs substrate by using a solution of ammonium hydroxide (NH_4OH) and hydrogen peroxide (H_2O_2). This is followed by the AlAs layer removal with a solution of hydrofluoric

acid (HF) and hydroperoxyl (HO_2). During this step the structure's edges will get etched, but the overall device will be protected by the capping layers. The resulting MQWL gain medium is released from its host substrate inside a solution of acetone, which is then steadily swapped with isopropanol (IPA) while ensuring the membrane sample floats in the solution. Consequently, the gain structure is broken into small pieces, and then capillary bonded to a substrate by lifting the latter with the membrane on top out of the solution and let it dry. In this work, the host substrates presented are silicon carbide (SiC) and oxidised silicon (SiO_2) substrate. The post – processing recipe has previously been used to make gain chips for MECSEL setups [15], [82].

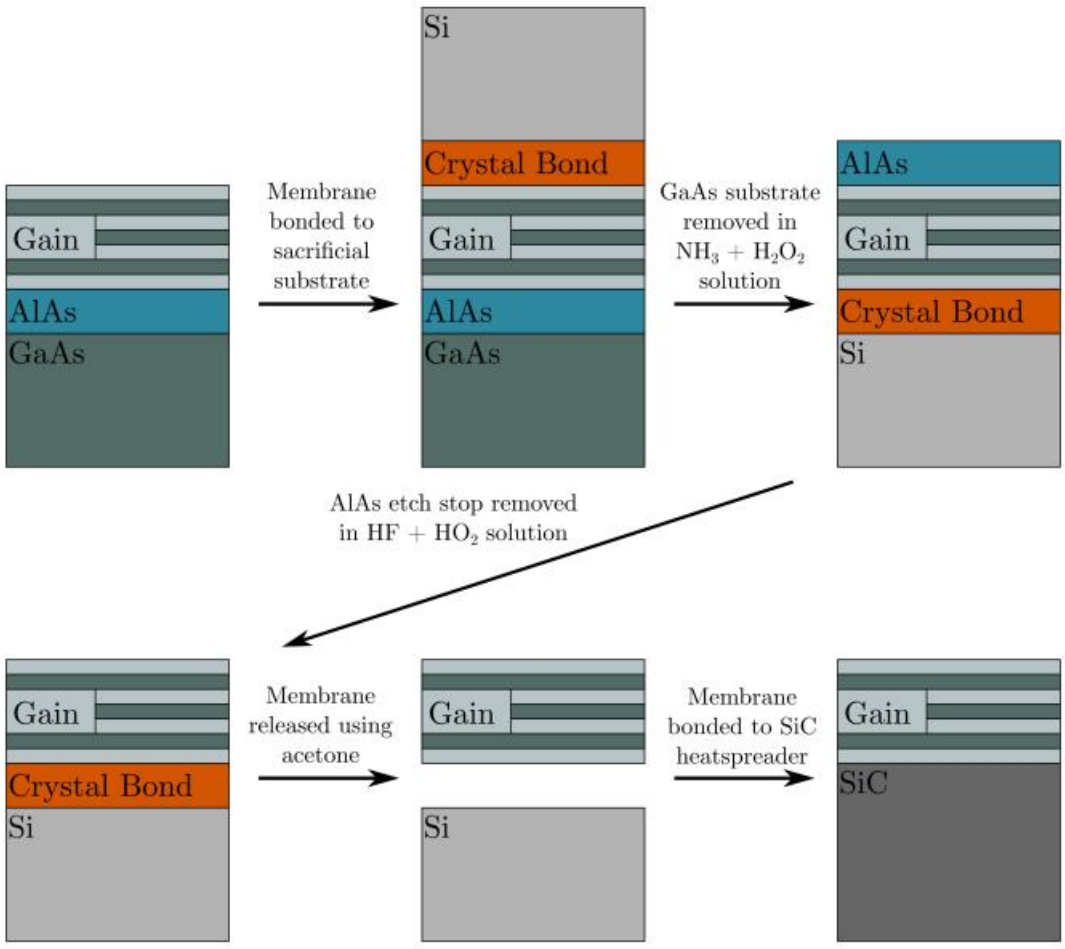

Figure 2.2 MQWL gain chip processing [84]. The QWs are grown on top of AlAs and GaAs sacrificial layers and their top side is crystal bonded to a Si sacrificial layer. The GaAs substrate is removed by using a solution of NH_4OH and H_2O_2. Then, the AlAs layer is removed with a solution of HF and HO_2. The gain medium is released from the Si substrate inside a solution of acetone, which is then steadily swapped with IPA while ensuring the membrane sample floats in the solution. The gain structure is broken into smaller pieces, and then capillary bonded to a new host substrate by lifting the latter with the membrane on top out of the solution and let it dry. The new host substrates are either SiC or SiO_2/Si.

2.2 Membrane Quantum Well Laser Imaging Setup and Methodology

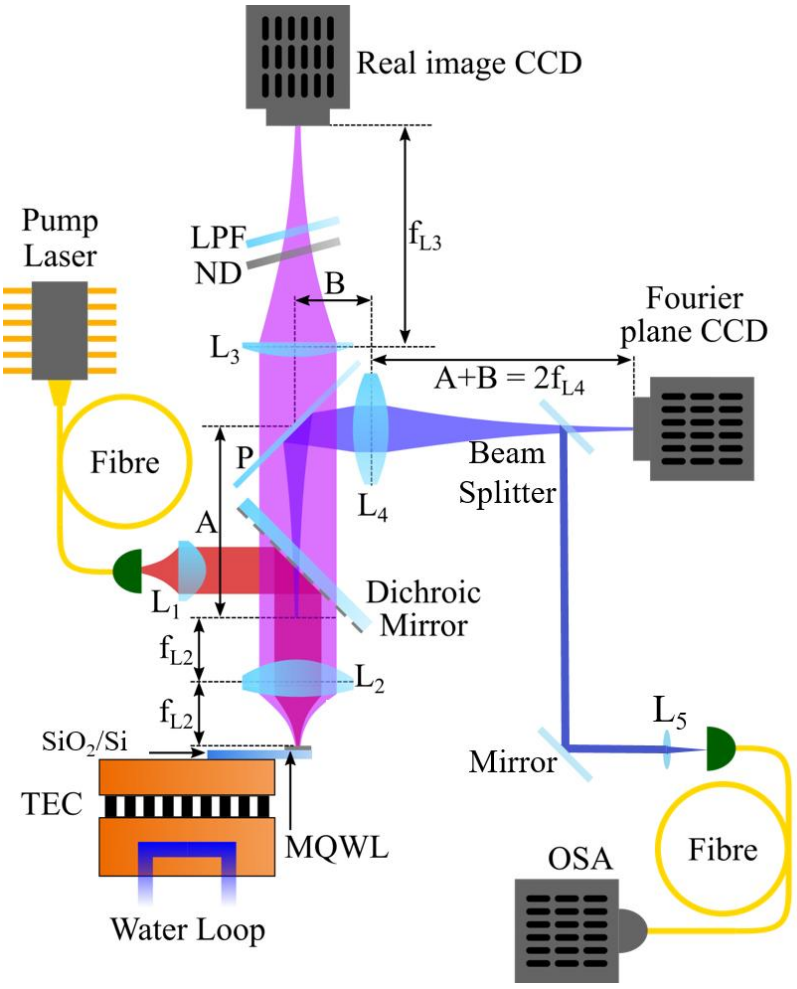

Figure 2.3 Schematic of the imaging setup for characterising the MQWL (modified from [22]). The MQWL emits from the material's end facets and scattered light is collected from the top. The pellicle beam splitter (P) splits the collected laser beam into two components, simultaneously transmitting them to the real image and Fourier plane CCD cameras to respectively capture the physical and reciprocal features of the membrane laser. The OSA records the membrane laser's optical frequencies.

The experimental setup presented in Figure 2.3 is used to characterise MQWLs on SiC or SiO_2/Si substrates. Overall, optical pumping is achieved by delivering non resonant laser light on top of the membrane. In turn, the membrane sample emits laser light from its end facets and scattered light is collected from the top. Afterwards, the collected light is collected and split into two components. Each component travels on a different optical path, with both ending on a charge-coupled device (CCD). One CCD captures the physical features or real space of the membrane and pump spot, and the other captures the reciprocal features, also known as Fourier plane or k - space, where k is the wave number domain.

A CW diode laser emits light at wavelength of $808\ nm$ and is delivered by an optical fibre to lens L_1, which collimates the beam. The collimated beam is then sent on to a dichroic mirror, which reflects $808\ nm$. The reflected beam is focused by lens L_2 on the surface of the membrane

gain chip. The membrane lases at $1\,\mu m$ wavelength, emitting CW light from its end facets. Scattered light is then collected by L_2 and sent to the dichroic mirror, which allows $1\,\mu m$ transmission. The beam is split into two components by a pellicle beam splitter (P), with one component propagating in the real space path and the other in the reciprocal space path. The real space path includes a lens, L_3, for focusing light, a neutral density (ND) filter to reduce the transmitted intensity, a long pass filter (LPF) to ensure transmission only for $1\,\mu m$ wavelength, and a CCD camera to image the real space. The reciprocal space path includes lens, L_4, to focus light on the CCD to image the Fourier plane. In addition, a beam splitter cube is placed on the reciprocal space path which separates the laser beam into two more beams. One light beam is transmitted straight to the reciprocal CCD camera, and the other is redirected to an optical spectrum analyser (OSA) to read the membrane laser's frequency spectrum.

The lenses are positioned such that the membrane's Fourier plane is imaged on the reciprocal space CCD. Lens L_2 is placed at focal length f_{L2} away from the membrane. The same lens produces the Fourier plane on its other side, f_{L2} away. Lens L_4 is positioned at a distance B away from the pellicle and $2f_{L4}$ away from the reciprocal space CCD such that distances A and B as indicated in Figure 2.3 meet the condition $A + B = 2f_{L4}$, where f_{L4} is the focal length of L_4. This condition allows the recreation of the Fourier plane on the reciprocal space CCD. In addition, lens L_3 is placed at focal length f_{L3} in front of the real space CCD to recreate MQWL real space images.

In Table 2.1 I present a list of lenses used to image the physical and reciprocal features of the MQWL on SiC or SiO_2/Si substrates. The lenses although differ, they are independent of the MQWL substrate and compose the same imaging setup presented in Figure 2.3. The plano – convex lenses collimate or converge a collimated beam (L_1 and L_3). The aspheric lens, L_2, is used to reduce spherical aberrations resulting in sharper pump spots and images. Double – convex or bi – convex lens, L_4, is used to relay images and imaging at close conjugates.

Table 2.1 Lens specifications

	SiC substrate setup				**SiO_2/Si substrate setup**			
	L_1	L_2	L_3	L_4	L_1	L_2	L_3	L_4
Type	Plano – convex	Aspheric	Double – convex	Double – convex	Plano – convex	Aspheric	Plano – convex	Double – convex
Focal length (mm)	30	8	300	150	25	30	150	75

Regarding the MQWL, the gain medium situated on a SiC or SiO_2/Si substrate is in contact with a heatsink, which consists of a thermoelectric cooler (TEC) sandwiched between two copper (Cu) blocks, with one being connected to a closed loop water circuit. The water – cooled Cu block removes excess heat accumulating in the membrane gain chip thus reducing intrinsic losses and lowering the laser threshold. The temperature is fixed at 14.0 ℃ as it is the coolest temperature achieved in the lab before water vapour condensates [22] but can go lower for better efficiency. To improve the heatsink's performance, a thermal paste is applied between the Cu block and MQWL substrate.

2.3 Membranes on Silicon Carbide

A He – Ne laser emitting at a wavelength of $\lambda_o = 633\,nm$ is used for aligning and calibrating the setup presented in Figure 2.3. For the setup's calibration, a transmission electron microscopy (TEM) copper grid consisting of $19\,\mu m \times 19\,\mu m$ square slits and a 25 μm grating period, Λ, is placed where the MQWL is supposed to be. The He – Ne laser illuminates the TEM from behind to collect the transmitted beam. The resulting real and reciprocal images are shown in Figures 2.4 and 2.5 respectively. Figure 2.4 depicts light going through the TEM's square gaps and the corresponding pixel dimension measurement. Knowing the slit dimensions, the pixel – to – physical dimension conversion is $c_r = (0.1498 \pm 0.0012)\,\mu m/pixel$. Figure 2.5 shows the diffraction pattern and the corresponding consecutive diffraction order pixel separation, which is proportional to a wave number, $k_o = 2\pi/\lambda_o$. Hence, the pixel – to – wave number conversion is $c_k = (0.2531 \pm 0.0026)\,rad.\mu m^{-1}/pixel$.

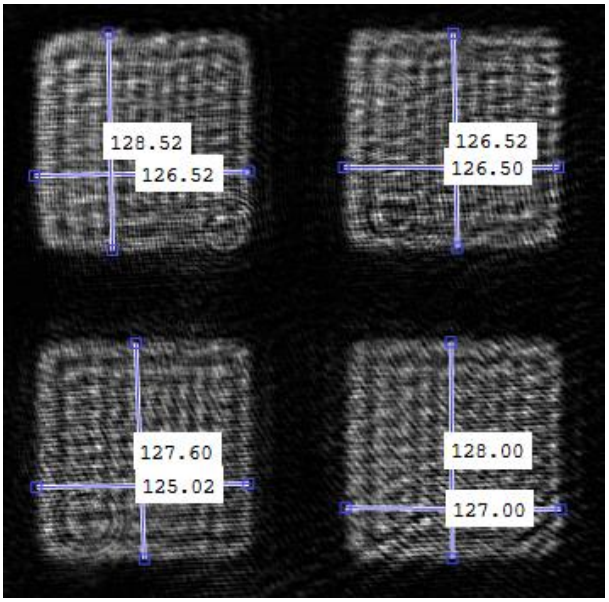

Figure 2.4 Real space image depicting the TEM grid's square slits as the He – Ne laser beam propagates through them. During the processing phase, I measure the pixel dimensions of each square to calculate the pixel – to – micrometre conversion.

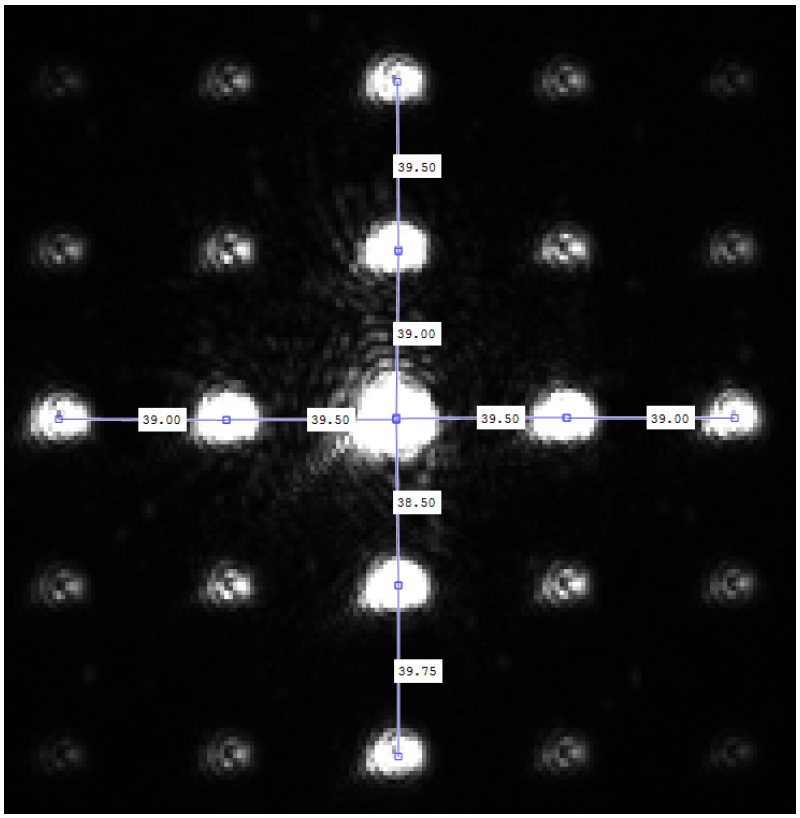

Figure 2.5 Reciprocal space image depicting the diffraction pattern created by illuminating the TEM grid. The pixel measurement between consecutive diffraction orders corresponds to one wave number, k_o.

Conversion factor c_k can be modified to allow pixel to angle conversion from Equation 2.1 [85]:

$$\theta_n = Arcsin\left(n\frac{2\pi}{k_0\Lambda}\right) \quad (2.1)$$

where n is the diffraction order. The resulting pixel – to – angle conversion is $c_\theta = (0.0370 \pm 0.0004)\,°/pixel$. From the conversion factors, I can characterise the membrane laser under investigation.

After calibration, the red laser is switched with the $808\,nm$ pump diode laser whose drive current threshold is $i_{th} = (267.94 \pm 10.00)\,mA$, and slope efficiency is $b = (1.126 \pm 0.002)\,W/A$. This step requires slight adjustment of the optics as the focal length does not vary greatly with wavelength shift, however lens L_2 remains in place to avoid ruining the calibration. Also, the membrane with the heatsink is placed on a translation stage which allows correction for the new wavelength.

After pumping the gain chip, the CCDs capture real and reciprocal images depicting features of the MQWL as shown in Figures 2.6a and 2.6b. The former shows the top view of the membrane and lasing from its end facets and spontaneous emission from the pump spot, albeit most of the pump wavelength being removed by the ND filter and LPF. The latter depicts the interference pattern formed from the coherent light sources from the membrane's edges. Stimulated emission is associated with bright spots at the membrane's end facets compare to spontaneous emission, however the transition cannot be determined precisely straight from the real space images, but reciprocal space images are able to determine the membrane's lasing threshold. Interference patterns are a result of coherent point light sources emitting at the same wavelength. The light sources appearing at the end facets are point sources and are incoherent or coherent at spontaneous or stimulated emission respectively. In the case of coherence, a prominent characteristic of lasers, the membrane gain medium resembles a double slit experiment. Therefore, the transition takes place as soon as the interference pattern is visible. In addition, circular interference fringes are also visible, caused by diffraction from the setup's optical elements. With increasing pump power, membrane lasing, and interference fringes become brighter.

Figures 2.6 were captured at 15.0 ℃ heatsink temperature and $488\,mA$ pump diode drive current; however, different temperature settings were examined ranging from 13.0 ℃ to 16.0 ℃. As the heatsink temperature increased, the membrane laser threshold rose, and the pump power had to increase to overcome temperature dependent intrinsic losses. These losses are associated with peak gain decrease due to semiconductor electrons being distributed over a wider energy range [86], and longer radiative charge carrier recombination duration [87].

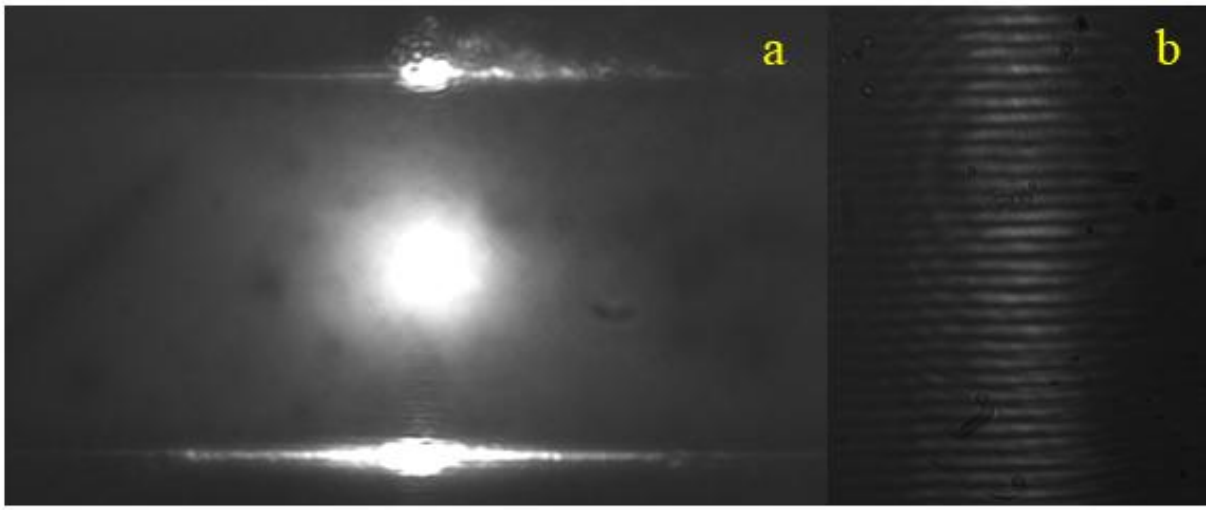

Figure 2.6 MQWL optically pumped with the 808 nm diode laser. Figure (a) depicts a top view of the membrane gain medium, the membrane's end facets or cavity's length, membrane lasing indicated by the bright spots at the end facets and spontaneous emission from the pump laser. This is a saturated image for purely demonstration purposes. Figure (b) portrays the corresponding interference pattern produced by the coherent laser spots at the membrane's end facets. Both images were captured at 15.0 ℃ heatsink temperature and $488\ mA$ pump diode injection current.

Further membrane gain medium characterisation involves determining the cavity length, L, which is possible by measuring the membrane length with a microscope or directly from the real and reciprocal space images. The latter option is chosen for the following experiments. From real space images, the pixels are directly measured from one end facet to another and then are converted to physical length with c_r. This results in $L = (61.051 \pm 1.576)\ \mu m$. From the reciprocal space images, pixels to angles are converted with c_θ and then a Fourier transform is applied to an averaged interference pattern to obtain the waveform's frequency components. The outcome is two spatial frequency components, with one corresponding to the direct current (DC) component at $0\ rad^{-1}$ and the other to the harmonic component at $58\ rad^{-1}$ as shown in Figure 2.7. Also, because the membrane lases at $\lambda_L = 1\ \mu m$ and $L >> \lambda_L$, effectively creating a double slit experiment, the interference pattern from two coherent point sources is given by Equation 2.2 [85]:

$$I(\theta) = 4I_s cos^2\left[\frac{\pi}{\lambda_L} Lsin(\theta)\right] = 2I_s\left\{1 + cos\left[2\frac{\pi}{\lambda_L} Lsin(\theta)\right]\right\} \quad (2.2)$$

where I_s and $\theta = Arcsin(\lambda_L/L)$ are the intensity from each source and the angle between successive maxima respectively. In addition, term $2I_s$ is the DC component and $2I_s cos\left[2\frac{\pi}{\lambda_L} Lsin(\theta)\right]$ is the harmonic component.

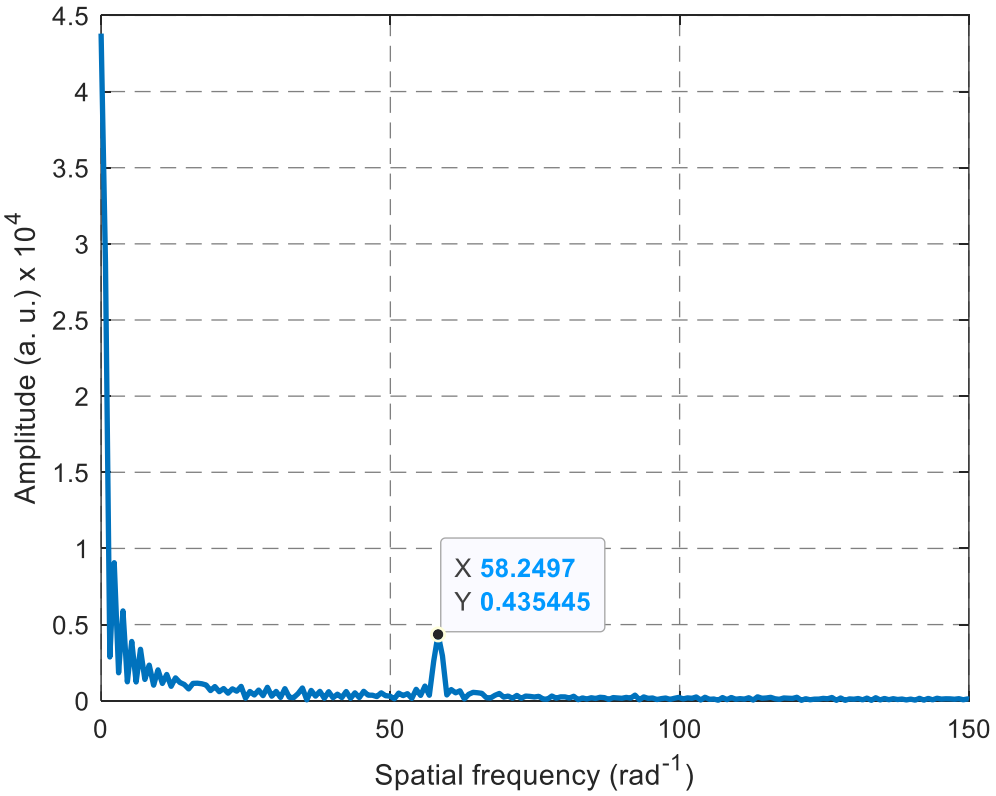

Figure 2.7 Fourier transform of an averaged interference pattern obtained from a reciprocal space image. Two frequency components are present. The DC component appears at $0\,rad^{-1}$, and the harmonic component appears at $58\,rad^{-1}$.

Considering the harmonic frequency and Equation 2.2, the frequency of the trigonometric function is $L/\lambda_L = 58$ or $L = 58\,\mu m$. This value differs from $L = (61.051 \pm 1.576)\,\mu m$ by $4.59\,\%$, due to systematic error and image calibration. By using the new length value, Equation 2.2 can be fitted to the averaged interference pattern and match the periodicity as seen in Figure 2.8.

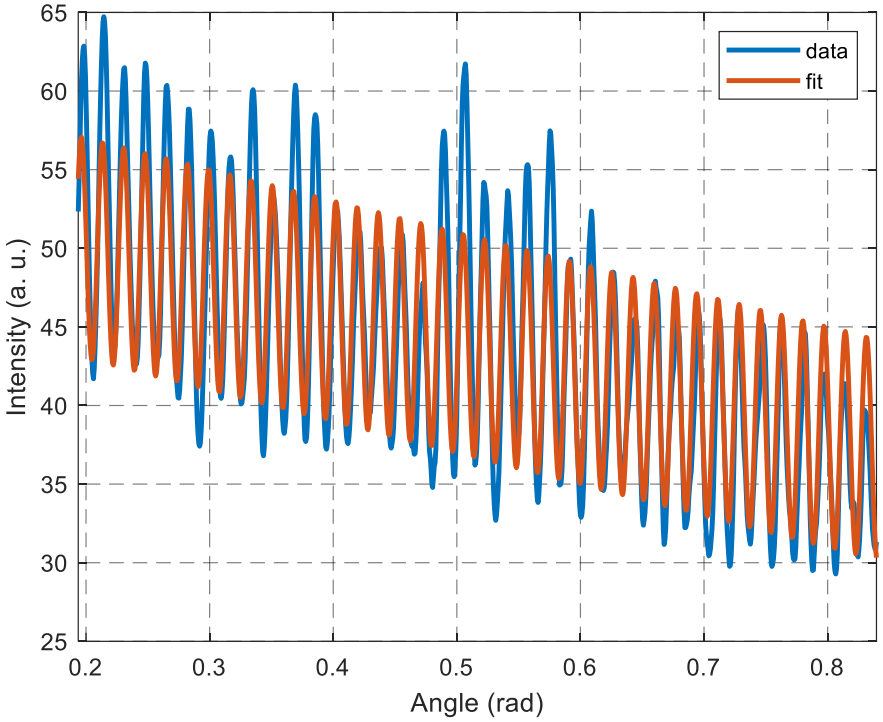

Figure 2.8 Fitting Equation 2.2 (orange curve) to an average interference pattern obtained from a Fourier plane image (blue curve) using the harmonic component obtained from the Fourier transform of the latter. The horizontal axis was converted from pixels to radians through the conversion factor. A linear term is included in the fitting equation to match the CCD's response.

The images shown in Figure 2.6 and the analysis presented above refer to a single cavity laser. In [22], it is shown that a MQWL can demonstrate multiple cavity lasing simultaneously as presented in Figure 2.9. Laser arrays are covered extensively in Chapter 3. Laser arrays are apparent when a rapid increase in collected power from the MQWL is noticeable (Figure 2.10), more than one pair of two laser spots at the gain chip's end facets are visible in the real space images (Figure 2.10 and Figure 2.11), and multiple interference patterns are observable in the reciprocal space images (Figure 2.11).

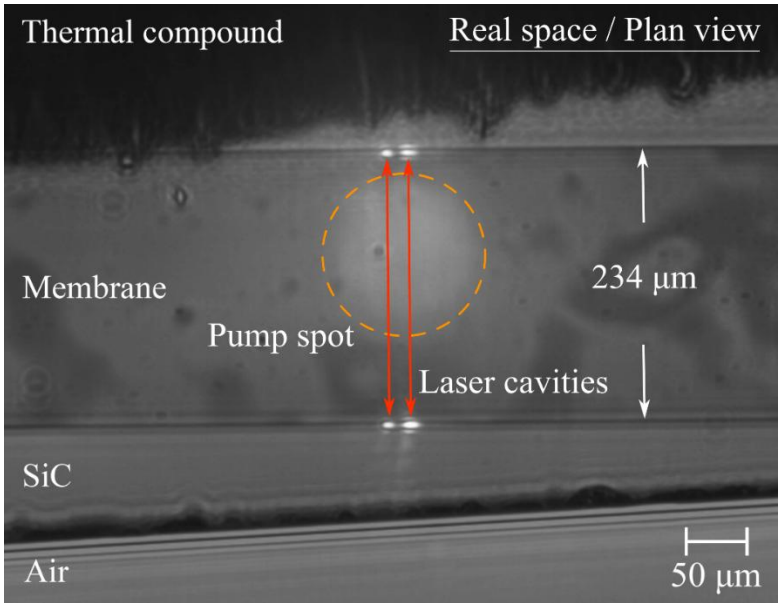

Figure 2.9 Top view image of a MQWL on SiC substrate [22]. Two laser cavities are operating simultaneously indicated by the two red arrows within the same pumping region (orange dashed circle).

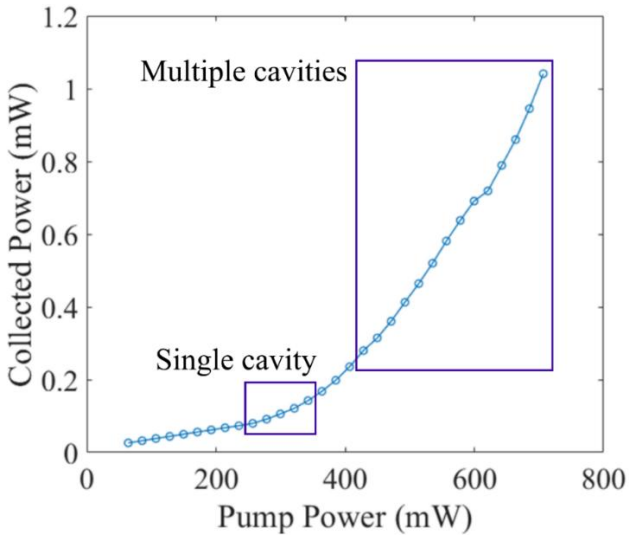

Figure 2.10 MQWL collected power versus pump power [22]. Collected power increases at different rates. Initially, only spontaneous emission occurs, then with increasing pump power laser threshold is attained and a single laser cavity is created, and finally, laser arrays appear which is associated with a rapid collected power increase.

When multiple laser cavities exist, it raises the question whether they operate on the same laser frequency and what is their relative phase relation. In Figure 2.11 [22], four columns of images with increasing pump power demonstrating single and multiple laser cavity operation are shown. From left to right, the first column displays real space images of one end facet from the top (a, e, i and m), the second column exhibits real space images of the laser mode from the MQWL's side (b, f, j and n), the penultimate column shows the corresponding reciprocal space

images (c, g, k and o), and, finally, the final column depicts the corresponding OSA laser wavelength readings (d, h, l and p). Furthermore, from top to bottom, the first row demonstrates dual cavity operation with a $1010.0\ nm$ wavelength (a – d), the second row exhibits single cavity lasing with the same wavelength (e – h), the third row shows dual cavity operation with skewed interference pattern fringes and two laser wavelengths potentially corresponding to different QW transitions, $1010.0\ nm$ and $1016.7\ nm$ (i – l), and the last row presents two laser cavities with the same two laser wavelengths (m - p).

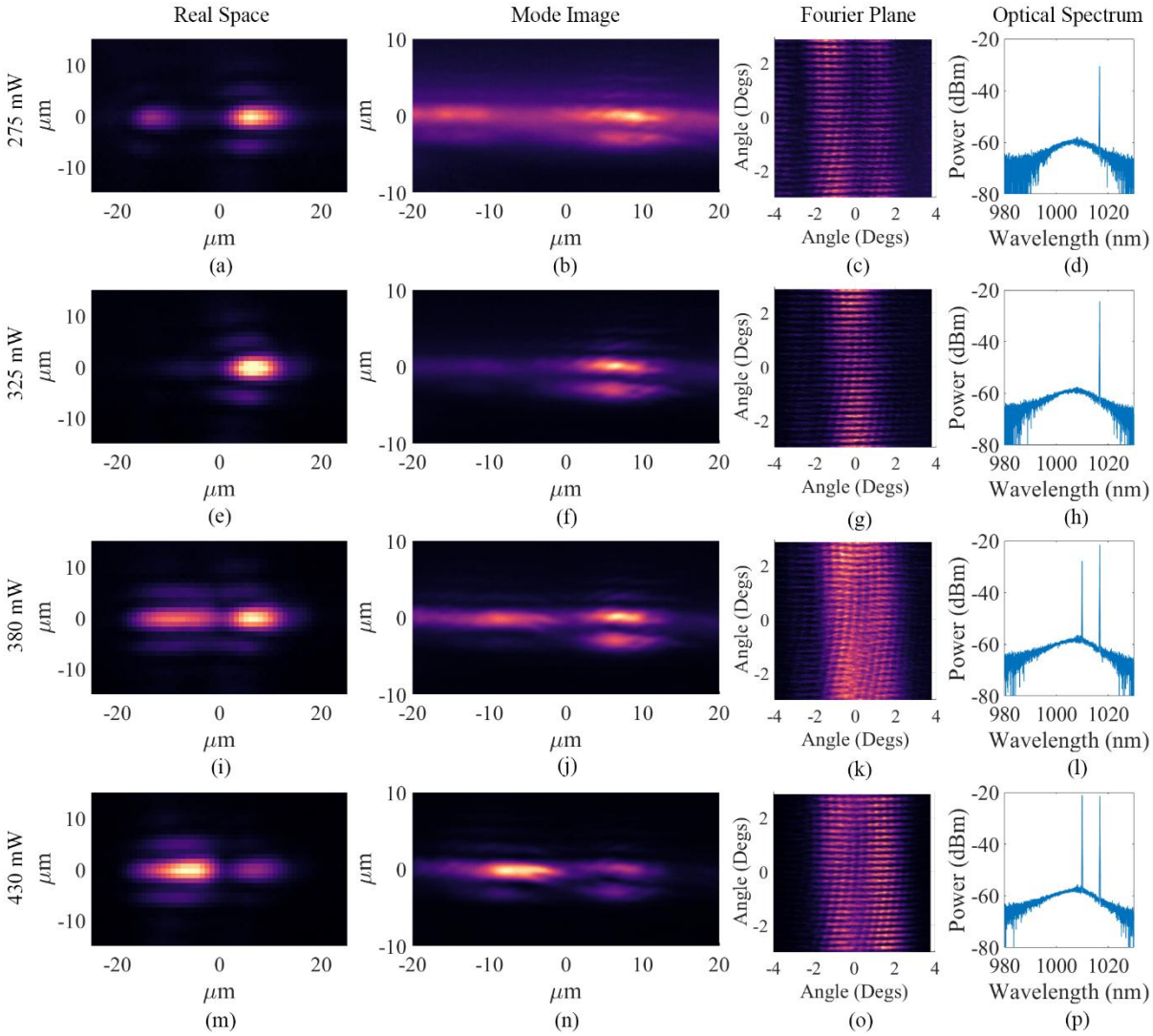

Figure 2.11 MQWL images and measurements for increasing pump power demonstrating single and dual laser cavity operation at one wavelength, 1010.0 nm, or two laser wavelengths, $1010.0\ nm$ and $1016.7\ nm$ [22]. The first column of images depict top view images of one of the MQWL's end facets whereas the second column shows its corresponding side view. The third and fourth columns display the associated interference patterns and laser emission wavelength, respectively.

Compared to the other cases with $275\ mW$ and $380\ mW$ pump powers, in Figure 2.11e – h corresponding to pump power $325\ mW$ one laser cavity ceases to exist possibly due to losses;

however, this was overcome by increasing the pump power making the material's gain greater than the cavity's losses. At some membrane locations instabilities occurred whether that was because of poor heatsinking or irregular membrane end facets.

Simulations were scripted in MATLAB to attempt to determine the nature of laser arrays referring to their mutual coherence and oscillation frequencies based on the data from Figure 2.11 [22]. The centre of attention are the two last cases, where the MQWL is pumped with $380\ mW$ and $430\ mW$ due to the existence of two laser lines. The model assumes four point sources, two for each laser cavity, and considers the cavity length, and different wavelength and phase difference combinations. The model generates interference patterns as shown in Figure 2.12.

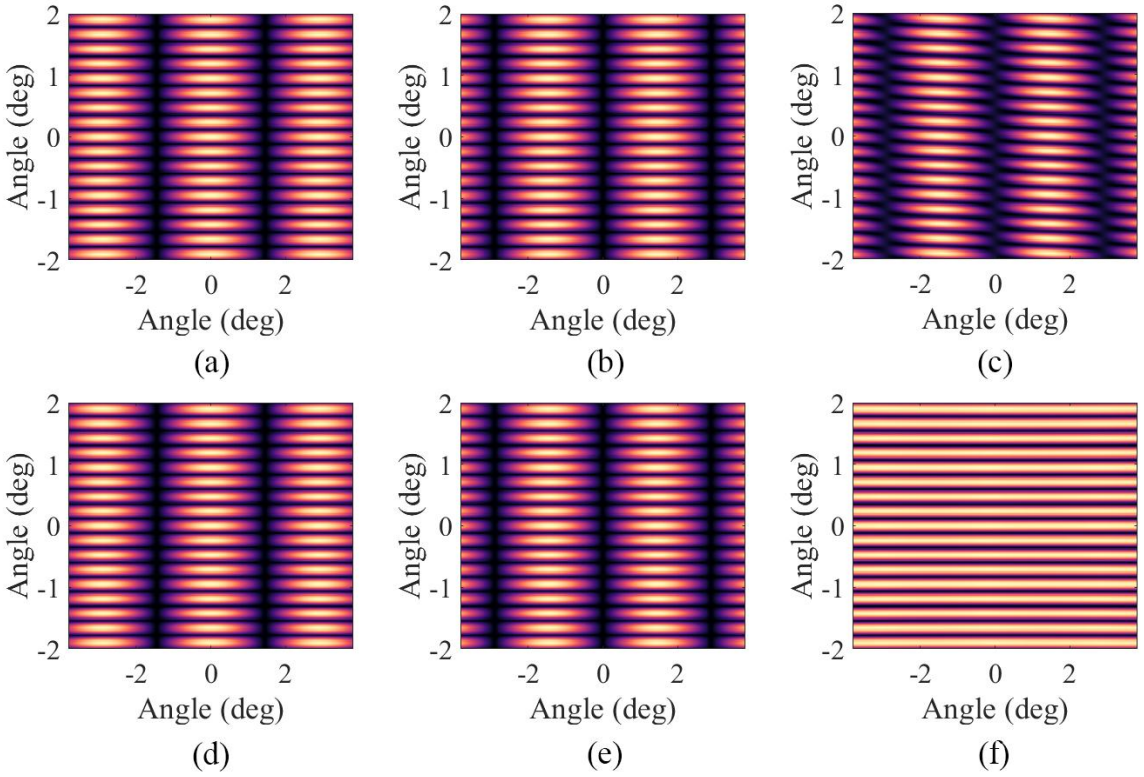

Figure 2.12 Numerical simulations of the interference patterns obtained from two laser cavities, and different wavelength and phase difference, $\Delta\varphi$, combinations [22]. The laser cavity length is $234\ \mu m$ and separation between lasers is $20\ \mu m$. The cavities and their respective wavelengths are denoted as c_1 and c_2, λ_{c1} and λ_{c2}. Subfigures refer to: (a) $\lambda_{c1,c2} = 1016.17\ nm$, $\Delta\varphi = 0\ rad$; (b) $\lambda_{c1,c2} = 1016.17\ nm$, $\Delta\varphi = \pi$; (c) $\lambda_{c1,c2} = 1016.17\ nm$, $\Delta\varphi = \pi$ with one point source having higher field amplitude; (d) both cavities oscillating with the same wavelengths, $\lambda_{c1,c2} = 1010.0\ nm$ and $\lambda_{c1,c2} = 1016.17\ nm$, $\Delta\varphi = 0$; (e) $\lambda_{c1,c2} = 1010.0\ nm$ and $\lambda_{c1,c2} = 1016.17\ nm$, $\Delta\varphi = \pi$; (f) each cavity oscillates with a different wavelength, $\lambda_{c1} = 1010.0\ nm$ and $\lambda_{c2} = 1016.17\ nm$.

By comparing the interference patterns of Figure 2.12 to the reciprocal space images in the third and fourth columns of Figure 2.11, the simulations potentially outline the physics behind

some of the observations in the Fourier plane images and corresponding laser frequencies. A comparison of the coherent superpositions shown in Figures 2.12a-b with Figure 2.11c show that both laser cavities indeed oscillate with the same wavelength, but Figure 2.12b matches the pattern in Figure 2.11c as no fringes exist at a 0° angle. This suggests that although the laser cavities are coherent, they have a phase difference $\Delta\varphi = \pi$ hinting that the adjacent lasers couple out – of – phase and that their intensities destructively interfere between them in the near – field [88], [89], [90].

A higher field amplitude was introduced to one of the point sources inducing skewed fringes (Figure 2.12c) corresponding to the arrangement in Figure 2.11k. With respect to the interference patterns presented in Figures 2.12d – e, I deduce that each cavity oscillates on both laser frequencies with $\Delta\varphi = \pi$ as no fringes exist at a 0° angle, matching Figure 2.12e with Figure 2.10o, which is expected for the lasers to be coherent to each other. If each laser cavity operated on a different frequency, then the horizontal periodicity of the interference patterns vanishes since the fast optical frequency requires more cycles so that the phase angles realign. This situation corresponds to Figure 2.12f and was not observed in the experiments.

2.4 Membranes on Oxidised Silicon

In this section a membrane gain medium under examination is positioned on a SiO_2/Si substrate to compare with the SiC bottom cladded membrane with another similar experimental setup and appropriate set of lenses presented in Table 2.1. This gain chip is also optically pumped from top to bottom with an 808 nm pump diode laser whose laser threshold and slope efficiency are 840 mA and 1.07 W/A respectively. After calibrating the experimental setup, it was found that the pixel – to – physical dimension conversion factor is $c_r = (0.956 \pm 0.004)\ pixels/\mu m$ and the pixel – to – angle conversion is $c_\theta = (0.0065 \pm 0.0001)\ °/pixel$ [22]. Using the conversion factors, the scaled real and reciprocal space images seen in Figure 2.13 are presented from which the cavity length derives and is $424\ \mu m$. Figure 2.13 depicts a single laser operation because it is associated with only one pair of laser spots at the membrane's end facets and one interference pattern.

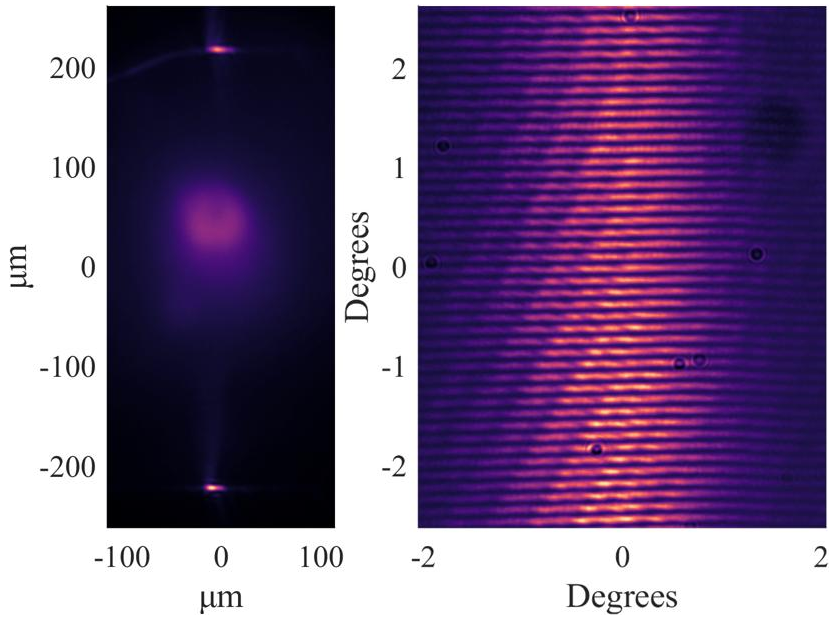

Figure 2.13 Scaled real space image and its corresponding reciprocal space image for the MQWL placed on a SiO_2/Si substrate. Like in Figure 2.6, in the real space image the end facets, laser spots at the end facets and pump spot spontaneous emission are visible, and in the reciprocal space image the fringes of the interference pattern are visible. A single laser cavity is oscillating as indicated by one pair of bright spots at the gain chip's end facets and only one interference pattern is visible.

In addition, the pump spot varied in size by translating lens L_1 to find the optimal pump collimation and threshold pump power. As the pump spot size changed, indicated by the spontaneous emission as seen in the real space CCD, the pump power had to adjust accordingly to compensate for cavity losses as depicted in Figure 2.14. As L_1 moves closer to or further away from the optical fibre's end facet, the pump's full – width at half – maximum (FWHM) increases and hence, the power density decreases. The latter's reduction cannot overcome the laser cavity's losses and therefore, the threshold pump power needs to increase. In the $48.5\ mm - 49.0\ mm$ regime, there is an optimal condition were the pump spot size, and the threshold pump power minimise. The lowest threshold value recorded was $211\ mW$ [22]; however, a value of 309 mW was also recorded in a different area of the same membrane chip. Both values are significantly lower than the $0.7\ W$ threshold pump power reported in [82] for a MECSEL with the same QW design. In [22] a threshold value as low as $60\ mW$ was recorded for a $70\ \mu m$ cavity length membrane on SiC substrate.

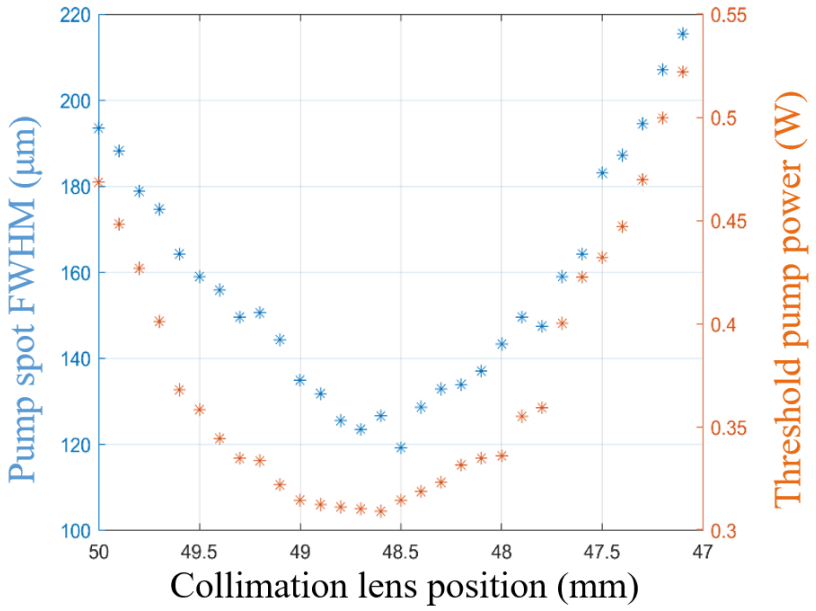

Figure 2.14 Pump spot focusing and defocusing and pump power adjustment against collimation lens L_1 translation. The left axis (blue) denotes the FWHM, which is obtained from the averaged spontaneous emission pump spot from the real space images. The right axis (orange) denotes the required pump power to attain membrane lasing. The bottom axis (black) denotes the distance of lens L_1 away from the fibre's end facet. The pump spot is collimated in the $48.5\ mm\ -\ 49.0\ mm$ regime where the least amount of pump power is required for the membrane chip to lase.

The pump spot size variation influences the MQWL's laser mode size and corresponding interference pattern fringes consequently. The larger the pump spot the wider the laser mode becomes (Figure 2.15) and the associated fringes in the Fourier plane become narrower because light exiting the laser cavity is subjected to less diffraction (Figure 2.15). Therefore, the pump spot's location on the membrane and size respectively have control over the laser spatial mode's position and shape.

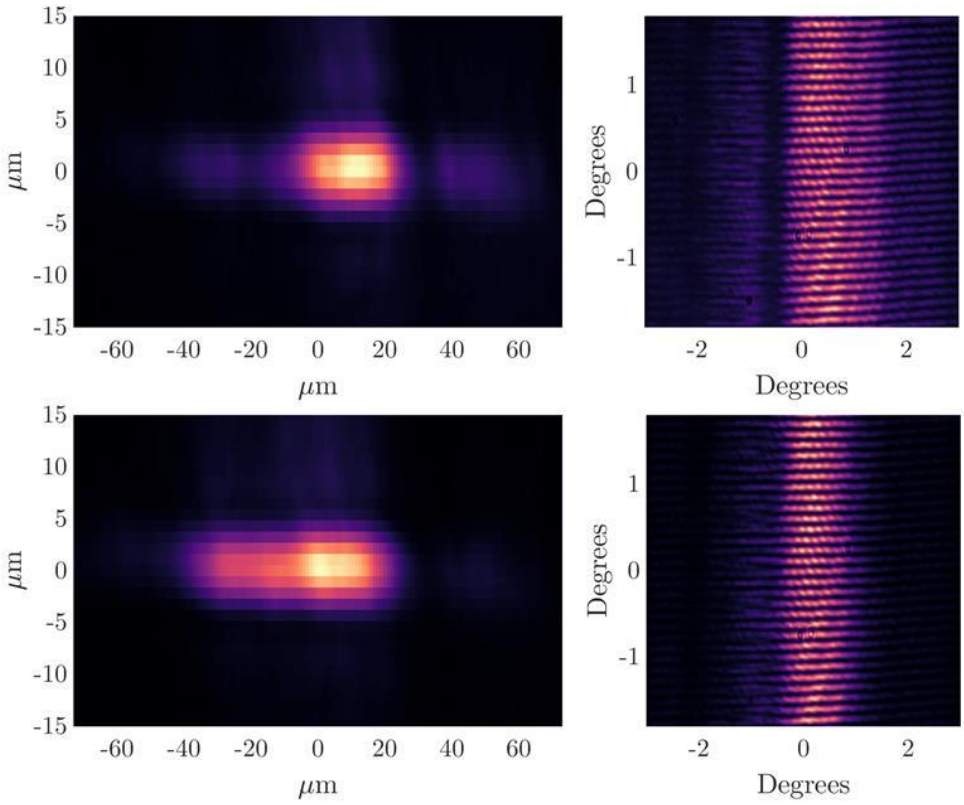

Figure 2.15 Top view of laser mode size at device's end facet. The left column displays the real space images depicting the membrane's laser mode appearing at one end facet. The right column displays the corresponding Fourier plane images. The bottom row was captured for a higher pump spot size compared to the top row. As the pump spot size increases, the laser's spatial mode width increases and hence, the corresponding interference pattern becomes smaller due to a smaller diffraction angle.

After locating the optimal conditions of pump beam collimation and membrane laser threshold minimisation were attained, experimentation proceeded with the spectral aspects of the MQWL. The membrane gain chip at 14.0 ℃ lases at $\lambda_L = 1013.47\,nm$ as depicted in Figure 2.16 and as expected because of the device's QW design [82]. In Figure 2.16, the power axis is measured in dBm, which means that the laser spectrum is represented in the logarithmic scale. The membrane laser's FWHM or lineshape width, that is at $3\,dBm$ from the laser line peak, is approximately $\Delta\lambda_{FWHM} = 0.3\,nm$.

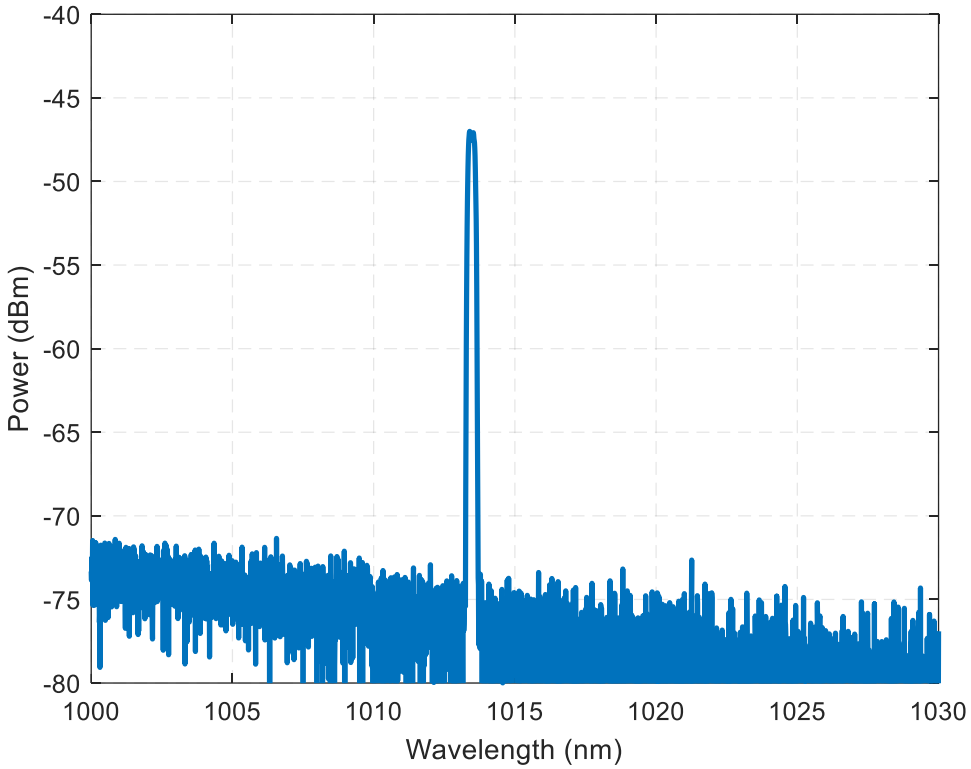

Figure 2.16 MQWL on a SiO_2/Si substrate emission spectrum with central wavelength $1013.47\ nm$ at 14.0 ℃ as obtained from the OSA. The vertical axis, which is associated with the power of the laser spectrum, is measured in dBm (logarithmic scale). The FWHM at $3\ dBm$ from the central wavelength of the depicted laser line is roughly $\Delta\lambda_{FWHM} = 0.3\ nm$.

The membrane laser's wavelength emission is susceptible to change should the heatsink temperature shift. The heatsink temperature varied via TEC controller from 12.0 ℃ to 30.0 ℃ with a 0.1 ℃ step to investigate the membrane's spectral tunability. Although condensation has been observed at 14.0 ℃ and can be an issue, it was not observed in this instance indicating that the material bonding quality in the heatsink configuration plays an important role. Because lasing ceased as the temperature increased, at 30.0 ℃ it was decided what magnitude of pump power should be applied to avoid adjustment to compensate for laser cavity losses. Hence, the pump power was constant at $0.49\ W$, above laser threshold from 12.0 ℃ to 30.0 ℃ heatsink temperature.

In Figure 2.17, the spectral evolution observed from the OSA is presented as the heatsink temperature increases. I should point out that the following thermal results and conclusions involve a single measurement from one MQWL chip. As temperature rises, the laser emission shifts to longer wavelengths because the InGaAs QW's band gap energy decreases. A mode shift was observed between 17.7 ℃ and 18.4 ℃ (Figure 2.18), where the central wavelength shifted by $0.2986\ nm$. A greater abrupt wavelength shift of $9\ nm$ occurs at 20.6 ℃. It is possible that these sudden spectral jumps are a result of sudden refractive index changes or different semiconductor

thermal expansions in the gain medium affecting the QW energy confinement levels, caused by strain due to biaxial tension, which in turn decreases the band gap energy increasing the laser emission wavelength [91] or greatly changing the laser cavity's resonance.

Regarding the FWHM evolution, each lineshape for every temperature recording throughout spectral tuning is approximately maintained at $0.3\,nm$. The temperature variation is not big enough to observe significant thermal broadening of the FWHM due to increased phonon interactions or carrier density increase as opposed to pump power increase with a constant heatsink temperature, 14 ℃ (Figure 2.19). As the pump power increases, the laser line expands allowing more additional longitudinal modes to oscillate. It is noteworthy that the membrane can withstand 30 ℃ and nearly $1\,W$ of pump power for a constant 14 ℃ temperature without burning.

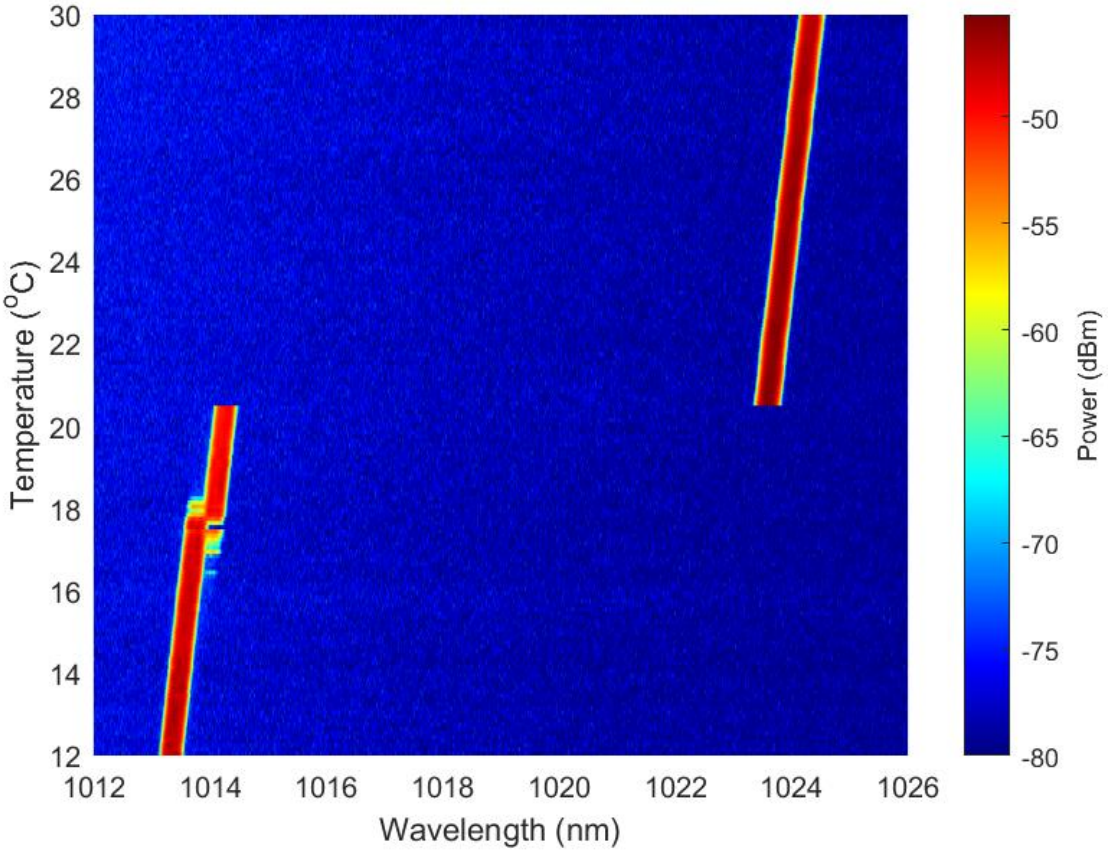

Figure 2.17 Temperature spectral tuning in $In_{0.13}Ga_{0.87}As/GaAs_{0.94}P_{0.06}$ QWs on SiO_2/Si substrate, for constant pump power, $0.49\,W$. Initially, the laser emission wavelength shifts linearly until it undergoes a sudden mode shift 17.7 ℃ were it carries on increasing linearly with heatsink temperature rise. A greater sudden $9\,nm$ shift occurs at 20.6 ℃. These sudden spectral changes are possibly due to the different semiconductor individual thermal expansions affecting the QW energy confinement levels or greatly changing the cavity's resonance or sudden material refractive index changes.

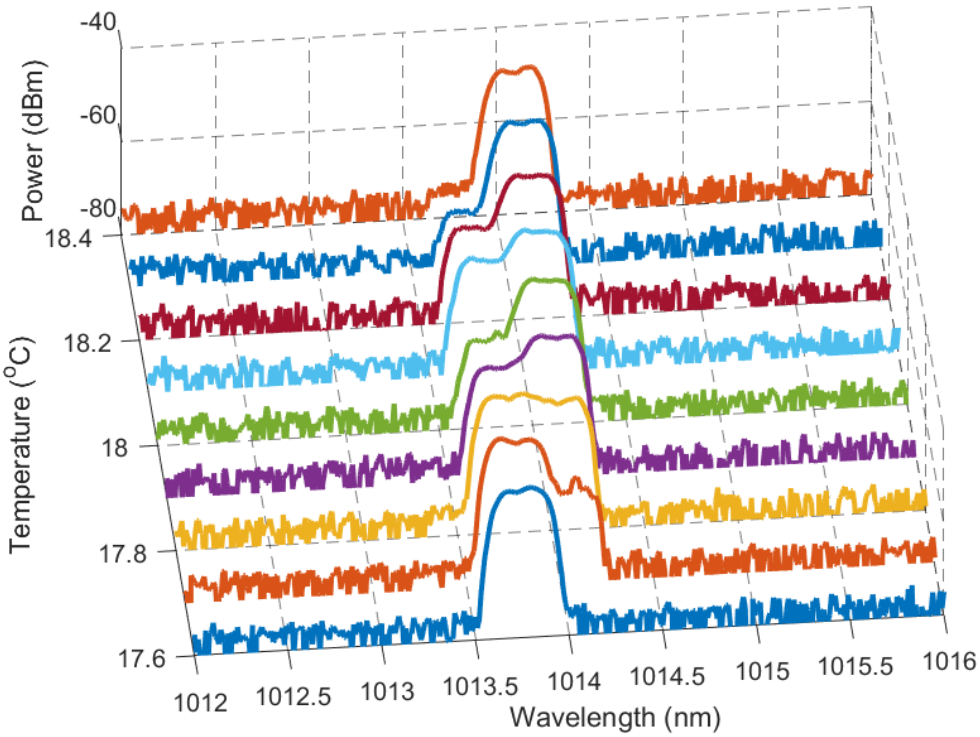

Figure 2.18 Mode competition occurring in $In_{0.13}Ga_{0.87}As/GaAs_{0.94}P_{0.06}$ QWs on SiO_2/Si substrate, for a constant $0.49\,W$ pump power. At $17.7\,℃$ energy begins to allocate to the next mode until the first disappears completely at $18.4\,℃$.

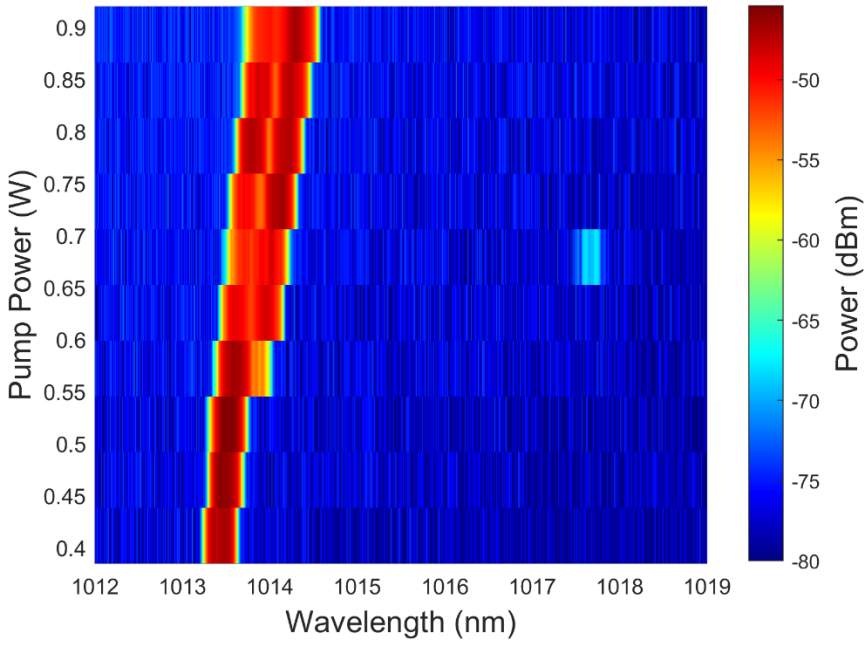

Figure 2.19 Spectrum evolution with increasing pump power and constant heatsink temperature, $14\,℃$. As the pump power rises, the intensity in the wings increases more rapidly than changing the heatsink temperature, and therefore the electrons recombining with holes increase, enhancing stimulated emission.

The overall linear thermal expansion, α_L, of the laser gain medium was determined first by considering the effect to a small temperature change in the mode frequency of the laser (Equation 2.3) [92]:

$$\frac{\Delta v}{v_0} = \frac{\Delta L}{L_0} = \alpha_L \Delta T \Rightarrow \frac{\lambda}{\lambda_0} - 1 = \alpha_L (T - T_0) \quad (2.3)$$

where v_o, L_o, λ_o, T and T_o respectively are the initial values of laser frequency, cavity length and laser wavelength, heatsink temperature measured in K, and the initial heatsink temperature. I fit a linear model within the interval $[12.0, 17.6]$ ℃ before mode hopping as shown in Figure 2.20, which gives me $a_L = (7.83 \pm 0.04) \times 10^{-5}\ K^{-1}$, one order greater than that of GaAs [93]. The thermal expansions after the sudden wavelength red shifts are like the previous value, $7.67 \times 10^{-5}\ K^{-1}$ and $7.80 \times 10^{-5}\ K^{-1}$ respectively.

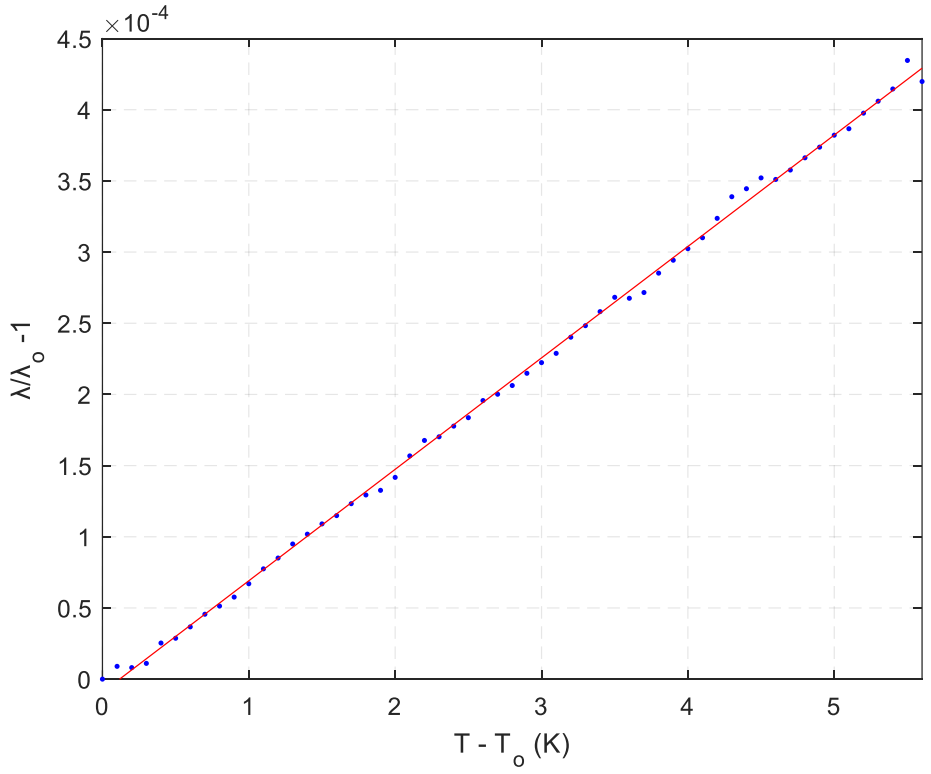

Figure 2.20 MQWL gain chip thermal expansion within the temperature range $[12.0, 17.6]$ ℃ before the first wavelength jump at 17.7 ℃. From equation 2.3, the linear fit derives the thermal expansion coefficient for the QW structure, which is $a_L = (7.83 \pm 0.04) \times 10^{-5}\ K^{-1}$.

Similarly, the rate of change in wavelength is worked out with respect to absolute temperature for each laser emission wavelength. The central wavelength increases linearly with temperature as shown in Figure 2.21, to which a linear fit is applied from which the laser

wavelength tunes at a rate of $(0.0792 \pm 0.0004)\ nm/K$. Wavelength tuning after the abrupt spectral jumps are similar to the mentioned value, $0.0781\ nm/K$ and $0.0799\ nm/K$. Temperature spectral tuning of a MQWL on SiC substrate and within the temperature range $[14.0, 20.0]$ ℃ gave a tuning rate of $0.075\ nm/K$ [22]. The latter differs from $0.0792\ nm/K$ by $5.30\ \%$. From this comparison, it is suggested that although SiC and SiO_2/Si have different heat conductivities [94], at low pump powers the latter can effectively dissipate heat and the MQWL's performance depends on the quality of the bond between membrane and substrate and heatsink.

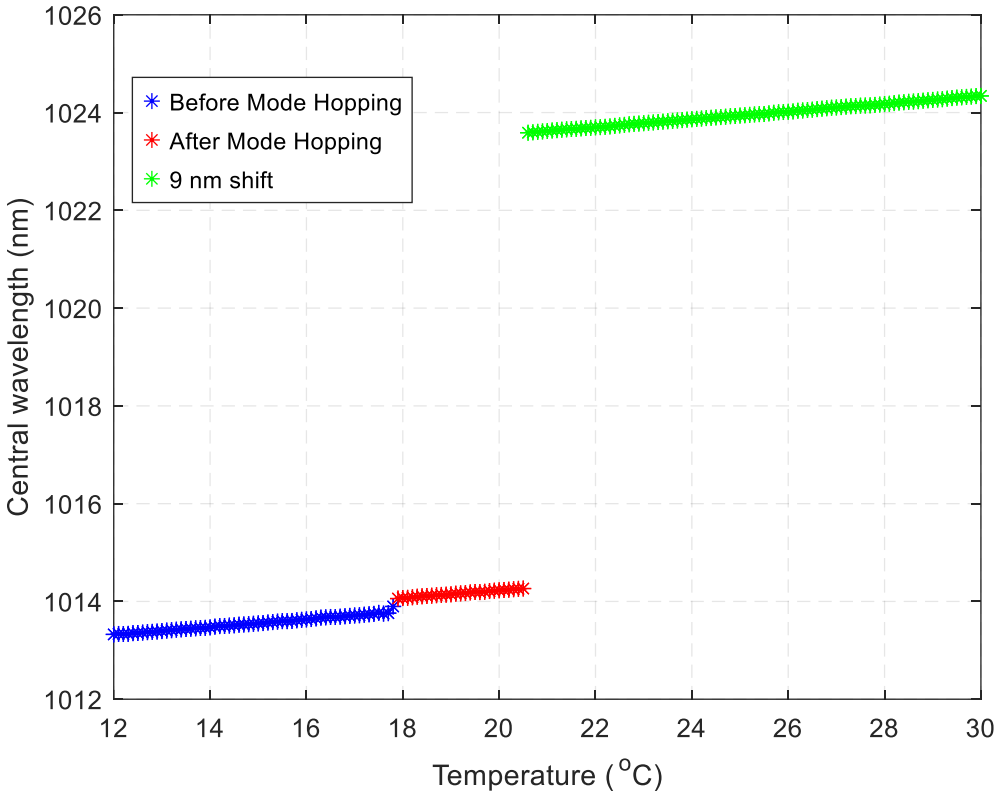

Figure 2.21 MQWL central laser emission wavelength shift with heatsink temperature rise. After fitting three different linear curves, the resulting tuning rates before and after the sudden wavelength jumps are $0.0792\ nm/K$, $0.0781\ nm/K$ and $0.0799\ nm/K$, respectively.

2.5 Membrane Laser Waveguide Simulations

As mentioned in Chapter 1, the MQWL also functions as a waveguide, which its guided modes appearing at the membrane's end facets can be simulated with COMSOL. The model is based on Figure 2.1 for which all semiconductor layers, its bottom cladding (SiO_2 or SiC) and top cladding (air) were added. The structure dimensions fall in the μm scale. The materials are defined by their refractive indices, n, which are presented in Table 2.2 at $1\ \mu m$ wavelength and $300\ K$ temperature and $293.15\ K$ for SiC and SiO_2 respectively. The wavelength and former temperature are also simulation parameters. The refractive index of $Ga_{0.94}In_{0.06}P$ was provided by

the MQWL chip manufacturers (21 Semiconductors [95]).

Mode analysis simulations were performed allowing to retrieve effective refractive indices, n_{eff}, of the guided modes by searching around the refractive index of $In_{0.13}Ga_{0.87}As$, where stimulated emission takes place. In Figures 2.22 and 2.23 the fundamental guided transverse electric (TE) modes for SiC and SiO_2 substrates respectively is presented. The fundamental modes are of interest due to its shape and effective area as it allows for greater overlap and therefore interaction with the QWs but also is subjected to less losses. The fundamental TE modes were determined once I calculated the polarisation fraction ($> 50\%$ for TE modes). Their respective effective refractive indices are 3.4923 and 3.4921.

Table 2.2 MQWL refractive index list at $1\ \mu m$ wavelength

Semiconductor	$\boldsymbol{n}$
$Ga_{0.94}In_{0.06}P$	3.219
GaAs	3.5096 [96]
$GaAs_{0.94}P_{0.06}$	3.4685 [97]
$In_{0.13}Ga_{0.87}As$	3.6341 [96]
SiC	2.5873 [98]
SiO_2	1.4504 [58]

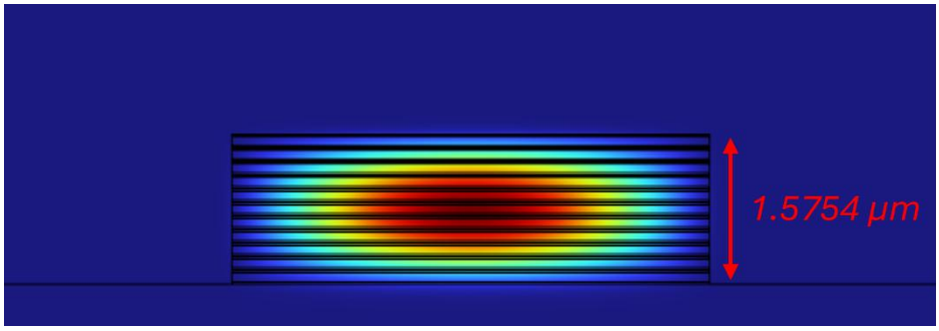

Figure 2.22 The fundamental TE guided mode inside the MQWL bottom cladded by SiC. The polarisation fraction and effective index at $1\ \mu m$ wavelength respectively are $100\ \%$ and 3.4923.

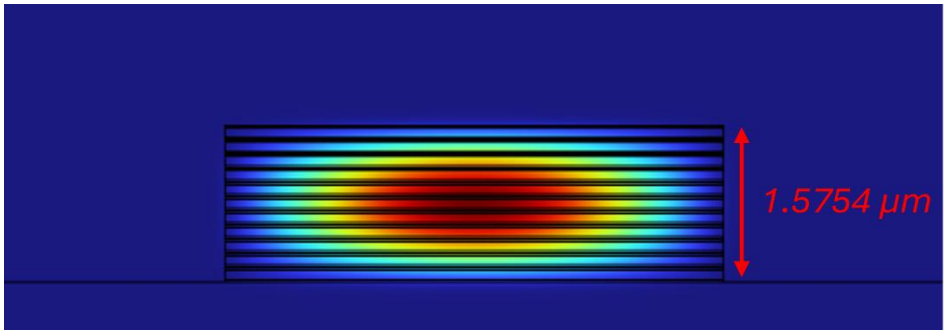

Figure 2.23 The fundamental TE guided mode inside the MQWL bottom cladded by SiO_2. The polarisation fraction and effective index at $1\ \mu m$ wavelength respectively are $100\ \%$ and 3.4921.

These simulations are crucial to obtain the group refractive index, n_g, to determine the waveguide's free spectral range (FSR) and how many laser longitudinal modes exist within the laser line. For this task a wavelength parametric sweep is required. In Figure 2.24 the plot of the effective refractive index with respect to the wavelength for the SiC substrate case is shown, which depicts a nonlinear behaviour. A third – order polynomial, $n_{eff} = A\lambda^3 + B\lambda^2 + C\lambda + D$, was fitted to the data.

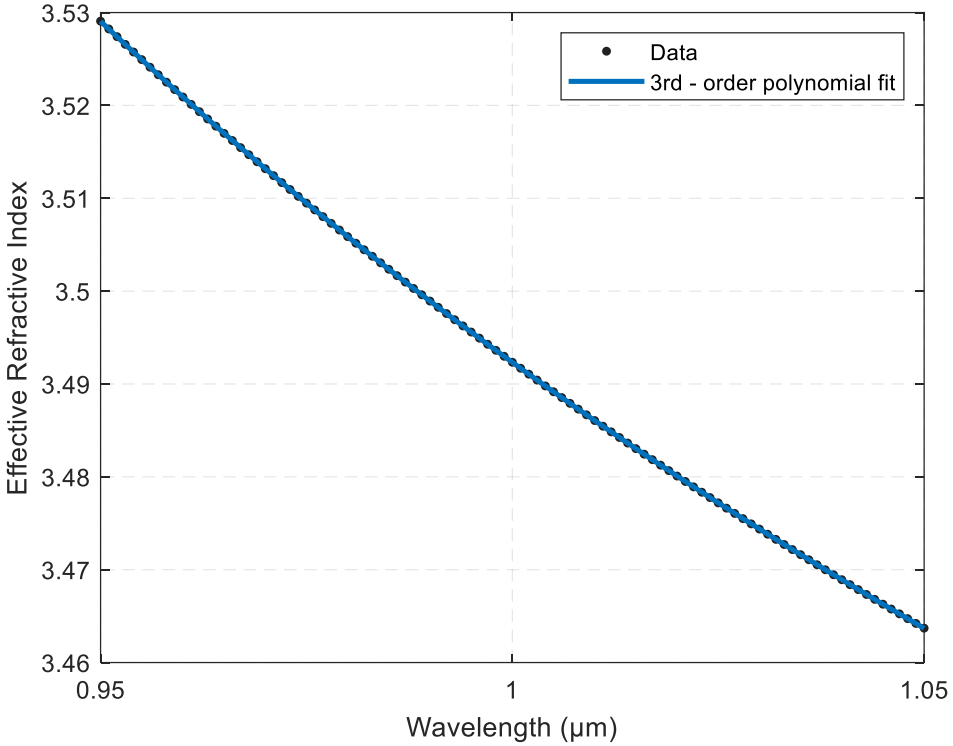

Figure 2.24 Material dispersion of MQWL gain chip. The graph was produced after running a wavelength parametric sweep in COMSOL to simulate the MQWL guided modes. The data follow a nonlinear behaviour which is best matched with a third – order polynomial fit.

The resulting fitting parameters are $A = (-4.315 \pm 0.031)\ \mu m^{-3}$, $B = (14.56 \pm 0.09)\ \mu m^{-2}$, $C = (-16.82 \pm 0.09)\ \mu m^{-1}$, and $D = (10.07 \pm 0.03)$. The group refractive index at $\lambda = 1\ \mu m$ can be calculated with two way either mathematically or graphically. In the first method, replace the polynomial in Equation 2.4 [24]:

$$n_g(\lambda) = n_{eff}(\lambda) - \lambda \frac{dn_{eff}}{d\lambda} \quad (2.4)$$

For $\lambda = 1\ \mu m$ the group refractive index is $n_g = (4.14 \pm 0.11)$. Graphically, the slope at $\lambda = 1\ \mu m$ gives $\Delta n_{eff}/\Delta\lambda = -0.65\ \mu m^{-1}$, and by substituting the values in Equation 2.4, the group refractive index is once again $n_g = 4.14$. Similarly, for SiO_2 substrate, the group refractive index is $n_g = 4.13$. From the group refractive index, the mode spacing or FSR is calculated by using Equation 2.5 [24]:

$$FSR = \frac{{\lambda_L}^2}{2n_g L} \quad (2.5)$$

For $\lambda_L = 1\ \mu m$ and $L = 424\ \mu m$, the FSR in the case of SiO_2 substrate is $0.2852\ nm$, which differs from the sudden mode red shift at 17.7 ℃ reported in Subchapter 2.4, by 4.49 %. Knowing that the FWHM is roughly $0.3\ nm$ the number of modes existing within the laser line can be calculated with Equation 2.6:

$$m = \frac{\Delta\nu_{FWHM}}{\Delta\nu_{FSR}} \quad (2.6)$$

yielding $m = 1.0519$ or $m = 1$ longitudinal mode existing in the laser cavity. This makes these lasers suitable for frequency stabilisation techniques [99], [100] for applications such as optical telecommunications as single mode laser pulse or CW is subjected to less distortion, especially if the QWs are tailored such that emission wavelength is near the zero – dispersion wavelength of the optical fibre or planar waveguide [101], [102].

2.6 Microstructures

The nature of MQWLs inspired the exploration of defining geometric structures on the QW device via photolithography. I aim to create geometric shapes such as linear cavities and disks to form defined laser arrays or observe whispering gallery modes (WGMs) respectively.

The first task was to create an appropriate mask to use for photolithography in the cleanroom facility. The mask itself consists of a layer of chrome on a glass substrate. The desired features designated to be transferred on the MQWL are engraved on the chrome layer based on the mask designed using KLayout (Figure 2.25).

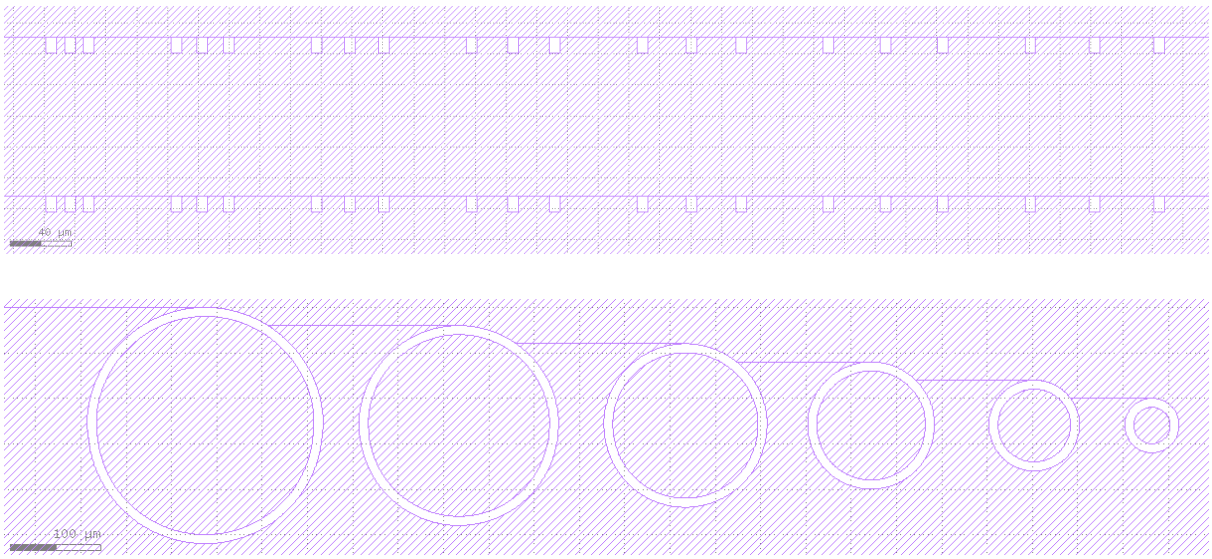

Figure 2.25 Segments of the photolithography mask design on a micrometre scale. Shaded areas represent the opaque chrome layer, whereas white areas represent transparent areas which allows light to shine through. The top image depicts grouped linear cavities of three with gradually increasing separation and constant length, and the cavities' end facets are defined by the white rectangles. The bottom image depicts disks of gradually decreasing radii. The width of white segments is $10\ \mu m$.

Once the final optical mask was obtained, it was decided to create micro disks on the selected membrane gain chip. The cleanroom process went as follows:

- Spin coating the membrane chip with positive photoresist (Microposit S1813 G2).
- Baking the coated membrane on a hot plate for $1\ min$ at 115 ℃. Then leave the membrane to cool down for $5\ min$.
- Placing the mask and baked membrane in the mask aligner, where photolithography is performed. Allowing for hard contact between mask and sample, and an exposure time of $4.5\ s$, UV radiation propagates through the transparent areas of the mask tackling the unconcealed photoresist, softening it in the process.

- Developing the UV treated sample with tetramethylammonium hydroxide solution (Microposit MF – 319 Developer) for $45\ s$ and then rinse with deionised (DI) water (H_2O). The unexposed portion of the photoresist remains insoluble to the photoresist developer.
- Because of concerns that by blow drying with nitrogen (N_2) the membrane would fly away from its substrate, the sample was baked for a few seconds at $115\ ℃$ until water was evaporated.

Hereafter, the membrane sample was wet etched by using a mixture of sulfuric acid (H_2SO_4), hydrogen peroxide (H_2O_2) and DI H_2O. Hydrochloric acid (HCl) was applied for $1\ min$ to remove the $20\ nm$ thick layer of GaInP, because the chemicals mentioned earlier react extremely slowly with it. I verified the GaInP removal with a stylus profiler, which has $2\ \mu m$ radius tip. The remaining QW structure remains unaffected by HCl.

Because the QW structure consists of $64.45\ \%$ of GaAs, a gentle solution of 1:2:80 mixing ratio of H_2SO_4, H_2O_2, and H_2O respectively was used. Initially, the etch rate of a pure GaAs sample was calibrated for reference purposes which at room temperature corresponds to a $(0.34 \pm 0.01)\ \mu m/min$ rate. Based on this etch rate and knowing the membrane's overall thickness not including the top GaInP layer, it was decided to etch for $6\ min$ during which etch depth measurements were performed every minute. The MQWL gain medium etch gave an etch rate of $(0.24 \pm 0.01)\ \mu m/min$ (Figure 2.26), roughly $30\ \%$ faster than etching pure GaAs.

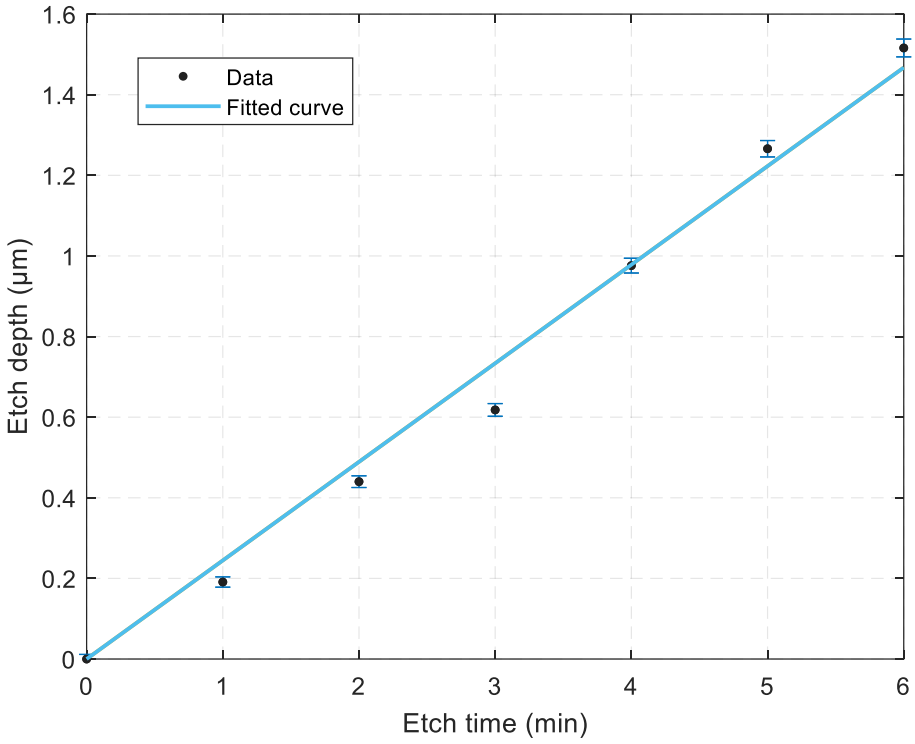

Figure 2.26 Wet etching of MQWL gain medium with a solution of 1:2:80 mixing ratio of H_2SO_4, H_2O_2, and DI H_2O respectively. The top 20 nm thick GaInP layer was removed with HCl. After removing the GaInP layer, the wet etch process yielded an etch rate of $(0.24 \pm 0.01)\ \mu m/min$ at room temperature.

At each measurement, the membrane was rinsed with DI water and then baked at 115 ℃ for a few seconds to evaporate water and then use the stylus profiler. After the final etch, the membrane is thoroughly rinsed with DI water, then stripped from its remaining photoresist with acetone and then isopropyl alcohol (IPA) and then rinsed again with DI water and finally baked at 115 ℃ for several seconds. The resulting patterned membrane gain medium is shown in Figure 2.27, where disks and rings are formed. The rings are the areas that were irradiated by UV light and then were subjected to wet etching. The rings at the edges are relatively etched all the way down to the silica substrate possibly due to side etching. Inward rings do not exhibit the same feature, but the bottom GaInP is left exposed, and some rings did not form possibly due to remaining top GaInP layer. A central etched spot is included in some disks to induce losses and therefore prohibit lasing along the disk's diameters and create WGMs.

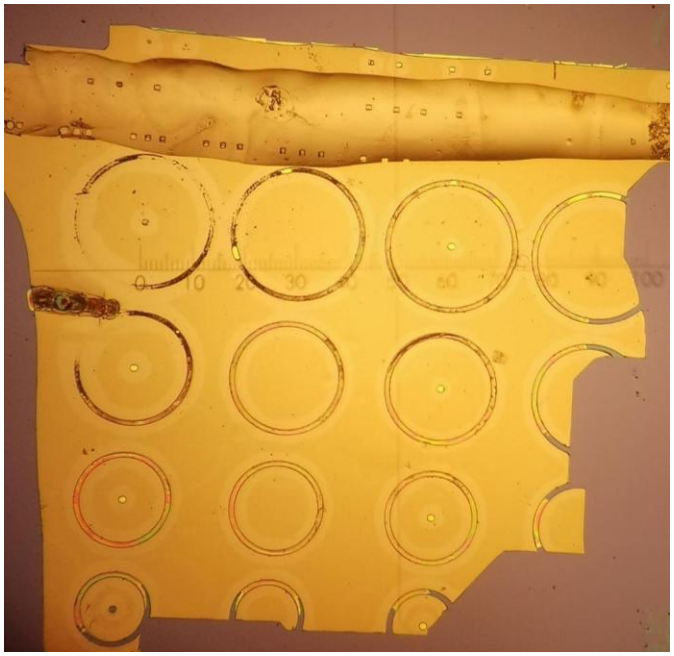

Figure 2.27 Micro disks on MQWL chip. The disks were created in a cleanroom environment through the process of photolithography and wet etching with 1:2:80 mixing ratio of H_2SO_4, H_2O_2, and H_2O respectively. The top GaInP layer was removed with HCl. Insufficient removal of the former resulted in poor etching of some micro disks. Disks which were patterned close to the chip's edges were subjected to side etching exposing the substrate.

Using the experimental setup presented in Figure 2.3, the micro disks are optically pumped with the $808\,nm$ diode laser to observe whispering gallery modes or lasing assuming that concentric optical cavities are formed due to the micro disks' curvature. Pumping power ranges from $170\,mW$ to $1.67\,W$ only recording the lowest and highest settings as shown in Figure 2.28. The lowest power is smaller than most laser threshold values recorded for membrane gain chips, so no lasing was expected. As the pump power ramped up, lasing was visible in the real space images but only spontaneous emission. At $1.67\,W$ pump power, still no stimulated emission took place even if the power was much higher than the recorded threshold conditions. Reciprocal space did not capture any interference pattern throughout the pump power sweep. Measurements with an OSA verified the absence of lasing. The photoluminescence was captured at $170\,mW$ and $1.67\,W$ pump powers (Figure 2.29), but there was no sign of sharp laser peaks to indicate the existence of stimulated emission.

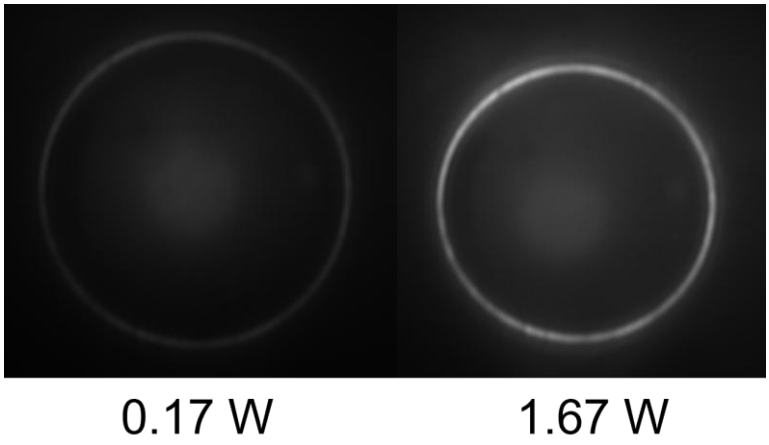

Figure 2.28 Real space images of optically pumping a micro disk at two different pump power settings. On the left, the micro disk is pumped with low power but even for an unprocessed membrane gain chip, this value can be very low to reach laser threshold. On the right, the same micro disk is pumped with very high power, which is higher than any laser threshold setting recorded. In both cases, spontaneous emission is visible, but no stimulated emission occurs.

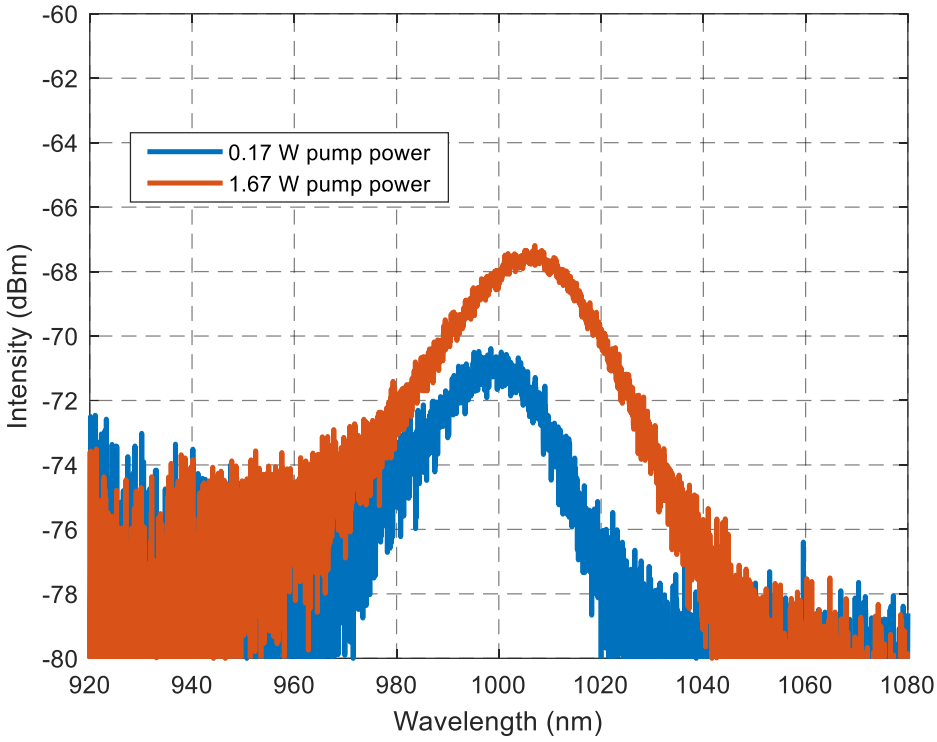

Figure 2.29 Photoluminescence of the micro disk at 170 mW and 1.67 W pump powers. The absence of sharp peaks indicate that the micro disc does not lase.

One reason why no lasing was observed at the edges of the micro disk is the roughness of the end facets after wet etching. An image from a scanning electron microscope (SEM) was captured to examine the sidewall topography (Figure 2.30). From the image, after wet etching with

1:2:80 mixing ratio of H_2SO_4, H_2O_2, and H_2O respectively, the resulting sidewalls are of poor quality.

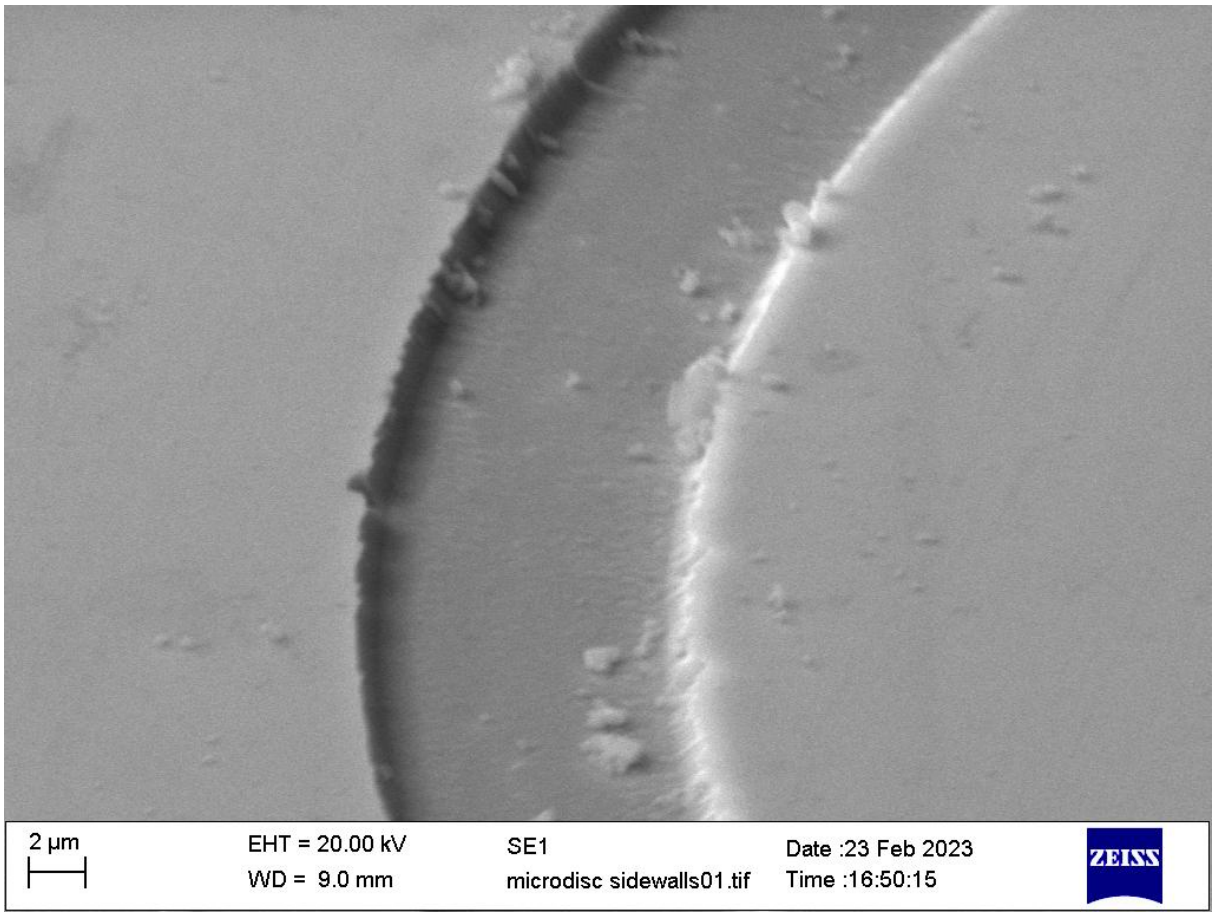

Figure 2.30 SEM image of the sidewalls of a micro disk. From the picture, the sidewalls are not smooth after wet etching with 1:2:80 mixing ratio of H_2SO_4, H_2O_2, and H_2O respectively indicating poor quality end facets of the newly formed structure.

2.7 Conclusions

The aims of this chapter were to explore the CW membrane quantum well laser, and to demonstrate its capabilities as a potential coherent light source for integrated photonic circuits. Optically pumped MQWLs on a SiC and oxidised silicon substrate were both tested by capturing real and reciprocal space images, which allowed examination of the physical and Fourier features of the membrane lasers. Real space imaging gave me information such as pump spot size on top of the membrane from spontaneous emission, length of membrane or cavity length, and the number of laser oscillators appearing, indicated by the bright spots at the membrane's end facets. Reciprocal space imaging recorded the interference pattern from which cavity length could be calculated through Fourier transform of the averaged wave form, but also it clearly

indicated when the membrane device transitioned from spontaneous to stimulated emission. Laser threshold was significantly lowered down to $211\ mW$ pump power compared to that of MECSEL configuration with the same QW design ($0.7\ W$ [82]).

A model in COMSOL was constructed to simulate the MQWL's cross section and guided modes to retrieve effective and group refractive indices, modal free spectral range, and from there I can calculate the number of longitudinal modes existing inside the laser cavity.

The creation of coherent laser arrays which couple into each other with a π – phase delay was demonstrated. This notion was suggested experimentally as no fringes appeared in the far – field patterns at $0°$ captured by the CCD camera and was supported by MATLAB simulations. Output optical power increased with the existence of multiple cavity oscillating simultaneously.

An attempt was made to fabricate microstructures such as disks and arrays on the MQWL gain chip for WGMs and laser arrays via photolithography and wet etching. Although fabrication is feasible, wet etching produced poor quality sidewalls making the structures very lossy.

Spectral features documented by the OSA showed that the emitted wavelength is 1 μm and the temperature change shifted the emission wavelength by $0.075\ nm/K$ and $0.0792\ nm/K$ for SiC and SiO_2/Si substrates respectively suggesting that although SiC conducts heat more efficiently than SiO_2/Si, the MQWL's performance depends on the quality of its bond with the heatsink. The FWHM remained unchanged during the small heatsink temperature variation, however the pump power increase resulted in thermal broadening of the laser's linewidth.

Chapter 3

Membrane Quantum Well Laser Arrays

In Chapter 2, it was shown that the membrane quantum well lasers are capable of lasing with one or multiple cavities resembling laser diode bars or arrays. In this chapter, additional experiments and simulations are carried out to further explore and understand the nature of these phase – locked laser emitters. In the previous chapter, an attempt was made to construct microstructures on the quantum well chips. Although structures were created, they had rough end facets, so lasing was not feasible due to high cavity losses. Alternatively, manipulating the pump spot shape would give the chance to pump the membrane gain medium such that microstructures are not required or, if they were fabricated with near vertical smooth sidewalls, the customised pump beam profile would match the fabricated geometry. In this chapter, phase – locked laser arrays with anti – phase and in – phase coupling in membrane quantum well lasers on an oxidised silicon substrate are demonstrated by utilising a digital micromirror device to spatially modulate the pump laser beam shape along with simulations to describe the nature of these devices. Dr Nicholas Klokkou finalised the experimental setup, performed the numerical simulations and conducted some of the experiments including the power transfer experiment.

3.1 Beam Shaping

First attempts of laser beam shaping were performed with cylindrical and axicon lenses. Cylindrical lenses shape the laser spot into a line, whereas axicon lenses transform laser spots into rings. The former was tested (Appendix A) to pump the membrane quantum well lasers along the cavity length, and the latter was experimented with (Appendix B) to pump MQWL ring resonators, after being created from photolithography.

The use of a cylindrical lens achieved lasing in MQWLs, however the conclusion was that although lasing was observed, the pump line profile would not compress along its longest dimension. Power was lost at the end facets, and hence the cylindrical lens was inefficient to implement. In the axicon setup, two axicon lenses were used, one for the beam ring creation and the other to collimate. However, due to the pump beam's expansion and possible tip

imperfections in the axicons, the second axicon would focus the ring beam down to a Bessel function profile with no apparent laser ring at sub – mm levels.

The above experiments lead to the discussions to consider a digital micromirror device (DMD) to give any geometric shape to the pump beam and excite the MQWL accordingly. The DMD consists of multiple reflective mirrors, digitally switchable, μm - sized mirrors or micromirrors organised in a two - dimensional array. Incident light is shaped into the image I feed from the computer to the DMD. After feeding the image, light modulation is achieved by rotating the micromirrors based on the colour pattern of the image (Figure 3.1), with some mirrors projecting light on the desired optical path, which are called “on – state” micromirrors, and others project light to a designated area for dumping, which are called “off – state” micromirrors. The new light pattern is used to pump the membranes from the top, to observe and explore single and multiple laser cavity dynamics. As the micromirrors incline, they form a diffraction grating and simultaneously diffract and reflect the incident laser beam [103], [104], [105].

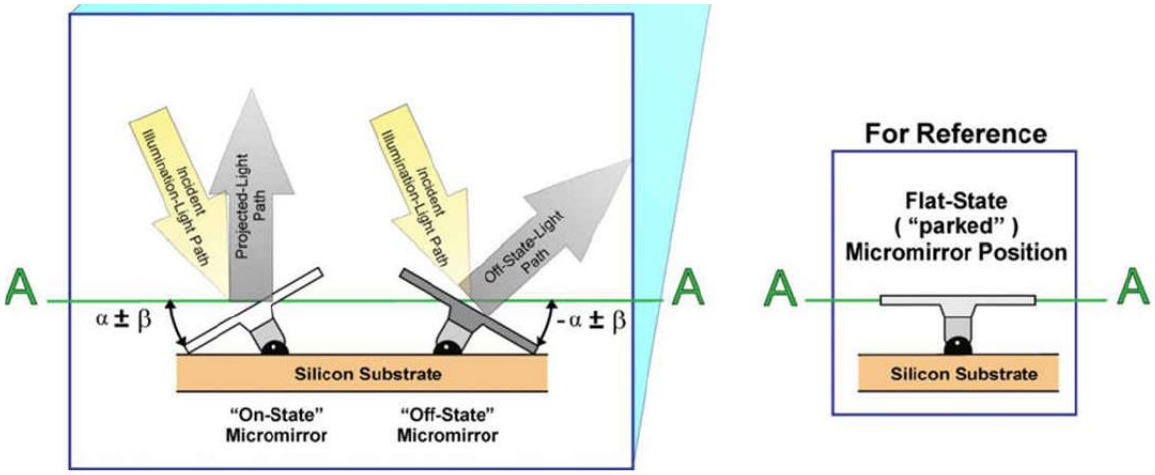

Figure 3.1 DMD micromirror flipping [106]. The micromirrors rotate about the reference line “A” depending on the image fed into the device’s software. Depending on the image, “on – state” and “off – state” micromirrors respectively project light on the desired optical path and dumping area, effectively shaping the pump spot based on the desired image.

3.2 Experimental Setup and Methodology of MQWL Arrays

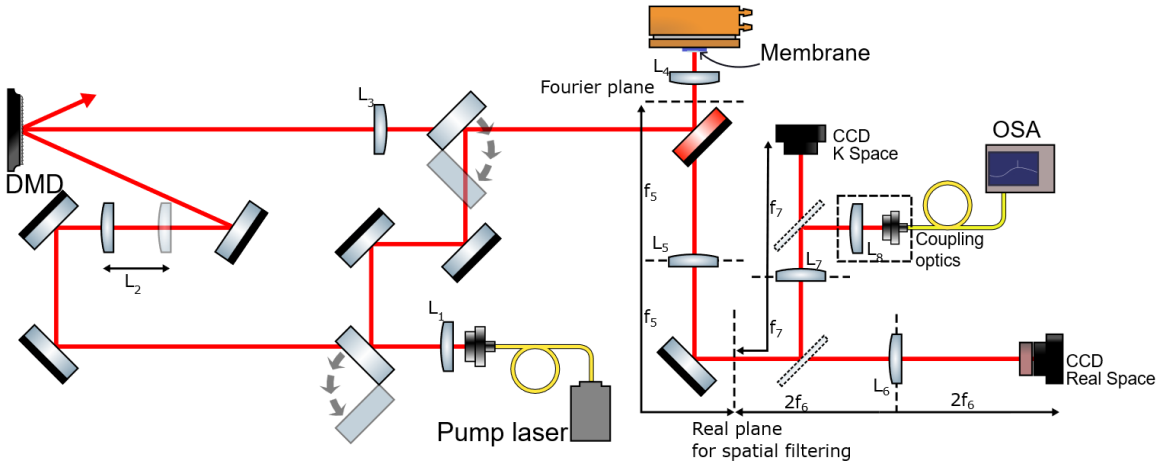

Figure 3.2 Schematic of the experimental setup used to characterise the MQWL which is optically pumped with a DMD. The DMD diffracts the incident light with each micromirror reflecting the image assigned to the device. The MQWL emits from the material's end facets and scattered light is collected from the top. The pellicle beam splitter (P) splits the collected laser beam into two components, simultaneously transmitting them to the real image and Fourier plane CCD cameras to respectively capture the physical and reciprocal features of the membrane laser. The OSA records the membrane laser's optical frequencies.

The MQWL chip under investigation used in this chapter has the same structure as the ones used in Chapter 2 but only with an oxidised silicon substrate. A similar experimental setup to the one presented in Chapter 2 is used to explore and characterise the membrane structure (Figure 3.2). The setup was designed by using the reZonator software along with matrix formulation. The design aimed to decide which lenses should be used to realise the setup from Figure 3.2 based on a Gaussian pulse of $M^2 = 1$. Although in reality the pump diode beam resembled a super Gaussian profile, the design gave a good insight of the optical elements required to build the setup. The chip along with its substrate is in thermal contact with a copper block, whose temperature is maintained by a thermoelectric element and a proportional – integral – derivative (PID) servo at 14 ℃. This value is the lowest temperature achieved in our lab before water vapour condensates. The thermoelectric element sinks heat transferred from the sample into a closed loop water cooled copper block.

The MQWL is optically pumped from top to bottom with a diode laser emitting at $808\ nm$,

which has a slope efficiency of $(1.0070 \pm 0.0013)\ mW/mA$ (Figure 3.3). Initially, the diode laser beam is collimated with a $f_{L1} = 15\ mm$ plano – convex lens (L_1) and then is directed by a series of mirrors onto the DMD at an $24°$ angle. The specific angle is essential so that the DMD reflects and diffracts the beam at a direction normal to its reference line (Figure 3.1). Lens L_2 with focal length $f_{L2} = 500\ mm$ is in place to maintain pump collimation as the pump diode laser consists of a multimode optical fibre making it difficult to perfectly collimate. The resulting diffracted pattern follows a sinc – squared function, but the zeroth order is collected and collimated with a $f_{L3} = 500\ mm$ doublet lens (L_3), as most of the beam energy is concentrated there. The zeroth order is sent to a dichroic mirror, which reflects the pump's wavelength and directs it through a $f_{L4} = 30\ mm$ doublet lens (L_4), which in turn focuses the beam on the gain chip, effectively imaging the DMD on top of it.

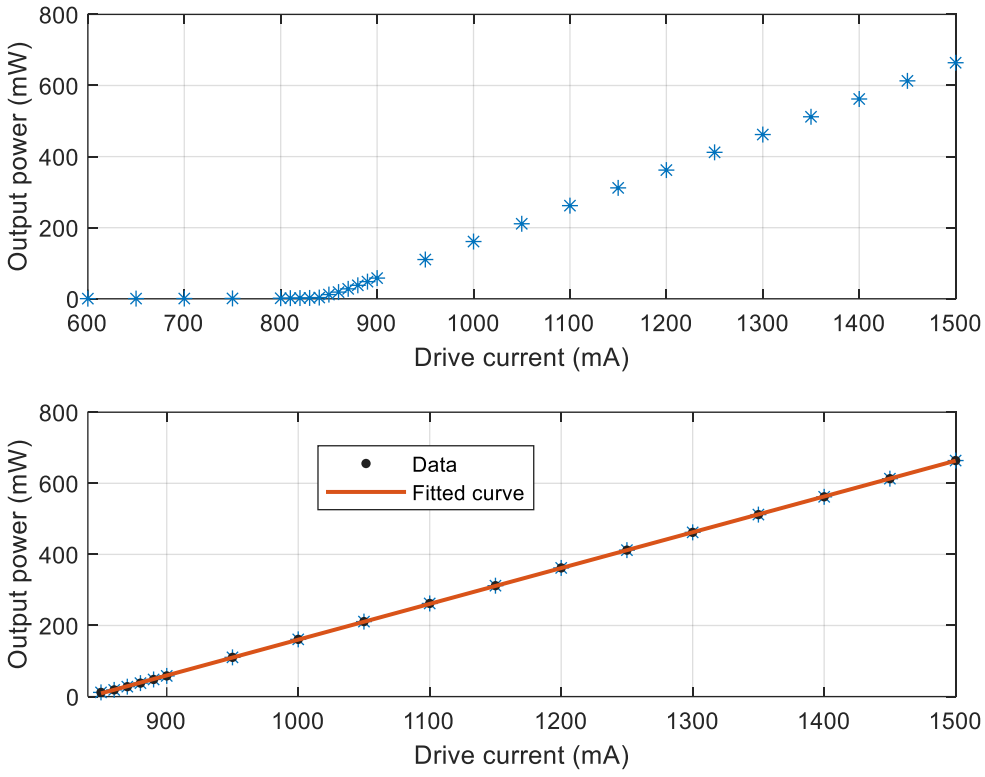

Figure 3.3 Pump diode laser P – I emission characteristic curve emitting at $808\ nm$. The top plot presents the diode laser's optical power against its injection current. After laser threshold, around $846.8\ mA$, stimulated emission is observed indicated by the sharp increase in optical power. The bottom plot displays a linear fit to the stimulated emission region matching the data behaviour and giving a slope efficiency of $(1.0070 \pm 0.0013)\ mW/mA$.

The membrane lases perpendicular to the material's growth direction, which emits a wavelength of roughly $1\ \mu m$ for the specific QW design. The scattered light from the end facets is collected from the top by the same focusing lens, L_4, and is transmitted by the dichroic mirror to lens L_5 with focal length $f_{L5} = 150\ mm$ for image spatial filtering at its focal plane. The processed light is sent to the imaging segment of the experimental setup. A pellicle placed in front of the focal plane of L_5 splits the collected light into two components, with one propagating in the real space imaging path and the other in the reciprocal space imaging path. The real space imaging path captures top view pictures revealing physical features of the membrane gain sample and the pump laser beam shape. The reciprocal space imaging path captures images displaying the resulting interference or diffraction pattern from the coherent laser emitters appearing at the membrane's end facets.

The former consists of a $f_{L6} = 150\ mm$ plano – convex lens (L_6), which focuses the laser light onto a charge coupled device (CCD) to capture images. The latter incorporates a $f_{L7} = 75\ mm$ plano – convex lens (L_7), positioned at a distance $A + B = 2f_{L7}$ away from the focal plane of L_5, and $2f_{L7}$ away from this path's CCD. Lens L_7 is placed in such a way to reproduce the Fourier plane on the CCD formed at f_{L4} between L_4 and the dichroic mirror. Both CCDs have a neutral density (ND) filter attached to them with the reciprocal space CCD also including a long pass filter along, that has a cut on wavelength of $900\ nm$. The calibration factors for the real and the reciprocal space CCD images respectively are $1.0348\ \mu m/pixel$ and $0.0086\ °/pixel$.

Finally, a pellicle was positioned between L_7 and the reciprocal space CCD. A portion of the light beam is sent through a $f_{L8} = 30\ mm$ plano – convex lens, L_8, and focused onto a multimode optical fibre, which in turn is connected to an optical spectrum analyser (OSA) to read the membrane laser's output spectrum.

Regarding the DMD, it sits on a water – cooled copper heatsink. This is necessary because pump power is lost when reshaping the pump spot and only transmitting the zeroth order diffraction. Thus, to achieve membrane lasing, the pump power needs to increase which results in additional heat deposition on the DMD, which requires cooling to dissipate it. Along with its motherboard, the heatsinked DMD screwed on a 3D printed mount (Figure 3.4), which is attached to a commercial lens mount and in turn is connected to a translation stage, thus allowing six degrees of freedom to optimise pump efficiency and alignment.

Before building the experimental setup presented in Figure 3.2, I performed a power loss measurement to determine how much the DMD reduces the pump diode optical power. I built a small setup consisting of a mirror, the DMD and two plano – convex lenses with $40\ mm$ and $30\ mm$ focal lengths, and an integrating sphere. The pump diode laser beam projected on the

DMD by the mirror at an $24°$ angle. The two lenses are placed in front of the DMD collecting a portion of the diffraction orders. The assigned DMD image is a circle. The integrating sphere is placed at three different positions, in front of the laser, in front of the mirror, and in front of the last lens. The power reading at each position for an $808\ nm$ wavelength is $161\ mW$, $159\ mW$ and $90\ mW$ respectively. The power drop due to the mirror is insignificant, however the DMD decreases it by $57\ \%$ considering that losses from the lenses are negligible. This shows that the pump power needs to increase much more compared to the setup used in Chapter 2.

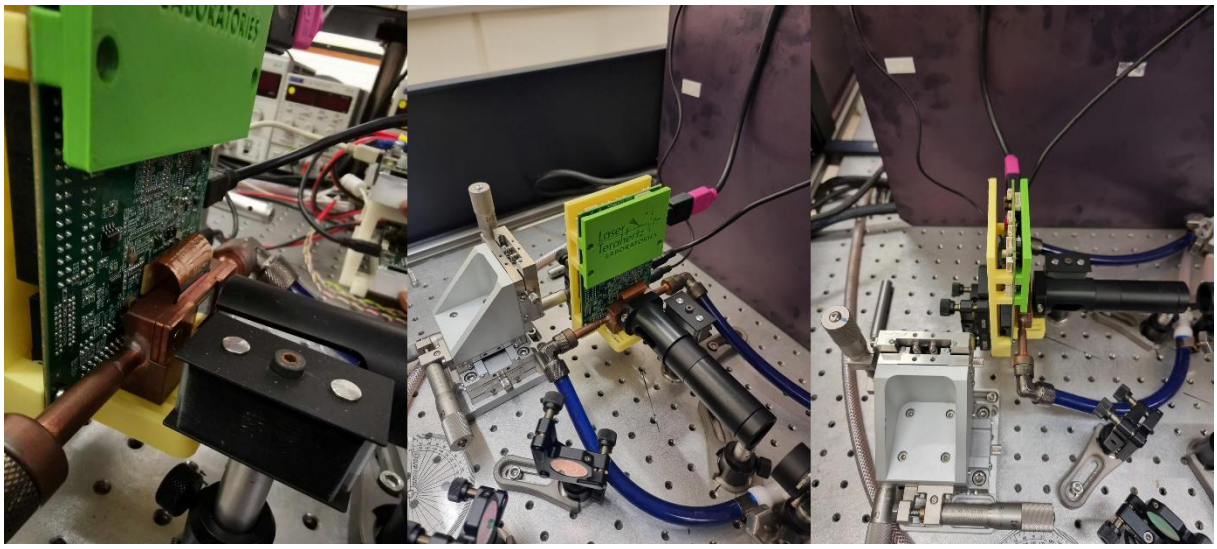

Figure 3.4 The DMD situated on a water – cooled heatsink, and its circuit board is attached to a 3D printed base, which features the group's logo. All components are attached to a commercial lens mount, which in turn is attached to a translation stage. This setup allows six (6) degrees of freedom to adjust the DMD's position and angle.

Microsoft PowerPoint was the presentation software of choice to display various images on top of the membrane chip through the DMD. The pump laser beam is mainly shaped to be one or two or even three rectangles to pump along the membrane length and stimulate one or multiple laser cavities. For example, Figure 3.5 depicts a top view image of the membrane device, where spontaneous emission from the two pump illumination rectangles is visible, which causes two laser cavities to oscillate simultaneously thus creating a laser array. The membrane's end facets are indicated from where the laser emitters appear.

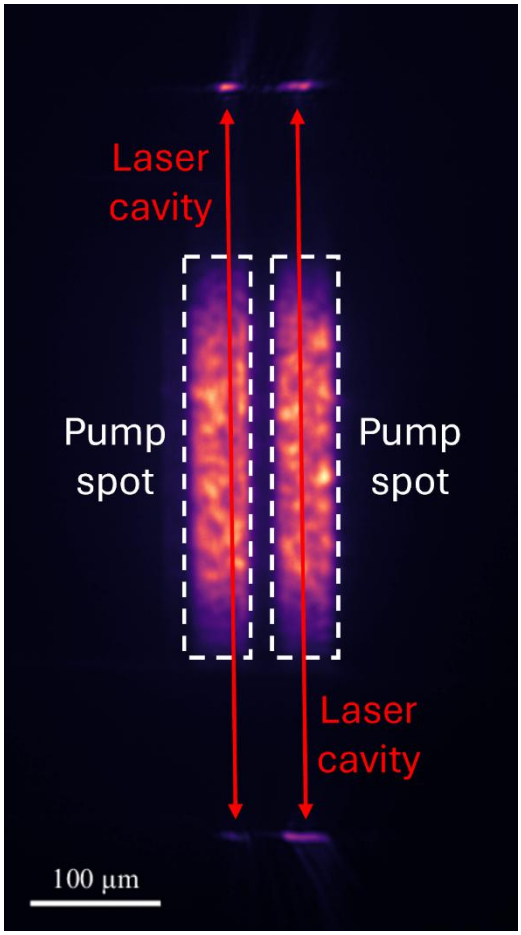

Figure 3.5 Top view image of the membrane quantum well laser array created by two pump stripes. The pump diode laser power output before interacting with the DMD is $4.23\ W$. The device is optically pumped from top to bottom after the pump laser was shaped to resemble two rectangles from the DMD as indicated by its spontaneous emission. Each rectangle stimulates a laser cavity as shown by the two laser emitter pairs appearing at the membrane's end facets, creating a laser array.

3.3 Experimental Results of MQWL Arrays

3.3.1 Anti – Phase and In – Phase Laser Cavity Coupling

The results presented in this sub – chapter exclusively involve laser arrays and their dynamics. To begin with, the ability of enabling laser oscillators to couple into each other anti – phase or in – phase is shown. Figure 3.6 depicts membrane lasing in a specific region. Figure 3.6a exhibits pumping with the diode laser after being shaped into a rectangle from the DMD with its width being approximately $50\ \mu m$. In Figure 3.6b, the membrane is pumped with another rectangle but $25\ \mu m$ away from the area pumped in Figure 3.6a. In Figure 3.6c, the image has

changed once again, now featuring both rectangles. In all cases of Figure 3.6, two rectangles were formed with $4.4\ W$ pump power before the DMD, with the difference that a pump stripe was concealed, one in Figure 3.6a and 3.6b. Laser are formed in Figure 3.6c. Each stripe stimulates a laser cavity with the laser emitters interfering with each other creating interference patterns featured in Figure 3.6d – f. In Figures 3.6d and 3.6e single interference patterns are observed, whereas in Figure 3.6f multiple ones. As no fringes appear at a zero angle displacement and as demonstrated in Chapter 2, this suggests that the adjacent laser oscillators couple to each other π – phase [88], [89], [90].

In addition, for a different separation between the laser stripes, in this case greater as shown in Figure 3.7a, the laser cavity coupling could also be in – phase [88], [89], [90], as presented in Figure 3.7b, based on the simulations from Chapter 2. Although for most laser stripe separations, the cavity coupling was anti – phase.

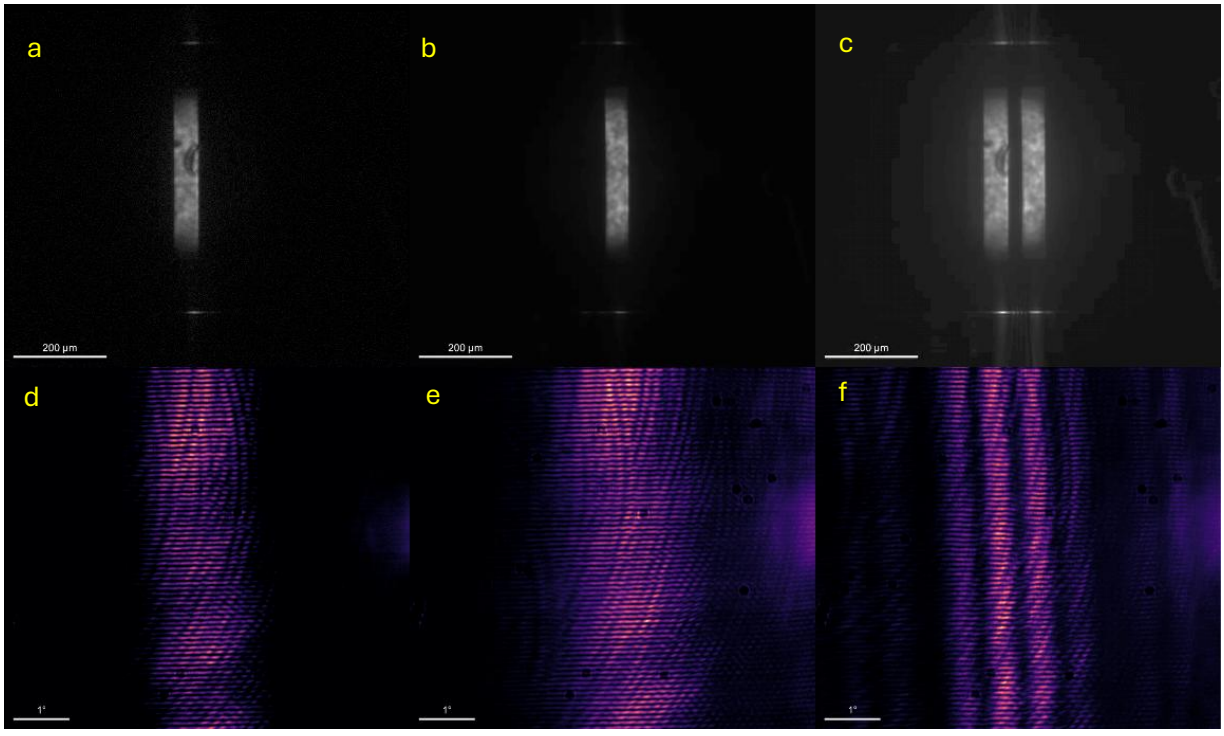

Figure 3.6 Optically pumped MQWL with the DMD. Image (a) shows a pump stripe of approximately $50\ \mu m$ wide imaged on top of the membrane causing lasing as indicated by its end facets, and its corresponding k – space with a characteristic interference pattern (d). Image (b) shows another pump stripe of the same width and at a distance of approximately $25\ \mu m$ away from the previous one; the k – space image again displays an interference pattern due to the membrane's lasing (e). Picture (c) shows lasing of the sample when both stripes are imaged on top of the sample; the interference on the x – axis of the k – space image of the configuration shows anti – phase coupling of the oscillators (f).

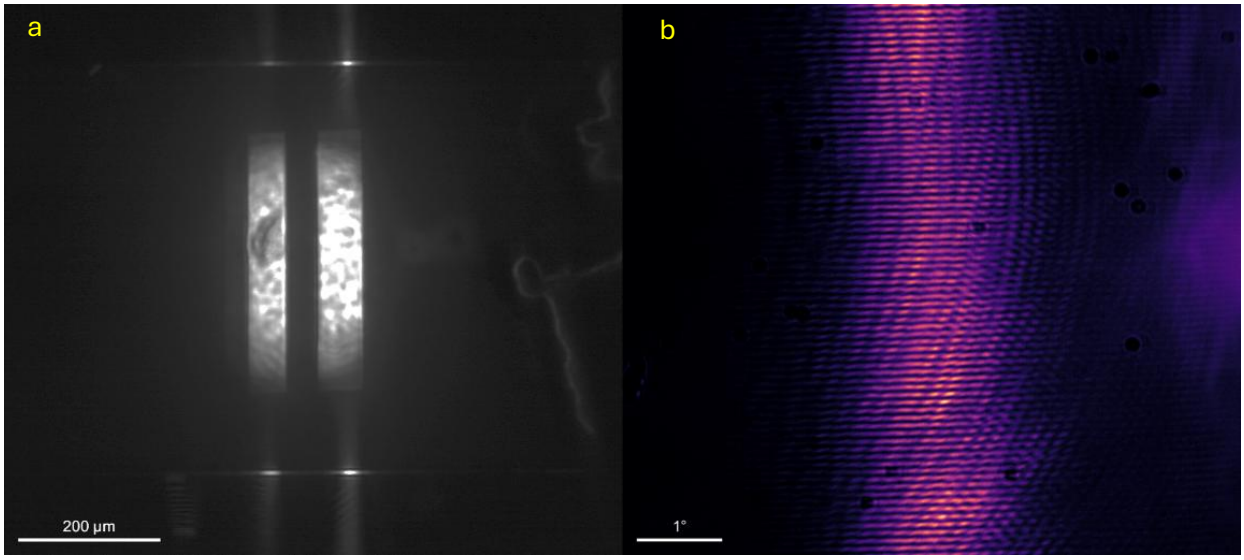

Figure 3.7 In – phase coupling of two laser oscillators. (a) Top view image of the MQWL chip, spontaneous emission caused by the pump diode laser, and stimulated emission appearing at the structure's end facets. Each laser stripe creates a laser cavity. (b) The corresponding interference from the laser emitters as displayed on the reciprocal space CCD where the pattern suggests that the laser cavities couple into each other in – phase [88], [89], [90].

A closer look at the case of Figure 3.6c and 3.6f was given. The gain sample is pumped by two adjacent and parallel rectangular light stripes after the circular pump spot is diffracted from the DMD. As shown in the real space image (Figure 3.8a), each stripe creates a laser oscillator, which interferes with each other resulting in the far – field patterns as depicted in the reciprocal space image (Figure 3.8b). Taking into consideration the far – field pattern simulation, it is deduced that the laser oscillators operate at a π – phase shift. This thought is supported by a simulation performed using MATLAB (Figure 3.8c), the same as the one used in Chapter 2. The coupling phase relationship is also validated by the fact that the laser intensity fields nearly destructively interfere between the laser cavities, as indicated in the real space image (Figure 3.8a) and upper (Figure 3.8d) and lower (Figure 3.8e) facet intensity profile scans [88], [89], [90].

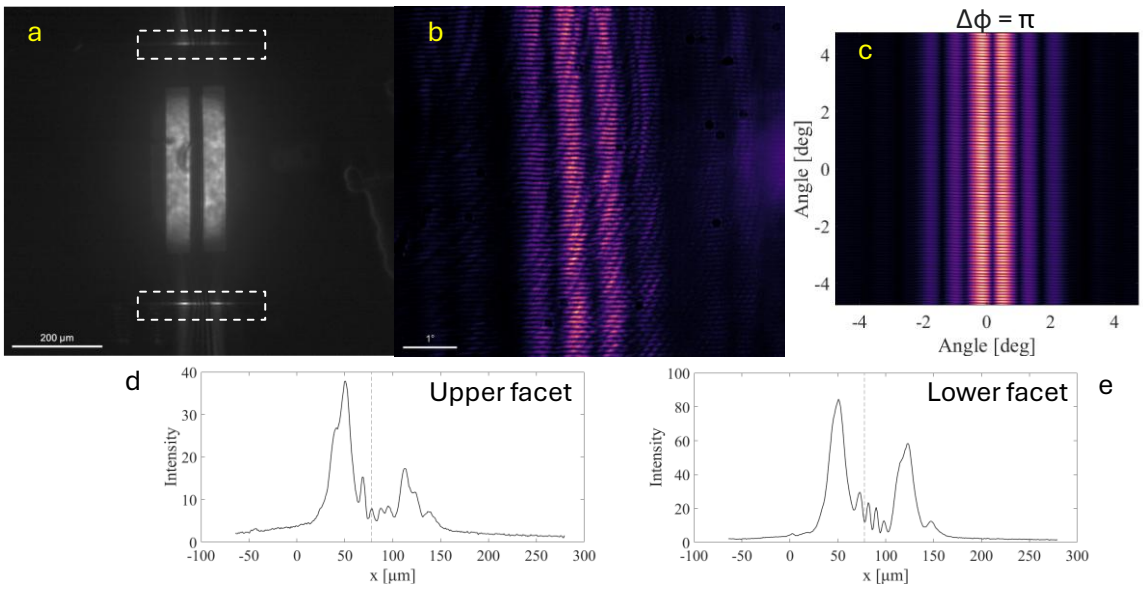

Figure 3.8 Out – of – phase coupling of two laser oscillators. (a) Top view of MQWL surface, the two pump laser stripes of same size and the laser emitters they create. (b) The corresponding far – field pattern, which suggests an out – of – phase laser cavity coupling, which in turn is supported by a simulation shown in (c). Antiphase coupling is also corroborated by the fact that the laser intensity fields nearly destructively interfere between the laser cavities, as indicated in the real space image and upper (d) and lower (c) facet intensity profile scans [88], [89], [90].

3.3.2 Laser Cavity Separation

The final experiment performed with the pump stripes is to vary the separation to examine whether the phase relationship between two laser cavities depends on their separation gap. The method followed involves pumping the membrane with two laser stripes to create two laser cavities under constant pump power, $4.4\ W$ deposited on the DMD, and then slightly increase or decrease the stripe separation. In most regions of the membrane, the separation did not affect the coupling phase suggesting that the characteristics of the membrane's area play a key role. However, one region was located where initially an anti – phase coupling occurs and then by decreasing or increasing the separation in – phase coupling takes place (Figure 3.9). In Figure 3.9a shows two pump stripes with the initial separation and their corresponding anti – phase far – field pattern in Figure 3.9b. The MQWL spectrum contains two laser frequencies, $1012.1\ nm$ and $1016.8\ nm$ (Figure 3.9c), both single mode, and have a FSR of $4.7\ nm$.

A slight decrease in the gap between the pump stripes (Figure 3.9d) results in the far – field pattern to change and indicating in – phase laser cavity coupling (Figure 3.9e). The MQWL spectrum does not change (Figure 3.9f). By slightly increasing the separation from Figure 3.9a (Figure 3.9g), in – phase coupling occurs (Figure 3.9h) but now the laser spectrum consists of one

laser frequency, $1012.1\ nm$ (Figure 3.9i). The reason for this potentially is that in this area the pump light covers, only one QW transition is occurring.

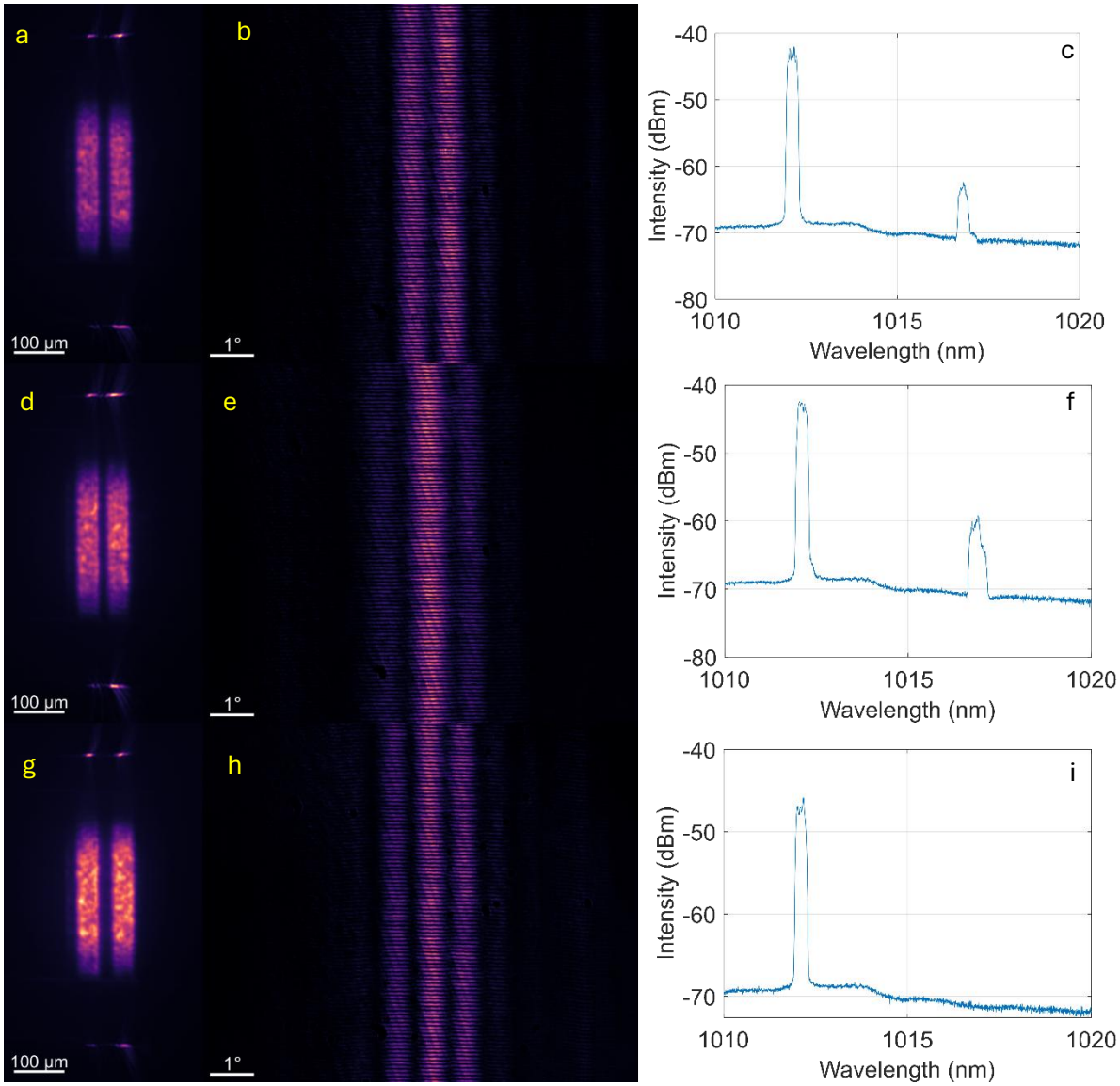

Figure 3.9 Switching from anti – phase coupling to in – phase. In this figure, the following are presented: (a) Lasing in optically pumped MQWL with two laser stripes, (b) the corresponding far – field pattern indicating an anti – phase laser cavity coupling, and (c) the MQWL output spectrum as read from the OSA. (d) Lasing with slightly smaller separation between stripes compared to (a), (e) the corresponding interference pattern now suggesting an in – phase laser cavity coupling, and (f) the same laser spectrum as in (c). Finally, (g) lasing with slightly greater separation between stripes compared to (a), (h) the corresponding interference pattern also demonstrating an in – phase laser cavity coupling, but the MQWL spectrum now consists of one single mode laser frequency possibly only one QW transition takes place, with the peak wavelength being $1012.1\ nm$. The pump power before the DMD is constant at $4.4\ W$.

Additional laser cavity separation experiments were taken to demonstrate power transfer from one cavity to another. The MQWL is pumped by two stripes, one remaining in the same position on the membrane's surface and the other gradually comes closer to the former. Figure 3.10a shows the change in pump stripe separation after performing line scans. Figure 3.10b depicts the line scans of one membrane end facet clearly showing when both cavities lase. Initially, the right pump stripe is not strong enough as it is at the edge of the zeroth order or is too far from the left pump stripe. As the right stripe comes into frame, it strengthens as the pump beam interacts with the DMD and eventually causes the area it pumps to lase. Around measurement 18 power is lost in the left cavity indicated by the intensity drop at the end facet line scan and the right end facet line scan increases in intensity. This suggests that optical power from the left laser cavity transfers to the right laser cavity. Figure 3.10c shows the evolution of horizontal line scan of the far – field patterns, where the phase coupling is mainly anti – phase. When the power transfer occurs, the k – space image exhibits an in – phase resonator coupling. The top sections of Figure 3.10 denoted by the red dashed region are the unsaturated images of the real and reciprocal space.

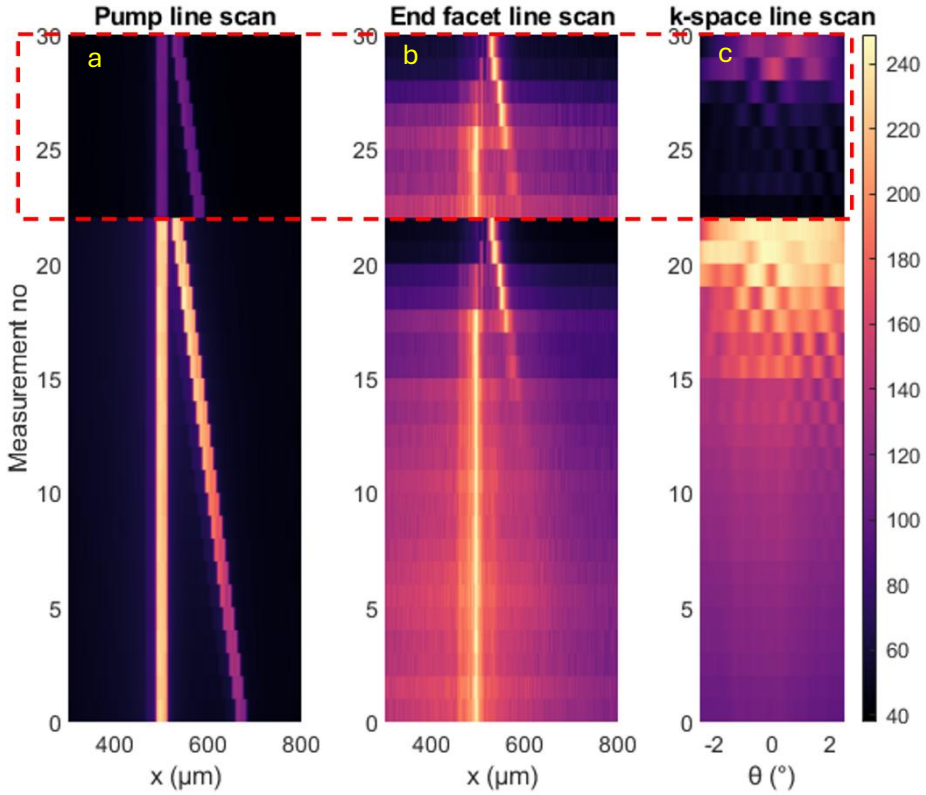

Figure 3.10 Power transfer from one laser cavity to another. As the right pump stripe approaches the left pump stripe (a), the area defined by the former also lases (b). Eventually, optical power is transferred from the left laser oscillator to the right one indicated by the intensity drop at the end facet line scan (b). The k – space line scans (c) show the evolution of phase coupling between oscillators, with coupling mainly being π – phase. In – phase occurs when the power transfer takes place. The section enclosed by the red dashed box involves the last measurements but unsaturated images.

3.3.3 Light Bridges

Another interesting feature made possible with the DMD setup is the demonstration of laser array bridging. In Figure 3.11a, an instance of three pump stripes of equal width and length simultaneously pumping the membrane is shown; however, no lasing occurs. If the middle stripe slightly shifts towards the left one as shown in Figure 3.11b, laser emitters are visible from the cavity defined by the left laser stripe as the middle stripe seeds light into it or diffuses electrons. Similarly, by slightly translating the middle stripe towards the right stripe as presented in Figure 3.11c, both laser stripes define a laser cavity coupling into each other.

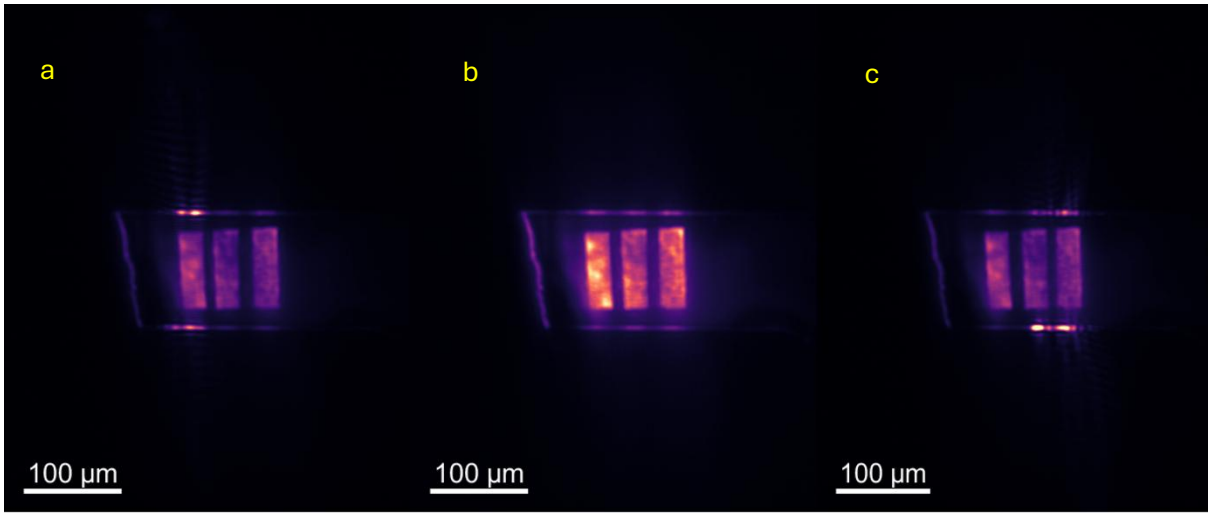

Figure 3.11 Three pump stripe configuration. In this sequence of real space images of the membrane's top view, the pump spot was modified in such a way to resemble three laser stripes with the same dimensions. In picture (a) the parallelograms are equally spaced from each other, and only spontaneous emission is observed as indicated from the material's end facets. In picture (b), the central laser stripe is translated slightly towards the left one, seeding it and therefore, allowing it to lase as indicated by the sharp intensity increase at the end facets. In picture (c), the central shape is shifted slightly towards the right one, seeding each other, which results in creating a laser array.

Additionally, these light bridges can control the laser mutual coherence. Two laser stripes pump the membrane, and a light rectangle is introduced in between them. Each laser stripe's power density is distributed over a greater area to induce lasing, and the two laser stripes are too far apart to seed each other to make a laser array. The small laser stripe introduced in between and equally spaced from the greater ones assists in creating laser cavities as shown in Figure 3.12a and their corresponding far – field pattern is of arbitrary phase shift (Figure 3.12b). By shifting the middle stripe upwards (Figure 3.12c), lasing remains in the areas defined by the greater laser stripes; however, the mutual phase relationship now indicates an anti – phase coupling (Figure 3.12d). As the middle stripe moves further upwards, laser emitters appear in the region where the middle stripe pumps the membrane as depicted in Figure 3.12e and the corresponding reciprocal space image still shows an anti – phase coupling (Figure 3.12f). The creation of a laser cavity in the middle is attributed to the fact that more power density is concentrated among all laser stripes.

Now the middle stripe is replaced with another stripe whose width is smaller and length greater with its sides connecting the greater laser stripes, effectively resembling a literal bridge connecting the right with the left stripe (Figure 3.13a). Like before, the middle stripe moves upwards to check how it affects the laser array and the phase relationship. The middle stripe seeds the adjacent laser cavities enabling them to lase. The corresponding interference pattern

shown in Figure 3.13b suggests an arbitrary phase relationship developing between the cavities. As the light bridge moves towards the centre of the MQWL surface (Figure 3.14a), lasing continues without a cavity forming between the areas defined by the greater laser stripes and laser cavity coupling is in antiphase as shown in Figure 3.14b, which is supported by a MATLAB simulation of the far – field pattern (Figure 3.14c). However, as the pump pattern becomes more complicated a better understanding is required of the physics behind the simulations of the far – field interference patterns.

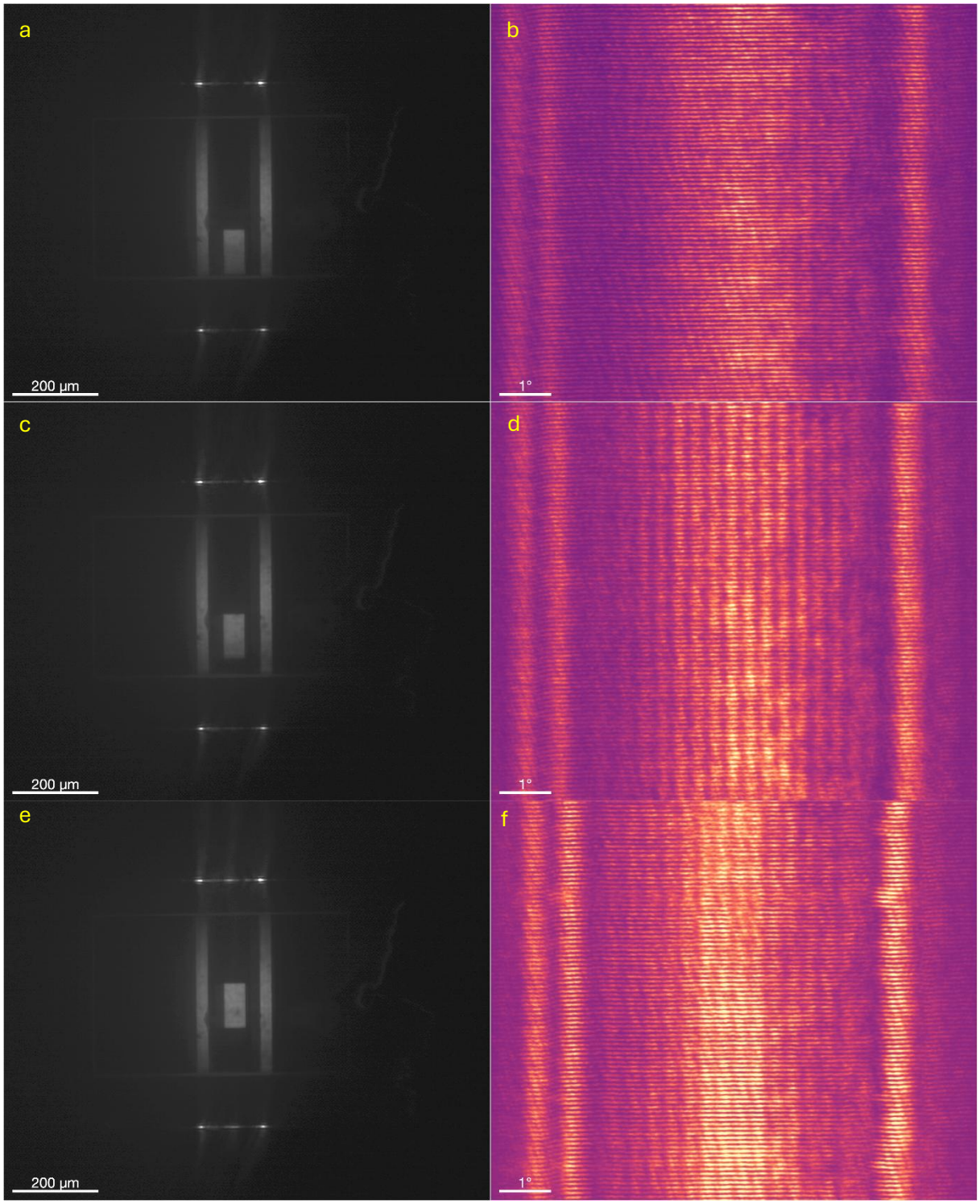

Figure 3.12 The light bridge. The left column of images depicts the membrane's top view along with the pump laser stripes. The right column shows reciprocal space images of the corresponding far – field interference patterns. In the real space images, (a), (c) and (e), the middle laser stripe progressively moves upwards while maintaining equal distance from the greater laser stripes. Initially, the phase relationship is arbitrary (b) but then develops into an anti – phase laser cavity coupling indicated in (d) and (f). In addition, the pump laser's power is mainly concentrated in the middle of the MQWL indicated by the appearance of laser emitters once the middle stripe has reached the centre of the membrane (e).

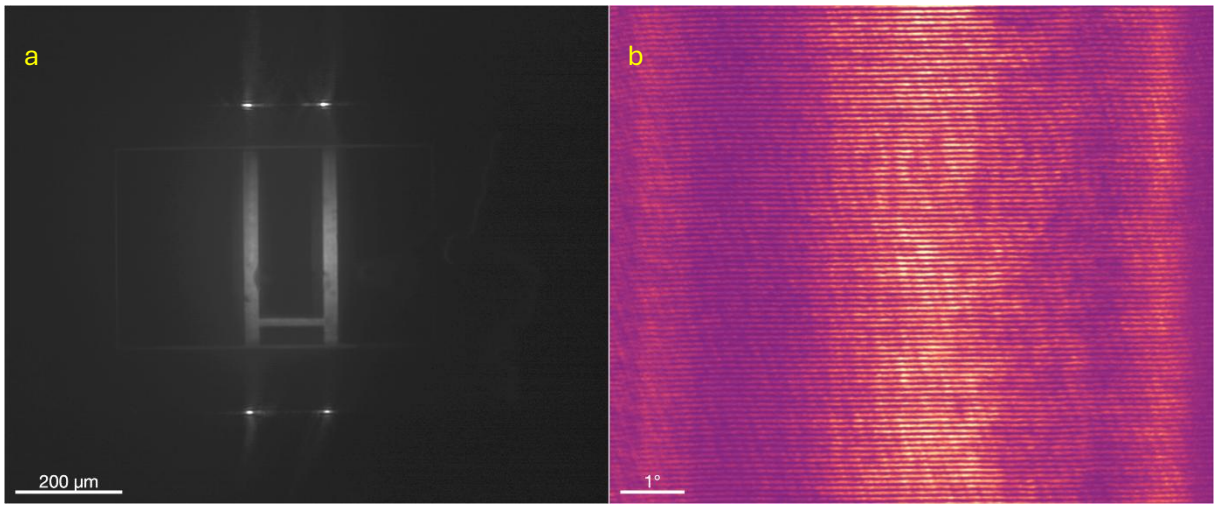

Figure 3.13 Light bridge with arbitrary phase cavity coupling. (a) The same configuration as shown in Figure 3.12 with the difference that the middle stripe has a smaller width and a greater length with its sides connecting the left and right laser stripes. The middle stripe still seeds the adjacent laser cavities enabling them to lase. The corresponding interference pattern shown in (b) suggests an arbitrary phase relationship between the cavities.

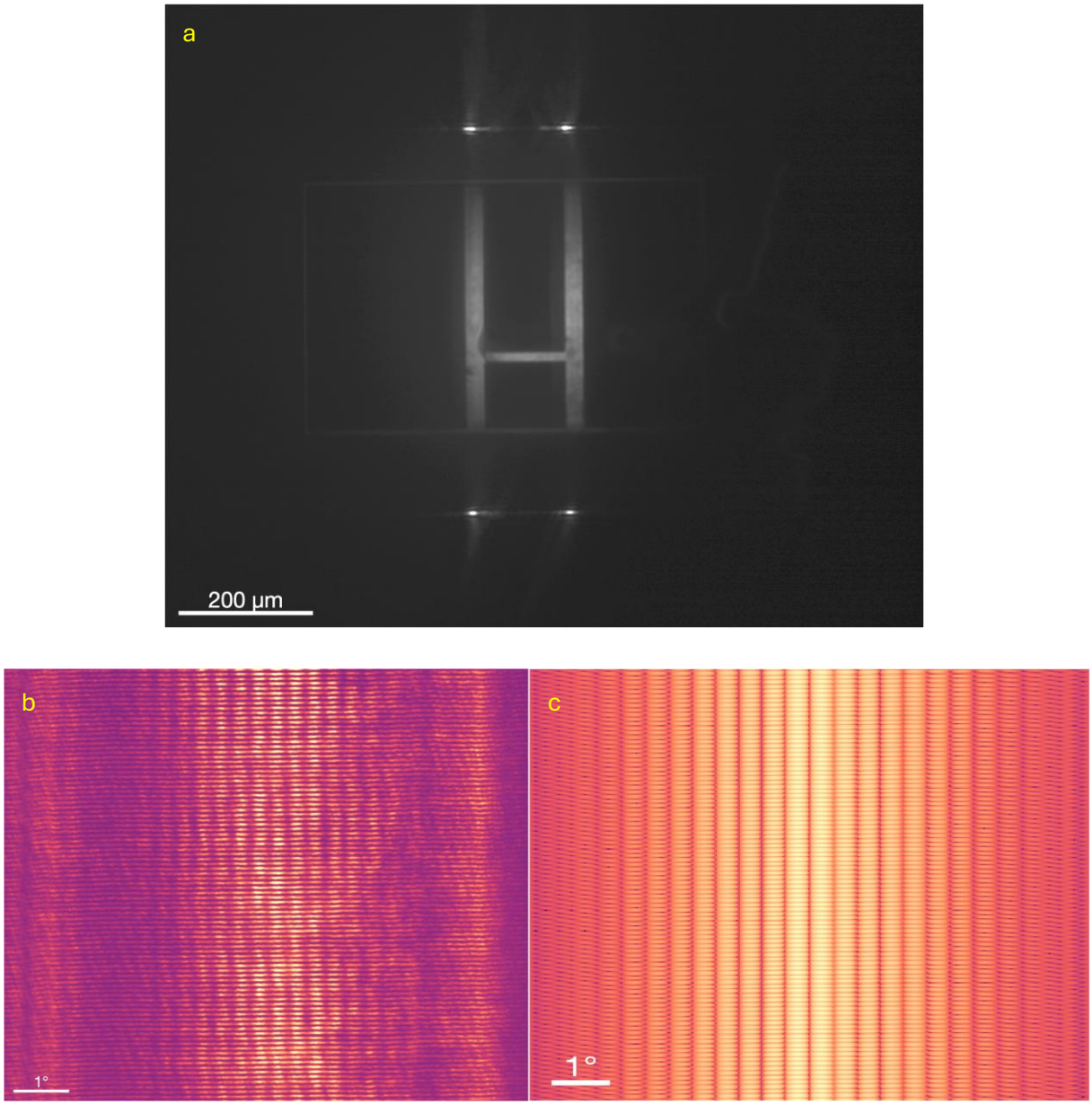

Figure 3.14 Light bridge with anti – phase cavity coupling. (a) Top view picture of the MQWL surface, the spontaneous emission from the pump pattern and the laser emitters appearing at the structure's end facets. Here, the light bridge is closer to the centre of the membrane's surface compared to the position presented in Figure 3.13a. (b) The corresponding far – field pattern suggests that the laser array operates in an antiphase configuration as supported by the simulation presented in (c).

3.3.4 Laser Array Coherence

In addition, experiments to verify whether the laser cavities operate at the same frequencies were conducted. This was shown in Chapter 2 but only by simulation. Of course, to have constructive interference among cavities, they must operate on the same wavelength. The method followed involves pumping the MQWL with two laser stripes to form two cavities as presented in Figure 3.15a. Its corresponding Fourier plane image indicates a π – phase cavity coupling (Figure 3.15b) and laser spectrum corresponds to two laser peaks, one at $1012.14\ nm$ and the other at $1016.84\ nm$ (Figure 3.15c). Their FSR is $4.7\ nm$. If the left stripe is blocked (Figure 3.15d), one laser cavity exists, and a singular interference pattern is observed in Figure 3.15e. However, the laser frequency output remains the same (Figure 3.15f). If I block the right block (Figure 3.15g and 3.15h), the same NIR frequencies are observed (Figure 3.15i). The longitudinal modes existing within the cavities for each laser harmonic frequency are within the range of 1.2 to 1.4, suggesting that only one longitudinal mode exists.

However, the $1012.14\ nm$ laser peak includes a spectral shoulder on its left (Figure 3.15c), whereas the shoulder vanishes in Figures 3.15f and 3.15i indicating a spectral blue shifting. To begin with, the shoulder appearing in Figure 3.15c possibly exists due to laser longitudinal mode competition, as two laser modes compete optical gain or population inversion available in the gain material [107]. As the oscillation of one longitudinal mode experiences the strongest amplification, it suppresses the other one and eventually eradicates it as shown in Figures 3.15f and 3.15i. Apparently, as soon as one of the stripes is cut – off, the weakest mode ceases to compete for population inversion, and all optical gain is dedicated to the other laser longitudinal mode.

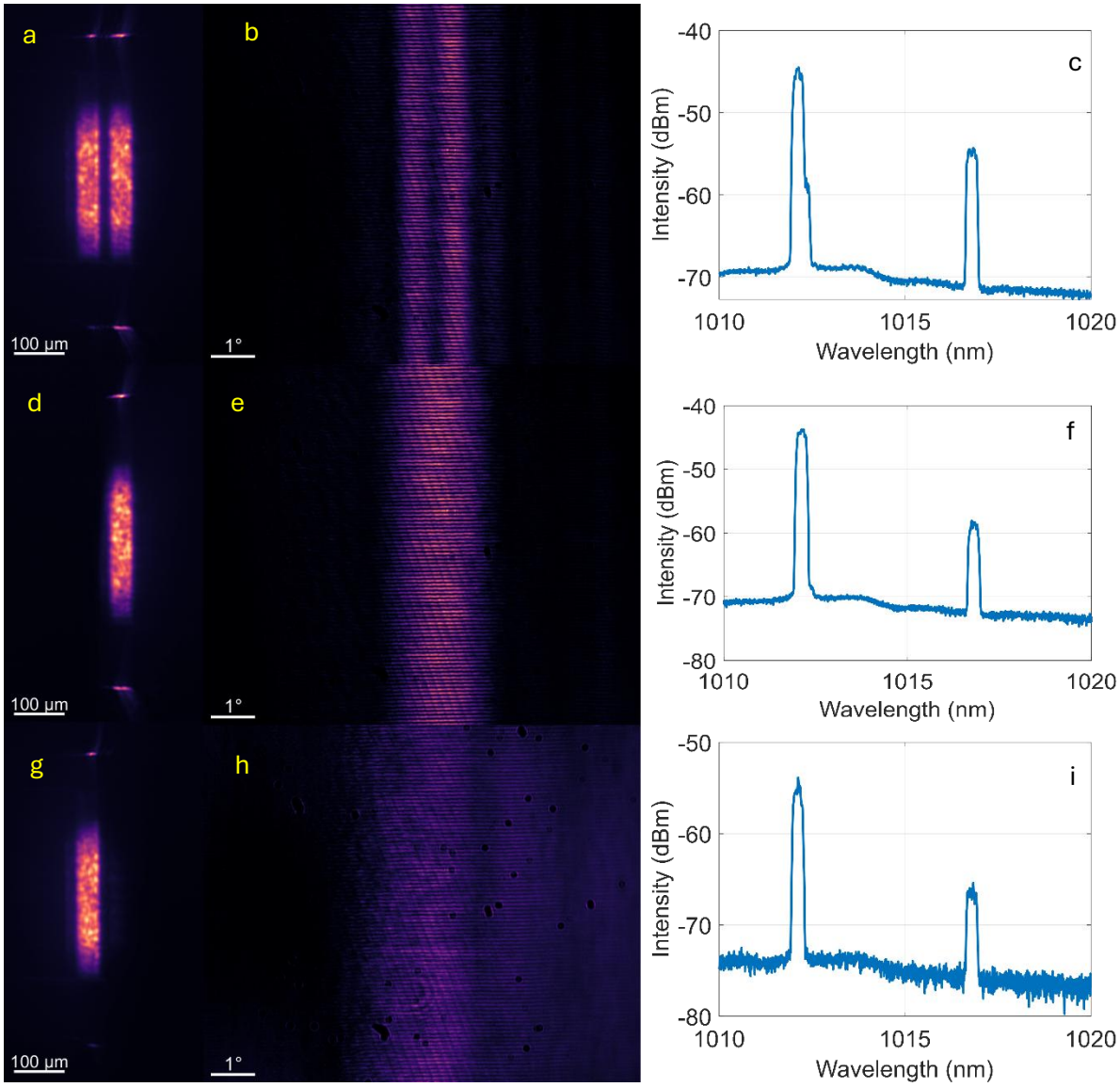

Figure 3.15 Verification of same – laser frequency operation between two cavities. In this figure I present the following: (a) Lasing in optically pumped MQWL with two laser stripes, (b) the corresponding Fourier plane of the two stripe pump indicating an anti – phase laser cavity coupling, and (c) the MQWL output spectrum as read from the OSA. (d) Lasing with the left stripe being cut off with a knife edge, (e) the corresponding interference pattern, and (f) the same laser spectrum as in (c). Finally, (g) lasing with the right stripe concealed, (h) the corresponding interference pattern, and (i) the laser spectrum. The pump power before the DMD is constant and $4.4\ W$. The laser spectrum remains the same despite cutting off a laser stripe.

3.4 Membrane Quantum Well Laser Array Simulations

In this sub – chapter attempts were made to create a COMSOL model to simulate laser arrays. The idea is to build a top view geometry as the membrane appears in the real space images, assign the same material properties in the entire geometry with the exception to define areas with optical gain. The refractive index of a material can be a complex variable with its real part being the actual refractive index and the imaginary part being the extinction coefficient. The extinction coefficient is associated with the material's absorption, however, in the presence of population inversion, the material enhances light propagating through it rather than attenuating it. Optical gain is introduced in COMSOL by introducing a negative extinction coefficient term.

First attempts involved creating a waveguide (Figure 3.16a), despite the fact that the membrane has the same refractive index everywhere. The core's refractive index is the effective refractive index obtained from the guided mode models presented in Chapter 2, which is 3.4923 for a silicon carbide substrate or 3.4921 for a silica substrate, which are practically they are the same. The refractive index of the cladding is slightly smaller to create a waveguiding effect. Surrounding the structure are perfectly matched layers (PMLs) to reduce any additional reflections as well as including scattering boundary conditions (SBCs) assigned to the boundaries for this purpose. The core thickness is $10\ \mu m$, the cladding thickness is $10\ \mu m$ and the PML thickness is $5\ \mu m$. The whole structure is $50\ \mu m$ long. The waveguide is excited with a $1\ \mu m$ wavelength and $1\ W/m$ wave through port into the core as shown in Figure 3.16a.

By a running the model, light propagates within the core (Figure 3.16a). This part was to check that waveguide functions properly. In Figure 3.16a, the waveguide is also split in half. The reason for this is because now optical gain is introduced to the second half core of the waveguide, which is $200\ cm^{-1}$. By running the model, waveguiding along the structure is observed, but also signal increase in the second half (Figure 3.16b).

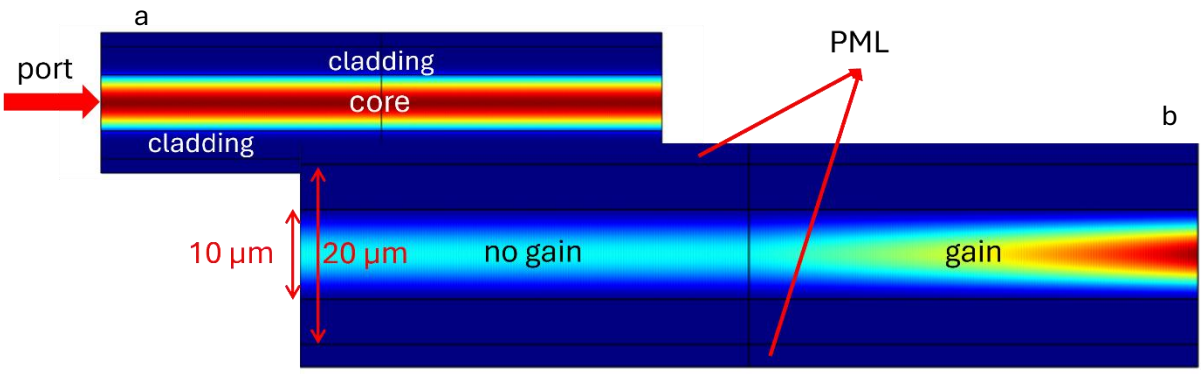

Figure 3.16 Waveguide simulation. The waveguide consists of the core, cladding and PMLs. The core has a refractive index of 3.492 and the cladding has a slightly smaller refractive index. The core thickness is $10\ \mu m$, the cladding thickness is $10\ \mu m$ and the PML's thickness is $5\ \mu m$. The whole structure is $50\ \mu m$ long. Waveguide excitation is achieved from port at the core and cladding with a $1\ W/m$ wave. The use of PML and SBC assigned to the boundaries reduces additional undesired reflections. (a) Waveguiding effect within core of waveguide structure. (b) Waveguiding effect within core of waveguide structure but with light intensity enhancement due to optical gain, $200\ cm^{-1}$, assigned to the right segment of the waveguide.

By increasing optical gain from $200\ cm^{-1}$ to $2000\ cm^{-1}$with a $200\ cm^{-1}$ step, it should be noted that although the waveguiding effect remains but with much higher intensity, light gain starts to behave differently after $800\ cm^{-1}$. In the first segment waveguiding takes place, however, in the second segment of the structure light intensity drops and then increases (Figure 3.17a and 3.17b).

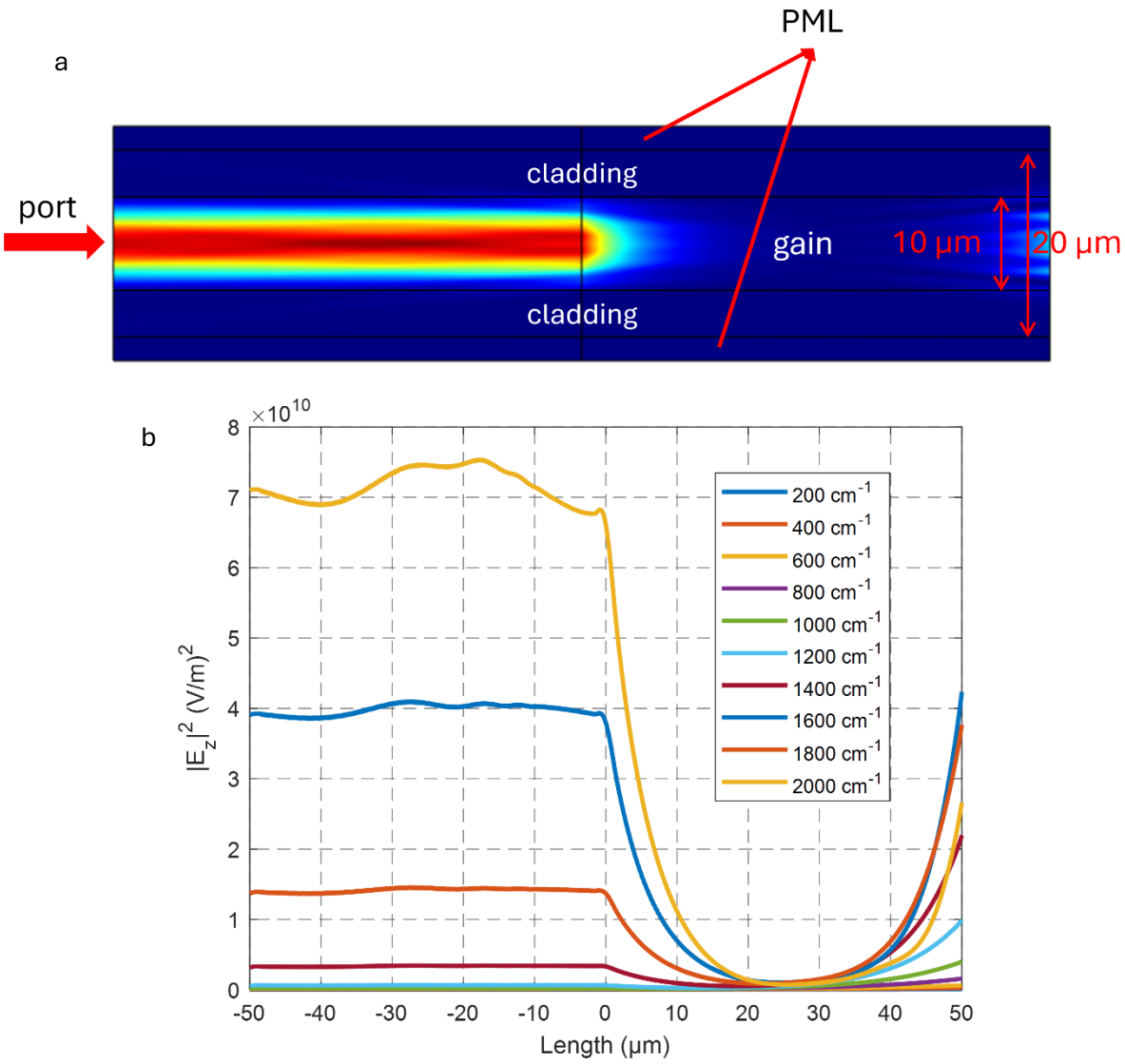

Figure 3.17 Waveguide simulation with gain in one area of the core. (a) Waveguiding along structure but with 2000 cm^{-1} assigned to the right – hand side. Once light enters the gain area it drops and increases. (b) Line scans along the core to show the light's behaviour inside the core in the areas with and without gain. At 0 μm light enters the gain region.

The reason for the unexpected behaviour of light lies within the mesh size. To begin with, the presence of higher intensity on the left – hand side probably is a result of a reflection effect due to high gain on the right – hand side. It was apparent that as optical gain increased, the mesh size needed to decrease to adjust the numerical calculations. After a mesh size investigation for constant gain, 2000 cm^{-1}, it was concluded that a mesh size of $\lambda/24$ was appropriate to obtain waveguiding with an exponential increase in light intensity (Figure 3.18a and 3.18b). For gain values from 200 cm^{-1} to 2000 cm^{-1}, all simulations demonstrate waveguiding and exponential growth (Figure 3.19). For higher gain a finer mesh would be required.

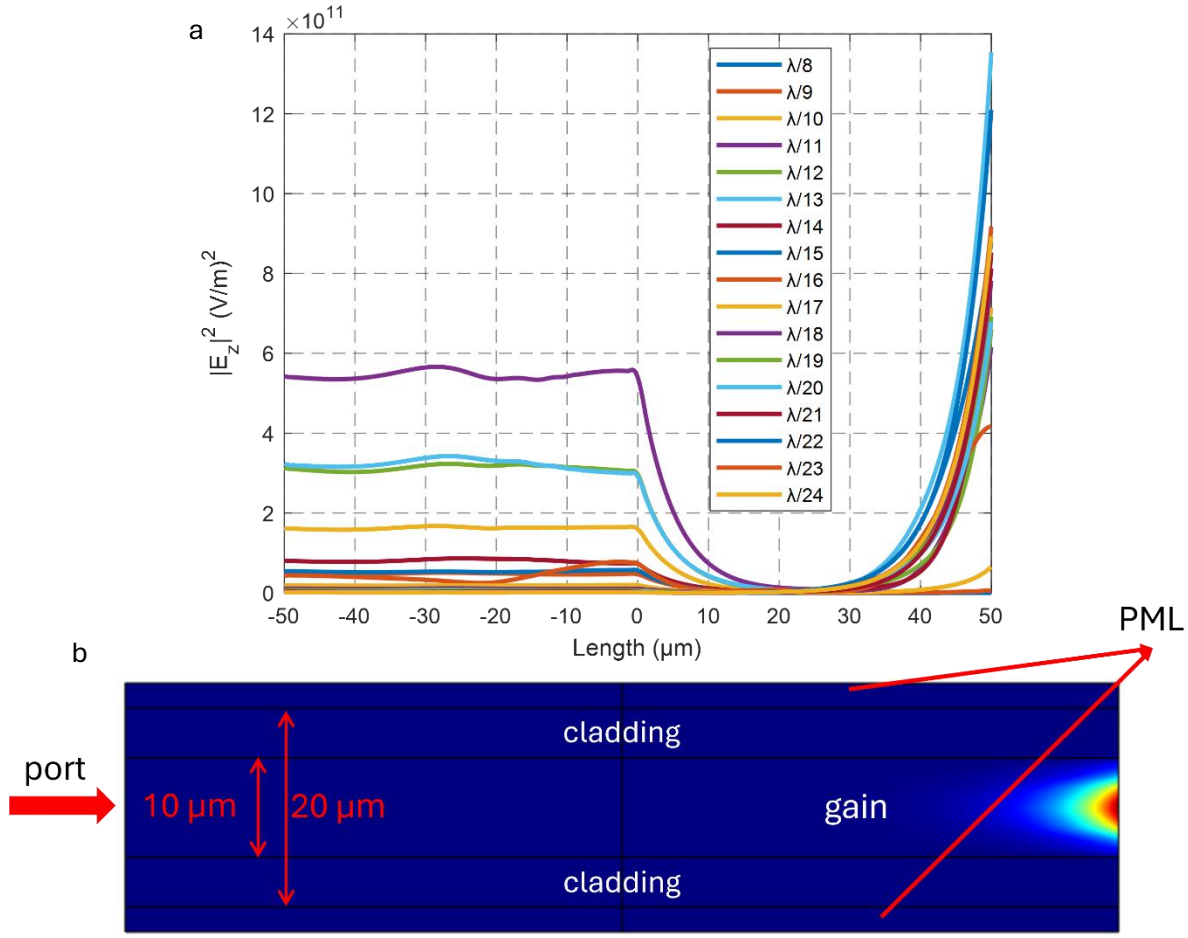

Figure 3.18 The issue with optical gain and the mesh size. (a) Line scans along the waveguide's core for a constant optical gain, 2000 cm^{-1}, and different mesh sizes. As the mesh size decreases, the light's intensity dip vanishes and its expected exponential growth in the second half of the structure. (b) Waveguiding within the core and along the structure. On the second half of the rectangle, light experiences gain and proceeds to increase exponentially.

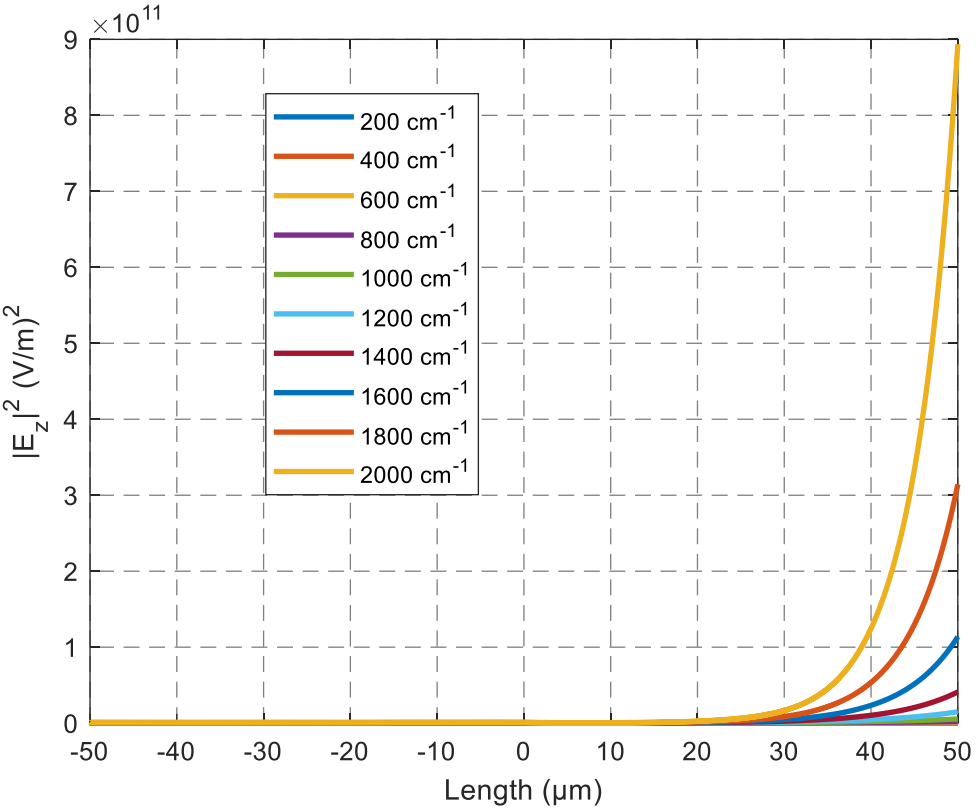

Figure 3.19 Line scans along the waveguide's core to exhibit light intensity behaviour for different gain values assigned to the second half of the waveguide and constant mesh size, $\lambda/24$. On the left – hand side of the waveguide, $-50\ \mu m$ to $0\ \mu m$, light propagates unaffected within the core. Once light enters the left – hand side segment of the waveguide, $0\ \mu m$ to $50\ \mu m$, it experiences optical gain subjecting it to an exponential growth.

From here the same structure presented in Figure 3.16a was kept but the same refractive index was assigned to the whole geometry, 3.492, effectively removing the waveguide. The mesh size is $\lambda/12$ and the optical gain assigned previously is now $600\ cm^{-1}$, for faster executions of the model. The value of gain is arbitrary. From the simulation run, light remains in the region which was previously the waveguide's core and experiences optical gain on the right – hand side of the structure (Figure 3.20).

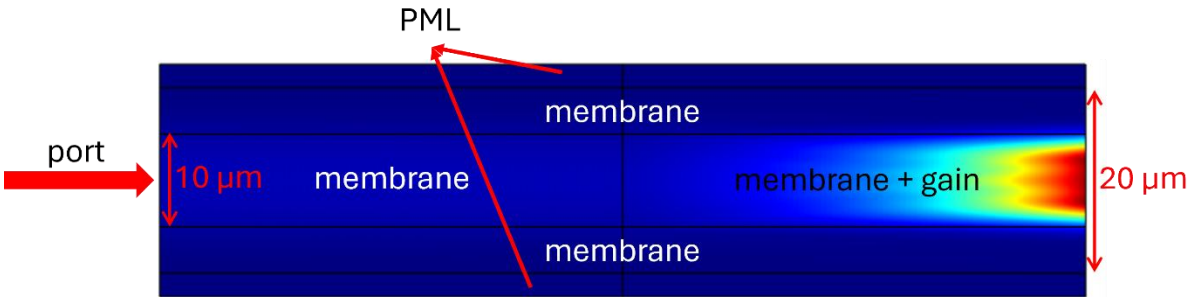

Figure 3.20 Single cavity MQWL simulation. The two – dimensional membrane quantum well laser model with the same refractive index, 3.492, assigned to the whole geometry. The mesh size is $\lambda/12$ and the optical gain is $600\ cm^{-1}$. An excitation wave is injected from the left and propagates in the membrane. Light amplifies exponentially once it encounters optical gain on the right – hand side segment.

The next step is to add optical to the left – hand side segment as shown in Figure 3.21, as stimulated emission takes place along the laser cavity rather than one region. Everything else remains the same as presented in Figure 3.20. The simulation's results (Figure 3.21b) differ a lot from the outcome in Figure 3.21 and the expected result. As a spatially uniform optical gain is applied along the geometry as shown in Figure 3.21, it is expected that the injected wave would exponentially increase in amplitude from the beginning and spread as it is not confined due to a refractive index contrast. In Figure 3.21, some light remains in the gain region experiencing gain, but the majority of light seems to exist outside the gain region from the start.

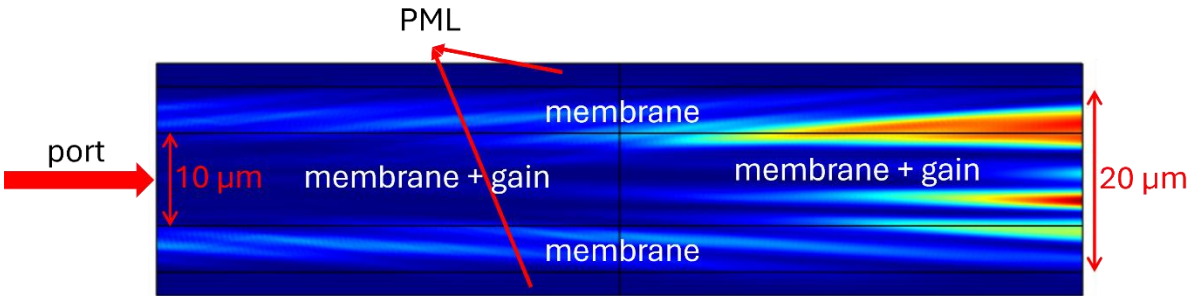

Figure 3.21 Single cavity MQWL with gain along the central geometry simulation. The two – dimensional membrane quantum well laser model with the same refractive index, 3.492, assigned to the whole geometry. The mesh size is $\lambda/12$ and the optical gain is $600\ cm^{-1}$. Uniform gain is assigned to specific regions as depicted on the image. An excitation wave is injected from the left and propagates in the membrane with some components of light amplifying within the gain region and others starting to intensify and propagate outside the gain region.

To further understand the behaviour of the MQWL model and have more control over it, a Gaussian pulse is introduced with a beam waist or standard deviation of 5 μm, which is defined from the "port" excitation boundary of the model. Optical gain still remains in the same regions as depicted in Figure 3.21. By running the simulation, a two - dimensional representation of the pulse's exponential amplification is obtained, which is shown in Figure 3.22a as well as line scans of the Gaussian pulse perpendicular to the structure's length at equally spaced locations along the MQWL (Figure 3.22b) clearly demonstrating the exponential amplification of the optical pulse.

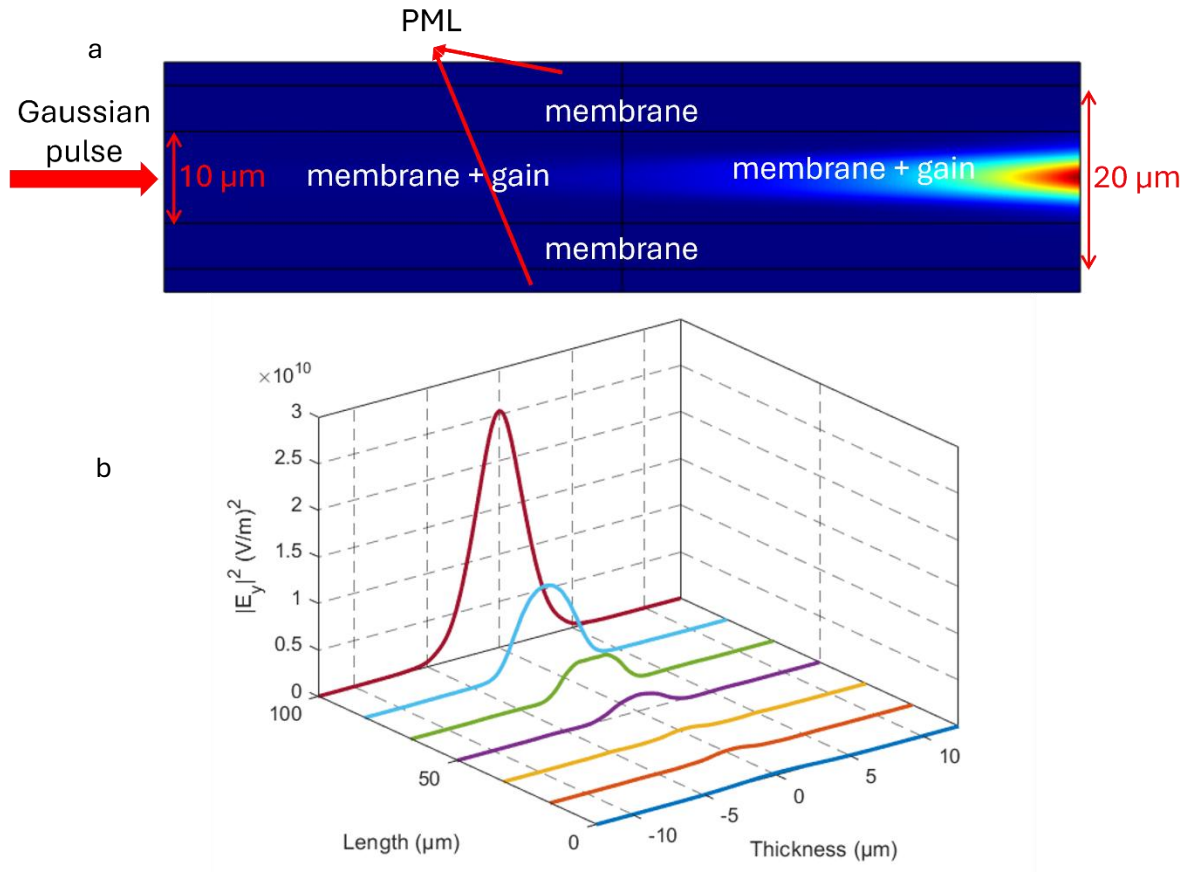

Figure 3.22 Single cavity MQWL probed with a Gaussian pulse simulation. (a) The two - dimensional membrane quantum well laser model with the same refractive index, 3.492, assigned to the whole geometry. The mesh size is $\lambda/12$ and the optical gain is $600\, cm^{-1}$. Uniform gain is assigned to specific regions as depicted in Figure 3.21a. A Gaussian light pulse is injected from the left and propagates in the membrane with the pulse exponentially amplifying. (b) Gaussian pulse line scans at equally spaced locations along the MQWL showcasing the exponential growth and gain – guiding.

Up to now, simulation of exponential amplification of an optical pulse inside a gain medium was shown, which resembles a MQWL device. The aim is to simulate a laser array. The structure presented in Figure 3.22a is expanded, essentially two regions of gain close to each other. The separation between the two gain regions is $2\ \mu m$. A Gaussian pulse is injected, the same as before, into one of the gain regions with the aim that its evanescent field will couple into the adjacent region. As this proved to be difficult, the gain increased from $600\ cm^{-1}$ to $1000\ cm^{-1}$ and decreased the mesh size to $\lambda/24$ making the model work in the intended way. By doing this, the optical pulse propagates in the initial gain region and exponentially intensifies and part of it couples into the adjacent gain area, in which it slightly amplifies (Figure 3.23).

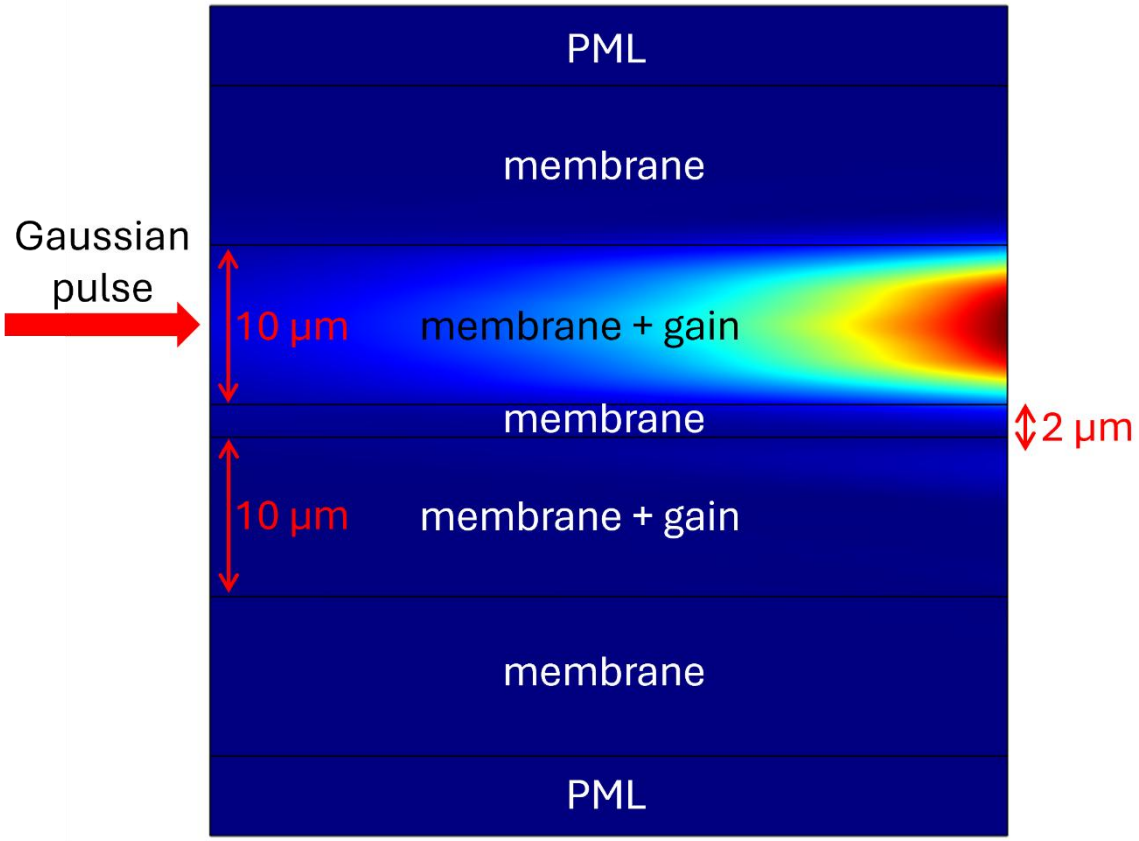

Figure 3.23 Simulation of the two - dimensional membrane quantum well laser model with two cavities and the same refractive index, 3.492, assigned to the whole geometry. The mesh size is $\lambda/24$ and the optical gain is $1000\ cm^{-1}$. Optical gain is assigned to the two regions adjacent to each other and separated by a small membrane gap of width $2\ \mu m$. A Gaussian optical pulse with a $5\ \mu m$ beam waist is injected into the top gain region, in which it propagates and exponentially amplifies. Part of the pulse couples into the adjacent gain area, where it slightly increases as it travels along the structure. This figure was produced by considering the norm of the electric field to see light in the second gain region.

3.5 Conclusions

The aims of this chapter were to explore the CW phase – locked membrane quantum well laser arrays in greater depth, compared to Chapter 2. The MQWL on an oxidised silicon substrate was optically pumped with an $808\ nm$ diode laser. A DMD was used to shape the pump laser profile based on the geometry assigned to it from the computer. The main choice of geometry was two parallel rectangles to pump the membrane at different and adjacent regions simultaneously effectively creating laser arrays.

Laser arrays were examined by capturing real and reciprocal space images, which allowed examination of the physical and reciprocal features of the membrane lasers. Real space images gave data regarding the physical dimensions of the membrane gain medium, the nature of the pump beam size and shape and number of laser emitters appearing at the end facets, which show how many laser oscillators exist simultaneously or lasers in an array. The reciprocal space CCD captures the far – field interference patterns, which are a result of superposition between the laser emitters at the membrane's end facets. From the k – space images it is deduced whether coupling between laser oscillators is in – phase or anti – phase or arbitrary. The majority of laser arrays in this Chapter's experiments are associated with anti – phase coupling. The phase relationship was shown to depend on the characteristics specific to the membrane's area due to growth quality [108] and the separation between laser oscillators. The introduction of a light bridge between two laser stripes seems to be lending optical power into the adjacent cavities making them lase possibly due to evanescent field coupling.

Accurate and direct measurements of optical power leading to coupling coefficient calculation could give a better insight of laser array cavity dynamics or investigating more QW chips the examine surface effects.

Various COMSOL models were created to simulated laser arrays by creating gain – guided geometries. The first versions included a waveguide, then a waveguide to which optical gain was introduced where the interplay between optical gain and the mesh size was explored. From there, the same refractive index was assigned to the whole geometry and keeping the optical gain in specific regions resembling a laser cavity. A Gaussian pulse was eventually introduced to excite the cavity to gain better control and understanding over the simulation. The Gaussian pulse was shown to exponentially grow as it propagated along the cavity. Hereafter, a second cavity was drawn next to the other one and excited one of them. The result was that the pulse propagated in the initial cavity amplifying, and part of it coupled into the adjacent cavity were it slightly amplified. Analytical simulations may improve by implementing more physical parameters such as phase and time, and in general gain more knowledge on laser arrays as they can be

complicated and become more complex by introducing the light bridges. Additional numerical simulations could be considered for developing laser cavity coupling [109], [110], [111], [112] based on coupling theory [113], [114], [115] besides phase relationship models or even use another software with built – in multiple QW model for predicting power efficiency [116].

Chapter 4

Tantalum Pentoxide Waveguides and Resonators

Besides experimentation with membrane quantum well lasers, the research group ventured in the field of nonlinear optics. Previously it demonstrated supercontinuum generation in linear tantalum pentoxide strip or ridge waveguides as shown in Figure 4.1 [43]. The next goal is to create Kerr frequency combs in tantalum pentoxide micro – ring or racetrack resonators. Kerr frequency combs in tantala micro – ring resonators were first reported in [56] (Figure 4.2) and were generated from rings with a strip waveguide cross – section. In this chapter, an attempt is made to create Kerr frequency combs in tantalum pentoxide micro – rings and racetrack resonators with rib waveguide cross – sections. Dr Oliver Trojak from the University of Southampton, and Dr Jonathan Silver from the National Physical Laboratory (NPL) conducted the resonator coupling experiments, with the former also doing the electron beam lithography. Initial COMSOL and MATLAB simulations were run by Dr Jake Daykin. The MATLAB numerical simulation generating SC spectra and Kerr frequency combs was developed by Dr Peter Horak from the University of Southampton.

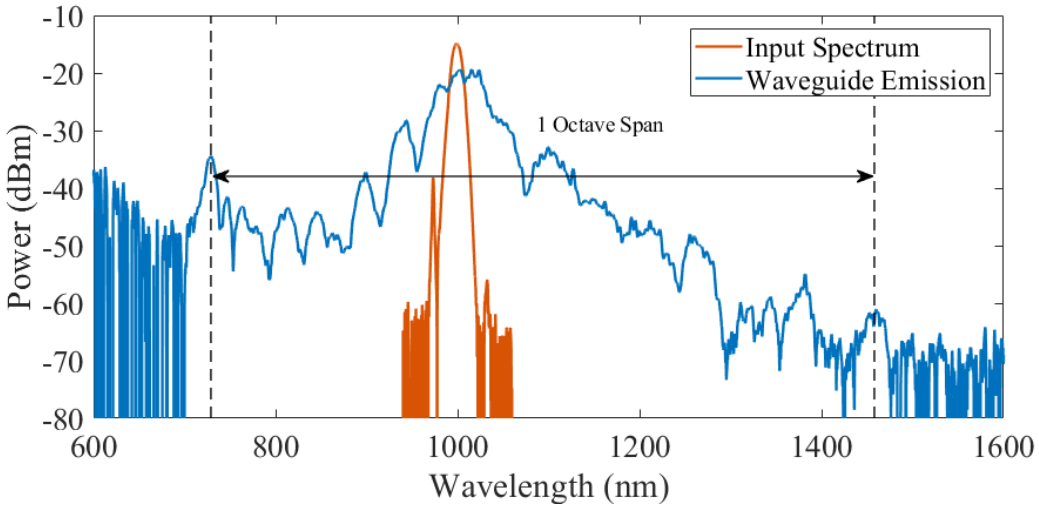

Figure 4.1 Octave spanning SC generation in tantalum pentoxide waveguides compared to the input light source spectrum [43]. The strip waveguide is straight whose tantalum pentoxide core is cladded by SiO_2, and its dimensions are $2.6\ \mu m \times 0.7\ \mu m$. Injection is achieved with $175\ mW$ laser emitting around $1\ \mu m$.

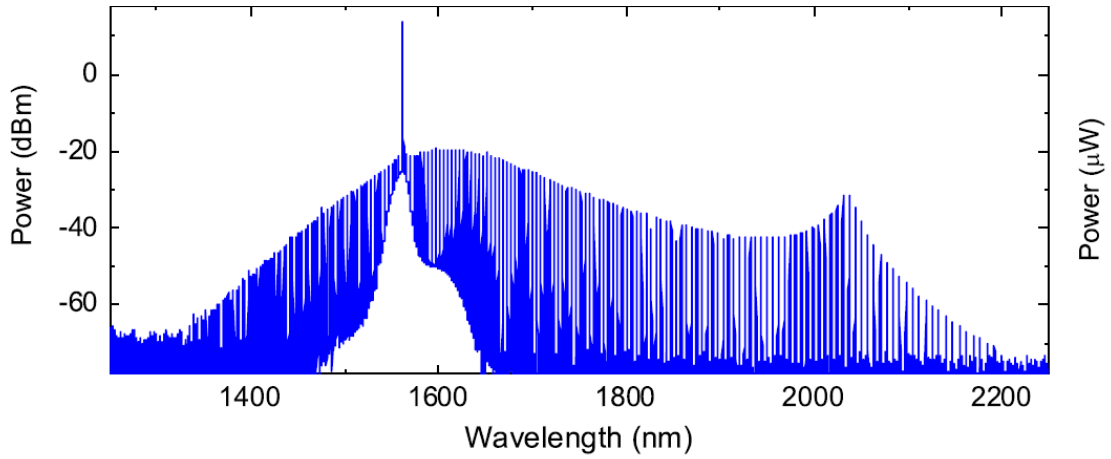

Figure 4.2 Kerr frequency comb generation in a tantala ridge ring resonator [56]. The micro – ring has a radius of $46\ \mu m$ and a thickness of $570\ nm$ whose tantalum pentoxide core is top cladded by air and bottom cladded by SiO_2. Optical probing was done with a $1.56\ \mu m$ wavelength laser.

4.1 Micro Resonator Simulations

COMSOL and MATLAB simulations were performed to determine suitable conditions to generate Kerr frequency combs in tantalum pentoxide micro resonators. The COMSOL simulation explores the guided modes existing in tantalum pentoxide rib waveguides top cladded by air and bottom cladded by silica, which is similar to the work presented in [56]. The refractive index of tantalum pentoxide used in the simulation is derived from [57]. The simulation produces effective refractive indices and effective areas for a wavelength sweep beginning from $1\ \mu m$ and ending at $2\ \mu m$ with a $0.01\ \mu m$ step. The effective refractive index and effective is fed into the MATLAB simulation.

The MATLAB simulation is based on the Lugiato – Lefever equation mentioned in Chapter 1. Besides the inputs from COMSOL, this simulation includes the values of waveguide losses, nonlinear indices of the core, laser power, power transmission, detuning term and assumes steady – state solutions $D_t A_c = 0$. To demonstrate the validity of the MATLAB script, it was used to generate Kerr frequency combs and compare to the spectra presented in [42] for silicon nitride (Si_3N_4) [117] and magnesium fluoride (MgF_2) [118] micro – ring resonators. In Figure 4.3 depicts a visual comparison of the simulations shown in [42] along with the MATLAB results, which match the Kerr frequency combs presented in [42].

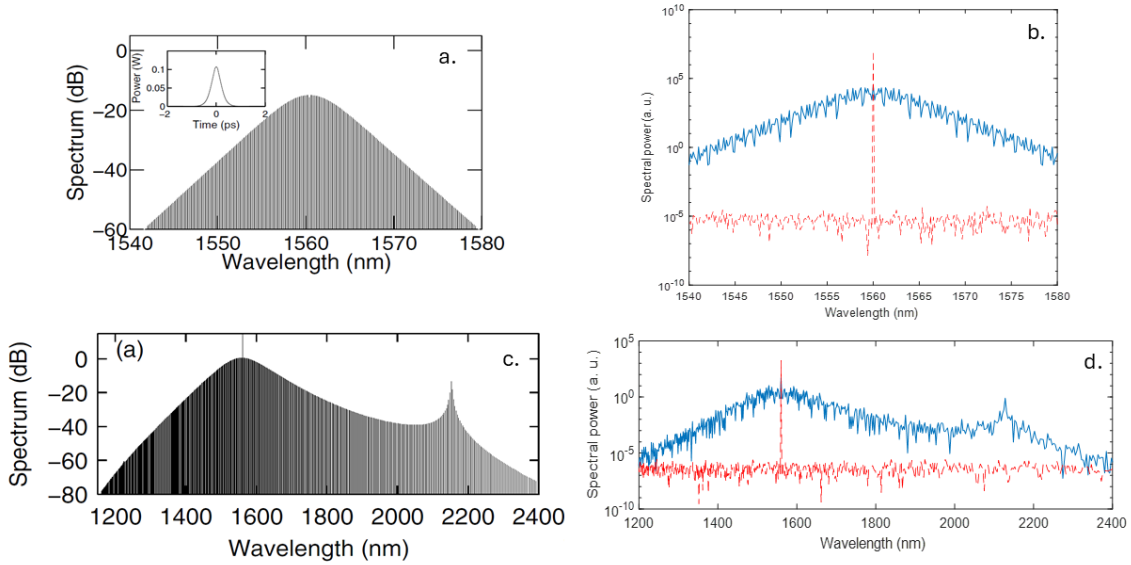

Figure 4.3 Simulated Kerr frequency combs as presented in [42] for (a) MgF_2 [118] and (c) Si_3N_4 [117], and their corresponding spectra (blue colour) as simulated with the MATLAB code, (b) and (d) for a $1.55\ \mu m$ pump wavelength (red colour). The general spectrum behaviour in (b) and (d) matches the behaviours of (a) and (c) respectively. The vertical axis in Figures (b) and (d) is presented on a logarithmic scale.

Knowing the MATLAB algorithm is able to replicate Kerr frequency combs from another research work, it can be readily used for the group's purposes. The code was initially conceived for previous work involving both tantalum pentoxide ridge and rib waveguides [84]. The MATLAB code along with the COMSOL model investigate the waveguide's dispersion curves based on the core's dimensions, thickness and width, and top cladding material, air or silica, and how those parameters affected the dispersion curves, which are crucial to determine the anomalous GVD region, if there is one, which in turn defines the region where spectral broadening mainly occurs due to soliton formation.

Initial MATLAB simulations focused on tantalum pentoxide micro – ring resonators assuming a $725\ nm$ thick and $1650\ nm$ wide waveguide cross – section with $100\ \mu m$ radius, as used in the COMSOL mode analysis. The nonlinear index at $1.56\ \mu m$ wavelength was included, which is $6.2 \times 10^{-19}\ m^2/W$ [56]. In addition, the pump power, detuning, and power transmission coefficient were assumed to be $30\ mW$, $\delta = 0$, and $\theta = 0.0011$. Finally, these simulations consider the dispersion parameter or GVD curve provided by COMSOL (Figure 4.4), which required the group refractive index, 2.18. The group refractive index is obtained after sweeping

the probe wavelength by searching for guided modes around the refractive index provided by tantalum pentoxide's Sellmeier equation [57].

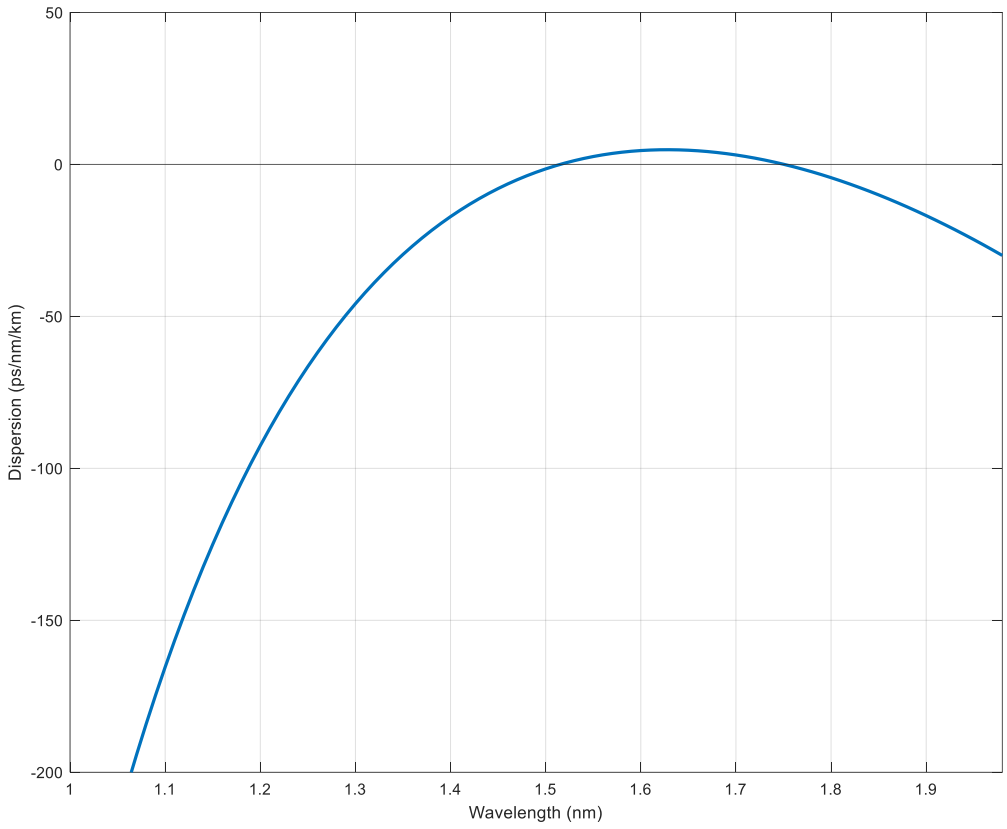

Figure 4.4 The dispersion parameter curve within $1 - 2\,\mu m$ wavelength domain for a $725\,nm$ high and $1650\,nm$ wide tantalum pentoxide waveguide cross - section with a $100\,\mu m$ radius. Wavelengths that appear in between the two zero – dispersion points fall in the anomalous GVD regime, where higher – order solitons are more probable to exist and hence, SC or Kerr frequency comb generation.

Based on the GVD curve shown in Figure 4.4, a parametric sweep was performed on the pump wavelength from $1.45\,\mu m$ to $1.80\,\mu m$ with a $0.05\,\mu m$ step. There are two zero – dispersion points around and wavelengths. Wavelengths lower or greater than or respectively fall in the normal GVD regime. Wavelengths that appear in between the two zero – dispersion points fall in the anomalous GVD regime.

Figures 4.5 and 4.6 show the numerical evolution of the Kerr frequency combs that exit the micro – ring resonator for the different aforementioned pump wavelengths. The red spectrum in each graph refers to light entering the micro – ring resonator, whereas the blue spectrum refers to light exiting the resonator after completing multiple roundtrips. For wavelengths within the

normal GVD regime, a few discrete optical frequencies are visible, but no sufficient spectral broadening is observed, as optical solitons are not supported. However, spectral broadening is observed in the anomalous GVD regime, for $1.55\,\mu m$, $1.60\,\mu m$, $1.65\,\mu m$, and $1.70\,\mu m$ pump wavelengths. The spectral expansion for $1.55\,\mu m$ roughly is $755\,nm$. However, spectral broadening in all other cases is similar probably because there is minimal variation of the GVD within the anomalous regime.

As mentioned in Chapter 1, the main attributes of spectral broadening in micro – ring resonators are SPM and FWM, however, the simulation only includes the former effect. In addition, although the algorithm includes only the second order of dispersion, dispersive waves are formed at longer wavelengths in all four cases of pump wavelength within the anomalous GVD regime.

Although the prospect of spectral broadening in tantalum pentoxide micro resonators whose cross – section dimensions are $725\,nm \times 1650\,nm$ is shown, a rib resonator with dimensions $800\,nm \times 1500\,nm$ and etch depth of $400\,nm$ was ultimately chosen for Kerr frequency comb production. In [84], it is shown that a micro – ring radius greater than $20\,\mu m$, results in the probe wavelength ranging from $1.35\,\mu m$ to $1.80\,\mu m$ is well within the anomalous GVD region. In addition, [84] demonstrates spectral broadening from a resonator with $180\,\mu m$ for various waveguide losses at $100\,dB/m$, $31.6\,dB/m$ and $10\,dB/m$ for $2000\,mW$, $200\,mW$ and $30\,mW$ (Figure 4.7) pump powers respectively at $1.55\,\mu m$. An attempt was made to demonstrate spectral broadening (Figure 4.8) with the same resonator structure but with $100\,\mu m$ radius, $6\,W$ pump power and $1\,\mu m$ probe wavelength albeit being in the normal GVD regime, and assuming the same nonlinear index as the one for $1.56\,\mu m$ and as well as extremely low waveguide losses, $1\,dB/m$. Previously it has been shown that spectral broadening can occur within the normal GVD regime in the absence of soliton compression and fission due to SPM [119], [120] and optical wave – breaking [120], [121], [122] offering narrower spectral broadening.

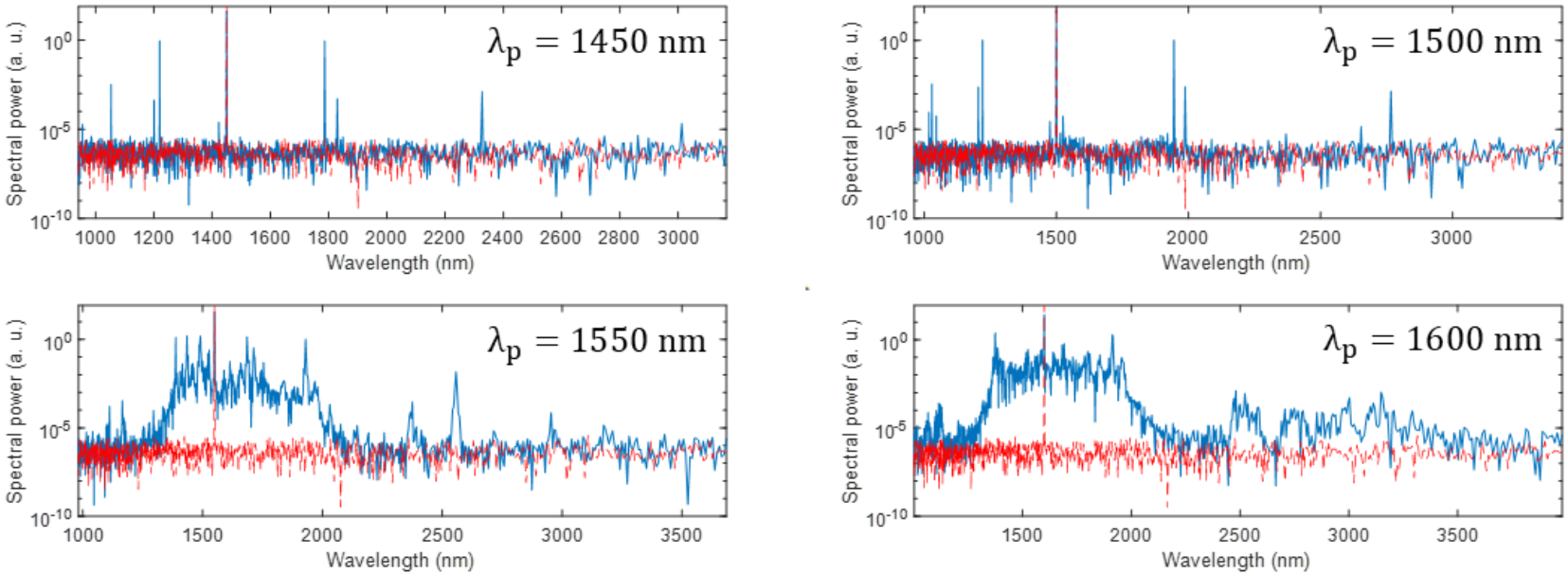

Figure 4.5 Evolution of spectral broadening during the transitioning from normal to anomalous GVD by varying the pump wavelength, λ_p, from $1.45\ \mu m$ to $1.60\ \mu m$ (Figure 4.4). Although some discrete optical frequency components are visible in the normal region, $1.45\ \mu m$, and at zero dispersion wavelength, $1.50\ \mu m$, spectral broadening is more prominent within the anomalous region ($1.55\ \mu m$, $1.60\ \mu m$). The red spectrum in each graph refers to light entering the micro – ring resonator, whereas the blue spectrum refers to light exiting the resonator after completing multiple roundtrips. The vertical axis is presented on a logarithmic scale.

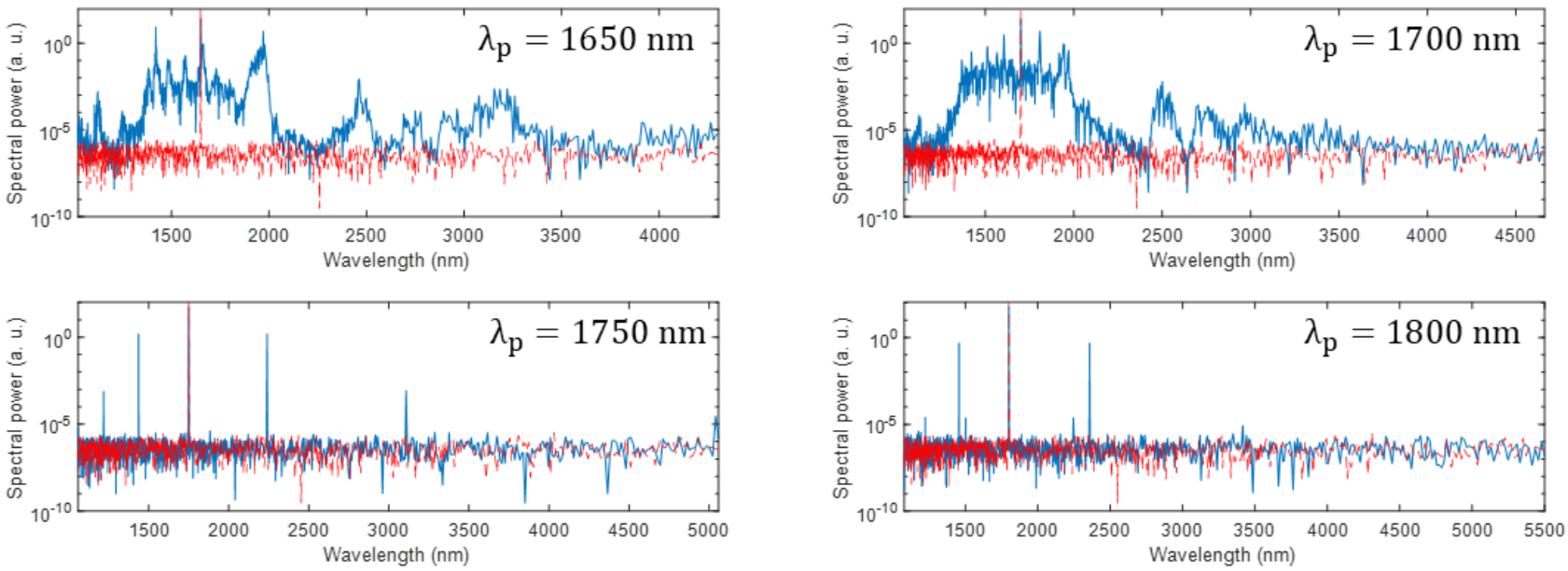

Figure 4.6 Evolution of spectral broadening during the transitioning from anomalous to normal GVD by varying the pump wavelength, λ_p, from $1.65\ \mu m$ to $1.80\ \mu m$ (Figure 4.4). Similarly like in Figure 4.5, although some discrete optical frequency components are visible in the normal region, $1.80\ \mu m$, and at zero dispersion wavelength, $1.75\ \mu m$, spectral broadening is more prominent within the anomalous region ($1.65\ \mu m$, $1.70\ \mu m$). The red spectrum in each graph refers to light entering the micro – ring resonator, whereas the blue spectrum refers to light exiting the resonator after completing multiple roundtrips. The vertical axis is presented on a logarithmic scale.

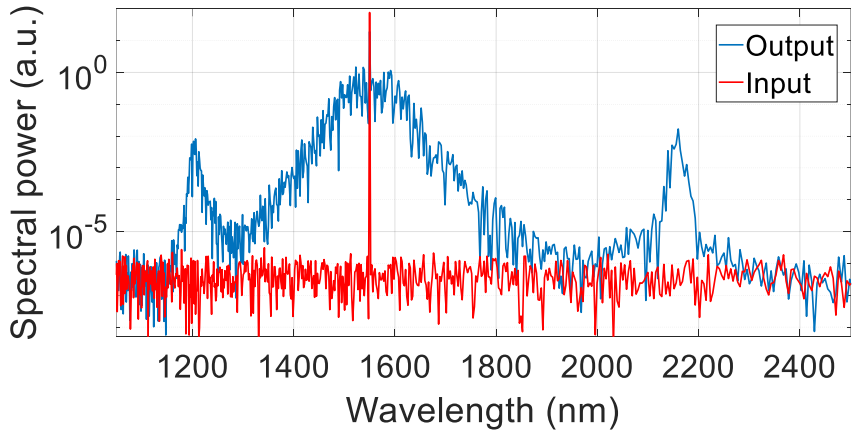

Figure 4.7 Simulated spectral broadening in Ta_2O_5 micro – ring resonator top cladded with SiO_2 with radius $180\ \mu m$, width $1500\ nm$, height $800\ nm$ and an etch depth of $400\ nm$, with $10\ dB/m$ propagation loss and pumped with $30\ mW$ at $1550\ nm$ [84]. The vertical axis is presented on a logarithmic scale.

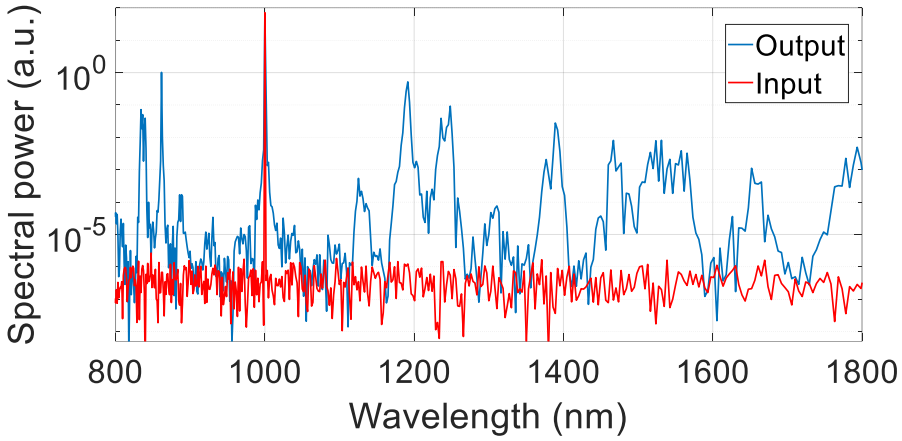

Figure 4.8 Simulated non – continuous spectral broadening in Ta_2O_5 micro – ring resonator top cladded with SiO_2 with radius $100\ \mu m$, width $1500\ nm$, height $800\ nm$ and an etch depth of $400\ nm$, with $1\ dB/m$ propagation loss and pumped with $6\ W$ at $1\ \mu m$. The vertical axis is presented on a logarithmic scale.

To simulate the output of the Ta_2O_5 micro – resonators, the MATLAB model is fed with simulated values for the effective index, which is then used to calculate the dispersion, and the effective area for the mode of interest inside the resonator. These values are extracted from the COMSOL simulations. Figure 4.9 presents the evolution of effective refractive index and effective area corresponding to the guided fundamental TE mode, TE_{00}, after performing a wavelength sweep from $1\ \mu m$ to $2\ \mu m$ with a $0.01\ \mu m$ step. The model considers the micro – ring resonator's cross section dimensions, $800\ nm \times 1500\ nm$, its bend radius, $100\ \mu m$, the etch depth, $400\ nm$, and $1\ \mu m$ thick SiO_2 top cladding. As the wavelength increases, the fundamental TE

mode becomes less confined to the waveguide's core, which is indicated by the simultaneous decreasing effective refractive index and increasing of effective area.

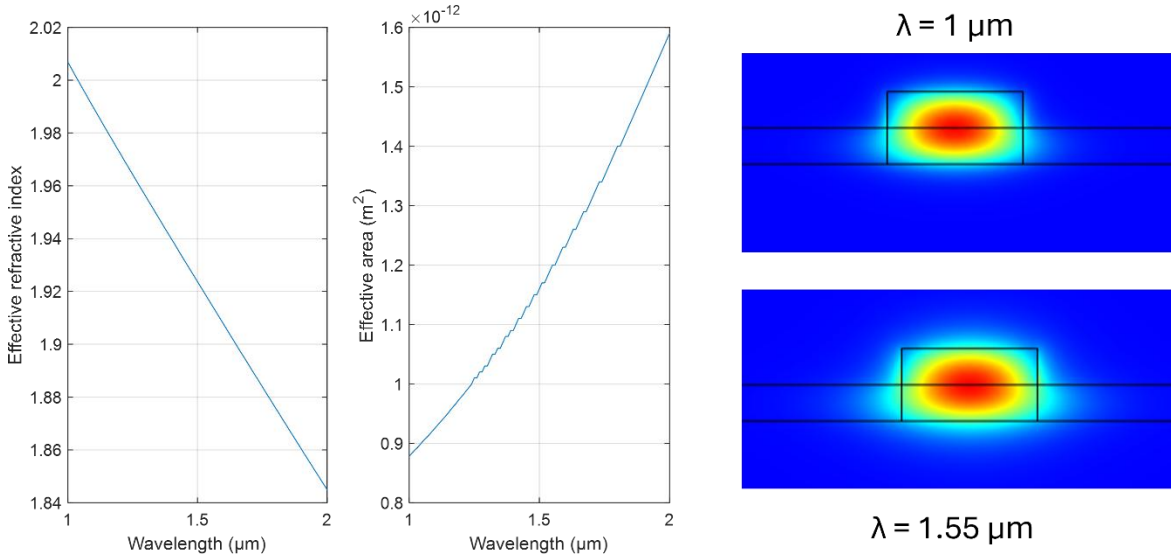

Figure 4.9 Effective refractive index and effective area change of the fundamental TE mode with respect to the probe wavelength in a Ta_2O_5 rib waveguide structure whose cross section dimensions are $800\ nm \times 1500\ nm$, etch depth is $400\ nm$, and bend radius is $100\ \mu m$. As the wavelength increases, the fundamental TE mode becomes less confined to the waveguide's core, which is indicated by decrease in effective refractive index and increase of effective area. The fundamental guided TE modes are also depicted for probe wavelengths $1\ \mu m$ and $1.55\ \mu m$.

4.2 Wafer Fabrication and Characterisation

In this section the fabrication process of tantalum pentoxide waveguides inside the cleanroom facility is presented (Figure 4.10). FiveNine Optics [123] provided the tantalum pentoxide wafers. The company coats 4 inch SiO_2/Si wafers with $800\ nm$ thick Ta_2O_5 by using ion beam sputtering (IBS), a technique where high – energy ions from the sputtering gas, typically argon (Ar) which is chemically inactive, bombard a tantalum pentoxide bulk target, which causes target atoms to escape and form a dense, thick and smooth film on top of the wafer, offering high uniformity [56].

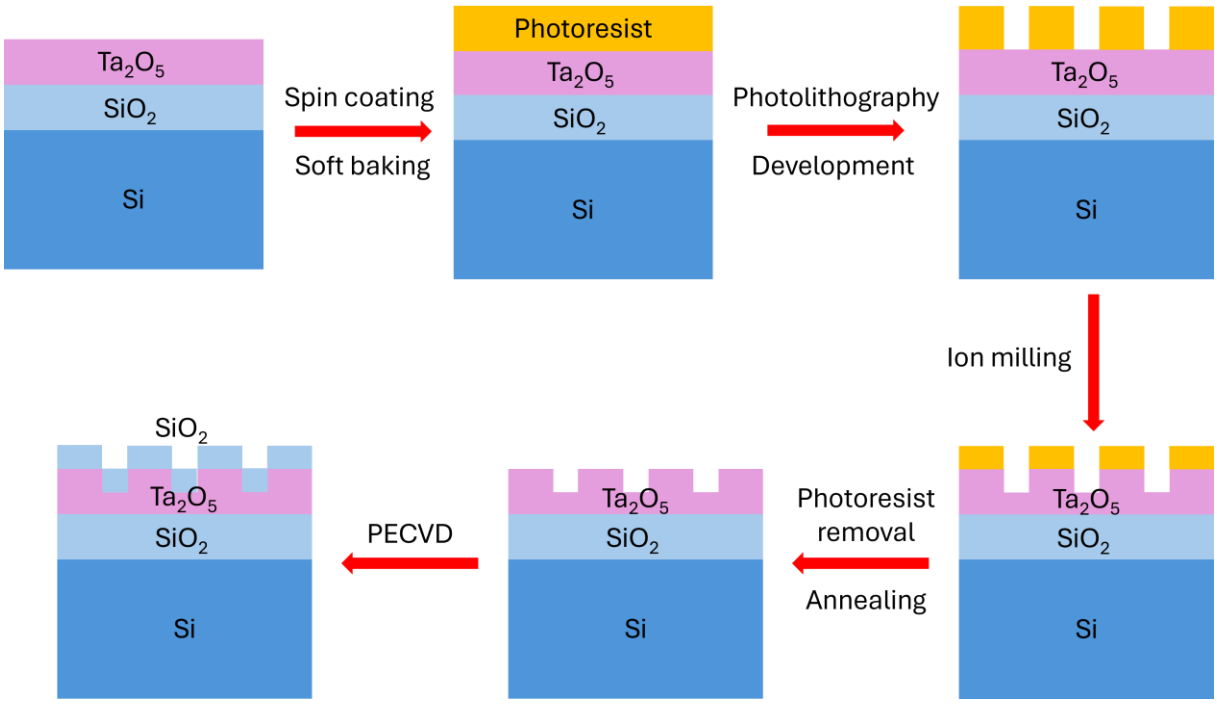

Figure 4.10 Tantalum pentoxide waveguide and resonator fabrication process inside the cleanroom. Tantalum pentoxide has been deposited via IBS on a SiO_2/Si wafer and then is subjected to positive photoresist deposition with the spin coater, and then soft baking on a hot plate. Afterwards, the wafer is placed in a mask aligner and its areas that are not covered by the designated photomask are exposed to UV radiation. The exposed photoresist is then removed during the development phase. To continue, the developed wafer undergoes ion beam etching, photoresist stripping revealing the rib waveguides and micro – resonators, and annealing. Finally, silica top cladding is deposited on the tantalum pentoxide wafer surface through plasma – enhanced chemical vapour deposition (PECVD).

Photolithography and then dry etching were used to create optical rib linear waveguides and micro – resonators. Initially, positive photoresist S1805 for finer structures was spin coated onto the tantala wafer. Spin coating gradually switched resolutions per minute (RPM; Figure 4.11). To begin with, RPM increases up to 1000 within $10\ s$ and remains constant for $10\ s$ to perform an initial slow uniform spread of the photoresist. Then RPM increase up to 5000, which gives a

photoresist thickness of roughly $500\,nm$ (Microposit 1800 series photo resists), and remain constant for $60\,s$ until it drops down to 0 RPM.

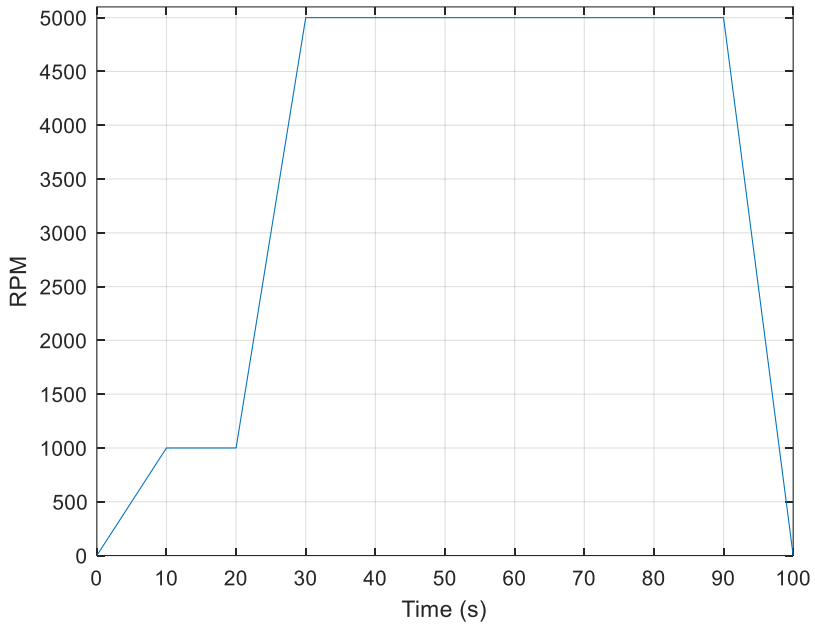

Figure 4.11 Spin coater revolution per minute settings to uniformly spread positive photoresist on a 4 inch tantalum pentoxide wafer.

The wafer is then soft baked on a hot plate at 115 ℃ for $1\,min$ and cools down for $5\,min$. This step will evaporate the solvent in which the photosensitive compound is dissolved. A mask aligner was then used for the photolithography process. The mask (Figure 4.12) chosen includes linear and micro – resonator waveguides whose width is $1.5\,\mu m$. The mask is separated in sets of resonators and straight waveguides characterised by the gap between resonator and bus waveguide, 1 μm, 1.2 μm, 1.4 μm and 1.6 μm. Each set contains resonators with increasing radius from 10 to 100 μm with a $10\,\mu m$ step and, also, increasing racetrack linear segment from 0 (ring) to 60 and then $120\,\mu m$ length (Figure 4.12b).

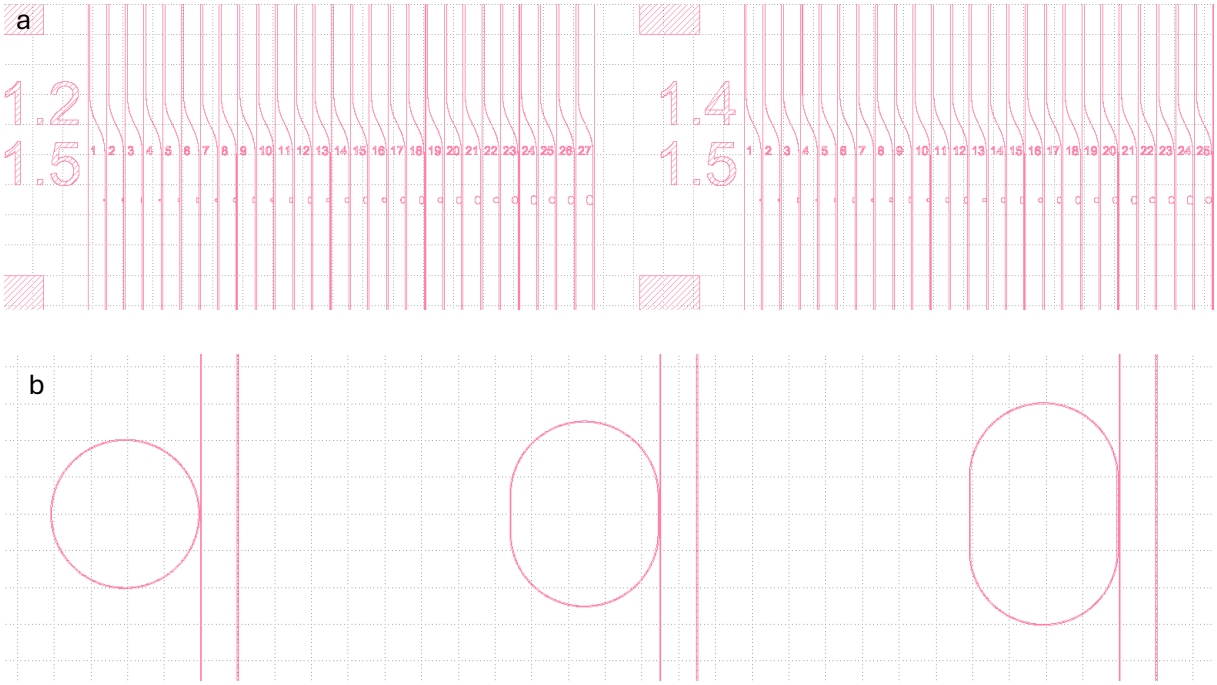

Figure 4.12 Sections of mask design for tantalum pentoxide 4 inch wafer. (a) The top numbers, 1.2 and 1.4, denote gap between resonators and bus waveguides in μm, whereas the bottom number, 1.5, denotes the waveguide width. The squares appearing in the design are used for separating sets and etch calibration. (b) Each different gap set contains a series of resonators that change in radius and racetrack linear segment length. Here, the ring and circular components of the racetracks have the same radius with increasing linear segment starting from $0\ \mu m$. The next series of micro – resonators will have a greater radius. Adjacent to the bus waveguide is another waveguide for measuring optical losses.

The Ta_2O_5 wafer is placed on the mask aligner, and the photomask is placed on top of the wafer with the "hard contact" setting chosen to reduce diffractive effects and increase resolution. As the photomask is in contact with the wafer, only the areas under the pink shapes (Figure 4.12) are covered and the remaining area is exposed. The mask aligner's UV lamp irradiates the mask and the exposed photoresist for $4.5\ s$. After investigation, the specific exposure time was chosen to avoid under – or over – exposure of the photoresist. After exposure, the MF – 319 developer is applied to dissolve the UV exposed photoresist for $45\ s$. Longer development times seems unnecessary after investigation. After development, the wafer is immediately held in a beaker full of DI water and moved around. Afterwards, the wafer is rinsed with the DI water gun and dried with N_2.

Before proceeding with the etching process, the photoresist thickness is measured by using a stylus profiler at different wafer sites to check for consistencies. The squares found throughout the wafer as mentioned in Figure 4.12a are used for this task. The average thickness measured is $(843 \pm 14)\ nm$. Because of the 500 RPM setting, a $500\ nm$ thick photoresist coating was expected, however, as the liquid is stored inside a fridge, it have been more viscous and therefore its spread across the wafer is slower.

Hereafter, ion beam milling (IBM) machine [124] is used to dry etch the Ta_2O_5 wafer to

realise the waveguide structures. The IBM utilises a beam of ions to bombard and remove tantalum pentoxide material that is not protected by the remaining photoresist. IBM uses a radio frequency (RF) antenna to produce the ion stream from the gas source. The RF signal ionises the gas source creating a plasma, from which ions are extracted and accelerated by a DC field towards the wafer target.

Ions are produced from a mixture of the inert Ar, $20\ sccm$ flow rate, that does not chemically react with tantalum pentoxide, and O_2, $6\ sccm$, which is a reactive species to increase etch rates and material selectivity (tantala and photoresist). The RF power is $500\ W$, the DC accelerating voltage is $250\ V$, the beam current is $80\ mA$, and the ion beam voltage is $500\ V$, which is related to the ion energy and sputter yield and hence, tantala atoms etched per ion. Additional settings include $300\ mA$ neutraliser whose electrons neutralise space – charge to control the waveguide sidewall profile and to optimise radial uniformity, and a plasma warmup of $30\ min$.

The wafer is securely held by a rotating holder and placed inside a vacuumed chamber to prevent unwanted air molecule collisions. The tilt angle of the wafer is $-20°$ to get near vertical waveguide sidewalls while removed tantala falls off. The wafer rotates at a slow rate, 5 RPM, to get a uniform etching. The holder's temperature is controlled by a cooler set at 15 ℃ to avoid wafer thermal stresses.

After inserting the aforementioned settings to the IBM machine, the tantalum pentoxide wafer is placed inside its chamber and then create the vacuum. The wafer is etched for $24\ min$ and $24\ s$, which removed $417\ nm$ of tantalum pentoxide (Figure 4.13), which is close to the desired etch depth of $400\ nm$. An ellipsometer was used to determine the wafer's etch depth, which is $462\ nm$, noting that the actual Ta_2O_5 film thickness is $820\ nm$.

The following fabrication steps involve stripping the remaining photoresist. To begin with, the plasma ashing apparatus is used to strip the photoresist with $600\ mL/min$ O_2 flow rate and $1000\ W$ microwave power for $10\ min$ and $5\ min$ cool down. The plasma asher completely removes the photoresist, however, an ultrasonic cleaner is also used to remove any residuals and dirt. The wafer is placed inside a beaker filled with acetone and in turn is placed inside the cleaner, which sonicates the wafer at 20 ℃ for $5\ min$. Then the wafer is transferred to a beaker full of IPA and repeated the ultrasonic treatment. Then, the wafer is removed and dried with N_2. During the transfer from the acetone beaker to the IPA one, the wafer is sprayed with acetone. When the wafer is removed out of the IPA beaker, it is sprayed with IPA.

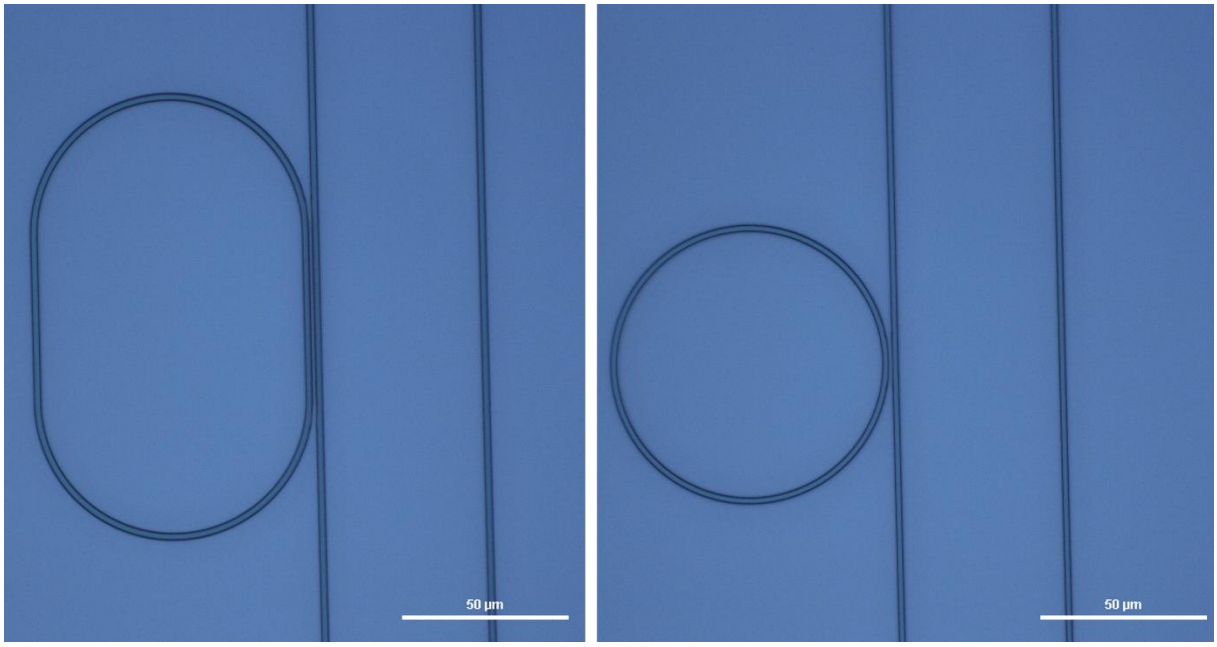

Figure 4.13 Examples of (a) racetrack and (b) ring resonators along with their bus waveguide and waveguide for loss measurements after ion beam etching. Images were taken from a microscope.

The next step of waveguide fabrication involves wafer annealing. Tantalum pentoxide has been previously annealed at 600 ℃, which results in optical loss reduction and low tensile stress in the centre of the wafer [42]. It has been reported that beyond 600 ℃ tantalum pentoxide becomes polycrystalline, a state which is not associated with low optical losses [42]. The tantala wafers are annealed at $565 - 580$ ℃ due to furnace temperature deviations. Furnace settings include ramping the temperature up at a rate of 2 ℃$/min$ and dwelling for 5 hrs and then ramping down to room temperature at a 1 ℃$/min$. The slow rates are crucial to avoid wafer thermal stresses. Annealing is achieved with a 2 L/min O_2 flow rate.

The final part of the fabrication process involves deposition of 1 μm thick silica film on top of the tantalum pentoxide wafer, providing the waveguides top cladding instead of air. Silica deposition was performed by Dr Oliver Trojak using the PECVD technique. A plasma is created by applying a RF signal to a gas source, which reacts with a precursor gas and results in the dissociation of the precursor gas molecules into reactive species that can be deposited on the substrate. In this case, tetraethyl orthosilicate ($Si(OC_2H_5)_4$; TEOS) is the precursor gas for the deposition of SiO_2. Liquid TEOS is vapourised and introduced into the chamber using a nitrogen bubbler, where it reacts with the plasma and breaks down into reactive species, which in turn react with the O_2 in the chamber to form SiO_2, which is then deposited onto the surface of the Ta_2O_5 wafer. The settings include 40 W RF power, 40 W low frequency (LF) power, 12 s RF power cycle, 8 s LF power cycle, 350 ℃ temperature and 500 $sccm$ O_2 flow rate.

Silica was not deposited on all of the wafers. The IBM machine used went through a gas purging procedure and since then the etch rates of tantalum pentoxide and other materials were

dropping. Another IBM machine in another cleanroom facility was implemented with the same settings mentioned above. In the following experiments, a tantalum pentoxide wafer which has a $180\ nm$ etch depth, as a result of the IBM malfunctioning, without silica top cladding is, also, investigated. All wafers were cleaved with a diamond scriber and a wafer pliers to create Ta_2O_5 chips to prepare for experimentation. After cleaving, SEM images were captured (Figure 4.14 – 4.16) to observe the waveguide cross sections.

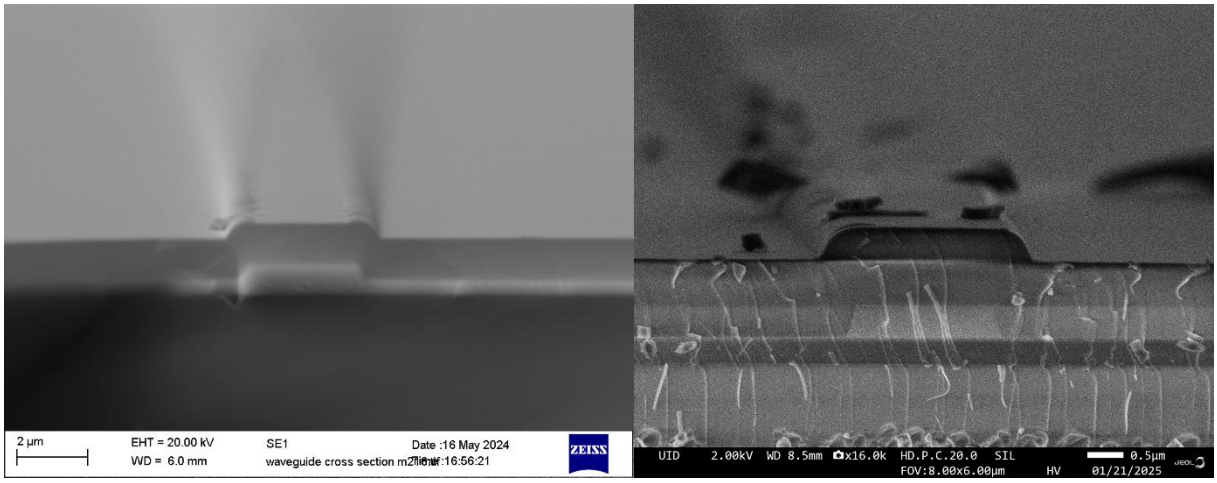

Figure 4.14 SEM image of tantalum pentoxide chip end facet from the first wafer (left) and from the last wafer (right). A relatively smooth rib waveguide is visible with its top and bottom silica cladding.

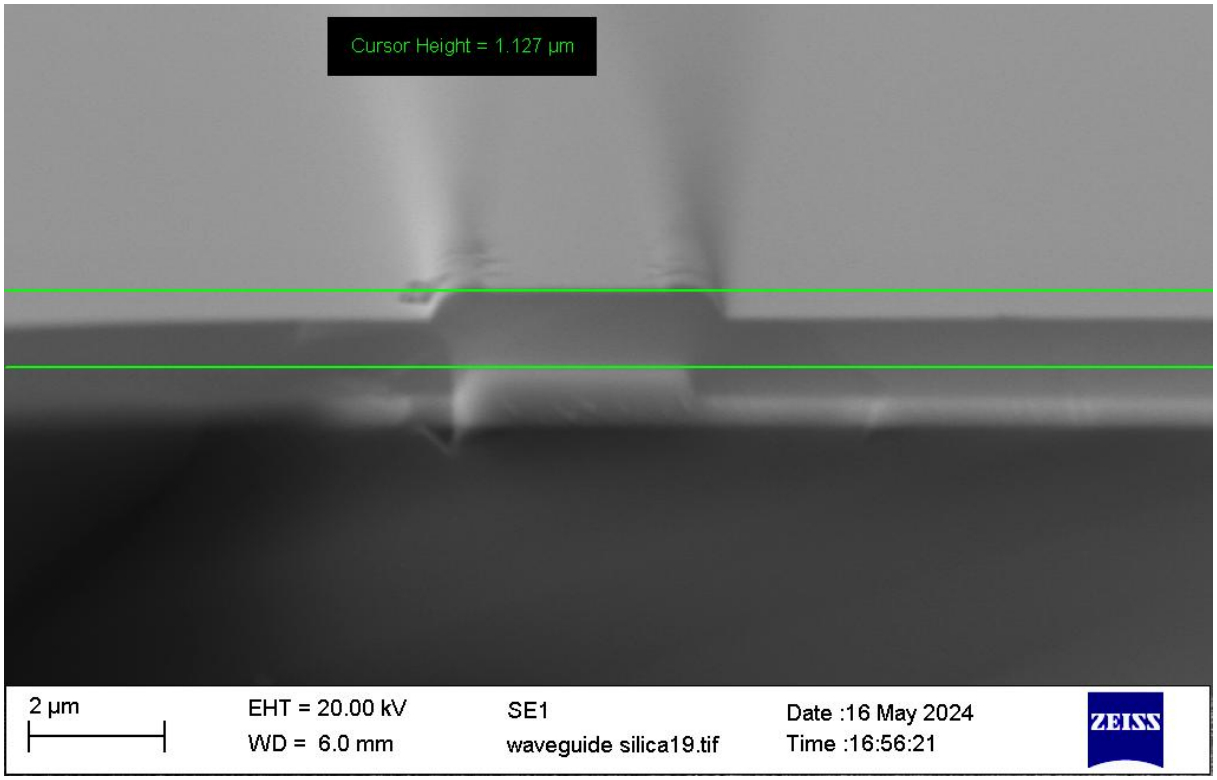

Figure 4.15 SEM image of tantalum pentoxide chip end facet. In this picture, the thickness of silica on top of the waveguide is measured, which is $1.127\ \mu m$.

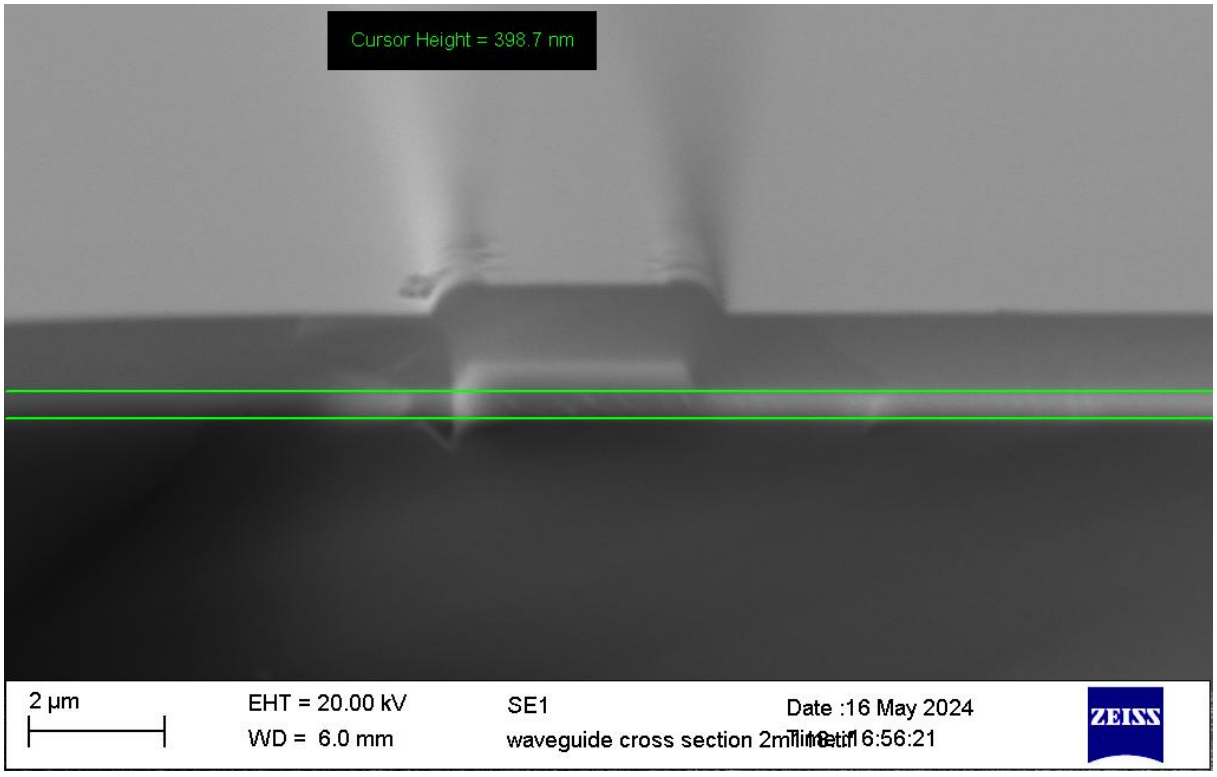

Figure 4.16 SEM image of tantalum pentoxide chip end facet. In this picture, the etch depth is measured, which is $401.3\ nm$.

4.3 Experimental Setup and Methodology of Tantala Waveguides and Resonators

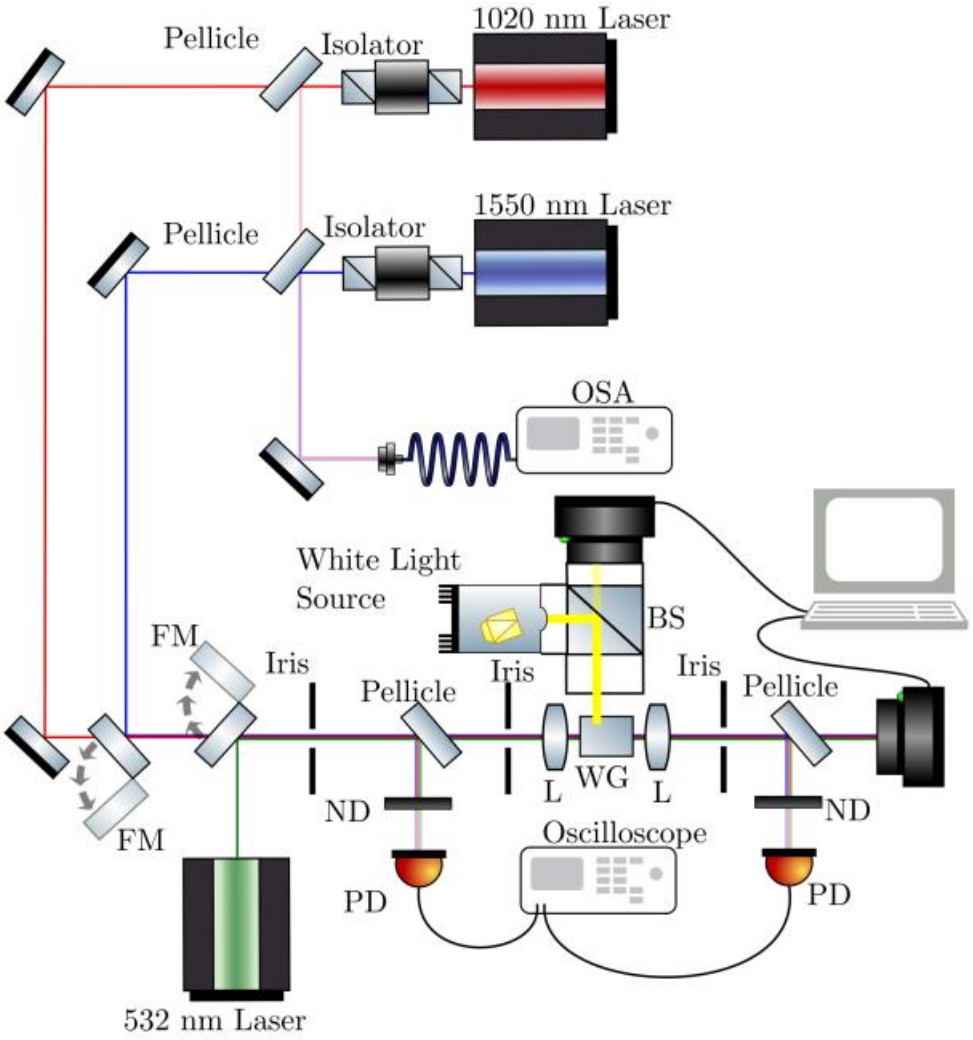

Figure 4.17 The experimental setup based on the non – destructive Fabry – Pérot interferometer for linear WG loss measurements [84]. The 1 μm laser beam goes through an optical isolator, and it is guided by two mirrors onto a pellicle component. The pellicle splits light and sends on fraction to a PD for measuring input power, and the other to a 20x microscope objective lens. The lens focuses the laser beam to allow coupling into the tantalum pentoxide WG chip. A 40x microscope objective lens collects light exiting the WGs and sends it to another pellicle. The pellicle sends one fraction of the light to a CCD to capture the chip's end facet and the other to a second PD to measure transmitted power. An oscilloscope is connected to the PDs to record measured powers. The laser's controller is also connected to the oscilloscope and allows for laser frequency sweep. A second CCD captures images of the chip from above. An OSA is used for recording laser and WG spectra. The schematic also includes two more laser sources, one emitting at 1.55 μm and the other at 532 nm.

The experimental setup [84] is based on the Fabry – Pérot interferometer for non – destructive loss measurements in linear resonators (Figure 4.17). The Fabry – Pérot interferometer consists of an optical cavity or a medium bound by two reflective surfaces, in this case tantalum pentoxide is bound by air, which has a smaller refractive index than that of the former material. Light injected inside the cavity forms a standing wave and partially escapes the boundaries. The resulting transmission spectrum is wavelength dependent and consists of peaks and troughs. The higher the finesse of the cavity, i.e. the more the wavelength is closer to the cavity's resonance, the sharper the peaks are and hence, the farther the peak value is from the trough value. The sharpness is related to the contrast, γ (Equation 4.1), which is crucial to determine for loss calculations:

$$\gamma = \frac{I_{max} - I_{min}}{I_{max} + I_{min}} \quad (4.1)$$

where I_{max} is the peak value and I_{min} is the trough value. Propagation losses measured in dB, a_{dB}, are then calculated by using Equation 4.2 [125]:

$$a_{dB} = 4.34\left[lnR - ln\left(\frac{1 - \sqrt{1 - \gamma^2}}{\gamma}\right)\right] \quad (4.2)$$

where R (Equation 4.3) is the reflectance at the tantala – air interface, which is [85]:

$$R = \frac{\left(n_{eff} - 1\right)^2}{\left(n_{eff} + 1\right)^2} \quad (4.3)$$

The effective refractive index is considered to calculate reflectance, and only the fundamental TE or transverse magnetic (TM) guided mode is assumed as higher – order modes have a greater effective area and hence, experience more losses.

The setup itself consists of the following components. A diode laser (Moglabs Tunable Cateye Laser) emitting at $1\ \mu m$ probes the waveguides, which resembles the MQWL source but, also, is used for measuring losses. Losses for a pump wavelength of $1550\ nm$ were not able to be calculated because the top view CCD used for coupling purposes is unable to image light at that wavelength making coupling into the waveguides significantly difficult. However, losses attributed to material absorption are near zero for $1550\ nm$ [52], [53]. The laser's output optical power was calibrated resulting in a slope efficiency of $(0.5483 \pm 0.0077)\ mW/mA$ and around 71 to $75\ mA$ current threshold (Figure 4.18). The laser beam goes through an optical isolator avoiding optical feedback, and it is guided by two mirrors through a neutral density filter (ND) and onto a pellicle beam splitter. A fraction of the beam is sent to a photodiode (PD) to measure input optical power, and the remaining beam is sent to a focusing 20x microscope objective lens (L). The laser beam is focused down to the tantalum pentoxide waveguide (WG) chip. The aim here is

to couple the laser beam into the WGs. If light is successfully coupled in the WGs (Figure 4.19a), the 40x microscope objective lens (L) on the other side will collect and send the output light onto another pellicle beam splitter. A fraction of this light is sent to another PD to measure output transmitted power, and the rest of the light is sent to a CCD to image the WG's end facet. If a bright spot appears at the end facet it indicates that light coupled in and out from the linear WG successfully (Figure 4.19b and 4.19c). Another CCD captures images of the chip from top. An OSA is used to record laser and WG spectrum.

The PDs are connected to an oscilloscope to record the input and output optical powers. The oscilloscope is also connected to the pump diode laser controller (Moglabs DLC [126]), to monitor and record the laser source's frequency sweep. Frequency sweeping is achieved by the controller as it supplies a voltage sawtooth ramp to the piezo electric actuators thus changing laser cavity length and therefore laser wavelength [126]. The sweeping range was determined with the OSA before the laser beam probed the WG chip. The spectrum recorded on the OSA with noise ranges from $1020.00 - 1024.00\ nm$ (Figure 4.20). By dropping the sweep rate, slower readings are received at the spectrum's edges, i.e. where a signal above noise is observed and where it drops completely. It seems that the sweep begins around $1022.15\ nm$ and ends at $1022.50\ nm$, which corresponds to $100\ GHz$. However, this method was prone to human error, therefore, the FWHM of the laser spectrum was considered, $1022.352\ nm - 1022.612\ nm$ (Figure 4.20), which is $75\ GHz$ and related it to the laser's scan range [127].

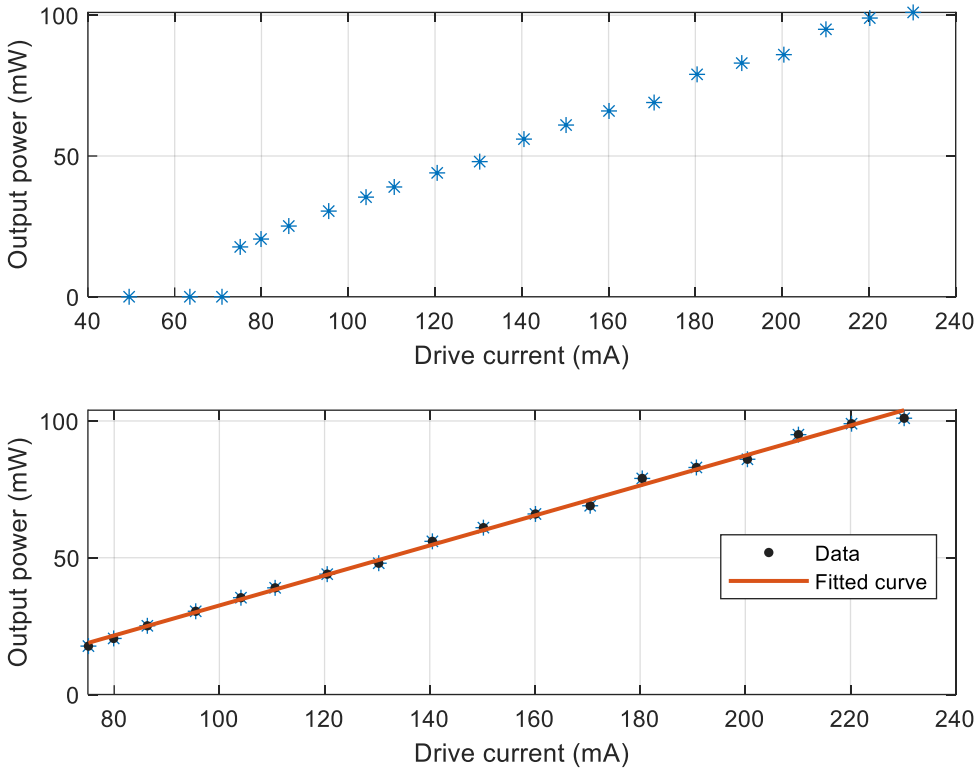

Figure 4.18 Pump diode laser P – I emission characteristic curve emitting at 1 μm. The top plot presents the diode laser's optical power against its injection current. After laser threshold, around 71 to 75 mA, stimulated emission is observed indicated by the sharp increase in optical power. The bottom plot displays a linear fit to the stimulated emission region matching the data behaviour and giving a slope efficiency of $(0.5483 \pm 0.0077)\, mW/mA$.

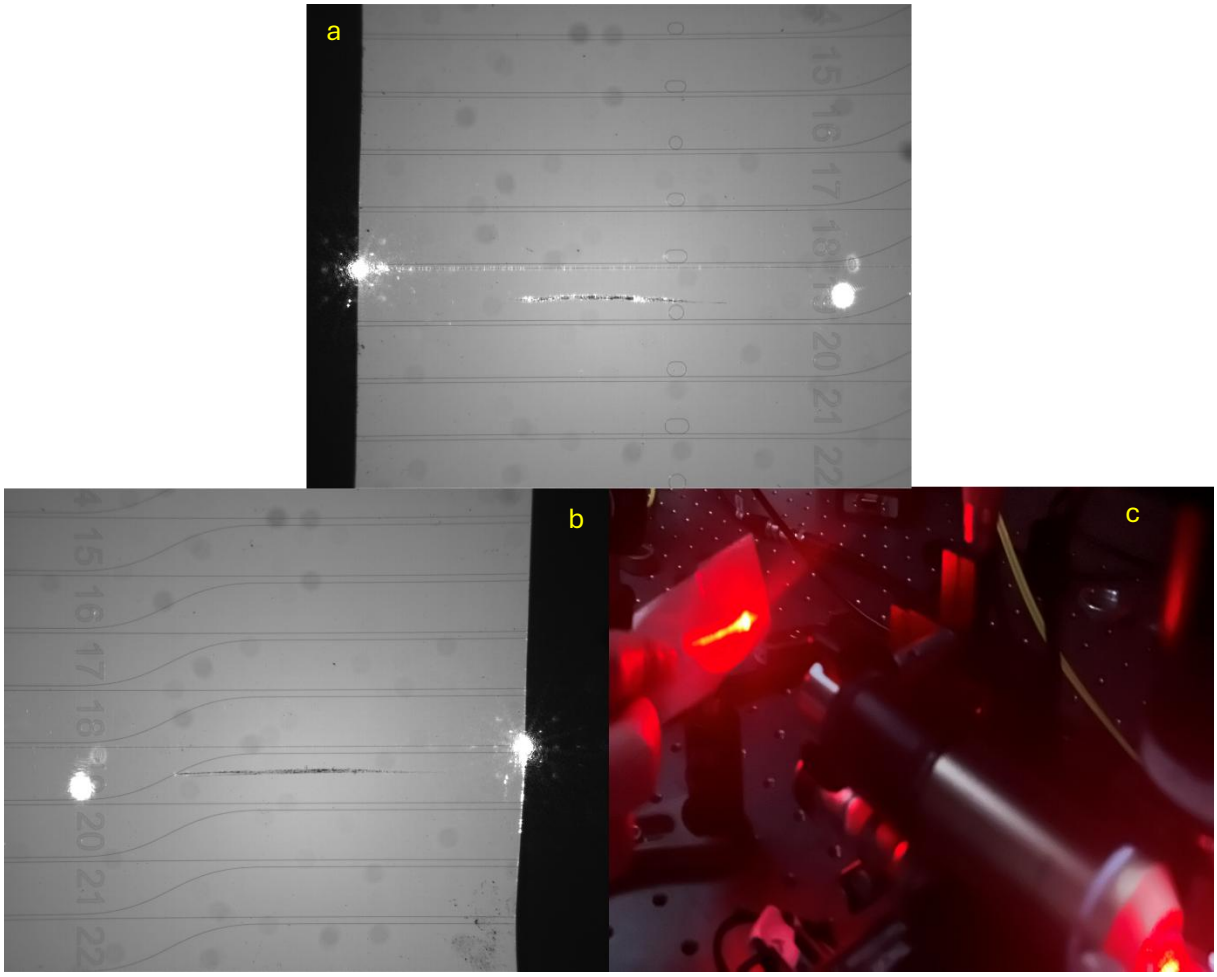

Figure 4.19 Coupling laser beam into tantalum pentoxide linear waveguide. (a) Top view of the tantalum pentoxide waveguide chip. The bright spot at the air – tantala interface indicates laser beam coupling into the linear waveguide. Light travelling along the waveguide is also visible. (b) Top view of the tantalum pentoxide waveguide chip's other facet. The bright spot due to scattering appearing at the tantala – air interface indicates that the guided light exits the waveguide. (c) Bright laser spot appearing on paper after exiting a waveguide and being collected by the 40x microscope objective lens. Red light laser was used for initial setup alignment.

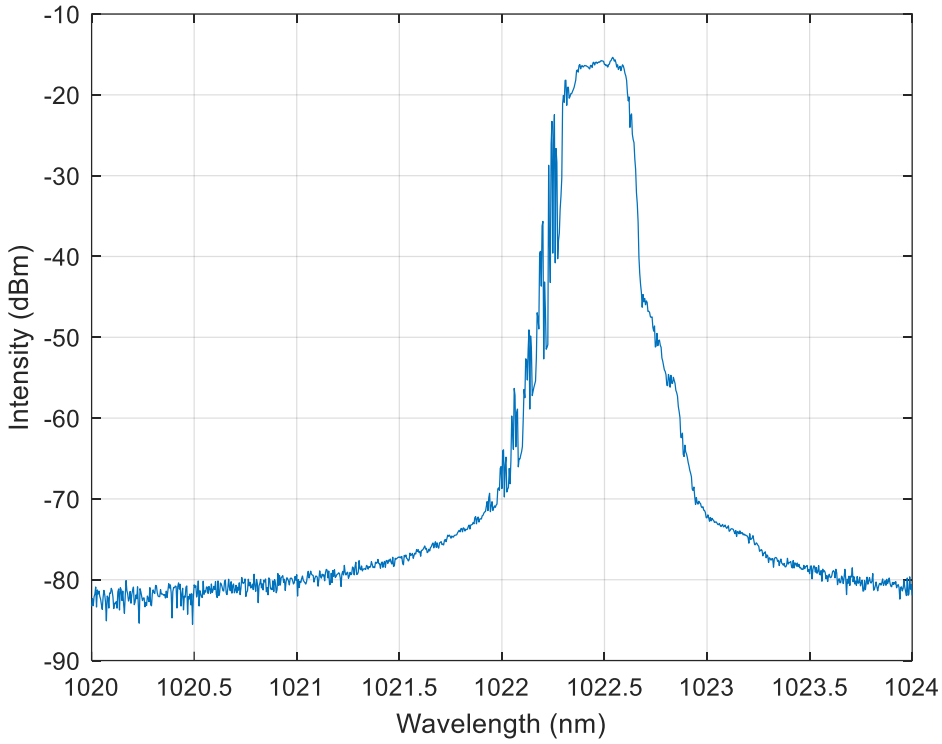

Figure 4.20 Diode laser spectrum as the laser's controller performs a frequency sweep. The sweep is achieved by the controller as it supplies a sawtooth ramp to the piezo electric actuators, which change the laser cavity length and therefore its emission wavelength. The frequency scan range corresponds to the FWHM of the laser spectrum, $1022.352\ nm\ -\ 1022.612\ nm$.

4.4 Experimental Results of Tantala Waveguides and Resonators

4.4.1 Ta_2O_5 Waveguide Optical Losses

In this section the findings on optical losses of linear tantalum pentoxide waveguides, and quality factors or Q – Factors determined are presented. Insertion losses [128], [129], material absorption, and sidewall and surface scattering [129], [130], [131] are some factors responsible for light losses in optical waveguides. Some results involve a spin coated tantalum pentoxide chip that underwent electron – beam or e – beam lithography to compare with photolithography. E – beam lithography is an alternative technique to photolithography, which uses a stream of focused electrons to create patterns on the target wafer. This technique does not require a photomask and offers higher resolution [132], [133].

Waveguides in $1\ cm$ chips from three different Ta_2O_5 wafers were examined. One has a near $400\ nm$ etch depth with top silica cladding, the other has the same etch depth a top cladding but was etched in another cleanroom, and the third wafer has a $180\ nm$ etch depth with no top silica

cladding. The resulting transmission spectra from their waveguides gave a harmonic waveform consisting of signal beats. An attempt was made to fit a sum of sinusoids to the harmonic waveforms as shown in Figure 4.21 to get the peak – trough contrast and, therefore, get the linear waveguide optical losses from Equations 4.1 – 4.3. From the simulations, the n_{eff} is 2 for the $400\ nm$ etch depth silica cladded waveguide and $1.02\ \mu m$ wavelength, and 2.01 for the $180\ nm$ partial etch air cladded waveguide and $1.02\ \mu m$ wavelength.

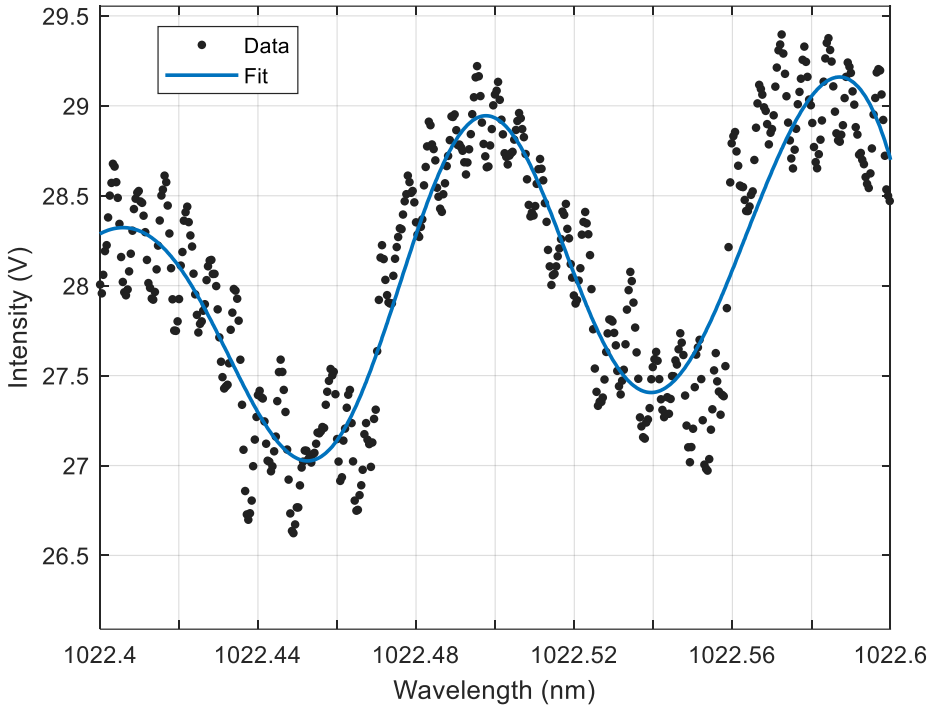

Figure 4.21 Transmission spectrum recorded from a linear tantalum pentoxide waveguide top cladded with silica. A sum of five sinusoids were fitted to the scattered data to match the harmonic waveform. From the peak – trough contrast, the average optical loss calculated is $863.30\ dB/m$.

In Table 4.1 optical losses are presented which were retrieved after examining the transmission spectra recorded at the output of multiple linear waveguides. The input optical power ranged from $104\ mW$ to $122\ mW$. The optical losses obtained are high and ranging from $618\ dB/m$ to $1287\ dB/m$. Such high losses for TE_{00} are possibly attributed to the unpolished waveguide end facets, such as high insertion loss, and structure sidewalls. TM_{00} would suffer from less sidewall scattering, however, the unpolished end facets would still contribute to the high losses.

Table 4.1 Ta_2O_5 linear waveguide optical losses

Wafer	Optical losses (dB/m)
1st wafer, 400 nm etch depth, top silica cladding	991.09, 1286.69
2nd wafer, 180 nm etch depth, no top silica cladding	618.01, 835.03
3rd wafer, 400 nm etch depth, top silica cladding	863.30, 879.37, 915.00, 1090.60

An attempt was also made to couple the laser beam into the resonators. Coupling was not possible, and as with the linear waveguides for loss measurements, no spectral broadening was observed from the bus waveguides due to the high losses (Figure 4.22 and 4.23). In Figure 4.22 a comparison of the laser spectrum before entering a racetrack resonator's bus waveguide and upon exiting is presented. The silica cladded racetrack resonator has a separation gap from the bus waveguide of $1.4\ \mu m$, linear segment of $100\ \mu m$ and radius of $60\ \mu m$. The input spectrum is greater in power, and the output is lower as light is subjected to the waveguide losses. The spectrum, however, does not broaden after travelling inside the resonator with the FWHM of each spectral profile remaining the same, around $0.28\ nm$.

Figure 4.23 presents the comparison of the output spectrum shown in Figure 4.22 with the output spectra from the same waveguide but with higher laser powers is plotted. As before, no spectral changes are observed as a higher power would increase the chances of observing nonlinear effects, but high optical losses and the fact that the probe wavelength falls in the normal GVD regime supress nonlinear interactions of the tantala atoms and the laser beam. In Figure 4.24 the transmission spectrum of the bus waveguide to calculate the optical loss is presented, which is estimated to be $870.91\ dB/m$.

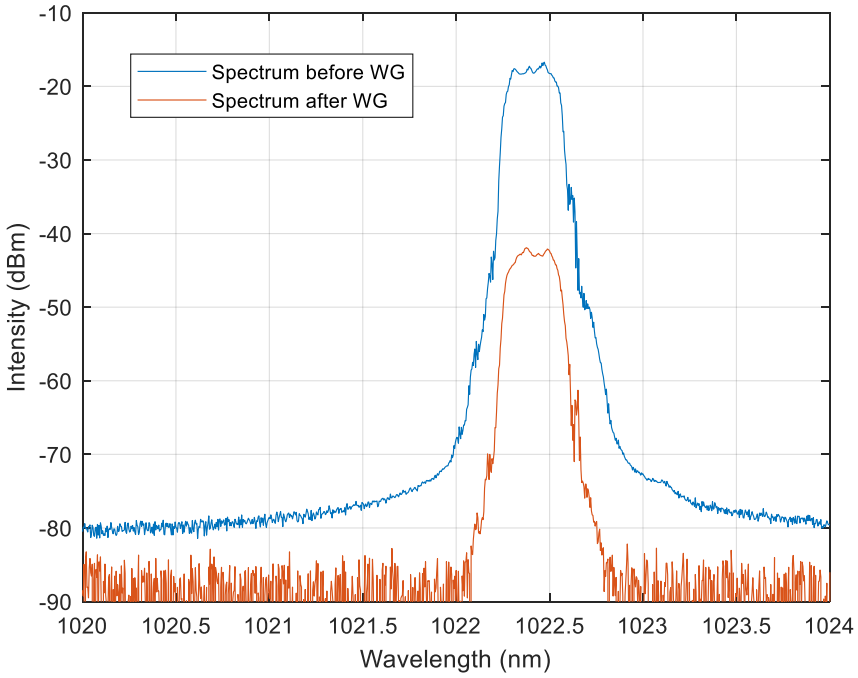

Figure 4.22 Comparison of the diode laser beam spectrum before entering and exiting the bus waveguide adjacent to a silica cladded racetrack resonator whose separation gap from the bus waveguide is $1.4\ \mu m$, its linear segment is $100\ \mu m$ and its radius is $60\ \mu m$. The input spectrum's power is higher before the waveguide and upon exiting it is lower. A lower power is expected due to insertion losses, material absorption [52][53], and sidewall scattering. As before, no spectral broadening was observed.

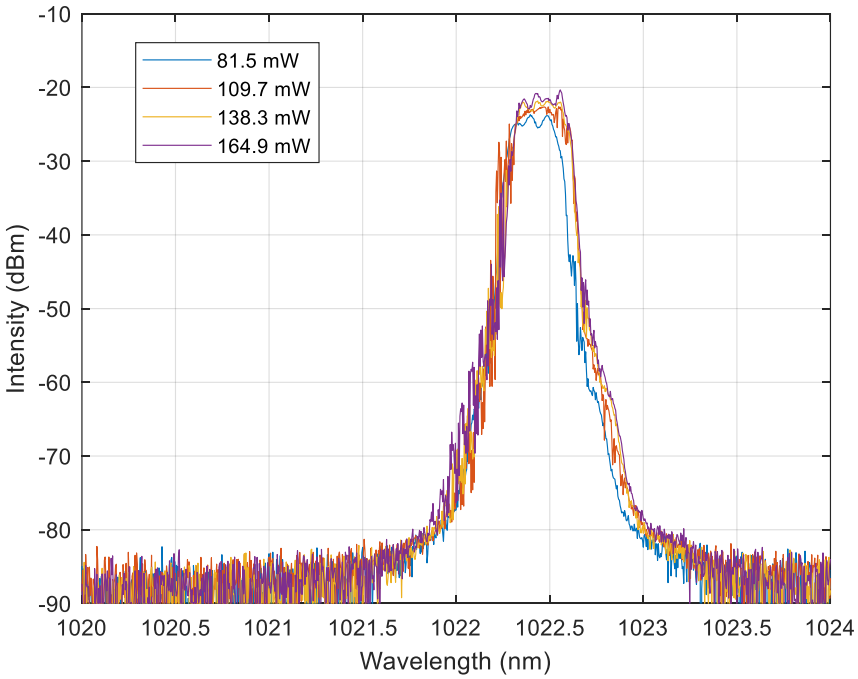

Figure 4.23 Comparison of the laser beam spectrum recorded after exiting the bus waveguide for different laser powers. As higher laser power would increase the possibility of nonlinear interactions inside the optical medium, this was not the case as no spectral broadening was present. High optical losses are a reason of the absence of spectral broadening but also the probe wavelength existing in the normal GVD regime.

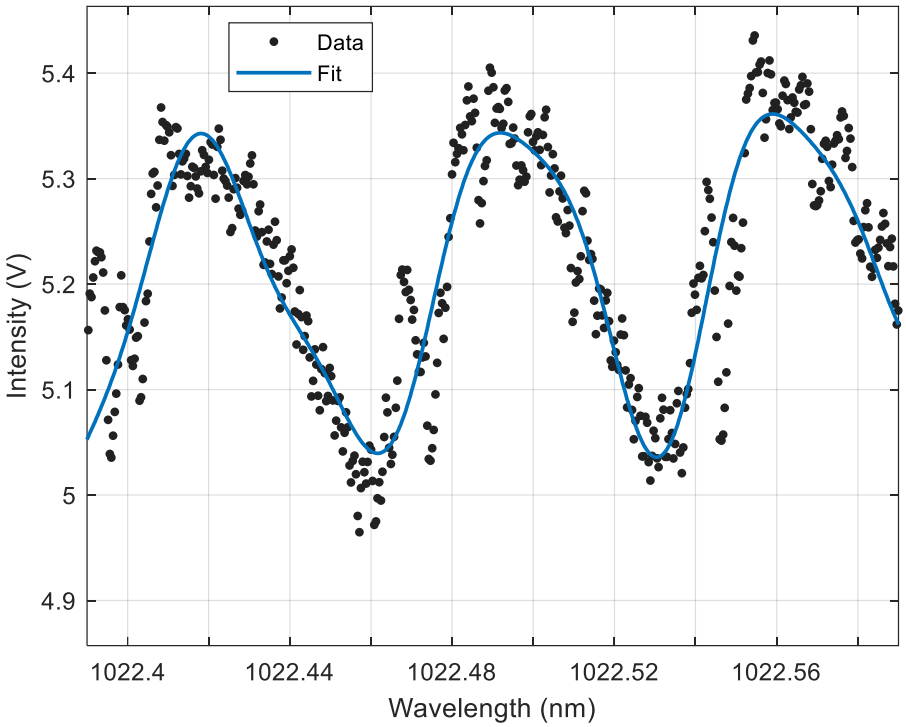

Figure 4.24 Transmission spectrum recorded from a tantalum pentoxide bus waveguide top cladded with silica adjacent to the racetrack resonator whose separation gap from the bus waveguide is $1.4\ \mu m$, its linear segment is $100\ \mu m$ and its radius is $60\ \mu m$. A sum of sinusoids were fitted to the scattered data to match the harmonic waveform. From the peak – trough contrast, the average optical loss calculated is $870.91\ dB/m$.

The waveguide losses obtained are very high for both probe wavelengths, $1\ \mu m$ and $1.55\ \mu m$, especially the former for which in order to observe spectral broadening, extremely high power is required that the laser from the setup cannot reach, and extremely low loss, $1\ dB/m$. For the latter wavelength, the losses calculated give an insight that Kerr frequency combs will be absent, which means low Q – factors are expected. The Q – factor is calculated by dividing the resonance wavelength by the FWHM at $3\ dB$ of the profile, $Q = \lambda_r/\delta\lambda_{FWHM}$. In [56] they report a Q – factor of 3×10^6 for $8\ dB/m$ propagation loss for the $1.55\ \mu m$ probe wavelength. NPL's experimental setup probed the tantalum pentoxide waveguides with a laser which sweeps its wavelength from $1545\ nm$ to $1555\ nm$.

4.4.2 Ta_2O_5 Resonator Coupling

The chips under investigation include three top silica cladded tantalum pentoxide chips with $400\ nm$ etch depth, two have $1\ \mu m$ separation gap between resonators and bus waveguides and the other $1.2\ \mu m$, two uncladded $180\ nm$ etch depth tantalum pentoxide chips, one has $1\ \mu m$ separation gap between resonators and bus waveguides and the other $1.2\ \mu m$, and, finally, seven cladded $400\ nm$ etch depth tantalum pentoxide chips from the last wafer, one has a $1\ \mu m$ separation gap between resonators and bus waveguides, one has $1.2\ \mu m$ gap, three have $1.4\ \mu m$ gap and the remaining two have $1.6\ \mu m$ gap. Regarding the $180\ nm$ partial etch waveguides, no resonance was observed and therefore, no Q – factors were recorded.

Regarding the chips from the first $400\ nm$ partial etch wafer, light coupling from the bus waveguide to the resonators was observed and resonance Q – factors were recorded. Q – factors ranged from 1×10^3 up to 1.5×10^4 with coupling coefficients ranging from 0.2 to 1.0, which is critical coupling. The Q – factors are two to three orders lower than that recorded in [42], which was expected given the high waveguide losses. In Figure 4.25, a transmission spectrum with critical coupling and 4×10^3 resonance is presented. It should be noted that strong coupling does not necessarily mean high resonance as the quality of the resonator plays a crucial role. The resonant wavelengths are $1546.98\ nm$, $1548.68\ nm$, $1551.76\ nm$, and $1554.6\ nm$. The corresponding FSR, i. e. the difference between two consecutive resonant wavelengths, is $1.7\ nm$, and the resonator's finesse, i. e. FSR over FWHM at $3\ dBm$, is 4.4.

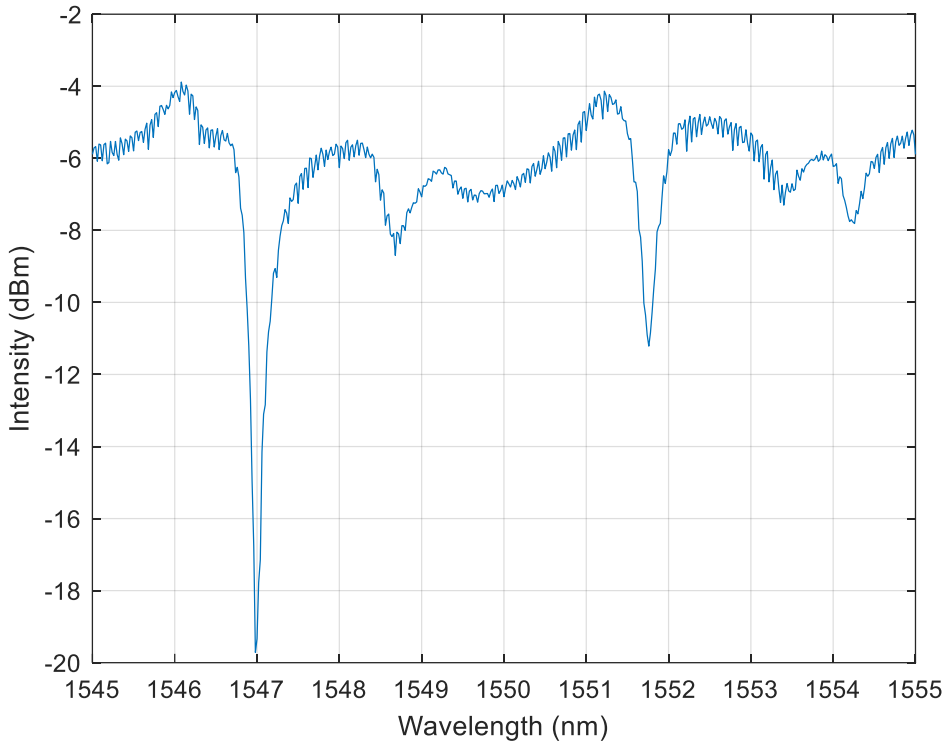

Figure 4.25 Resonance in silica cladded resonator with $1\ \mu m$ separation gap from bus waveguide. The resonance wavelengths are $1546.98\ nm$, $1548.68\ nm$, $1551.76\ nm$, and $1554.6\ nm$ with the calculated Q – factor being 4×10^3. Coupling is critical. The FSR is $1.7\ nm$ and the resonator's finesse is 4.4.

In Figure 4.26, resonance observed in two different resonators from the same silica cladded chip is presented with $1\ \mu m$ separation gap with the highest recorded Q – factor, 1.5×10^4, but different coupling coefficients, 0.2 and 0.6. The purpose of this comparison is to showcase that the amount of light coupling into the interferometer is independent from how strong the resonance is. Coupling is affected by the size of the separation gap, whether it is a point (micro – ring) or directional coupler section (racetrack), and the quality of the structures. Resonance is affected by optical losses, whether that is absorption from the material or the inability of a medium to function as a waveguide. The higher the Q – factor, the more light remains inside the resonator and builds up to interact nonlinearly with the atoms of the optical medium.

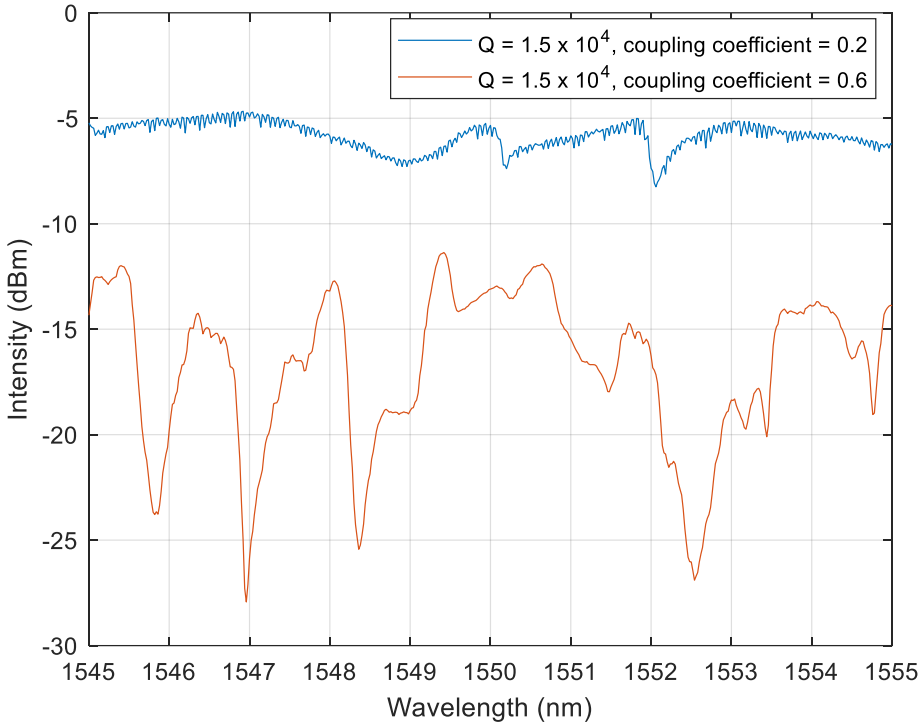

Figure 4.26 Comparison between the transmission spectra from two different silica cladded tantalum pentoxide resonators with $1.0\ \mu m$ separation gaps. Although both resonators exhibit the same Q – factor, 1.5×10^4, they have different coupling coefficients, 0.2 (blue) and 0.6 (orange). The resonator that has a greater coupling coefficient allows more light to enter the interferometer from the bus waveguide.

In Figure 4.27, another transmission spectrum depicting resonance is presented, but for a resonator with a $1.2\ \mu m$ separation gap from its bus waveguide. The Q – factor is roughly 1.5×10^4, and its coupling coefficient is 0.3. Resonant wavelengths include $1546.54\ nm$, $1548.5\ nm$, $1550.02\ nm$, $1551.62\ nm$, and $1553.42\ nm$. The corresponding FSR is $1.96\ nm$, and its finesse is roughly 12.25 indicating sharper resonance compared to the resonance presented in Figure 4.25. In Table 4.2 I summarise the resonator details from Figures 4.25 to 4.27.

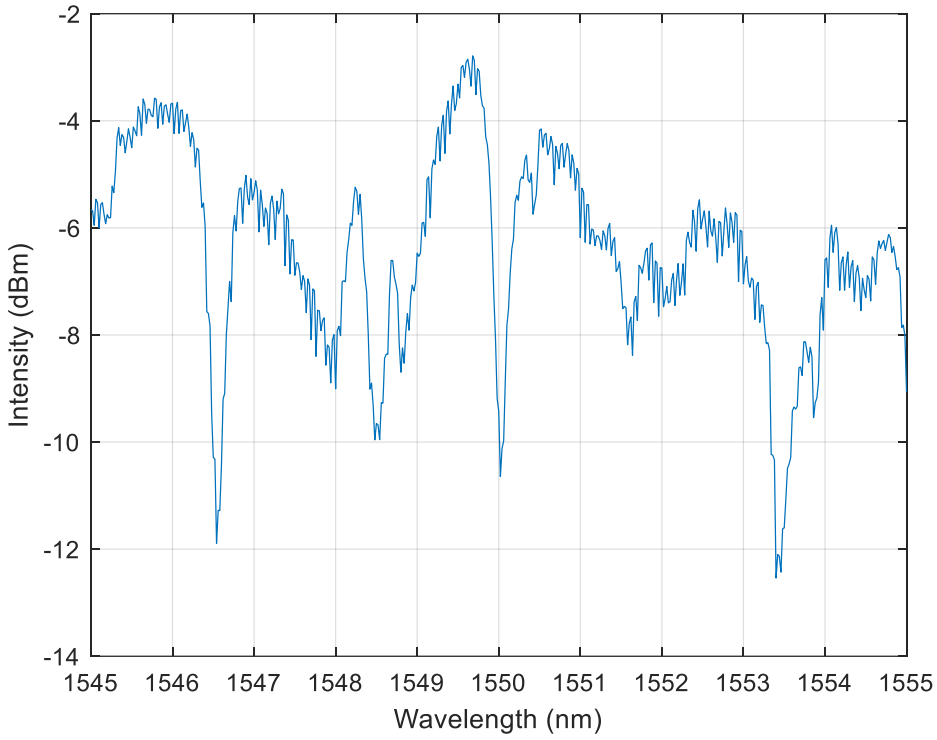

Figure 4.27 Transmission spectrum with resonance of a silica cladded tantalum pentoxide resonator with a $1.2\ \mu m$ separation gap from its bus waveguide. The Q – factor is roughly 1.5×10^4, and its coupling coefficient is 0.3. Resonant wavelengths include $1546.54\ nm$, $1548.5\ nm$, $1550.02\ nm$, $1551.62\ nm$, and $1553.42\ nm$. The corresponding FSR is $1.96\ nm$, and its finesse is roughly 12.25.

Table 4.2 Resonator details from Figures 4.25, 4.26 and 4.27

Resonator type	$R\ (\mu m)$	$L\ (\mu m)$	$\lambda_r\ (nm)$	Q	κ	$Gap\ (\mu m)$
Racetrack	40	100	1546.98	4×10^3	Critical	1.0
Ring	50	0	1552.06	1.5×10^4	0.2	1.0
Racetrack	100	100	1546.98	1.5×10^4	0.6	1.0
Racetrack	70	100	1546.54	1.5×10^5	0.3	1.2

Regarding the waveguides from the final tantalum pentoxide wafer, which is silica cladded, Q – factors ranging from 1×10^4 up to 2.2×10^5 were estimated, which are greater than the ones obtained from the first wafer. In general, the third wafer was more carefully processed. Looking back at Table 4.1, the optical losses measured in the third wafer are lower than the ones measured for the first wafer. Experimentation was performed on one chip with waveguides, whose separation gaps are $1.6\ \mu m$, and despite not observing Kerr frequency combs resonance observed in most waveguide resonators. As the laser wavelength was swept to attain resonance, it was tuned to the narrowest resonance that could be found for each resonator and coupling was optimised for that particular resonance wavelength.

In Figure 4.28, a few examples of resonance are presented. The resonant wavelengths are $1554.54\ nm$, $1555.57\ nm$, $1552.07\ nm$, and $1551.53\ nm$ at Figure 4.28a, b, c, and d, respectively. Figure 4.28a and 4.28e depict resonance associated with vertical multimode propagation as imaged at the bus waveguide's output end facet. A multimode propagation would indicate high losses due to a great effective area and corresponds to a relatively low intrinsic Q – factor, 6.03×10^4. The coupling coefficient for this resonator is 0.314. Figure 4.28b and 4.28f on the other hand demonstrate resonance with single mode propagation, which is associated with a higher Q – factor, 1.77×10^5, as a single mode has a smaller effective area and, therefore, is subjected to lower losses compared to multimode propagation. Its coupling coefficient is 0.548. Figure 4.28c and 4.28g display another resonance with fundamental mode propagation in a multimode waveguide with a Q – factor of 1×10^5 and a near – critical coupling of 0.929. Finally, Figure 4.28d and 4.28h depict resonance with horizontal multimode propagation with a Q – factor of 1.4×10^5 and a near – critical coupling of 0.190. The results in Figure 4.28d and 4.28e show that the quality of the waveguide plays a crucial role as despite having multimode propagation, a higher Q – factor is obtained compared to the one from the single mode propagation in Figure 4.28c and 4.28g, but still lower than the fundamental mode propagation in Figure 4.28b and 4.28f.

The input optical power varied from 40 to $200\ mW$ with the exception of the one resonator, where single mode propagation was observed (Figure 4.28f). The single mode waveguide was pumped with $1.4\ W$ in hopes of creating spectral broadening, but the Q – factor is still low enough. However, no sidebands out to $\pm\ 100\ nm$ from the probe wavelength when analysing the output light on the OSA.

Additionally, in Figure 4.29a and 4.29b two more resonance examples are shown, one that demonstrates the greatest Q – factor, 2.16×10^5, and the other exhibits the strongest coupling, 0.963. The resonant wavelengths respectively and approximately are $1547.05\ nm$ and $1555.80\ nm$. What is more, the former resonator has a coupling coefficient of 0.056, the lowest recorded coupling coefficient, and the latter has a Q – factor of 1.45×10^5. Although the resonator in Figure 4.29b has a good combination of Q – factor and coupling coefficient, the resonator presented in Figure 4.28b has the best out of all tested resonators of this chip. The ideal case is to attain critical coupling with the highest Q – factor possible. Table 4.3 presents the concentrated resonator details and results from the third wafer's chip, where R is the radius of the ring or racetrack (circular segment), L is the linear segment of the racetrack, λ_r is the peak resonant wavelength and κ is the coupling coefficient.

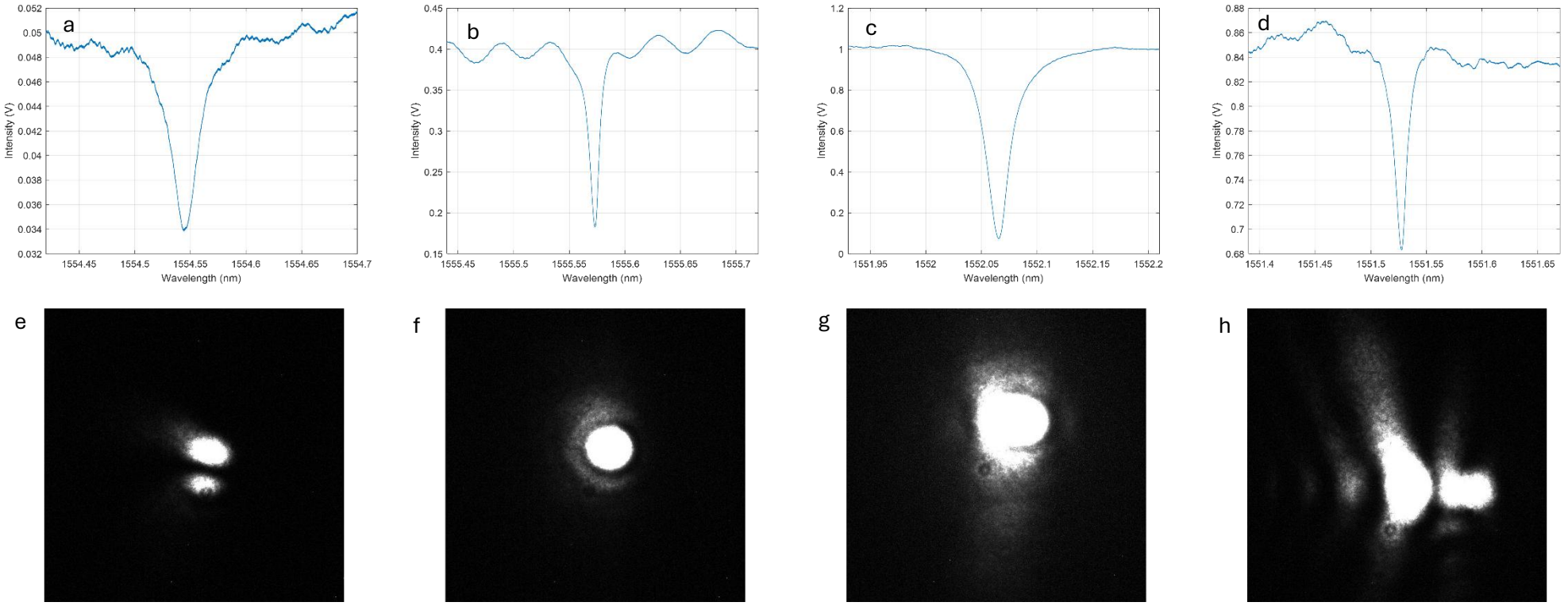

Figure 4.28 Resonance with single mode and multimode propagation. Top row: resonance in silica cladded tantalum pentoxide resonators from the third wafer: (a) $\lambda_r = 1554.54\,nm$, $Q = 6.03 \times 10^4$, and $\kappa = 0.314$, (b) $\lambda_r = 1555.57\,nm$, $Q = 1.77 \times 10^5$, and $\kappa = 0.548$, (c) $\lambda_r = 1552.07\,nm$, $Q = 1 \times 10^5$, and $\kappa = 0.929$, and (d) $\lambda_r = 1551.53\,nm$, $Q = 1.4 \times 10^5$, and $\kappa = 0.190$, where λ_r is the peak resonant wavelength and κ is the coupling coefficient. Bottom row: corresponding mode propagation imaged at the waveguide's output end facet: (e) vertical multimode propagation, (f) single mode propagation, (g) single mode propagation in a multimode waveguide, and (h) horizontal multimode propagation.

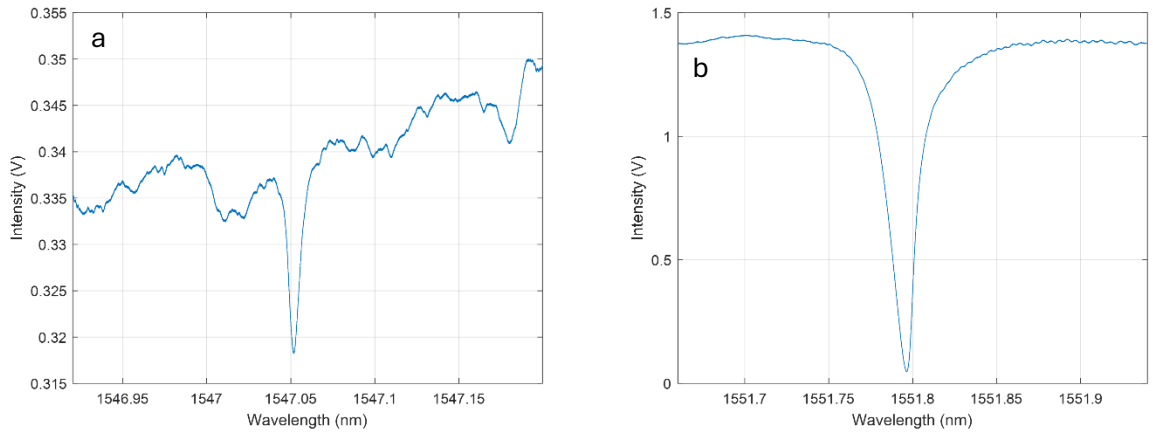

Figure 4.29 Two resonance cases from the silica cladded tantalum pentoxide chip from the third wafer. (a) This resonator exhibited the greatest Q – factor, 2.16×10^5, but the lowest coupling coefficient, 0.056, at $1547.05\ nm$ resonance. (b) This resonator exhibited a relatively high Q – factor of 1.45×10^5, with the highest critical coupling (near critical coupling), 0.963, at $1555.83\ nm$ resonance.

Table 4.3 Third Ta_2O_5 wafer resonator results with $1.6\ \mu m$ separation gap

Resonator type	$R\ (\mu m)$	$L\ (\mu m)$	$\lambda_r\ (nm)$	Q	κ
Racetrack	50	50	1554.54	6.03×10^4	0.314
Ring	70	0	1547.05	2.16×10^5	0.056
Racetrack	70	50	1555.57	1.77×10^5	0.548
Racetrack	80	100	1552.07	1×10^5	0.929
Racetrack	90	100	1555.80	1.45×10^5	0.963
Ring	100	0	1551.53	1.4×10^5	0.190

4.4.3 E – Beam Fabricated Ta_2O_5 Resonator Coupling

Finally, in this section, results from the e – beam processed silica cladded tantalum pentoxide chip are presented, which was cleaved from the same set of FiveNine Optics wafers. This chip was prepared by spin coating ma – N 2405 e – beam resist on its surface and then was exposed to the electron stream based on the pattern given by the mask's computer file. Afterwards, the chip was developed with ma – D 525 developer, then etched with inductively coupled plasma (ICP) giving the resulting waveguides an etch depth of $419\ nm$, then stripped from the remaining resist, and, finally, $1\ \mu m$ SiO_2 was deposited on top by implementing the TEOS PECVD technique.

The mask used for this tantala chip differs and includes only micro – ring resonators with all waveguide widths being $1.5\ \mu m$, and diffraction gratings to couple in and out light to and from the

optical waveguide with optical fibres. As before, transmission spectra were recorded for every waveguide under examination, along with resonance wavelength determination, and Q – factor and FSR calculation. As an example, in Figure 4.30 the transmission spectrum from a ring resonator is shown, which has a 0.6 μm gap from the bus waveguide, a ring radius of $240\ \mu m$, and a $1568.7381\ nm$ resonance wavelength. From the transmission spectrum, the Q – factor and FSR are 34691 and $89.7\ GHz$, respectively.

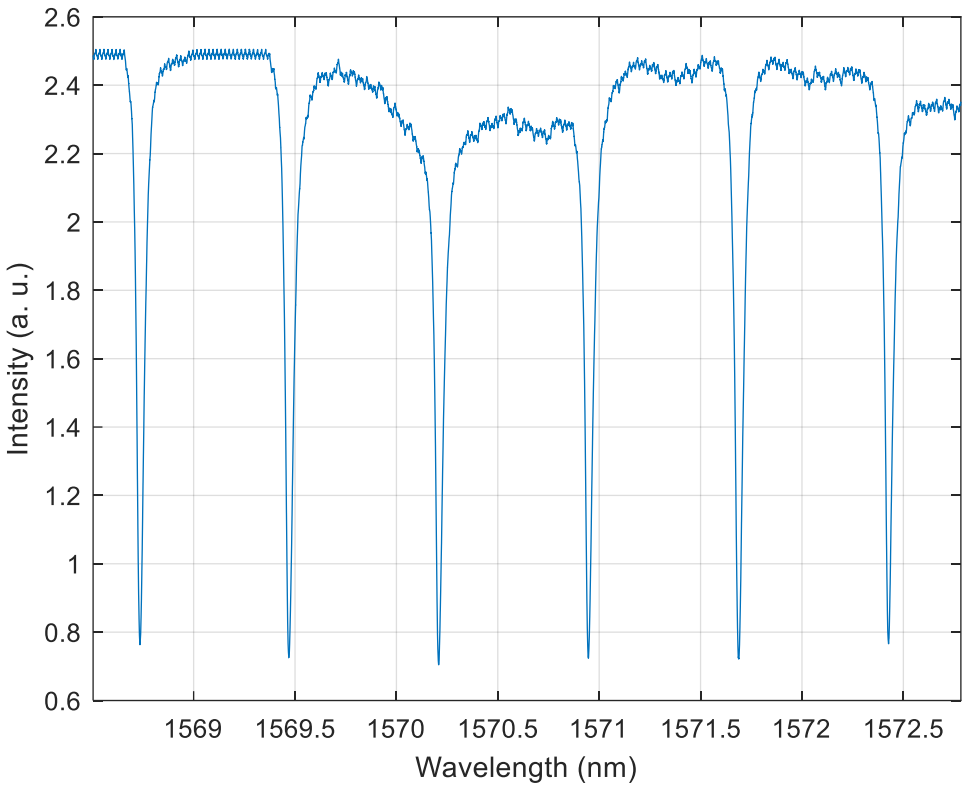

Figure 4.30 Transmission spectrum from a $1.5\ \mu m$ wide micro – ring resonator with $0.6\ \mu m$ gap from the bus waveguide and $240\ \mu m$ radius. The corresponding resonance wavelength, Q – factor and FSR are $1568.7381\ nm$, 3.5×10^4, and $89.7\ GHz$, respectively.

The total findings regarding resonance wavelength, Q – factor, FSR and coupling coefficients are presented in Table 4.4. Most estimated Q – factors are of the order 10^4. Small micro – ring radii appear to give smaller Q – factor, of the order 10^3, possibly due to curvature losses, however, the $50\ \mu m$ radius ring gives a 1.7×10^4 Q – factor. The highest recorded Q – factor is 5.9×10^4 corresponding to a $240\ \mu m$ radius and $0.8\ \mu m$ gap between resonator and bus waveguide. The FSR values are very high for the small radii ring resonators, $40 - 50\ \mu m$, which translates to a cavity finesse range 13.48 – 37.45, whereas for the $240\ \mu m$ ring resonators the finesse increases from 9.20 to 27.48 as the gap between resonator and bus waveguide increases

despite the fact that the FSR is relatively constant. Regarding the $240\ \mu m$ ring resonators, it should be noted that as the gap increases, the resonance condition improves, which is indicated by the narrower line width and the higher finesse as expected [134],[135]. Also, a high finesse is calculated with small FWHM for the $50\ \mu m$ ring resonator whose distance from the bus waveguide is $0.6\ \mu m$, which comes down to the quality of the waveguide fabrication process. To conclude this section, after examining all of the waveguides, no Kerr frequency comb generation was observed as the Q – factor remains low [56].

Table 4.4 E – beam lithography Ta_2O_5 chip micro – ring resonator results

$R\ (\mu m)$	$\lambda_r\ (nm)$	Q	$FWHM\ (nm)$	$FSR\ (GHz)$	Finesse	$Gap\ (\mu m)$	κ
40	1551.56494	4872	0.31847	534.5	13.48	0.4	0.299
45	1556.52655	9361	0.16627	473.3	23.00	0.4	0.653
50	1556.88073	16858	0.09235	427.8	37.45	0.6	0.346
240	1562.46684	19798	0.07892	89.2	9.20	0.4	0.800
240	1568.7381	34691	0.04522	89.7	16.28	0.6	0.689
240	1561.36452	59031	0.02645	89.4	27.48	0.8	0.407

Both UV and electron lithography optical rib waveguides reached Q – factors as high as 10^5, however, none exhibited SC or Kerr frequency comb generation at $1.55\ \mu m$ probe wavelength. The e – beam lithography chip presumably had similar optical losses by comparing the resulting Q – factors to the photolithography chips. The e – beam chip's mask design avoids insertion losses at the chip's end facets by introducing grating couplers. The output grating coupler is not limiting to couple out Kerr combs, should the micro resonator generate them, as it is designed for broadband uses [136], [137], [138], but the spectral response varies in intensity. Both chip designs were promising for spectral broadening, but high losses did not allow for this, and potentially additional dispersion engineering and simulations are required or different approaches in the fabrication processes to offer higher quality structures.

4.5 Conclusions

In this chapter, tantalum pentoxide rib linear and resonator waveguides were fabricated with the prospect of generating Kerr frequency combs. The rib structures were fabricated inside the cleanroom with a process which included photoresist deposition, baking, UV or e – beam lithography, developing, dry etching by ion milling, photoresist removal, annealing, and silicon dioxide deposition. The rib linear waveguide's cross section is $800\ nm$ tall and $1.5\ \mu m$ wide with

a $400\ nm$ etch depth as COMSOL and MATLAB simulations suggest with the exception of $180\ nm$ etch depth. Resonators included both micro – ring and racetrack geometries with varying perimeter and constant gap between interferometers and linear bus waveguides.

Three tantalum pentoxide wafers were prepared with photolithography and a single chip from the same batch of wafers was processed using e – beam lithography to compare the two processes. Regarding the wafers, one of them is uncladded with an etch depth of $180\ nm$ due to technical issues presented in the ion beam milling apparatus. Nevertheless, all wafers were characterised and examined for comb generation.

Transmission spectra were recorded at the University of Southampton and NPL by scanning the probe laser wavelength from which waveguide losses and resonator characteristics such as coupling coefficients, resonant wavelengths, cavity quality factors, free spectral range, full – width at half – maximum and finesse were acquired. Optical losses were determined at $1\ \mu m$ giving values ranging from $618\ dB/m$ up to $1290\ dB/m$, values that are too far away from the desired losses for comb generation as presented in the simulations. Resonance was observed in the vicinity of the $1.55\ \mu m$ probe laser wavelength, the optical telecommunications transmission wavelength, with Q – factors varying from 10^3 up to 10^5 with no Kerr frequency combs present. Compared to the work presented in [56] for ridge tantalum pentoxide waveguides with the same width, the Q – factor needs to be of the order 10^6. Quality factors could be improved by implementing an integrated Fabry – Pérot cavity [139], design optimisation [140], [141], and sidewall polishing to reduce scattering losses [131].

Chapter 5

Conclusions and Future Work

In this thesis, I reported my findings on active and passive components designated for photonic integrated circuits. The former refers to the membrane quantum well laser operating as a single cavity laser or laser array for potential use as a coherent light source and optical amplifier. The latter refers to the tantalum pentoxide linear waveguides and micro – ring and racetrack resonators with a rib cross – section for SC and Kerr frequency comb generation.

Membrane quantum well lasers are edge emitting epitaxially grown laser devices based on semiconductor materials, where lasing is possible due to population inversion occurring within the multiple quantum wells, the device's end facets, which form the laser cavity, and strong waveguiding due to the high refractive index contrast, air – MQWL – substrate, SiC or SiO_2. The waveguiding effect confines the laser's standing wave allowing for it to interact more with the QW energy states to induce stimulated emission. From the waveguide mode simulations, the intensity of the fundamental transverse electric and magnetic mode is concentrated in structure's centre, suggesting that a different QW design is in need. The new design would require the QWs to be closer to each other to overlap more with the guided modes and, hence, enhance stimulated emission and reduce laser threshold.

MQWLs were optically pumped to demonstrate its capabilities without introducing electrodes should they be co – packaged with optical waveguides. The devices were characterised with an OSA to record the CW laser spectrum, which is in the vicinity of $1\ \mu m$, and an imaging setup to capture real and reciprocal space images. The former gave information of the physical properties of the structure and pump spot, whereas the latter demonstrated the transition from spontaneous emission to stimulated emission as indicated by the appearance of an interference pattern. Temperature spectral tuning showed that whether the substrate is SiC or SiO_2 the rate of change of wavelength with respect to heat sink temperature is the same. This result suggests that despite the fact that SiC is more heat conductive, it comes down to the contact quality of the various heatsink components to extract excess heat. This finding increases the potential use of the MQWL in PICs on silicon – on – insulator (SOI) wafers.

Recorded threshold values reported in [22] and this thesis include $60\ mW$ for a $70\ \mu m$ laser cavity on SiC, $120\ mW$ for a $124\ \mu m$ laser cavity on SiO_2, $211\ mW$ for a $387\ \mu m$ laser cavity on SiO_2, and $309\ mW$ for a $424\ \mu m$ laser cavity on SiO_2, exhibiting a relatively linear behaviour

between laser threshold and cavity length. These values are significantly lower than the $0.7\ W$ threshold reported in [82] for the same QW design used for a MECSEL setup.

An attempt was made to fabricate various geometries in the cleanroom based on photolithography and wet etching such as linear cavities and micro resonators for WGMs. Although possible, wet etching was proved to be a poor choice as it gave rough end facets resulting in high laser and resonator losses. Reactive ion etching (RIE) was discussed as a potential dry etching method to define various geometries and provide near vertical sidewalls and relatively smooth surfaces [142], [143], [144].

MQWLs demonstrated an interesting feature, the ability of operating as phase – locked laser arrays extending their application range to power scaling. This was shown after recording the output power from a single cavity operation to multiple ones. For this, numerical simulations and experiments verified that cavities indeed operated on the same laser wavelengths otherwise they would not be coherent to interfere constructively. The numerical simulations and experiments also suggested mainly out – of – phase light coupling between cavities.

Pumping with a DMD unlocked the possibility to shape the pump spot to generate laser arrays from the same semiconductor device without varying the spatial optical gain making them also low – cost to fabricate. Light bridges were shown to assist in creating laser cavities in areas were no lasing occurred due to higher cavity losses and also affect the coupling phase. Simulations based on gain – guided lasers were developed to simulate optical gain and laser arrays. Although this was possible, more physical parameters must be included such as phase and time, and, in general, more understanding as the laser arrays can be complex and can become even more complex by introducing various pump geometry schemes.

My PhD work concluded with the inclusion of tantalum pentoxide linear waveguides and micro resonators with a rib cross – section, whose width is $1.5\ \mu m$ and etch depth $400\ nm$, to generate Kerr frequency combs based on both analytical and numerical models. The former simulated waveguiding and information such as effective refractive indices and effective areas for dispersion engineering and to insert in the numerical model to simulate comb generation. Based on those simulations, the optical passive components were fabricated in the cleanroom with both photolithography and e – beam lithography for comparison, which was followed by dry etching, annealing and silica deposition to clad the waveguides.

Optical losses were high at $1\ \mu m$ probe wavelength, which was supported by the absence of Kerr frequency combs and relatively low Q – factors with the highest ones reaching values of the order of 10^5 at $1.55\ \mu m$ probe wavelength. Kerr frequency combs produced by tantalum pentoxide ridge micro – rings with similar designs and processes have been previously reported in [56], where the Q – factor is of the order of 10^6. Although no significant differences were apparent from the photolithography and e – beam lithography chips, the fabrication process needs to be revisited to reduce losses, introduce end facet and sidewall polishing, and, also,

additional simulations and dispersion engineering is required to further investigate the possibility of generating Kerr frequency combs.

The final aim of my PhD was to couple light from a MQWL to tantalum pentoxide waveguides. This was not necessarily for SC or Kerr frequency comb generation, but rather for evaluating the application and performance of this laser as a waveguide light source whether it is operating as a single cavity or laser array (Figure 1.8). Methods of co – packaging the laser with the waveguides would include a corner reflector with a grating coupler, butt – coupling with or without a lens and placing it in an etched pit of the wafer [24]. Placing the MQWL gain chip on the substrate already proved to be a tedious feature as its positioning can be random making it difficult for characterisation and to use in applications. It would be interesting to explore the possibility of growing the device on the wafer or find other means to position it as desired [145] or even have it the QWs suspended in air [146]. This feature would result in a low – cost and faster PIC fabrication.

Laser arrays are crucial for power scaling [147], [148] and optical phased array technologies [149], [150], [151], [152], [153] and on – chip coupling laser arrays with optical waveguides has proven to be beneficial [154], [155], [156]. These technologies are both significant for utilisation in various applications. Some of those include photodynamic therapy [157], automotive LiDAR [158], optical interconnects [159], optical amplifiers [160], [161], [162], gas sensing [146] and spectral broadening [145].

As a final remark, membrane quantum well lasers, especially based on InGaAs, distinguish themselves from other edge emitting semiconductor lasers because of their ability to produce phase – locked arrays without making gain – guided devices. The optical source can be improved by adjusting the index contrast to strengthen waveguiding, and its design can be modified to bring closer the QWs and interact even more with the fundamental TE or TM guided mode to enhance population inversion and therefore, stimulated emission. Different MQWLs cross – sections can be explored such as rib waveguides and investigate their potential. These compact coherent light sources along with tantalum pentoxide waveguides and resonators or other materials such as silicon, could potentially improve the existing technology and be implemented in the various applications.

Appendix A

Cylindrical Lens Experimentation

This section involves uniformly pumping the MQWL with a line shaped laser profile created by a cylindrical lens. To understand the lens' properties, a He-Ne laser was used to observe the beam shape transformation. The laser's fundamental mode is circular, but when passing through a cylindrical lens, the profile shapes into a line. Cylindrical lenses have a plano - concave or plano - convex configuration, expand or focusing light respectively.

The following experiment was not applied to a membrane quantum well laser. Instead, a CCD camera was used to resemble a membrane device. In addition, the He-Ne laser represents the MQWL's pump diode laser. The laser beam goes through a pair of identical plano – convex lenses of $40\ mm$ focal length each, with one being placed on a translation stage as shown in Figure A.1. One lens focuses the beam and the other collimates it. The reason for this is to have control over the optimal intensity distribution on the end target, in my case the CCD. The cylindrical lens, which has an effective focal length of $10\ mm$, shapes the beam into a line (Figure A.2), which is collected by the aspheric lens of $10\ mm$ focal length. Light coming out of the latter passes through a reflective neutral density filter to avoid the CCD's saturation. Finally, the line is collected and focused by a plano – convex converging lens with $75\ mm$ focal length onto the CCD camera.

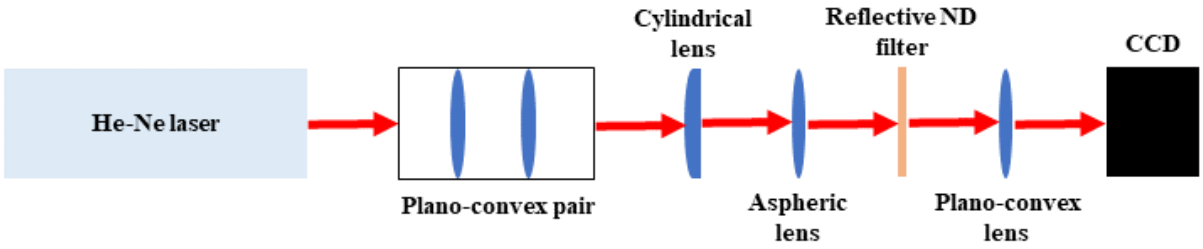

Figure A.1 Experimental setup of beam shaping with a cylindrical lens. The distance between the plano - convex lens pair is adjustable to optimise intensity on the CCD, with the first one focusing and the second collimating. The collimated laser beam transforms into a line by the cylindrical lens, which is then collected by an aspheric lens reducing distortions and spherical aberrations. The ND filter in turn dims the laser beam and is focused by a plano – convex lens onto the CCD camera.

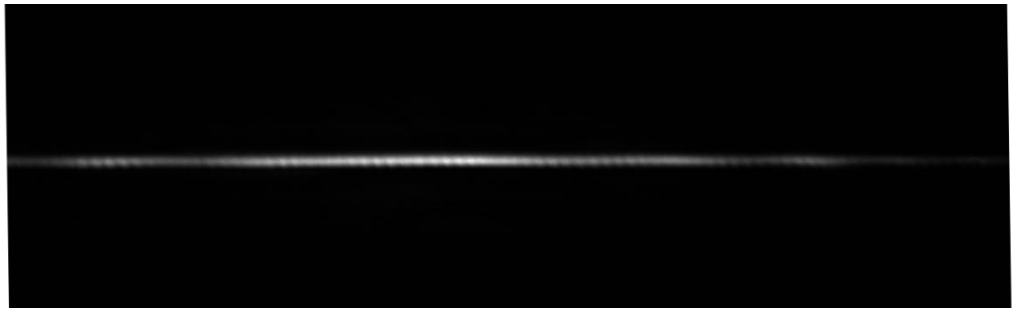

Figure A.2 The line shaped laser beam created by the cylindrical lens and captured by the CCD when the separation between the plano – convex lens pair is $12.4\ mm$.

I performed an experiment where I varied the relative position of the plano – convex lens pair to determine the optimal intensity of the line shaped laser beam leading to the intensity evolution presented in Figure A.3. I concluded that roughly twice the lens focal length corresponding to $12.4\ mm$ on the translation stage's screw gauge gave the maximum intensity distribution. After a Gaussian fit to that laser line profile, which matches it superbly (Figure A.4), I get that the optimum FWHM is $(3.65\ \pm\ 0.06)\ \mu m$.

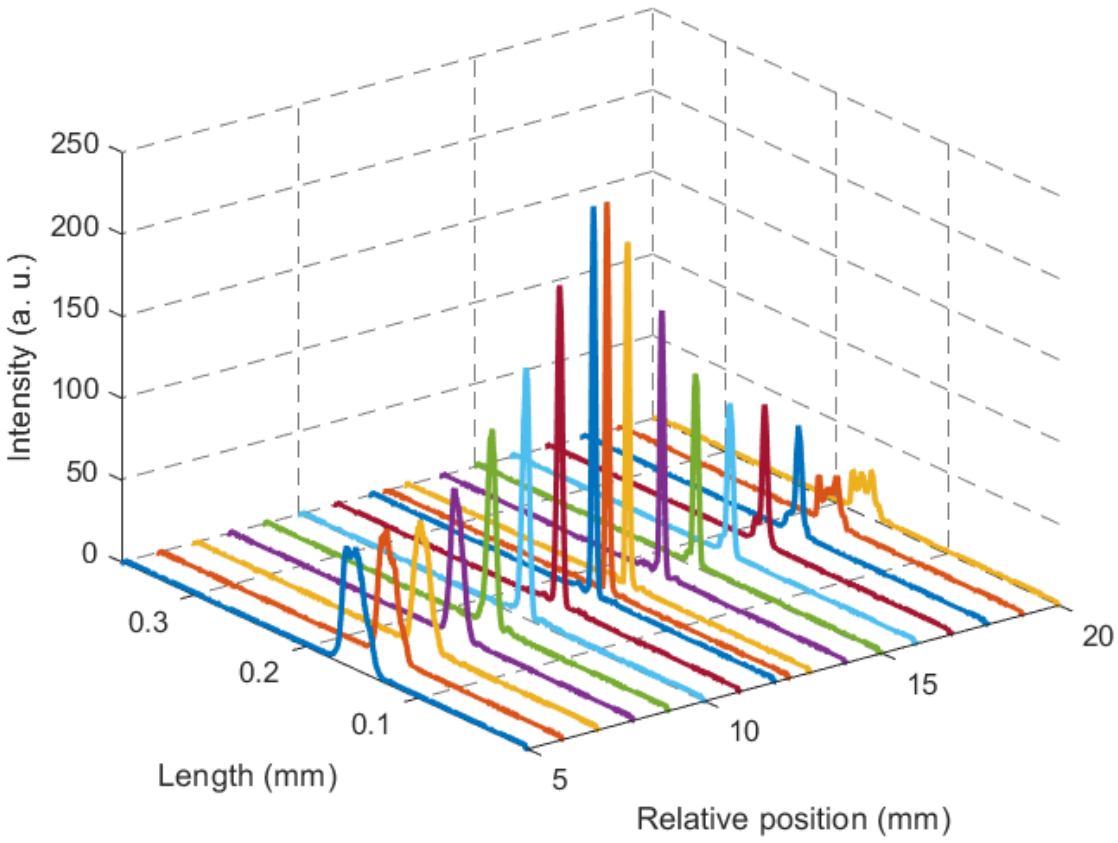

Figure A.3 Line shaped laser beam intensity evolution with respect to the plano – convex lens pair separation. At $12.4\ mm$ separation the laser line intensity is maximum. As that distance shortens or increases, the laser beam defocuses, where diffraction effects were more visible.

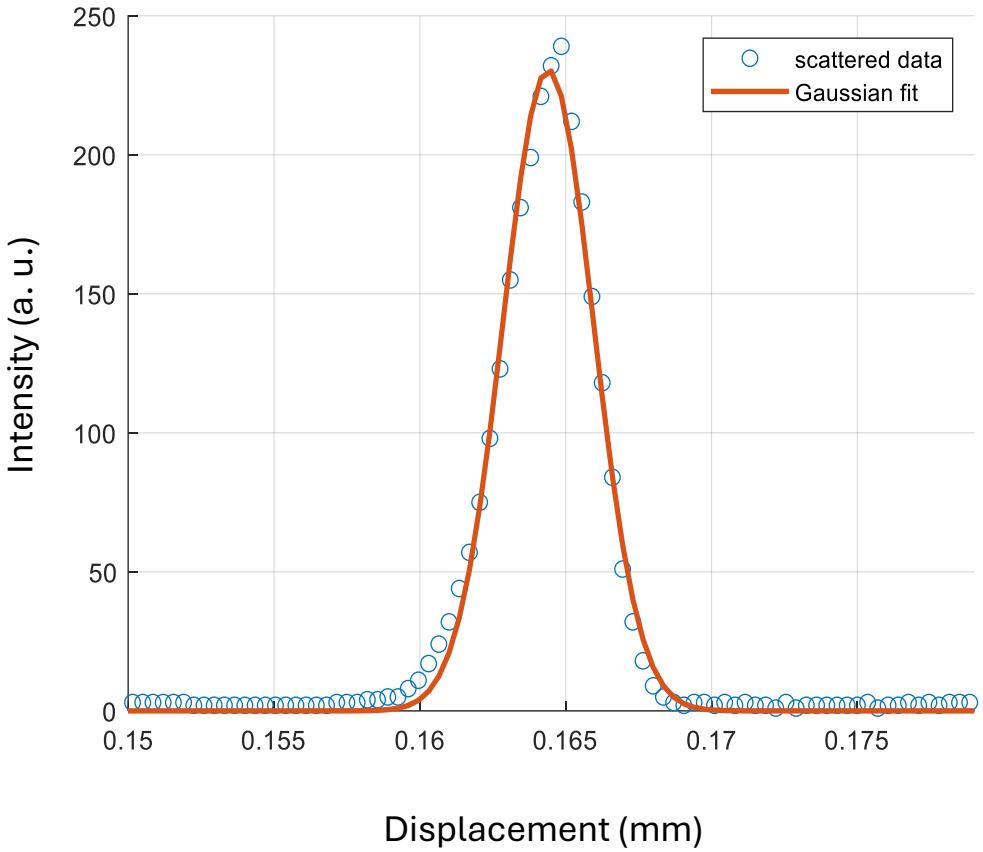

Figure A.4 Gaussian fit of the data retrieved from the maximum intensity profile corresponding to a $12.4\ mm$ separation between the plano – convex lens pair. The Gaussian normal distribution matches the line shaped laser beam profile giving a FWHM of $(3.65 \pm 0.06)\ \mu m$.

Appendix B

Axicon Lens Experimentation

Ring shaped laser beam formation with axicon lenses is of interest to pump MQWL microring resonators. The aim is to create laser ring profiles whose radius will match the micro resonator's radius. The axicon has a planar and a conical surface and transforms a laser beam into an annular beam (Figure B.1). The axicon initially focuses the beam rays, which in turn interfere within the overlap region called depth of focus (DOF). In DOF, the axicon replicates the properties of a Bessel beam or a beam comprised of rings (Figure B.2). After the DOF, the rays spread out resulting in Figure B.1.

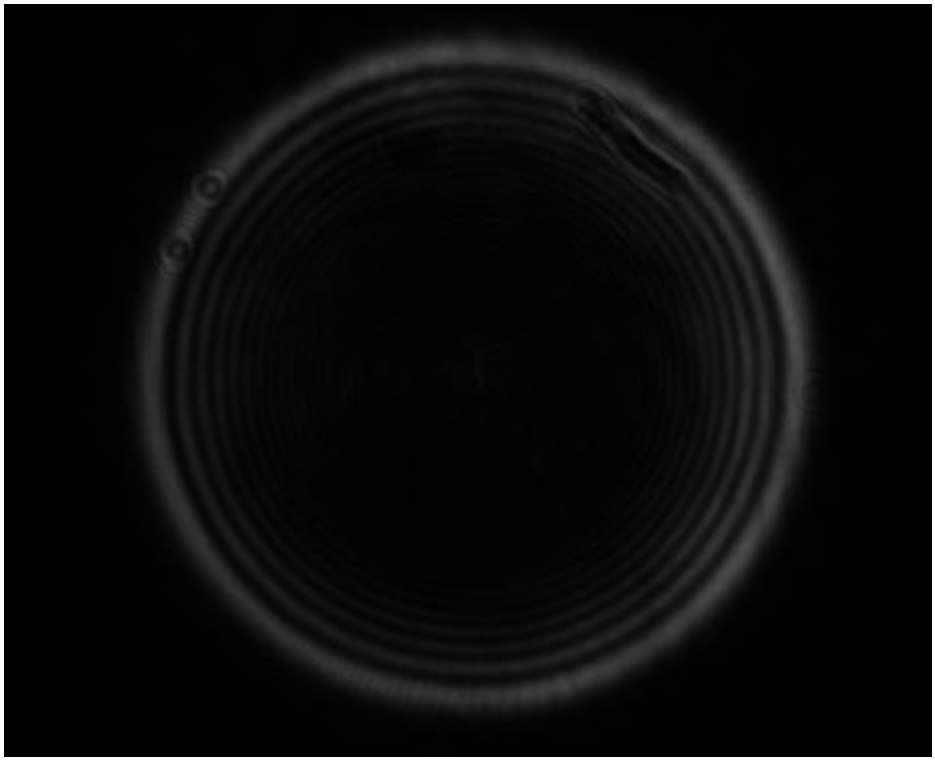

Figure B.1 Ring formation after a He – Ne laser beam propagates through an axicon lens.

A single axicon creates a ring whereas a second identical axicon would collimate it [163]. Beam shaping abilities of a single axicon and identical axicon pair were examined (Figure B.3) on a He-Ne laser beam emitting at $633\ nm$. The axicons are made of fused silica and have $5.0°$ and $2.3°$ physical and deflection angles respectively.

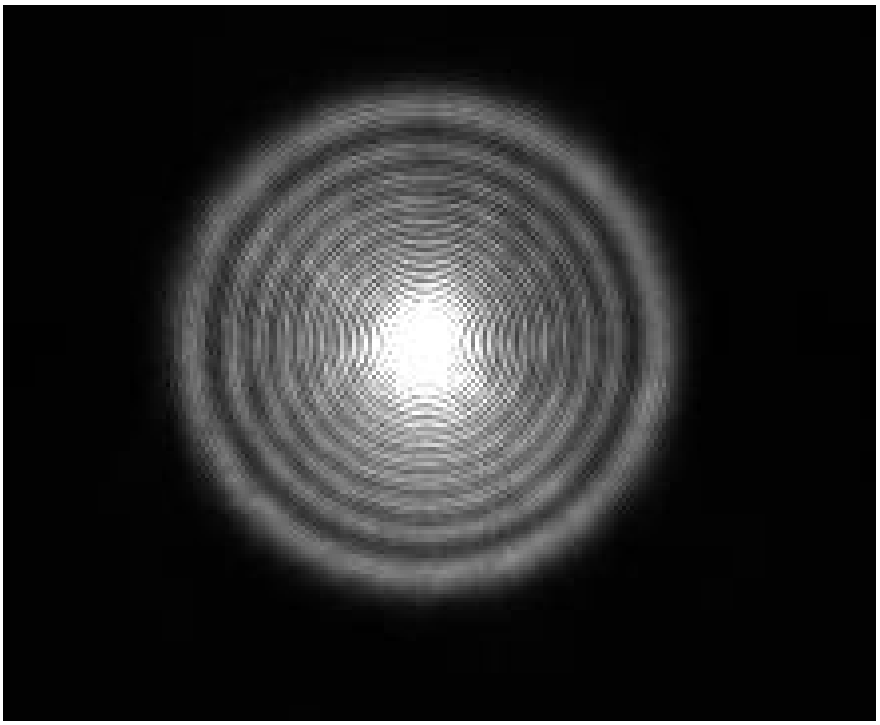

Figure B.2 The Bessel function profile of a He – Ne laser beam formed within the overlap region or DOF.

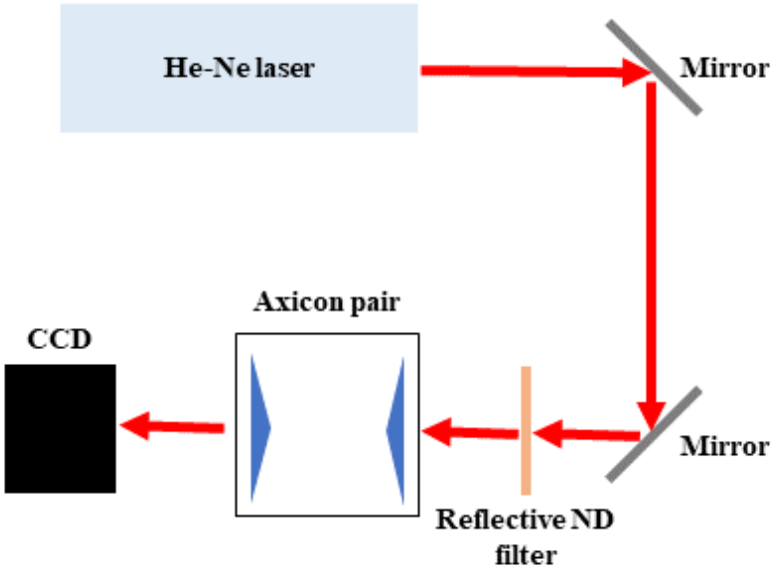

Figure B.3 Axicon lens experimental setup. The He – Ne laser beam is guided with two mirrors through a neutral density filter and two axicon lenses. A calibrated CCD is placed in front of the axicon lenses to capture the ring formation. The mirrors besides guiding, also align the laser beam vertically and horizontally. The ND filter is used to reduce laser power and avoid saturation on the CCD. The axicons create the rings. For my first experiments I only use one axicon.

To investigate the effect of the single axicon, images of ring beams were captured at different locations by varying the distance between the axicon's tip and a CCD. To investigate the effect of an identical axicon pair, the tips face each other, and their relative distance is varied. In addition, for fixed axicon separations, ring profiles were recorded for different CCD positions. Assuming a Gaussian profile, the beam's FWHM before deflection is required in both setups and was estimated at $(0.560 \pm 0.001)\, mm$.

In the case of a single axicon, a ring is formed (Figure B.1) after the laser beam is deflected and expands linearly at a constant rate of 0.0424 ± 0.0004 as the separation between axicon and CCD increases as presented in Figure B.4. Considering the axicon's material and physical angle, the theoretical ring radius is given by [164]:

$$R_r = 0.040089L \; (B.1)$$

Hence, the accuracy of my result is $5.76\ \%$ showing good agreement between experimental and theoretical value.

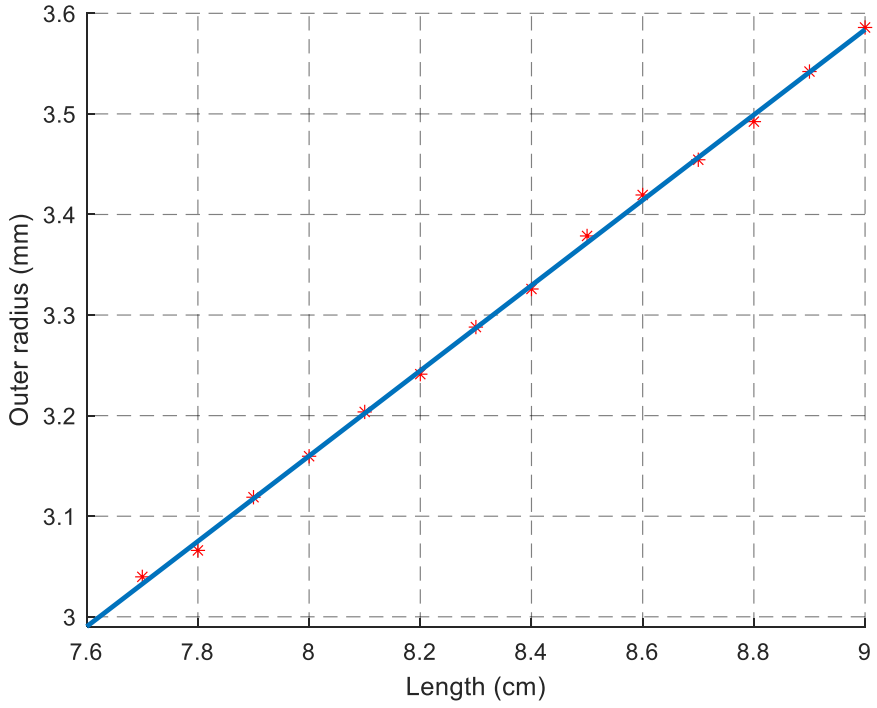

Figure B.4 Outer ring radius expansion with increasing distance between axicon and CCD. The outer ring radius growth is linear and with the appropriate fit matching the data well, giving a 0.0424 ± 0.0004 slope.

In regards of the double axicon configuration, the ring was focusing rather than collimating. This is expected as the beam diffracts upon exiting the laser head and continues to expand until it encounters an optical element. By applying Snell's law multiple times at a double axicon setup, the beam deflects and expands until it encounters the second axicon, at which it deflects again

and focuses as shown in Figure B.5. Before interacting with the axicons, the He – Ne laser lineshape FWHM increases linearly at a rate of $(1.1 \pm 0.2) \times 10^{-4}$ as shown in Figure B.6. In addition, the axicon's might have tip imperfections and their physical angle tolerance is $0.01°$ [163].

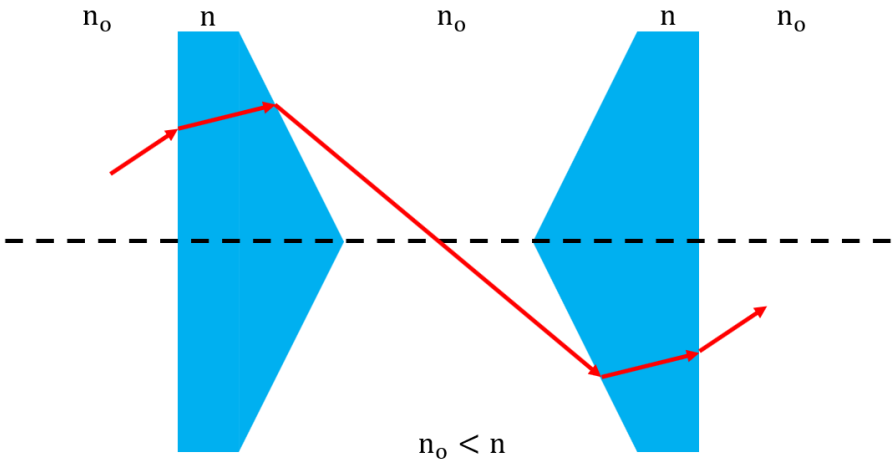

Figure B.5 He – Ne laser ray propagation through two identical axicon lenses. The laser beam deflects from the first axicon and then expands until it encounters the second axicon, which in turn deflects and focuses the beam.

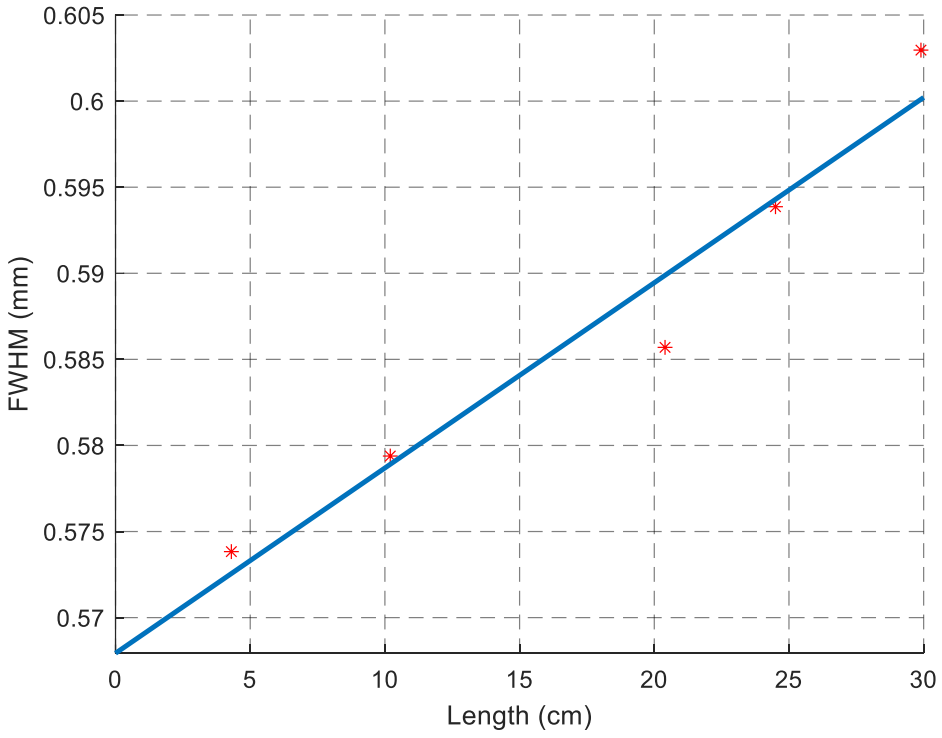

Figure B.6 He – Ne laser beam expansion with increasing distance before interacting with an axicon lens. The growth is linear and fitting to the data I receive a $(1.1 \pm 0.2) \times 10^{-4}$ rate.

The formed ring profiles are converging at a constant rate of roughly 0.002 for every axicon separation (Figure B.7), even when I switch their positions (Figure B.8). When the rings are focused, they start to replicate the Bessel function formed within the overlap region as seen in Figure B.2. With the given configuration, it seems impossible to achieve a clear ring profile at sub - mm radii and hence cannot pump a microring resonator waveguide.

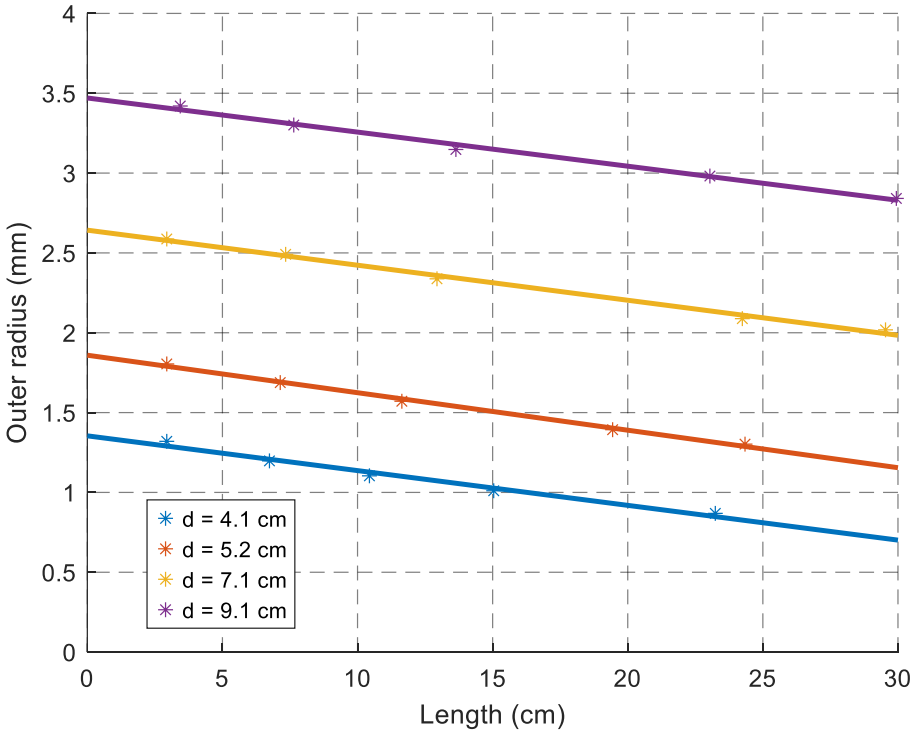

Figure B.7 The second axicon focuses the rings for fixed axicon lens separations. The rate of each linear decrease of the outer ring radius is on average 0.002.

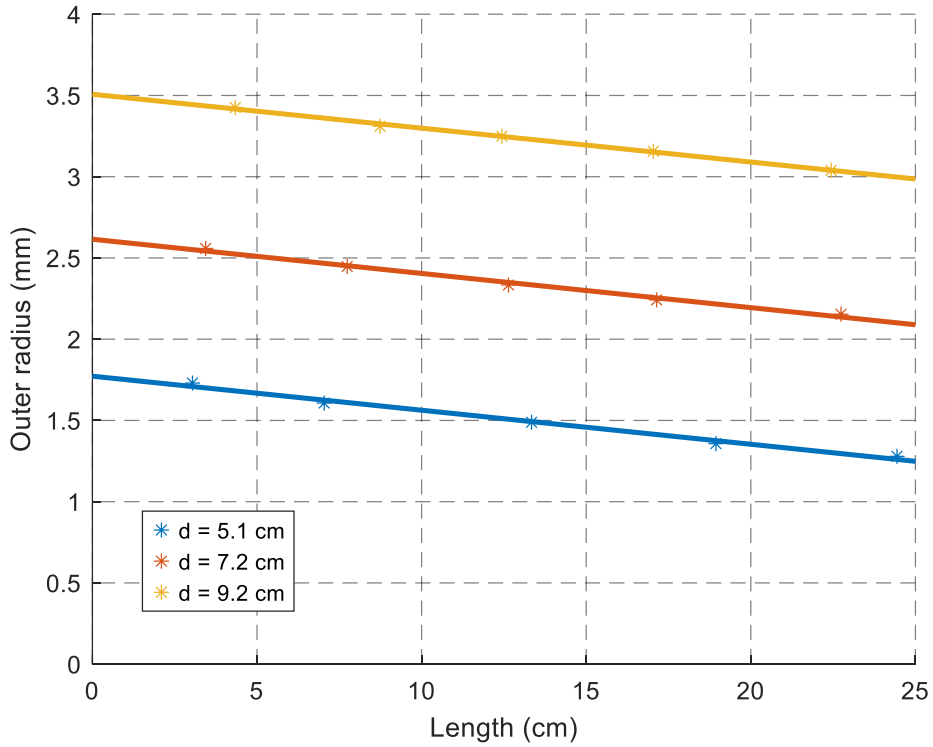

Figure B.8 Outer ring radius convergence after switching the axicon lens positions. As before, the second axicon focuses the rings down to a Bessel beam profile with a rate of approximately 0.002 at fixed lens positions.

Appendix C

Burnt Developer – Photoresist Removal

During my attempt to define microstructures on the membrane quantum well laser chips, I forgot to rinse the chip with deionised water after developing. Instead, after developing, I placed the chip on the hot plate for a few seconds for it to dry fast. However, this resulted in burning the developer and any photoresist residuals. I rinsed with water and then baked again at 115 ℃ for another few seconds. The final result is shown in Figure C.1.

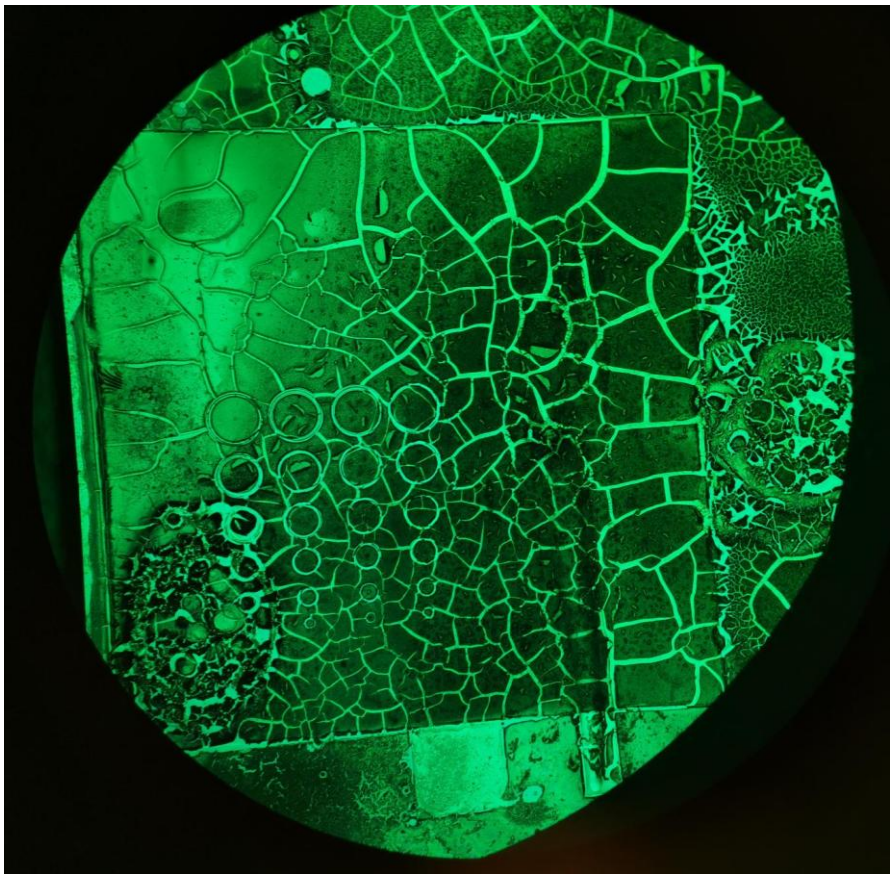

Figure C.1 Burnt developer and photoresist residuals on surface of membrane quantum well laser chip.

The MQWL chip featured in Figure C.1 cannot be processed any further in this state until its surface is cleaned. There were several options to do this, but only one worked in the end. The cleansing steps taken were as follows: (a) sonicate in deionised water bath at 80 ℃ for two hours

(Figure C.2a), (b) sonicate in acetone bath at 50 ℃ for $2\ hrs$ (Figure C.2b), as 56.5 ℃ is acetone's boiling point [165], (c) repeat the acetone bath for an additional two hours (Figure C.2c), (d) sonicate in a SVC – 14 photoresist stripper bath at 80 ℃ for $30\ min$ (Figure C.2d), and, finally, (e) use plasma asher for $10\ min$ at 125 ℃, $1000\ W$ of microwaves and $600\ mL/min$ oxygen flow (Figure C.2e). Although steps (a) – (d) managed to remove part of the burnt stains it was the plasma asher that ultimately cleaned the surface of the MQWL chip.

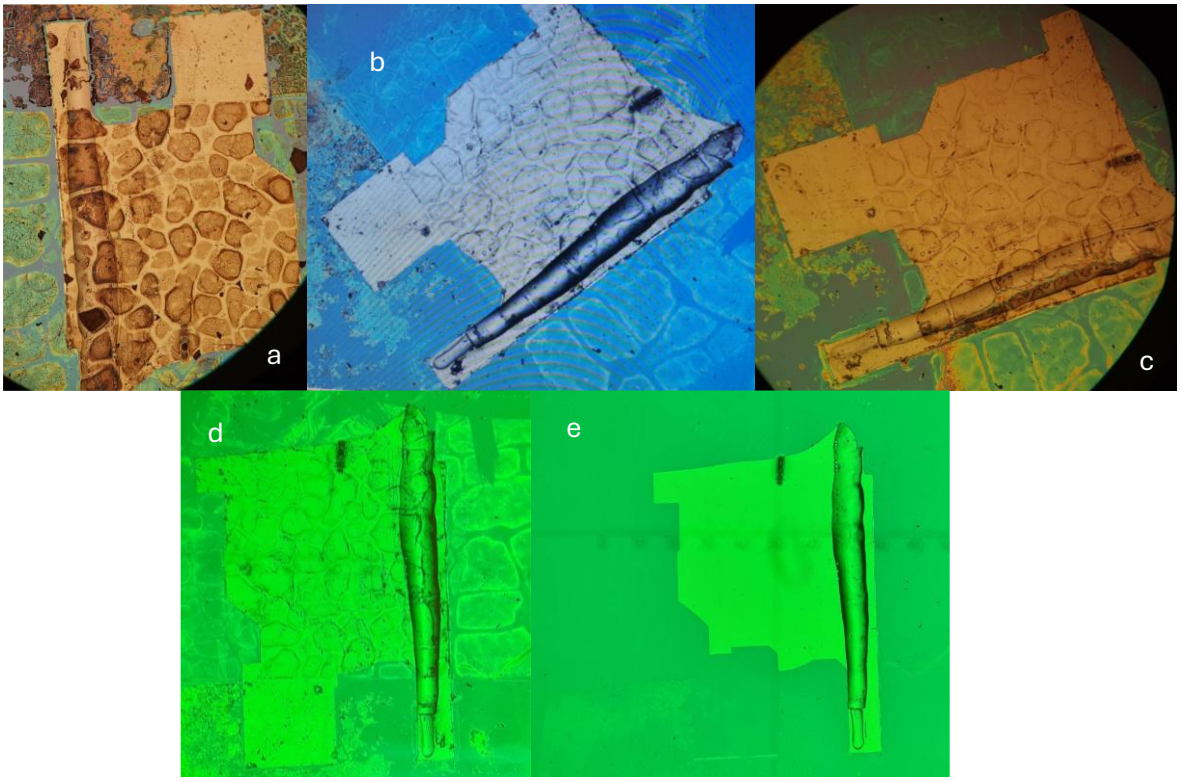

Figure C.2 The membrane gain medium after every cleaning process (a) sonication with deionised water, (b) sonication with acetone bath, (c) second sonication with acetone bath, (d) sonication with SVC – 14 bath, and (e) plasma ashing. The last process was effective to remove burnt developer and photoresist residuals on the surface of the membrane.

Appendix D

Cleanroom Equipment

Below I present a list of all the equipment I used in the cleanroom to process the MQWLs and fabricate the tantalum pentoxide waveguides and resonators.

1. Spin coater for photoresist deposition: SCS/G3P – 8 Resist Spinner
2. Mask aligner: Suss Microtec/ MA – 6 Mask Aligner
3. Developer bench: Lamarflo
4. Acid bench: Lamarflo
5. Plasma asher: PVA/Tepla 300
6. Reactive ion etcher: Oxford Instruments Plasma Technology (“OPT”)/Plasmalab80+
7. Ion beam milling: Oxford Instruments Plasma Technology (“OPT”)/Ionfab300+
8. Stylus profiler: KLA Tencor/Alpha Step IQ
9. Stylus profiler: KLA Tencor/16+
10. Thermal evaporator: BOC Edwards/E306a
11. SEM: Zeiss/EVO LS25, Oxford Instruments/INCA 250 EDX
12. Furnace: Severn Thermal Solutions/1200 °C Tube Furnace
13. Microscope: Nikon/LV150
14. Microscope: Nikon LV100D

List of References

[1] M. Jetter and P. Michler, *Vertical External Cavity Surface Emitting Lasers*. Wiley - VCH, 2021.

[2] A. C. Tropper, H. D. Foreman, A. Garnache, K. G. Wilcox, and S. H. Hoogland, "Vertical-external-cavity semiconductor lasers," *J Phys D Appl Phys*, vol. 37, no. 9, May 2004, doi: 10.1088/0022-3727/37/9/R01.

[3] U. Keller and A. C. Tropper, "Passively modelocked surface-emitting semiconductor lasers," *Phys Rep*, vol. 429, no. 2, pp. 67–120, Jun. 2006, doi: 10.1016/j.physrep.2006.03.004.

[4] O. Svelto, *Principles of lasers*. Springer US, 2010. doi: 10.1007/978-1-4419-1302-9.

[5] J. Wilson and J. Hawkes, *Optoelectronics an introduction*, 3rd ed. Prentice Hall, 1998.

[6] P. S. Zory Jr., *Quantum Well Lasers*. Academic Press, Inc., 1993.

[7] S. O. Kasap, *Electronic Materials & Devices*, 4th ed. McGraw - Hill Education, 2018.

[8] C. Weisbuch and J. Nagle, "The Physics of the Quantum Well Laser," *Phys Scr*, vol. 19, pp. 209–214, 1987.

[9] H.-P. Shiao, H.-Y. Lee, Y.-J. Lin, Y.-K. Tu, and C.-T. Lee, "Growth and Performance Study of Aluminum-Free InGaAs/GaAs/InGaAsP Strained Quantum-Well Pump Lasers," 2001.

[10] P. Zhang, "Structural optimization of quantum wells used in a 1-μm vertical-external-cavity surface-emitting laser," *J Nanophotonics*, vol. 5, no. 1, p. 059502, Jan. 2011, doi: 10.1117/1.3562569.

[11] R. E. Nahory, M. A. Pollack, W. D. Johnston, and R. L. Barns, "Band gap versus composition and demonstration of Vegard's law for In 1-xGaxAsyP1-y lattice matched to InP," *Appl Phys Lett*, vol. 33, no. 7, pp. 659–661, 1978, doi: 10.1063/1.90455.

[12] J. S. Blakemore, “Semiconducting and other major properties of gallium arsenide,” *J Appl Phys*, vol. 53, no. 10, 1982, doi: 10.1063/1.331665.

[13] P. Zhang, Y. Song, J. Tian, X. Zhang, and Z. Zhang, “Gain characteristics of the InGaAs strained quantum wells with GaAs, AlGaAs, and GaAsP barriers in vertical-external-cavity surface-emitting lasers,” *J Appl Phys*, vol. 105, no. 5, 2009, doi: 10.1063/1.3081974.

[14] Y. P. Varshni, “Temperature dependence of the energy gap in semiconductors,” *Physica*, vol. 34, pp. 149–154, 1967.

[15] H. Kahle *et al.*, “Semiconductor membrane external-cavity surface-emitting laser (MECSEL),” *Optica*, vol. 3, no. 12, p. 1506, Dec. 2016, doi: 10.1364/optica.3.001506.

[16]. S Lutgen, T. Albrecht, P. Brick, W. Reill, J. Luft, and W. Späth, “8-W high-efficiency continuous-wave semiconductor disk laser at 1000nm,” *Appl. Phys. Lett*, vol. 37, pp. 3620–3622, 2004, doi: 10.1364/OA_License_v1#VOR.

[17] L. Fan *et al.*, “Extended tunability in a two-chip VECSEL,” *IEEE Photonics Technology Letters*, vol. 19, no. 8, pp. 544–546, Apr. 2007, doi: 10.1109/LPT.2007.893898.

[18] Z. Yang, A. R. Albrecht, J. G. Cederberg, and M. Sheik-Bahae, “80 nm tunable DBR-free semiconductor disk laser,” *Appl Phys Lett*, vol. 109, no. 2, Jul. 2016, doi: 10.1063/1.4958164.

[19] M. Guina, A. Rantamäki, and A. Härkönen, “Optically pumped VECSELs: Review of technology and progress,” *J Phys D Appl Phys*, vol. 50, no. 38, Aug. 2017, doi: 10.1088/1361-6463/aa7bfd.

[20] C. Hessenius, M. Fallahi, J. Moloney, and R. Bedford, “Lateral lasing and ASE reduction in VECSELs,” in *Vertical External Cavity Surface Emitting Lasers (VECSELs)*, SPIE, Feb. 2011, p. 791909. doi: 10.1117/12.875595.

[21] C. Wang, K. Malloy, and M. Sheik-Bahae, “Influence of coulomb screening on lateral lasing in VECSELs,” *Opt Express*, vol. 23, no. 25, p. 32548, Dec. 2015, doi: 10.1364/oe.23.032548.

[22] J. R. C. Woods *et al.*, “Coherent waveguide laser arrays in semiconductor quantum well membranes,” *Opt Express*, vol. 30, no. 18, p. 32174, Aug. 2022, doi: 10.1364/oe.457577.

[23] L. J. Van Ruyven, “Double heterojunction lasers and quantum well lasers,” *J Lumin*, vol. 29, pp. 123–161, 1984.

[24] Lukas. Chrostowski and Michael. Hochberg, *Silicon photonics design : from devices to systems*. Cambridge University Press, 2016.

[25] J. M. Dudley, G. Genty, and S. Coen, “Supercontinuum generation in photonic crystal fiber,” *Rev Mod Phys*, vol. 78, no. 4, pp. 1135–1184, 2006, doi: 10.1103/RevModPhys.78.1135.

[26] G. P. Agrawal, *Nonlinear Fibre Optics*, 6th ed. Academic Press, 2019.

[27] P. Del’Haye, A. Schliesser, O. Arcizet, T. Wilken, R. Holzwarth, and T. J. Kippenberg, “Optical frequency comb generation from a monolithic microresonator,” *Nature*, vol. 450, no. 7173, pp. 1214–1217, Dec. 2007, doi: 10.1038/nature06401.

[28] T. J. Kippenberg, R. Holzwarth, and S. A. Diddams, “Microresonator-Based Optical Frequency Combs,” *Science (1979)*, vol. 332, Apr. 2011, [Online]. Available: www.sciencemag.org

[29] Y. K. Chembo, “Kerr optical frequency combs: Theory, applications and perspectives,” *Nanophotonics*, vol. 5, no. 2, pp. 214–230, Jun. 2016, doi: 10.1515/nanoph-2016-0013.

[30] W. Bogaerts *et al.*, “Silicon microring resonators,” *Laser Photon Rev*, vol. 6, no. 1, pp. 47–73, Jan. 2012, doi: 10.1002/lpor.201100017.

[31] Z. Li *et al.*, “Research on characteristics of racetrack resonant sensor based on diamond,” *Superlattices Microstruct*, vol. 134, Oct. 2019, doi: 10.1016/j.spmi.2019.106237.

[32] J. M. Choi, R. K. Lee, and A. Yariv, “Control of critical coupling in a ring resonator-fiber configuration: application to wavelength-selective switching, modulation, amplification, and oscillation,” *Opt Lett*, vol. 26, no. 16, 2001.

[33] A. Yariv, “Critical Coupling and Its Control in Optical Waveguide-Ring Resonator Systems,” *IEEE PHOTONICS TECHNOLOGY LETTERS*, vol. 14, no. 4, p. 483, 2002.

[34] S. Darmawan and M. K. Chin, “Critical coupling, oscillation, reflection, and transmission in optical waveguide-ring resonator systems,” *J. Opt. Soc. Am. B*, vol. 23, no. 5, pp. 834–841, May 2006.

[35] M. Bahadori *et al.*, “Design Space Exploration of Microring Resonators in Silicon Photonic Interconnects: Impact of the Ring Curvature”.

[36] J. Pfeifle *et al.*, “Coherent terabit communications with microresonator Kerr frequency combs,” *Nat Photonics*, vol. 8, no. 5, pp. 375–380, 2014, doi: 10.1038/nphoton.2014.57.

[37] L. Lundberg *et al.*, “Frequency Comb-Based WDM transmission systems enabling joint signal processing,” *Applied Sciences (Switzerland)*, vol. 8, no. 5, May 2018, doi: 10.3390/app8050718.

[38] P. Trocha *et al.*, “Ultrafast optical ranging using microresonator soliton frequency combs,” *Science (1979)*, vol. 359, pp. 887–891, Feb. 2018, [Online]. Available: http://science.sciencemag.org/

[39] N. Kuse and M. E. Fermann, “Frequency-modulated comb LIDAR,” *APL Photonics*, vol. 4, no. 10, Oct. 2019, doi: 10.1063/1.5120321.

[40] S. N. Frequency Comb and T. W. Picqué, “Nathalie Picqué and Theodor W. Hänsch, Frequency comb spectroscopy,” *Nat Photonics*, vol. 13, pp. 146–157, 2019, doi: 10.1038/s41566--018--0347--5.

[41] L. Stern *et al.*, “Direct Kerr frequency comb atomic spectroscopy and stabilization,” 2020. [Online]. Available: https://www.science.org

[42] S. Coen, H. G. Randle, T. Sylvestre, and M. Erkintalo, “Modeling of octave-spanning Kerr frequency combs using a generalized mean-field Lugiato-Lefever model,” *Opt Lett*, vol. 38, no. 1, 2007.

[43] J. R. C. Woods *et al.*, “Supercontinuum generation in tantalum pentoxide waveguides for pump wavelengths in the 900 nm to 1500 nm spectral region,” *Opt Express*, vol. 28, no. 21, p. 32173, Oct. 2020, doi: 10.1364/oe.403089.

[44] L. A. Lugiato and R. Lefever, “Spatial Dissipative Structures in Passive Optical Systems,” 1987.

[45] C. Chaneliere, J. L. Autran, R. A. B. Devine, and B. Balland, “Tantalum pentoxide (Ta2O5) thin films for advanced dielectric applications,” 1998.

[46] A. S. Pavlovic, “Some dielectric properties of tantalum pentoxide,” *J Chem Phys*, vol. 40, no. 4, pp. 951–956, 1964, doi: 10.1063/1.1725287.

[47] P. Rabiei, A. Rao, J. Chiles, J. Ma, and S. Fathpour, “Low-loss and high index-contrast tantalum pentoxide microring resonators and grating couplers on silicon substrates,” *Opt Lett*, vol. 39, no. 18, p. 5379, Sep. 2014, doi: 10.1364/ol.39.005379.

[48] M. Itoh, T. Kominato, M. Abe, M. Itoh, and T. Hashimoto, “Low-loss silica-based SiO2-Ta2O5 waveguides with extremely high Δ fabricated using sputtered thin films,” *Journal of Lightwave Technology*, vol. 33, no. 2, pp. 318–323, Jan. 2015, doi: 10.1109/JLT.2014.2381644.

[49] C. Lacava, A. Aghajani, P. Hua, D. J. Richardson, P. Petropoulos, and J. S. Wilkinson, “Nonlinear optical properties of ytterbium-doped tantalum pentoxide rib waveguides on silicon at telecom wavelengths,” in *Optical Fiber Communication Conference*, Optica Publishing Group, Mar. 2016. doi: 10.5258/SOTON/382841.

[50] M. Belt, M. L. Davenport, J. E. Bowers, and D. J. Blumenthal, “Ultra-low-loss Ta_2O_5-core/SiO_2-clad planar waveguides on Si substrates,” *Optica*, vol. 4, no. 5, p. 532, May 2017, doi: 10.1364/optica.4.000532.

[51] C. Wu, X. Ding, Z. Wu, and S. Feng, “High repetition rate flat coherent optical frequency comb generation based on the normal dispersion tantalum pentoxide optical waveguide,” *OSA Contin*, vol. 2, no. 9, p. 2704, Sep. 2019, doi: 10.1364/osac.2.002704.

[52] J. D. Traylor Kruschwitz and W. T. Pawlewicz, “Optical and durability properties of infrared transmitting thin films,” *AppliedOptics*, vol. 36, no. 10, pp. 2157–2159, Apr. 1997.

[53] S. Boughaba, G. I. Sproule, J. P. Mccaffrey, M. Islam, and M. J. Graham, “Synthesis of tantalum pentoxide films by pulsed laser deposition: material characterization and scale-up,” *Thin Solid Films*, vol. 358, pp. 104–113, Sep. 1999, [Online]. Available: www.elsevier.com/locate/tsf

[54] H. Kanamori, H. Yokota, G. Tanaka, M. Watanabe, Y. Asano, and S. Tanaka, “Transmission Characteristics and Reliability of Pure-Silica-Core Single-Mode Fibers,” *JOURNAL OF LIGHTWAVE TECHNOLOGY*, no. 8, 1986.

[55] A. J. Maker and A. M. Armani, “Low-loss silica-on-silicon waveguides,” *Opt Lett*, vol. 36, no. 19, pp. 3729–3731, Sep. 2011.

[56] H. Jung, S.-P. Yu, D. R. Carlson, T. E. Drake, T. C. Briles, and S. B. Papp, "Tantala Kerr nonlinear integrated photonics," *Optica*, vol. 8, no. 6, p. 811, Jun. 2021, doi: 10.1364/optica.411968.

[57] T. J. Bright *et al.*, "Infrared optical properties of amorphous and nanocrystalline Ta 2O5 thin films," *J Appl Phys*, vol. 114, no. 8, Aug. 2013, doi: 10.1063/1.4819325.

[58] I. H. Malitson, "Interspecimen Comparison of the Refractive Index of Fused Silica*t," *J Opt Soc Am*, vol. 55, no. 10, pp. 1205–1209, Oct. 1965.

[59] A. K. Chu, H. C. Lin, and W. H. Cheng, "Temperature Dependence of of Ta205 Dielectric Films Refractive Index," *J Electron Mater*, vol. 26, no. 8, 1997.

[60] A. Arbabi and L. L. Goddard, "Measurements of the refractive indices and thermo-optic coefficients of Si3N4 and SiOx using microring resonances," *Opt Lett*, vol. 38, no. 19, pp. 3878–3881, Sep. 2013.

[61] J. Komma, C. Schwarz, G. Hofmann, D. Heinert, and R. Nawrodt, "Thermo-optic coefficient of silicon at 1550 nm and cryogenic temperatures," *Appl Phys Lett*, vol. 101, no. 4, Jul. 2012, doi: 10.1063/1.4738989.

[62] C.-Y. Tai *et al.*, "Determination of nonlinear refractive index in a Ta2O5 rib waveguide using self-phase modulation," *Opt Express*, vol. 12, no. 21, Oct. 2004, doi: 10.1364/OA_License_v1#VOR.

[63] R. Y. Chen, M. D. B. Charlton, and P. G. Lagoudakis, "Chi 3 dispersion in planar tantalum pentoxide waveguides in the telecommunications window," *Opt Lett*, vol. 34, no. 7, pp. 1135–1137, Apr. 2009.

[64] A. S. Tong, F. Bondu, G. Senthil Murugan, J. S. Wilkinson, and M. Dussauze, "Effect of sodium addition and thermal annealing on second-order optical nonlinearity in thermally poled amorphous Ta2O5 thin films," *J Appl Phys*, vol. 125, no. 1, Jan. 2019.

[65] L. Jensen, M. Mende, S. Schrameyer, M. Jupé, and D. Ristau, "Role of two-photon absorption in Ta2O5 thin films in nanosecond laser-induced damage," *Opt Lett*, vol. 37, no. 20, Oct. 2012.

[66] E. W. Van Stryland, M. A. Woodall, H. Vanherzeele, and M. J. Soileau, "Energy band-gap dependence of two-photon absorption," *Opt Lett*, vol. 10, no. 10, pp. 490–492, Oct. 1985.

[67] A. Z. Subramanian, C. J. Oton, D. P. Shepherd, and J. S. Wilkinson, “Erbium-doped waveguide laser in tantalum pentoxide,” *IEEE Photonics Technology Letters*, vol. 22, no. 21, pp. 1571–1573, 2010, doi: 10.1109/LPT.2010.2072495.

[68] A. Aghajani, G. S. Murugan, N. P. Sessions, S. J. Pearce, V. Apostolopoulos, and J. S. Wilkinson, “Spectroscopy of ytterbium-doped tantalum pentoxide rib waveguides on silicon,” *Opt Mater Express*, vol. 4, no. 8, p. 1505, Aug. 2014, doi: 10.1364/ome.4.001505.

[69] A. Aghajani, G. S. Murugan, N. P. Sessions, V. Apostolopoulos, and J. S. Wilkinson, “Waveguide lasers in ytterbium-doped tantalum pentoxide on silicon,” *Opt Lett*, vol. 40, no. 11, p. 2549, Jun. 2015, doi: 10.1364/ol.40.002549.

[70] B. Unal *et al.*, “Neodymium-doped tantalum pentoxide waveguide lasers,” *IEEE J Quantum Electron*, vol. 41, no. 12, pp. 1565–1573, Dec. 2005, doi: 10.1109/JQE.2005.858775.

[71] A. S. K. Tong *et al.*, “Spectroscopy of thulium-doped tantalum pentoxide waveguides on silicon,” *Opt Mater Express*, vol. 10, no. 9, p. 2201, Sep. 2020, doi: 10.1364/ome.397011.

[72] K. Schmitt, K. Oehse, G. Sulz, and C. Hoffmann, “Evanescent field Sensors Based on Tantalum Pentoxide Waveguides – A Review,” *Sensors*, vol. 8, pp. 711–738, 2008, [Online]. Available: www.mdpi.org/sensors

[73] C. Zhang *et al.*, “Tantalum pentoxide: a new material platform for high-performance dielectric metasurface optics in the ultraviolet and visible region,” *Light Sci Appl*, vol. 13, no. 1, Dec. 2024, doi: 10.1038/s41377-023-01330-z.

[74] P. K. Tien, “Integrated optics and new wave phenomena in optical wave guides,” *Rev Mod Phys*, vol. 49, no. 2, pp. 361–420, Apr. 1977.

[75] M. Pollnau and Y. E. Romanyuk, “Optical waveguides in laser crystals,” *C R Phys*, vol. 8, no. 2, pp. 123–137, Mar. 2007, doi: 10.1016/j.crhy.2006.04.002.

[76] J. I. Mackenzie, “Dielectric Solid-State Planar Waveguide Lasers: a Review,” *IEEE Journal of Selected Topics in Quantum Electronics*, vol. 13, no. 3, pp. 626–637, Jun. 2007.

[77] M. Jelínek, “Functional planar thin film optical waveguide lasers,” *Laser Phys Lett*, vol. 9, no. 2, pp. 91–99, Feb. 2012, doi: 10.1002/lapl.201110098.

[78] J. J. Degnan, “The Waveguide Laser: A Review,” 1976.

[79] T. L. Koch *et al.*, “Waveguide InGaAs/InGaAsP Multiple-Quantum-Well Lasers,” *IEEE Photonics Technology Letters*, vol. 2, no. 2, pp. 88–90, Feb. 1990.

[80] J. P. Donnelly *et al.*, “AlGaAs-InGaAs slab-coupled optical waveguide lasers,” *IEEE J Quantum Electron*, vol. 39, no. 2, pp. 289–298, Feb. 2003, doi: 10.1109/JQE.2002.807200.

[81] J. Yang, Z. Mi, and P. Bhattacharya, “Groove-coupled InGaAs/GaAs quantum dot laser/waveguide on silicon,” *Journal of Lightwave Technology*, vol. 25, no. 7, pp. 1826–1831, 2007, doi: 10.1109/JLT.2007.899165.

[82] S. Mirkhanov *et al.*, “DBR-free semiconductor disc laser on SiC heatspreader emitting 10.1 W at 1007 nm,” *Electronic Letters*, vol. 53, no. 23, pp. 1537–1539, Nov. 2017, doi: 10.15132/10000126.

[83] K. Watanabe, Y. Wang, H. Sodabanlu, M. Sugiyama, and Y. Nakano, “Strain effect for different phosphorus content of InGaAs/GaAsP super-lattice in GaAs p-i-n single junction solar cell,” *J Cryst Growth*, vol. 401, pp. 712–716, Sep. 2014, doi: 10.1016/j.jcrysgro.2014.02.053.

[84] J. Daykin, “Supercontinuum and Frequency Comb Generation in Tantalum Pentoxide Waveguides,” University of Southampton, 2024.

[85] H. J. . Pain, *The physics of vibrations and waves*. John Wiley, 20082005.

[86] P. Blood, *Quantum Confined Laser Devices: Optical gain and recombination in semiconductors*. Oxford University Press, 2015.

[87] Y. Ishitani, “Temperature dependence of recombination processes of photogenerated carriers in a quantum-well structure,” *J Appl Phys*, vol. 86, no. 12, pp. 6816–6821, 1999, doi: 10.1063/1.371730.

[88] D. Botez and D. E. Ackley, “Phase-Locked Arrays of Semiconductor Diode Lasers,” *IEEE Circuits and Devices Magazine*, vol. 2, no. 1, pp. 8–17, 1986, doi: 10.1109/MCD.1986.6311765.

[89] G. P. Agrawal, “Lateral-mode analysis of gain-guided and index-guided semiconductor-laser arrays,” *J Appl Phys*, vol. 58, no. 8, pp. 2922–2931, 1985, doi: 10.1063/1.335840.

[90] M. Spreemann, B. Eppich, F. Schnieder, H. Wenzel, and G. Erbert, “Modal behavior, spatial coherence, and beam quality of a high-power gain-guided laser array,” *IEEE J Quantum Electron*, vol. 46, no. 11, pp. 1619–1625, 2010, doi: 10.1109/JQE.2010.2055044.

[91] Sadao Adachi, *Physical Properties of III-V Semiconductor Compounds*. John Wiley & Sons, 1992.

[92] B. Brocklesby, “Lecture Notes in Lasers, MSc Optical Fibre and Photonic Engineering,” 2019, *University of Southampton*.

[93] E. D. Pierron, D. L. Parker, and J. B. McNeely, “Coefficient of expansion of GaAs, GaP, and Ga(As, P) compounds from -62°to 200°C,” *J Appl Phys*, vol. 38, no. 12, pp. 4669–4671, 1967, doi: 10.1063/1.1709201.

[94] G. A. Slack, “Thermal conductivity of pure and impure silicon, silicon carbide, and diamond,” *J Appl Phys*, vol. 35, no. 12, pp. 3460–3466, 1964, doi: 10.1063/1.1713251.

[95] “21 Semiconductors,” https://www.21semiconductors.com/.

[96] “BATOP GmbH,” https://batop.de/.

[97] G. D. Clark Jr and N. Holonyak Jr, “Optical Properties of Gallium Arsenide-Phosphide,” *Physical Review*, vol. 156, no. 3, pp. 913–924, Apr. 1967.

[98] S. Singh, J. R. Potopowicz, L. G. Van Uitert, and S. H. Wemple, “Nonlinear optical properties of hexagonal silicon carbide,” *Appl Phys Lett*, vol. 19, no. 3, pp. 53–56, 1971, doi: 10.1063/1.1653819.

[99] A. Sollberger, A. Heinamaki, and H. Melchior, “Frequency Stabilization of Semiconductor Lasers for Applications in Coherent Communication Systems,” *JOURNAL OF LIGHTWAVE TECHNOLOGY*, no. 4, 1987.

[100] Z. Fang, H. Cai, G. Chen, and R. Qu, *Single Frequency Semiconductor Lasers*. Springer, 2017. [Online]. Available: http://www.springer.com/series/4810

[101] D. Botez, “Single mode lasers for optical communications,” *Future Trends in Fiber Optic Communications*, vol. 340, pp. 32–49, 1982, [Online]. Available: http://spiedl.org/terms

[102] G. P. Agrawal, “Longitudinal-mode stabilization in semiconductor lasers with wavelength-selective feedback,” *J Appl Phys*, vol. 59, no. 12, pp. 3958–3961, 1986, doi: 10.1063/1.336696.

[103] D. Dudley, W. Duncan, and J. Slaughter, “Emerging Digital Micromirror Device (DMD) Applications DLP TM Products New Applications,” 2003.

[104] G. Gauthier, T. A. Bell, A. B. Stilgoe, M. Baker, H. Rubinsztein-Dunlop, and T. W. Neely, “Dynamic high-resolution optical trapping of ultracold atoms,” in *Advances in atomic, molecular, and optical physics*, vol. 70, Academic Press, 2021, ch. 1, pp. 1–101. doi: 10.1016/bs.aamop.2021.04.001.

[105] C. Pereira, M. Abreu, A. Cabral, and J. M. Rebordão, “Characterization of Light Diffraction by a Digital Micromirror Device,” in *Journal of Physics: Conference Series*, Institute of Physics, 2022. doi: 10.1088/1742-6596/2407/1/012048.

[106] “Texas Instruments DLP 4500, DLP4500 data sheet, product information and support,” https://www.ti.com/product/DLP4500.

[107] C. C. Huang, Y. S. Su, and C. F. Lin, “Investigation of laser-mode anticompetition in semiconductor lasers,” *IEEE J Quantum Electron*, vol. 41, no. 1, pp. 1–8, Jan. 2005, doi: 10.1109/JQE.2004.838168.

[108] J. Katz, S. Margalit, and A. Yariv, “Diffraction coupled phase-locked semiconductor laser array,” *Appl Phys Lett*, vol. 42, no. 7, pp. 554–556, 1983, doi: 10.1063/1.94025.

[109] P. Verly, R. Tremblay, and D. Marcuse, “Computer Simulation of Laser Photon Fluctuations: Theory of Single-Cavity Laser,” *Physics of Semiconductor Laser Devices*, vol. 20, no. 10, pp. 1218–1221, 1984.

[110] D. Marcuse, “Computer Simulation of Laser Photon Fluctuations: Coupled-Cavity Lasers,” *IEEE J Quantum Electron*, vol. QE-21, no. 2, pp. 154–161, Feb. 1985.

[111] Z. Jiang and M. Mccall, “Numerical simulation of a large number of coupled lasers,” *J. Opt. Soc. Am. B*, vol. 10, no. 1, pp. 155–163, Jan. 1993.

[112] S. Yanchuk, A. Stefanski, T. Kapitaniak, and J. Wojewoda, “Dynamics of an array of mutually coupled semiconductor lasers,” *Phys Rev E Stat Nonlin Soft Matter Phys*, vol. 73, no. 1, Jan. 2006, doi: 10.1103/PhysRevE.73.016209.

[113] M. B. Spencer and W. E. Lamb, “Theory of Two Coupled Lasers,” *Phys Rev A (Coll Park)*, vol. 5, no. 2, pp. 893–898, Feb. 1972.

[114] D. Marcuse, “Coupling Coefficients of Coupled Laser Cavities,” *IEEE J Quantum Electron*, vol. 22, no. 2, 1986.

[115] S. Wang and H. G. Winful, “Dynamics of phase-locked semiconductor laser arrays,” *Appl. Phys. Lett.*, vol. 52, no. 21, pp. 1774–1776, Mar. 1988.

[116] W. G. Daniel, “Numerical Simulations of Gain and Power of a Multi-Quantum Well Laser,” in *2021 SBFoton International Optics and Photonics Conference: Keep on Shining, SBFoton IOPC 2021*, Institute of Electrical and Electronics Engineers Inc., May 2021. doi: 10.1109/SBFotonIOPC50774.2021.9461970.

[117] Y. Okawachi, K. Saha, J. S. Levy, Y. H. Wen, M. Lipson, and A. L. Gaeta, “Octave-spanning frequency comb generation in a silicon nitride chip,” *Opt Lett*, vol. 36, no. 17, pp. 3398–3400, Sep. 2011.

[118] I. S. Grudinin, L. Baumgartel, and N. Yu, “Frequency comb from a microresonator with engineered spectrum,” *Opt Express*, vol. 20, no. 6, pp. 6604–6609, 2012.

[119] L. E. Hooper, P. J. Mosley, A. C. Muir, W. J. Wadsworth, and J. C. Knight, “Coherent supercontinuum generation in photonic crystal fiber with all-normal group velocity dispersion,” *Opt Express*, vol. 19, no. 6, pp. 4902–4907, Mar. 2011.

[120] M. A. Hossain *et al.*, “Tailoring supercontinuum generation using highly nonlinear photonic crystal fiber,” *Opt Laser Technol*, vol. 44, no. 6, pp. 1889–1896, Sep. 2012, doi: 10.1016/j.optlastec.2012.01.029.

[121] W. J. Tomlinson, R. H. Stolen, and A. M. Johnson, “Optical wave breaking of pulses in nonlinear optical fibers,” *Opt Lett*, vol. 10, no. 9, 1985.

[122] C. Finot, B. Kibler, L. Provost, and S. Wabnitz, “Beneficial impact of wave-breaking for coherent continuum formation in normally dispersive nonlinear fibers,” *J. Opt. Soc. Am. B*, vol. 25, no. 11, pp. 1938–1948, Nov. 2008.

[123] “FiveNine Optics, FiveNine Optics – Boulder, Colorado | R > 99.999%.” Accessed: May 28, 2025. [Online]. Available: https://www.fivenineoptics.com/

[124] “IBE, Oxford Instruments, Ion Beam Etching & Milling (IBE) - Oxford Instruments.” Accessed: May 28, 2025. [Online]. Available: https://plasma.oxinst.com/technology/ion-beam-etching

[125] A. Aghajani, “Waveguide Lasers in Ytterbium Doped Tantalum Pentoxide for Integrated Photonic Circuits,” University of Southampton, 2015.

[126] “Diode Laser Controller, MOGlabs.” Accessed: May 28, 2025. [Online]. Available: https://www.moglabs.com/products/electronics/laser-electronics/diode-laser-controller

[127] “Tunable Littrow Lasers, MOGlabs.” Accessed: May 28, 2025. [Online]. Available: https://www.moglabs.com/products/lasers/tunable-lasers/ldl

[128] R. W. Beatty, “Insertion Loss Concepts,” in *Proceedings of the IEEE*, Jun. 1964, pp. 663–671.

[129] R. G. Hunsperger, *Integrated Optics Theory and Technology*, 6th ed. Springer, 2009.

[130] K. P. Yap *et al.*, “Correlation of Scattering Loss, Sidewall Roughness and Waveguide Width in Silicon-on-Insulator (SOI) Ridge Waveguides,” *Journal of Lightwave Technology*, vol. 27, no. 18, pp. 3999–4008, Sep. 2009, doi: 10.1109/JLT.2009.2021562.

[131] R. Wolf, I. Breunig, H. Zappe, and K. Buse, “Scattering-loss reduction of ridge waveguides by sidewall polishing,” *Opt Express*, vol. 26, no. 16, p. 19815, Aug. 2018, doi: 10.1364/oe.26.019815.

[132] R. F. W. Pease, “Electron beam lithography,” *Contemp Phys*, vol. 22, no. 3, pp. 265–290, 1981, doi: 10.1080/00107518108231531.

[133] A. A. Tseng, K. Chen, C. D. Chen, and K. J. Ma, “Electron beam lithography in nanoscale fabrication: Recent development,” *IEEE Transactions on Electronics Packaging Manufacturing*, vol. 26, no. 2, pp. 141–149, Apr. 2003, doi: 10.1109/TEPM.2003.817714.

[134] M. Bahadori *et al.*, “Design Space Exploration of Microring Resonators in Silicon Photonic Interconnects: Impact of the Ring Curvature,” *Journal of lightwave technology*, vol. 36, no. 13, pp. 2767–2782, Jul. 2018.

[135] H. Jayatilleka, M. Caverley, N. A. Jaeger, S. Shekhar, and L. Chrostowski, “Crosstalk Limitations of Microring-Resonator Based WDM Demultiplexers on SOI,” in *IEEE Optical Interconnects Conference*, IEEE, 2015, pp. 48–49.

[136] D. Taillaert, P. Bienstman, and R. Baets, “Compact efficient broadband grating coupler for silicon-on-insulator waveguides,” *Opt Lett*, vol. 29, no. 23, p. 2749, 2004, [Online]. Available: http://www.opticsexpress.org.

[137] Z. Xiao, F. Luan, T.-Y. Liow, J. Zhang, and P. Shum, “Design for broadband high-efficiency grating couplers,” *Opt Lett*, vol. 37, no. 4, 2012.

[138] R. Marchetti *et al.*, “High-efficiency grating-couplers: Demonstration of a new design strategy,” *Sci Rep*, vol. 7, no. 1, Dec. 2017, doi: 10.1038/s41598-017-16505-z.

[139] J. Wu, T. Moein, X. Xu, G. Ren, A. Mitchell, and D. J. Moss, “Micro-ring resonator quality factor enhancement via an integrated Fabry-Perot cavity,” *APL Photonics*, vol. 2, no. 5, May 2017, doi: 10.1063/1.4981392.

[140] C. Ciminelli, V. M. N. Passaro, F. Dell’Olio, and M. N. Armenise, “Quality factor and finesse optimization in buried InGaAsP/InP ring resonators,” *Journal of the European Optical Society*, vol. 4, 2009, doi: 10.2971/jeos.2009.09032.

[141] R. Arefin, M. O. Faruque, R. Al Mahmud, and R. H. Sagor, “Design of a Tunable Ring Resonator with Enhanced Quality Factor,” in *9th International Conference on Electrical and Computer Engineering*, IEEE, Feb. 2017, pp. 369–372.

[142] W.-X. Chen, L. M. Walpita, C. C. Sun, and W. S. C. Chang, “Ion beam etching of InGaAs, InP, GaAs, Si, and Ge,” *Journal of Vacuum Science & Technology B: Microelectronics Processing and Phenomena*, vol. 4, no. 3, pp. 701–705, May 1986, doi: 10.1116/1.583600.

[143] K. Kobayashi, H. Miyatake, and M. Hirayama, “Reactive Ion Etching Techniques for Silicon Sidewall Angle Control in Microengineering,” *J. Electrochem. Soc*, vol. 139, p. 1700, 1992.

[144] J. Fang, G. M. Smith, S. Member, D. V Forbes, and J. J. Coleman, “An InGaAs-GaAs Strained Layer Single Quantum-Well Ring Laser with a Reactive Ion-Etched Tetragonal Cavity,” *Quantum Elec (Woodbury)*, vol. 31, 1995.

[145] Z. Wang *et al.*, “Novel Light Source Integration Approaches for Silicon Photonics,” Jul. 01, 2017, *Wiley-VCH Verlag*. doi: 10.1002/lpor.201700063.

[146] K. M. Yoo, J. Midkiff, A. Rostamian, C. J. Chung, H. Dalir, and R. T. Chen, “InGaAs Membrane Waveguide: A Promising Platform for Monolithic Integrated Mid-

Infrared Optical Gas Sensor," *ACS Sens*, vol. 5, no. 3, pp. 861–869, Mar. 2020, doi: 10.1021/acssensors.0c00180.

[147] J. Levy and K. Roh, "Coherent Array of 900 Semiconductor Laser Amplifiers," in *In Laser Diodes and Applications*, SPIE, Apr. 1995, pp. 58–69. [Online]. Available: http://proceedings.spiedigitallibrary.org/

[148] L. Zeni, S. Campopiano, A. Cutolo, and G. D. ' Angelo, "Power semiconductor laser diode arrays characterization," *Opt Lasers Eng*, vol. 39, pp. 203–217, Feb. 2003.

[149] P. F. Mcmanamon *et al.*, "Optical Phased Array Technology," *Proceedings of the IEEE*, pp. 268–298, Feb. 1996.

[150] P. McManamon, "An overview of optical phased array technology and status," in *Liquid Crystals: Optics and Applications*, SPIE, Sep. 2005, p. 59470I. doi: 10.1117/12.631412.

[151] M. J. R. Heck, "Highly integrated optical phased arrays: Photonic integrated circuits for optical beam shaping and beam steering," *Nanophotonics*, vol. 6, no. 1, pp. 93–107, Jan. 2017, doi: 10.1515/nanoph-2015-0152.

[152] Y. Yi, D. Wu, V. Kakdarvishi, B. Yu, Y. Zhuang, and A. Khalilian, "Photonic Integrated Circuits for an Optical Phased Array," *Photonics*, vol. 11, no. 3, p. 243, Mar. 2024, doi: 10.3390/photonics11030243.

[153] M. Gagino, A. Millan-Mejia, L. Augustin, K. Williams, E. Bente, and V. Dolores-Calzadilla, "Integrated optical phased array with on-chip amplification enabling programmable beam shaping," *Sci Rep*, vol. 14, no. 1, Dec. 2024, doi: 10.1038/s41598-024-60204-5.

[154] J. D. Crow, L. D. Comerford, J. S. Harper, M. J. Brady, and R. A. Laff, "Gallium arsenide laser-array-on-silicon package," *Appl Opt*, vol. 17, no. 3, pp. 479–485, Feb. 1978.

[155] G. H. Duan *et al.*, "Hybrid III--V on Silicon Lasers for Photonic Integrated Circuits on Silicon," *IEEE Journal of selected topics in quantum electronics*, vol. 20, no. 4, pp. 158–170, Jan. 2014.

[156] L. W. Snyman *et al.*, "Optical sources, integrated optical detectors, and optical waveguides in standard silicon CMOS integrated circuitry," in *Silicon-based*

Optoelectronics II, SPIE, Mar. 2000, pp. 20–36. [Online]. Available: https://www.researchgate.net/publication/259241866

[157] I. Charamisinau *et al.*, "High Power Semiconductor Red Laser Arrays for Use in Photodynamic Therapy," *IEEE Journal of Selected Topics in Quantum Electronics*, vol. 11, no. 4, pp. 881–891, Dec. 2005.

[158] C. P. Hsu *et al.*, "A Review and Perspective on Optical Phased Array for Automotive LiDAR," *IEEE Journal of Selected Topics in Quantum Electronics*, vol. 27, no. 1, pp. 1–16, Sep. 2020, doi: 10.1109/JSTQE.2020.3022948.

[159] T. Shimizu *et al.*, "Multichannel and high-density hybrid integrated light source with a laser diode array on a silicon optical waveguide platform for interchip optical interconnection," *Photonics Res*, vol. 2, no. 3, pp. A19–A24, Jun. 2014, doi: 10.1364/prj.2.000a19.

[160] M. G. Oberg, B. Broberg, and S. Lindgren, "InGaAsP-InP Laser Amplifier with Integrated Passive Waveguides," *IEEE J Quantum Electron*, vol. QE-23, no. 6, Jun. 1987.

[161] I. Kim *et al.*, "InGaAs/InGaAsP MQW Optical Amplifier Integrated with Grating-Assisted Vertical-Coupler Noise Filter," *IEEE PHOTONICS TECHNOLOGY LETTERS*, vol. 5, no. 1, pp. 1319–1321, Nov. 1993.

[162] P. W. Juodawlkis, J. J. Plant, R. K. Huang, L. J. Missaggia, and J. P. Donnelly, "High-power 1.5-μm InGaAsP-InP slab-coupled optical waveguide amplifier," *IEEE Photonics Technology Letters*, vol. 17, no. 2, pp. 279–281, Feb. 2005, doi: 10.1109/LPT.2004.839770.

[163] N. Ochiai, J. Shou, and Y. Ozeki, "Axicon-based beam shaping for low-loss nonlinear microscopic optics," *Journal of the Optical Society of America B*, vol. 36, no. 5, p. 1342, May 2019, doi: 10.1364/josab.36.001342.

[164] "Axicons, Edmund Optics, An In-Depth." Accessed: May 29, 2025. [Online]. Available: https://www.edmundoptics.com/knowledge-center/application-notes/lasers/an-in-depth-look-at-axicons/

[165] R. F. Remler, "The Solvent Properties of Acetone," *Ind Eng Chem*, vol. 15, no. 7, pp. 717–720, Jul. 1923, [Online]. Available: https://pubs.acs.org/sharingguidelines